AIX-MARSEILLE UNIVERSITÉ

ECOLE DOCTORALE Physique et Sciences de la Matière

LABORATOIRE D'ASTROPHYSIQUE DE MARSEILLE

Thèse présentée pour obtenir le grade universitaire de docteur

Discipline : Astronomie et Cosmologie

David Corre

Exploring the dawn of the Universe with the Sino-French SVOM mission

Soutenue le 30/11/2018 devant le jury composé de :

Philippe AMRAM	LAM	Président de Jury
Johan FYNBO	University of Copenhagen	Rapporteur
Emeric LE FLOC'H	CEA Saclay	Rapporteur
Karl GORDON	Space Science Telescope Institute	Examinateur
Susanna VERGANI	GEPI	Examinateur
Alain KLOTZ	IRAP	Invité
Olivier LA MARLE	CNES	Invité
Véronique BUAT	LAM	Co-Directeur de thèse
Stéphane BASA	LAM	Directeur de thèse

Numéro national de thèse/suffixe local : 2017AIXM0001/001ED62

Résumé

Les sursauts gamma sont des événements cosmiques les plus énergétiques de l'Univers depuis sa formation. Leur durée varie de quelques millisecondes à plusieurs minutes et l'énergie libérée dans ce laps de temps est équivalente à celle du soleil durant sa vie entière. De par la luminosité extrême de leur émission multi-longueur d'ondes, ils constituent une opportunité unique de sonder l'Univers lointain.
Cette thèse s'inscrit dans le cadre de la préparation de la mission spatiale franco-chinoise SVOM (Space Variable Object Monitor) opérationnelle à l'horizon 2021 et qui aura pour but de détecter et caractériser les sursauts gamma. Cette mission est le successeur de la mission spatiale SWIFT, elle repose sur un ambitieux système de suivi multi longueur d'ondes, combinant des télescopes gamma, X et visible à bord d'un satellite et un complexe réseau de télescopes de suivi au sol dans le visible et proche infrarouge suivant automatiquement et très rapidement les alertes provenant du satellite. Le but est de déterminer la position et la distance du sursaut gamma dans les minutes suivant la détection du sursaut. Une fois détectés, les cas les plus intéressants scientifiquement (e.g, sursaut à très grande distance, sursaut dans un environnement très poussiéreux) seront alors observés par de plus grands télescopes comme le VLT, ALMA, E-ELT ou le JWST pour des observations plus précises et en fonction des moyens d'observation disponible au moment du sursaut.
Cette thèse comporte deux parties distinctes, la première est consacrée au développement d'un logiciel de simulation complet de COLIBRI (Catching OpticaL and Infrared BRIght), un des deux télescopes robotiques de suivi au sol sous responsabilité française, afin d'estimer ses performances scientifiques et de s'assurer que le design optique en cours de développement réponde bien au cahier des charges scientifique. La deuxième partie porte principalement sur l'étude de la propriété des poussières au sein des galaxies dans lesquelles se produisent ces sursauts gamma, ainsi qu'à l'étude de leur activité de formation stellaire.
Le chapitre I présente une introduction générale aux concepts de base de la physique des GRBs, de leur utilisation comme sonde de l'univers lointain et des concepts de base sur la poussière dans les galaxies.

Le chapitre II débute par la présentation des caractéristiques instrumentales de COLIBRI, puis décrit les codes développés pour estimer les performances scientifiques de COLIBRI avant de présenter les performances estimées.
COLIBRI est un télescope robotique de diamètre 1.3m qui sera basé à l'Observatorio Astronómico Nacional au Mexique et opérationnel dès 2020. Ce télescope a pour mission d'observer toutes les alertes provenant du satellite SVOM. Chaque observation doit débuter au plus tard 30 secondes après la réception de l'alerte. L'objectif principal de COLIBRI est de fournir après 5 minutes d'observation la position de la nouvelle source transitoire avec une précision inférieure à 0.5" et de donner une indication sur la distance qui nous sépare d'elle. Il est prévu que ce télescope soit équipé de 3 voies, 2 dans le domaine visible et 1 dans le domaine infrarouge couvrant au total le domaine de longueur ∼400-1700nm.
La contribution de ma thèse à COLIBRI a été de développer des logiciels permettant d'évaluer ses performances scientifiques afin d'aider à l'élaboration de son design optique et de s'assurer qu'il satisfasse le cahier des charges scientifique. Tous les codes ont été développés en Python et sont open-source. J'ai donc développé un Exposure Time Calculator (ETC) qui permet de calculer soit le temps d'exposition, la magnitude de la source soit le signal sur bruit désiré en fonction des deux autres quantités. Cet ETC prend en compte le design optique du télescope au travers de la transmission des éléments optique le constituant (mirroirs, lentilles, coating utilisé, filtre, etc), les caractéristiques du détecteur (rendement quantique, bruit thermique, bruit de lecture, gain) mais également certaines caractéristiques du site d'observation

(transmission de l'atmosphère, luminosité du ciel, seeing). COLIBRI pourra atteindre une magnitude AB d'environ 21.2 et 19.5 dans les bandes r et J pour un temps de pose de 30s et environ 24 et 22 pour un temps de pose d'1 heure (20×30s). L'utilisation de l'ETC sur un échantillon de sursauts gamma détectés par le passé par d'autres télescopes a permis de montrer que la sensibilité de COLIBRI aurait permis de détecter plus de 95% des sursauts gamma de cet échantillon si l'observation avait commencé 1 minute après le trigger des sursauts. Même en commençant à observer 12 heures après le trigger et en dépit de la baisse de luminosité, COLIBRI aurait pu détecter 80% des sursauts dans le proche infrarouge. Dans un avenir proche, cet ETC sera mis à disposition, sur un site internet, des astronomes souhaitant observer avec COLIBRI afin de préparer leurs observations. Afin de modéliser la réponse de COLIBRI pour un sursaut gamma à différents temps d'observation et dans différentes bandes, un code qui simule des courbes de lumière de rémanence de sursauts gamma en suivant le modèle synchrotron est utilisé.
Dans cette thèse, un simulateur d'image a également été développé afin de fournir des images réalistes aux pipelines de réduction des données de COLIBRI lorsqu'ils seront opérationnels. Des champs de vue réalistes peuvent être simulées en effectuant des requêtes dans les catalogues Pan-STARRS, 2MASS, NOMAD-1. A l'aide du code simulant les courbes de lumière de sursauts gamma, il est possible de placer un sursaut gamma n'importe où dans un champ de vue réaliste et de simuler les images brutes de COLIBRI pour ce sursaut à différent temps d'observation. Le simulateur d'image tout comme l'ETC ne sont pas spécifiques à COLIBRI et ont été développé dans l'optique d'être utilisés pour d'autres télescopes visible et proche infrarouge.

Le chapitre III concerne un des objectifs de COLIBRI qui est de fournir une indication sur la distance du sursaut après 5 minutes d'observations. Dans ce but j'ai développé un code permettant de calculer le redshift photométrique à l'aide d'un algorithme MCMC. Ce code est basé sur la détection de 2 signatures spectrales très caractéristiques que sont la transition Lyman-α et le Lyman break à 121.5 × (1+z)nm et 91.2 × (1+z)nm. Ce code a été validé sur un échantillon de 19 sursauts ayant un redshift mesuré spectroscopiquement. Ensuite j'ai quantifié la précision de l'estimation du redshift photométrique par COLIBRI sur 2 échantillons différents de 500 GRBs, l'un empirique basé sur des observations quelques minutes après le trigger et l'autre basé sur le modèle théorique synchrotron qui permet de simuler les sursauts à différents temps d'observation. Pour chaque échantillon, une stratégie d'observation de 5 minutes a été adoptée pour se rapprocher des conditions d'observations de COLIBRI, avec des temps de pose de 30s en faisant défiler les filtres après chaque exposition. Pour les 2 échantillons la précision relative est de l'ordre de 10% pour $3.5 < z < 8$ et environ 10% pour $z > 8$. L'échantillon basé sur le modèle synchrotron montre que la précision reste du même ordre de grandeur à t_0+1min, t_0+12h et t_0+24h, avec t_0 le début du sursaut, même si naturellement le nombre de sursauts détectés diminue. L'analyse refaite sans détecteur proche infrarouge pour l'échantillon empirique montre que la précision relative sur l'estimation du redshift photométrique est du même ordre de grandeur que précédemment mais les sursauts ne peuvent être détecté que juqu'à $z\sim 7$ et les sursauts à faible SNR détectés auparavant à l'aide de CAGIRE ne le sont plus.
La conclusion de ce travail est que la réponse rapide de COLIBRI, moins de 30s après réception de l'alerte, combinée à sa bonne sensibilité et à l'utilisation d'un détecteur proche infrarouge en font un télescope idéal pour la recherche et la détection de sursauts gamma à haut redshift et également ceux dont la grande quantité de poussière à l'intérieur de la galaxie hôte atténue fortement la luminosité. Du fait de cette faible luminosité, ces derniers ne représentent qu'une minorité des sursauts gamma déjà observés car il est nécessaire de les observer dans les dizaines minutes suivant le trigger avant que leur luminoisté ne chute en dessous du seuil de détection de l'instrument. COLIBRI est optimisé pour en détecter davantage. Ces

sursauts sont particulièrement intéressants car ils représentent un moyen unique d'étudier les propriétés de la poussière dans les galaxies très distantes. L'étude des propriétés de la poussière dans les galaxies hôtes de sursauts gamma ainsi que leur activité de formation stellaire constitue la deuxième partie de ma thèse.

Une partie des GRBs que détectera SVOM seront situés dans des galaxies contenant beaucoup de poussières. Dans cette deuxième partie de ma thèse je me suis intéressé à la caractérisation de ces galaxies et des poussières qu'elles abritent. Ce sujet est important pour l'utilisation des galaxies hôtes comme traceur de la population de galaxies lointaines, sélectionnées de façon très differentes de celles détectées dans les grands relevés aveugles. Je me suis particulièrement intéressé à l'étude des propriétés de la poussière dans les galaxies hôtes de sursauts gamma ainsi qu'à leur activité de formation stellaire. Le chapitre IV débute par la définition de deux concepts, l'extinction et l'atténuation associées à l'effet de la poussière sur le flux émis par une source ponctuelle ou un objet étendu respectivement.

Les photons émis par les étoiles au sein des galaxies interagissent avec les grains poussière en étant soient absorbés ou diffusés, ces photons sont donc sont perdus pour l'observateur. Les photons ultraviolet (UV) interagissent plus avec les grains de poussières que les photons visibles et proche infrarouge. La poussière a donc pour effet de "rougir" le spectre observé. Pour un objet ponctuel, comme une étoile, les photons émis dans notre direction qui interagissent avec la poussière sont absordés ou diffusés hors de notre ligne de visée et sont donc perdus. l'effet de la poussière sur le flux avec la longueur d'onde est appelée "courbe d'extinction" et ne dépend que des propriétés de la poussière. Les caractéristiques principales de ces courbes d'extinction sont la présence ou non d'une bosse à 2175Å(bump UV), généralement relié à l'absorption de photons par des graphites, et la forme de la pente UV plus ou moins pentue et reliée à la taille et au type de grain. Un sursaut gamma est considéré comme ponctuel et une courbe d'extinction peut-être mesurée sur sa ligne de visée [Zafar et al., 2011 ; Zafar et al., 2012 ; Zafar et al., 2018b ; Schady et al., 2012 ; Japelj et al., 2016].

Par contre pour un objet étendu, ici la galaxie hôte du sursaut, la lumière nous provient de plusieurs étoiles qui sont localisées à différents endroits. En plus des photons qui seront absorbés et diffusés hors de notre ligne de visée, certains photons émis par une étoile initialement dans une autre direction peuvent être diffusés dans notre ligne de visée. Pour un objet étendu, l'effet de la poussière sur le flux avec la longueur d'onde est appelée "courbe d'atténuation" et dépend donc également de la géométrie de la galaxie (distribution des étoiles et de la poussière) en plus des propriétés intrinsèques de la poussière.

La courbe d'atténuation au sein des galaxies hôtes de sursauts gamma peut être mesurée à l'aide d'observations spectroscopique ou photométrique couvrant le domaine UV et visible. En observant des galaxies locales brillantes en UV Calzetti et al., 1994 ; Calzetti et al., 2000 ont mis en évidence une courbe d'atténuation sans bosse UV et une pente modérée en UV. Depuis lors, de nombreux travaux ont étudié les courbes d'atténuation de galaxies à bas et haut redshift trouvant des cas avec et sans bump UV ainsi que des pentes UV variées. Ces travaux mettent en évidence une non-universalité de la forme de la courbe d'atténuation [Buat et al., 2011 ; Buat et al., 2012 ; Buat et al., 2018 ; Wild et al., 2011 ; Kriek et Conroy, 2013 ; Reddy et al., 2015 ; Reddy et al., 2016 ; Salmon et al., 2016 ; Battisti et al., 2016 ; Battisti et al., 2017].

Les courbes d'atténuation sont également étudiées à l'aide de codes de transfert radiatif qui permettent d'étudier comment leurs formes varient avec différents types de poussière et différentes répartition des étoiles et de la poussière au sein de la galaxie.

L'obtention de la courbe d'extinction et de la courbe d'atténuation pour la même galaxie nous permet d'obtenir une information sur les propriétés de la poussière à l'aide de la première et d'extraire des infor-

mations sur la géométrie de la distribution étoiles-poussière à l'aide de la seconde. Les sursauts gamma offrent une opportunité unique de mesurer les deux pour des galaxies distantes. Le but de notre étude est donc de créer un échantillon de sursauts gamma pour lesquels les courbes d'extinction et d'atténuation sont bien contraintes.

Dans un premier temps, nous avons sélectionné les sursauts gamma dont la courbe d'extinction a été mesurée dans le domaine UV et visible. Notre échantillon contient 30 courbes d'extinction pour lesquelles on a comparé certaines propriétés de la poussière obtenues le long de ligne de visée du sursaut gamma à des propriétes de la galaxie hôte. Les courbes d'extinction ayant une bosse UV sont en général trouvées sur les lignes de visée avec une forte quantité de poussière et dans les galaxies les plus massives. Nous mettons également en évidence que la détection de ces courbes d'extinction s'est faite uniquement lorsque le sursaut gamma a pu être observé dans les 3 heures suivant sa détection. Au-delà seules des courbes d'extinction sans bosse UV avec une pente UV importantes, semblables à celles mesurées sur des lignes de visées du Petit Nuage de Magellan ont été détectées.

Pour étudier la courbe d'atténuation des galaxies hôtes des sursauts gamma, il est nécessaire de bien couvrir l'ensemble de leur spectre d'émission. Ainsi nous avons sélectionné uniquement les 7 galaxies sur les 30 qui ont été détectées dans au moins 5 filtres allant du domaine UV au proche infrarouge dans le référentiel de la galaxie. Pour mesurer la courbe d'atténuation nous avons ajusté des modèles à ces mesures avec le code CIGALE. Nous avons choisi de modéliser l'atténuation dû à la poussière à l'aide de la loi d'atténuation de Noll et al., 2009 dont nous avons montré qu'elle est suffisament flexible pour reproduire une grande variété de courbe d'atténuation provenant d'un code de transfert radiatif [Seon et Draine, 2016] pour différents types de poussières et différentes distribution étoile/poussière.

Pour 6 de nos 7 galaxies la courbe d'atténuation est suffisament bien contrainte et une grande variété de cas est observé avec des pentes UV très variables ainsi qu'une détection possible d'un bump UV pour l'une des galaxies. Certaines courbes d'atténuation sont trouvées plus pentues que les courbes d'extinction. En utilisant la courbe d'extinction pour déterminer le type de poussière nous avons comparé nos courbes d'atténuation avec celles simulées par un code de transfert radiatif afin d'obtenir des informations sur la distribution étoile/poussière au sein de ces galaxies. On observe une diversité de cas et aucune géométrie n'est capable de reproduire toutes nos observations.

En comparant la pente de la courbe d'atténuation avec les propriétés physiques de la galaxie, nous avons trouvé que la pente de la courbe d'atténuation varie à l'inverse de la masse de la galaxie, de son taux de formation stellaire et de son contenu en poussière (ou plus exactement de la quantité absolue d'atténuation).

Afin d'étendre l'étude de ces corrélations, nous avons construit un échantillon de 23 galaxies hôtes et son étude est l'objet du chapitre V. Les résultats confirment les corrélations précédemment trouvées et semblent indiquer qu'elles sont principalement liées à la quantité de poussière à l'intérieur de ces galaxies. Ces résultats sont en accord ceux obtenus à partir de l'observation de galaxies locales et lointaines [Kriek et Conroy, 2013 ; Salmon et al., 2016 ; Salim et al., 2018] ainsi que ceux obtenus à l'aide de codes de transfert radiatif [Witt et Gordon, 2000 ; Chevallard et al., 2013 ; Seon et Draine, 2016]. En comparant nos résultats à ceux des codes de transfert radiatif, nous avons pu obtenir des informations sur la distribution étoile/poussière au sein de ces galaxies. Les courbes d'atténuation pentues sont généralement associées à une distribution locale de la poussière homogène et à une distribution stellaire entourée d'une couche de poussière. Les courbes d'atténuation plus plates sont mieux reproduites avec une distribution locale de poussière hétérogène, i.e. répartie dans des nuages moléculaires.

Un des résultats secondaires de notre analyse a été de trouver une estimation des masses stellaires à l'aide du SED fitting plus faible que celles mesurées pour le Swift Gamma-Ray Burst Host Galaxy Legacy Survey (SHOALS) [D. A. Perley et al., 2016b] qui sont basées sur la luminosité de la bande IRAC1 ($3.6\mu m$) du satellite Spitzer. Sur les 23 galaxies de notre échantillon 6 d'entre elles peuvent être considérées comme des galaxies à sursaut de formation d'étoiles.
Cet étude a permis de démontrer l'intérêt des sursauts gamma pour l'étude des propriétés de la poussière dans les galaxies distantes ainsi que de fournir des informations sur la distribution étoile/poussière au sein de ces galaxies. Nous avons trouvé que la courbe d'atténuation obtenue pour les galaxies hôtes de sursaut gamma n'est pas universelle et est principalement affectée par la quantité de poussière à l'intérieur de la galaxie. Notre étude a également permis de réestimer à la baisse les masses stellaires de ces galaxies par rapport au survey SHOALS. Sur les 23 galaxies de notre échantillon, 17 d'entre elles suivent la séquence principale des galaxies formant des étoiles alors que les 6 autres correspondent à des galaxies à sursaut de formation d'étoiles.

Mots clés : sursauts gamma, galaxies, poussière, simulateur d'image, estimation distance sursauts gamma

Abstract

Gamma-ray bursts (GRBs) are the most energetic cosmic explosions. Due to their extreme luminosity they can be observed very far away in the Universe and thus offer a unique opportunity to probe the dawn of the Universe. Their study impacts many fields in astrophysics, from ultra-relativistic physics to stellar and galaxy evolution among others. This thesis takes place within the french-chinese SVOM (Space Variable Object Monitor) mission dedicated to the detection and study of GRBs to be launched in 2021. SVOM is a ground and space based multi-wavelength observatory with γ- and X rays detectors as well as a visible telescope on-board the satellite. When the satellite will detect a new transient source in γ-rays domain, an alert is sent to two 1m class telescopes on the ground operating in the optical and near infrared (NIR) domain to refine the accuracy on the position of the source and to get an estimate of its distance within the first minutes after the alert. The first part of this thesis is dedicated to the modelling of COLIBRI (Catching OpticaL and Infrared BRIght), a 1.3m optical/NIR robotic follow-up telescope of SVOM, to estimate its scientific performances.

The chapter I introduces basic concepts of GRBs physics, their use as probe of the high-redshift Universe and probe of the ISM of distant star-forming galaxies, and basic concepts on dust extinction.
In chapter II, instrumental details of COLIBRI are first presented, then the Exposure Time Calculator (ETC) and image simulator developed for COLIBRI are described along with the estimated scientific performances of COLIBRI. The chapter III presents an end-to-end simulations aiming at estimating the photometric redshift accuracy of COLIBRI. For this purpose we have developed a photometric redshift algorithm based on the detection of two spectral signatures : Lyman-α and Lyman break respectively located at 121.6×(1+z) nm and 91.2×(1+z)nm. After the validation of the algorithm with observed GRBs, we used two mock samples of GRB light curves to estimate an averaged relative accuracy of $\sim$ 10% for $3.5 < z < 8$ and 14% for z > 8. For z < 3, Lyman-α does not enter the wavelength coverage of COLIBRI and only an upper limit is returned.

The second part of this thesis aims at studying the dust properties of GRB host galaxies (GRBHs) as GRBs offer a unique opportunity to study dust properties of distant galaxies. In chapter IV, we first start by introducing the concept of dust attenuation and how it differs from dust extinction. Then, we checked that the attenuation laws of Noll et al., 2009 ; Salim et al., 2018 is flexible enough to reproduce the variety of shapes of attenuation curves produced by a radiative transfer model [Seon et Draine, 2016] for different types of dust and different geometrical distribution of dust and stars. This study also gives a physical representation of the parameters used in the Noll et al., 2009 ; Salim et al., 2018 attenuation recipe in terms of geometrical distribution of dust and stars in the ISM. Finally, we compared the extinction curves measured along 7 GRB line of sights with the attenuation curves derived for the whole galaxy using a SED fitting code, CIGALE, where the dust attenuation is modelled by the attenuation law of Noll et al., 2009. There is a great variety of shapes with attenuation curves found to have similar, steeper and flatter slope than the extinction curves. By comparing our attenuation curves with the results of the radiative transfer model of Seon et Draine, 2016 different dust/stars geometries are associated to each GBRH. We also found that steep (flat) attenuation curves correlate with low (high) amount of dust attenuation, less (more) massive and star forming galaxies.
In chapter V, we have built a larger sample of 23 dusty GRBHs to study whether these correlations were

due to the small size of the previous sample. We performed a SED fitting for each of these objects and the results confirmed the correlations found with the smaller sample. The derived attenuation curves show a great diversity of shapes illustrating the non-universality of the attenuation curve. We find that the UV slope of the attenuation curve correlates with physical properties of the galaxy with flatter UV slopes associated to higher A_V^{stars}, stellar mass and SFR. There is an indication that the main driver of these correlations is the amount of dust attenuation. Furthermore, we compared our results to the radiative transfer model of Seon et Draine, 2016 and found that at least for two dust models, GRBHs with steep attenuation curves are best reproduced for an homogeneous local dust distribution with stellar sources surrounded by a dust layer. However, GRBHs with flat attenuation curves are best reproduced with a clumpy dust distribution and stellar sources not surrounded by a dust layer. As a by-product of the SED fitting, we found in general lower stellar mass estimates than in the Swift Gamma-Ray Burst Host Galaxy Legacy Survey (SHOALS). From the 23 GRBHs, 17 are following the main sequence of star forming galaxies and 6 are considered starburst galaxies.

Keywords : gamma-ray bursts, galaxies, dust, photometric redshift, optical/NIR telescope modelling

Remerciements

Je tiens tout d'abord à remercier mes deux directeurs de thèse Stéphane Basa et Véronique Buat pour l'aide et le support que vous m'avez apporté au cours de ces trois ans. Tout d'abord, merci Stéphane de m'avoir ouvert les portes de l'astrophysique, laisser manipuler IRiS :), pour ton soutien et tes conseils tout au long de ma thèse et c'est avec plaisir que je continuerai à collaborer avec toi.
Merci Véronique pour ta patience, ton soutien dans les moments difficiles, les passionnantes et innombrables discussions sur les propriétés de la poussière interstellaire. Ce n'était pas évident de faire le lien entre les deux parties de la thèse et je pense qu'on y est plutôt bien arrivé :)
Je remercie également Alain Klotz pour ses conseils et les codes qu'il m'a donné au début de ma thèse, cela m'a beaucoup aidé.

Merci à toutes les personnes que j'ai croisé pendant ces trois années au LAM, Florence pour ta gentillesse et ton efficacité, Samuel pour ta disponibilité et tes conseils, Sara pour tes conseils en stats et ta source intarissable de cartoons, Sarah, Abhi et les sorties plongées, les deux Anna, Darko, Mario, Jean-Charles et Simon pour les conseils Python, Denis, Debopam, Fangting, Arturo, Vincent, Paul, Siju. Je remercie également ceux dont j'ai oublié de citer le nom ici.

Je remercie également les membres du Jury d'avoir accepté de prendre le temps de lire ma thèse et de la juger. Merci à tous pour vos conseils et suggestions.

Et enfin je remercie ma famille pour leur aide et leur soutien indéfectible, notamment ma mère sans qui je n'aurais pu écrire ces lignes aujourd'hui.

Table des matières

Table des figures

Liste des tableaux

1. The GRB phenomenon

1.1. GRB discovery

The first gamma-ray burst (GRB) was fortuitously discovered by the US military Vela satellites in 1967, and published in 1973 [Klebesadel et al., 1973], whose mission was to detect atmospheric nuclear detonations to ensure compliance with the Partial Test Ban Treaty signed with the Soviet Union in 1963. In the following two decades, this new phenomenon was further observed with γ-rays and X-rays detectors, which allowed scientists to start characterising GRBs : their spectra were following a power law shape [Cline et al., 1973], their temporal duration followed a bimodal distribution and they were isotropically distributed in the sky suggesting an extragalactic origin [Mazets et al., 1981]. However the sample was too small and heterogeneous to draw firm statistical conclusions.

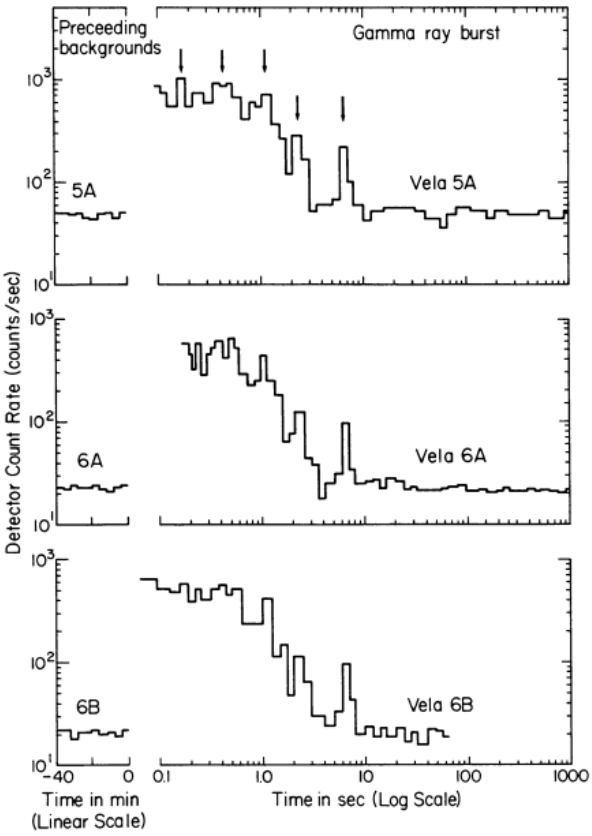

Figure I.1– GRB discovery : light curves of a GRB recorded at three Vela satellites on August 22, 1970. (Credit : Klebesadel et al. 1973)

In 1991, the NASA launched the Compton Gamma-Ray Observatoy (CGRO) dedicated to the observation of the high-energy Universe with four instruments sensitive to the energy range from 30 keV to 30 GeV, and among them the Burst And Transient Source Experiment (BATSE) especially designed for the study of GRBs. During its nine years of operation BATSE detected 2704 GRBs leading to the first revolution of our knowledge of GRBs. First, it confirmed the classification of GRBs in two different classes based on their duration on a large and homogeneous sample [Fishman et al., 1994] : short GRBs are

defined by $T_{90} < 2$ s and long GRBs by $T_{90} > 2$ s where T_{90} corresponds to the time over which 90% of the burst counts are recorded (Fishman et al. 1994, see Figure I.2). The short bursts tend to have a higher hardness ratio than the long ones (Kouveliotou et al. 1993, see Figure I.2). Secondly, it confirmed the isotropy of the angular distribution with a more sensitive instrument and on a larger sample (see Figure I.3). Both the isotropic distribution of faint and bright GRBs and large number of GRBs put severe constraints on models predicting a Galactic origin with neutron stars in the galactic halo. Consequently, the hypothesis of an extragalactic origin became more credible, but the gigantic amount of energy at stake remained difficult to explain.

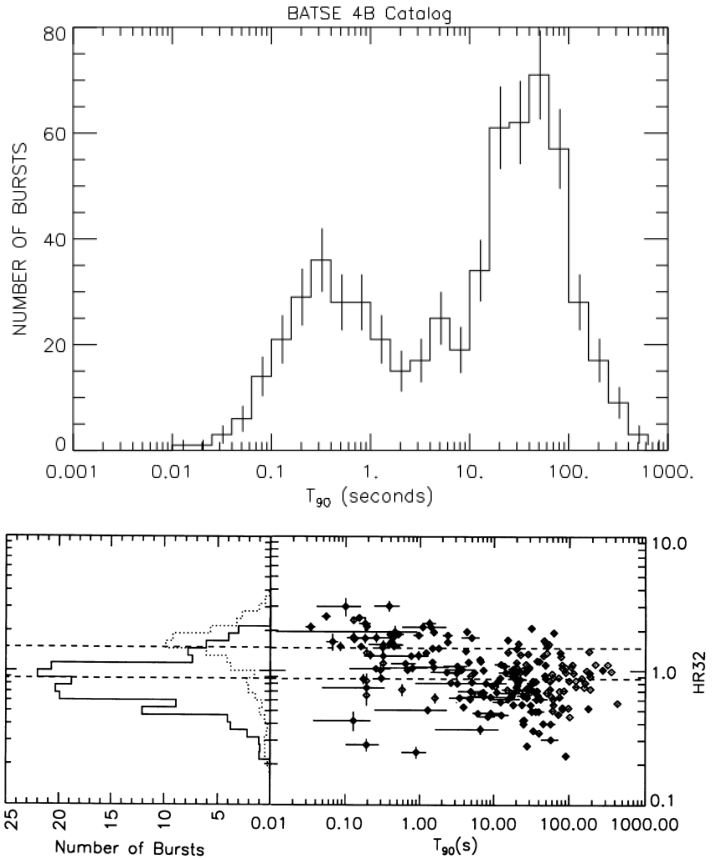

Figure I.2– *Top :* Distribution of T_{90} from the 4B BATSE Catalog [Meegan et al., 1998]. T_{90} corresponds to the time over which 90% of the burst counts are recorded. *Bottom :* Distribution of hardness as a function of T_{90}. The hardness ratio is defined as the ratio of counts in two BATSE channels : Channel 3 (100-300 keV) divided by Channel 2 (50-100 keV). (Credit : Fishman et al. 1994 ; Kouveliotou et al. 1993)

The launch of BeppoSAX satellite in 1996 by the Italian Space Agency, with an important contribution of the Netherlands Agency for Aerospace programs, opened the GRB afterglow era and eventually closed the debate on the origin (Galactic or extragalactic) of GRBs. The major advantage of BeppoSax over previous missions was its capability to obtain arcminute localisation through a combination of large field of view instruments to first detect the GRB and X-ray detectors with smaller fields of view to then refine the localisation. On February 28, 1997 BeppoSax detected the first X-ray counterpart of a GRB detected a few hours before [Costa et al., 1997]. The localisation of the GRB was sent to ground-based telescopes who further discovered the first optical counterpart of a GRB [Groot et al., 1997 ; van Paradijs et al., 1997]. Less than 3 months later, the brightness of the afterglow of GRB 970508 peaking about 40h after the trigger allowed the measurement of its spectrum with the Keck Telescope by M. R. Metzger et al., 1997 which exhibited absorption lines of FeII, MgI and MgII and permitted the first measurement of a

spectroscopic redshift at z=0.767-0.835. This closed the debate on the distance and the next step was to investigate the mechanism releasing such a huge amount of energy in a few seconds.

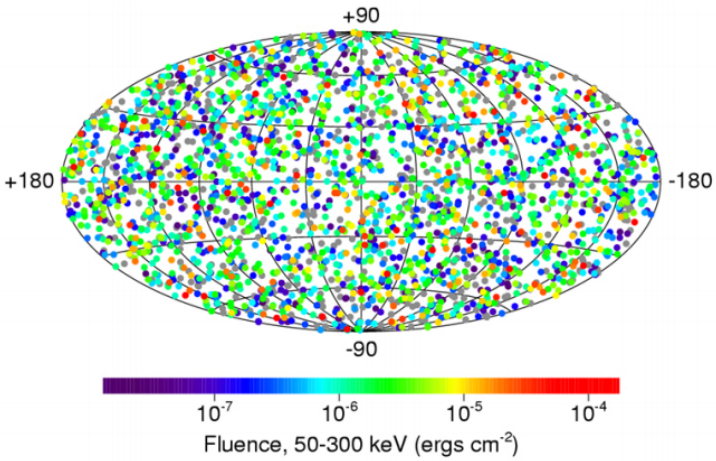

Figure I.3– Angular distribution of 2704 bursts in the BATSE catalog projected on an Aitoff-Hammer projection in Galactic coordinates. The color encodes the fluence. (Credit : NASA)

1.2. The fireball scenario

As GRBs are extragalactic events, their fluxes imply gigantic amount of energy which can reach up to 10^{54-55}erg if the emission is isotropic and is released in a few seconds. This is more than the energy produced by the Sun during its entire lifetime. This makes GRBs the most energetic explosions in the Universe. An important constraint on the source comes from the millisecond variability measured in GRB γ-ray light curves. Indeed, the shortest time fluctuations, Δt, of an astronomical source constrain its size to be $R < c\Delta t$, because all temporal fluctuations faster than the light crossing time of the source are smeared out by propagation delays within the source. Consequently, the millisecond variability observed for GRBs implies an emitting region with size R <300 km for a non-relativistic source. Such huge amount of energy released in a compact region imply the formation of a high temperature ejecta, a "fireball", mostly consisting in high energy photons and electron-positron pairs via $\gamma\gamma \rightarrow e^{-}e^{+}$. The creation of electron-positrons pairs from high energetic photons is very efficient to suppress photons with an energy above ∼1 MeV. However, such photons have been observed in many GBRs. This problem was solved by considering that the fireball is expanding relativistically in the circumburst medium (CGM) in a collimated jet with Lorentz factors $\Gamma \sim$ 100-1000 [Paczynski, 1986; Piran, 1999]. A relativistic expansion provides an efficient way of reducing the pair creation as the size of the typical size of the emitting region is now $\Gamma^2 c\Delta t$ instead of $c\Delta t$ which reduces the density of photons and in the moving frame of the fireball photons are softer by a factor Γ. The typical size of the source became $R < \Gamma^2 c\Delta t = 3 \cdot 10^6$ km for a relativistic flow with a Lorentz factor, Γ, of 100 and $\Delta t \sim$ 1ms [Vedrenne et Atteia, 2009] . The release of the emission through a collimated jets also significantly reduces the energy reservoir of the central engine relaxing the energetic constraint on the progenitor.

The fireball shock model based on internal and external shocks was first introduced by Rees et Meszaros, 1992 and Rees et Meszaros, 1994 respectively and a detailed review is given in Mészáros, 2006. Internal shocks aim at reproducing the variable prompt γ-ray emission. These shocks occur inside the relativistic ejecta between shells ejected from the central engine at different Lorentz factors, when a faster shell overtakes a slower one. The prompt emission of γ-ray is mostly produced by synchrotron and inverse Compton radiation from electrons accelerated to relativistic velocities within internal shocks in the fireball [Rees et Meszaros, 1994]. External shocks result of the interaction of these shells with the

CGM which produces the multi-wavelength afterglow emission. They occur when the GRB jet is slowed down by the surrounding CGM : either a cold interstellar medium (ISM) or a stratified wind ejected by the progenitor [Rees et Meszaros, 1992]. Then two shocks form, a forward shock propagating into the surrounding CGM and a reverse shock propagating back into the ejecta. The electrons accelerated within these shocks eventually cool through synchrotron emission producing the multi-wavelength (from X-rays to radio) afterglow emission. The different phases of the fireball model are illustrated in Figure I.4.
To reproduce the observed non-thermal spectra of GRBs, the fireball must have a small baryonic contamination, $10^{-4}\ M_{\odot}$ at most. These baryons transform the initial radiative energy into kinetic energy, and later on their interaction with the surrounding medium within the relativistic shocks allow the fireball energy to be radiated in a non-thermal spectrum [Rees et Meszaros, 1992].
The launch of the Neil Gehrels Swift Observatory by the NASA in 2004 [Gehrels, 2004], led to the discovery of new features in some GRB light curves that were not anticipated by the fireball model : shallow temporal decay phases in the early X-ray afterglow, very luminous X-ray flares, achromatic break between X-ray and optical afterglows [Nousek et al., 2006 ; B. Zhang et al., 2006 ; Chincarini et al., 2007]. This suggests a more complex evolution of the jet dynamics and of the shocked regions than the standard fireball (some theoretical issues of the fireball model are discussed in Mészáros 2006). Although more complexity is required for some GRBs, the fireball shock model offers the most successful theoretical framework to reproduce both prompt and afterglow emission for the long and short class GRBs. However, it is independent of the nature of the central engine powering the GRB. In the next section, the most favoured progenitors are discussed.

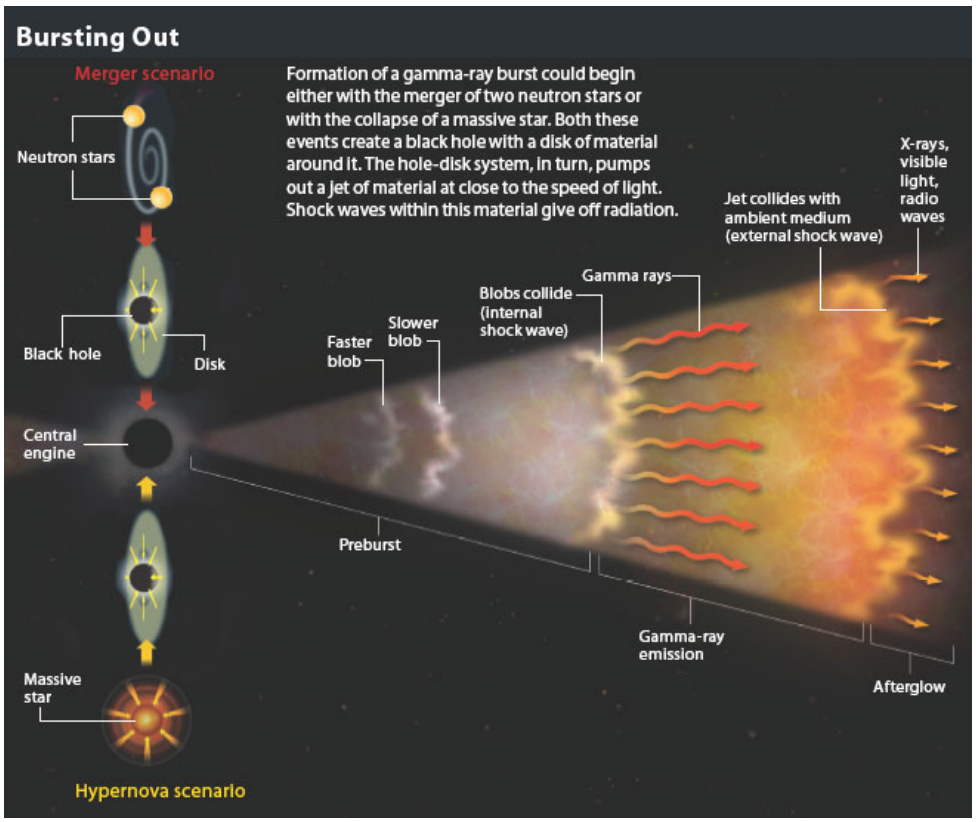

Figure I.4– Illustration of the internal-external shock fireball model. On the left are illustrated the two most favoured progenitors leading to the creation of a black hole with an accretion disk. (Credit : Gehrels et al., 2007)

1.3. GRB progenitors

The main difficulty to understand the nature of the progenitors lies in the fact that the GRB emission is released far from the central engine. Consequently we cannot observe directly the progenitor and its properties are inferred by indirect means. The shortest time variability of the order of the millisecond implies a compact central engine. The total duration of the burst lasting up to few tens of seconds implies that the central engine has a prolonged activity. The non repetition of these events implies that the progenitor is likely to be destroyed. For these reasons, GRBs were associated with a newborn black hole with a massive accretion disk ($\sim 0.1 M_{\odot}$). This system can arise from the coalescence of binary compact stellar remnants [Narayan et al., 1992] or the explosion of a massive star such as collapsars [Woosley, 1993]. Both scenarios result in a spinning black hole with the debris forming an accretion disk. The GRB can be the result of the release of the gravitational energy of the matter falling in the black hole. An alternative source of energy can be the spin energy of the black hole through the Blandford-Znajek mechanism [Blandford et Znajek, 1977].
In the following we briefly review the two most successful models associated to the long and short GRBs : the collapsar model and the merger of compact objects respectively.

1.3.1. Collapsar model

A collapsar is a very massive, at least 20 to 30 $M_{\odot}$, and fast rotating star, likely Wolf-Rayet star, whose iron core directly collapses to form a black hole at the end of its stellar evolution [Woosley, 1993]. After the collapse, the residual matter of the progenitor is accreted by the black hole. After a few tens to hundreds of seconds after the collapse, the accretion of matter at the polar regions becomes less intense and a partial evacuation of matter in the polar regions is achieved with the fast rotation of the black hole [Fryer et al., 1999]. The energy in the accretion disk can then be dissipated by neutrinos annihilation which can produce relativistically expanding blastwave of radiation and pairs along the rotational axis [Woosley, 1993]. To avoid the problem of a significant baryonic contamination in the fireball, the progenitor should have lost its hydrogen envelope through stellar winds before the collapse, which relates the progenitor of collapsars with those of type Ib/Ic supernovae (SN) characterised by a lack of hydrogen lines in their spectra [MacFadyen et Woosley, 1999]. Further constraints on the progenitor star are provided by numerical simulations which showed that a collapsar can produce an accretion disk powering a GRB only if the collapsing core has a high angular momentum [MacFadyen et Woosley, 1999]. However Wolf-Rayet stars are expected to have strong stellar winds which reduce the angular momentum by mass loss. This mass loss is function of the metallicity and GRBs can be produced by Wolf-Rayet stars with low metallicities [Hirschi et al., 2005 ; Yoon et Langer, 2005 ; Woosley et Bloom, 2006]. An other mechanism involves a binary system where the binary companion removes the hydrogen envelope of the progenitor star while its angular momentum is preserved [van Dyk et al., 1996 ; Fryer et al., 2007]. A more detailed review of the collapsar model can be found in Fryer et al., 1999 ; W. Zhang et al., 2004 ; Woosley et Bloom, 2006 ; Fryer et al., 2007.
The strongest observational evidence that links GRBs to the death of massive stars is the association of a GRB with a SN. The first convincing association was for the long GRB 980425 and SN 1998bw, where the SN occurred approximately one day after the GRB within the GRB localisation error box with a very low chance of coincidence of 10^{-4} [Kulkarni et al., 1998 ; Galama et al., 1999]. Unfortunately the afterglow was not detected and so no comparison of the spectral features could be made with the spectrum of SN 1998bw . The first unambiguous association of a GRB with a type Ic SNe was made 5 years later for the long GRB 030329 and SN 2003dh [Stanek et al., 2003 ; Hjorth et al., 2003]. The spectrum of

the afterglow evolves from a typical power-law continuum to a spectrum very similar to the one of SN 1998bw a few days later (see Figure I.5), providing an unambiguous evidence of the emergence of a SN in the GRB afterglow spectrum a few days after the GRB detection. A few other spectroscopic GRB/SN associations has been made with the launch of Swift (e.g. Xu et al. 2013 ; J. Greiner et al. 2015). A spectroscopic detection of a GRB/SN connection is only possible at low redshift ($z \lesssim 0.5$), and at larger redshift the evidence of GRB-SN association is obtained with the presence of bumps in GRB afterglow light curves appearing a few tens of days. These bumps correspond to an extra emission component which are well modelled by a SN emission [Zeh et al., 2004]. A more detailed review of the GRB/SN connection can be found in Hjorth, 2013.

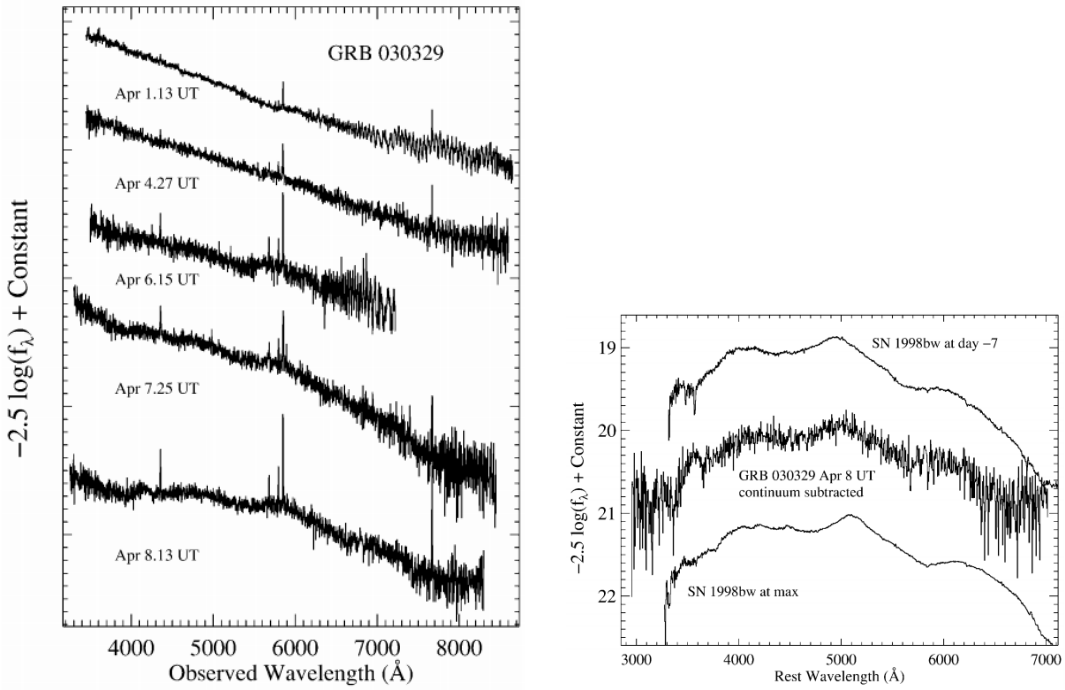

Figure I.5– *Left :* Spectrum of GRB 030329 taken at different time after the burst. The early spectra is well approximated by a power-law continuum ($F_\nu \propto \nu^{-0.9}$). After April 5, broad peaks typical of SN spectra appear. *Right :* Spectrum of GRB 030329 measured the 8th of April with continuum subtracted. The spectrum shape is very similar to the one of SN 1998bw a week before maximum light. (Credit : Stanek et al. 2003)

1.3.2. Merger scenario

A fast rotating black hole with an accretion disk can also be produced by the coalescence of two compact objects [Paczynski, 1986 ; Eichler et al., 1989]. The most frequently discussed scenarios are the coalescence of two neutron stars (NS-NS) or a black hole with a neutron star (BH-NS). Short GRB afterglows are much less luminous than the long GRB ones making the detection of an optical spectrum more difficult and rare. Therefore the coalescence of two compact objects was only supported by some indirect evidence : the estimated rate of NS-NS merger [Phinney, 1991 ; Narayan et al., 1992 ; van den Heuvel et Lorimer, 1996] was found similar to the rate of GRBs [Fenimore et al., 1993] ; large offsets between GRB position and the host galaxy centre, larger than for long GRBs [Bloom et Prochaska, 2006 ; Fong et Berger, 2013 ; Tunnicliffe et al., 2014] ; short GRBs are found in all types of galaxies, and a significant fraction is even found in elliptical galaxies with old stellar population and no ongoing star formation [Berger et al., 2007 ; Berger, 2009] suggesting that the stellar population of short GRB host galaxies is older than in the long GRB host galaxies [Bloom et Prochaska, 2006 ; Prochaska et al., 2006] ; the lack of short GRB-SN association (see, e.g., [D. B. Fox et al., 2005 ; Rowlinson et al., 2010]. A

more convincing evidence that the progenitor of short GRB is a compact binary merger was the first clear indication of a kilonova associated with the short GRB 130603B which is responsible for a re-brightening of the NIR afterglow about 9 days after the burst [Tanvir et al., 2013]. Indeed, the theoretical framework of a compact binary merger predicts that the merger will create a significant quantity of neutron-rich radioactive species, whose decay should form a transient emission a few days after the burst [Rosswog et al., 1999 ; B. D. Metzger et al., 2010]. The ultimate observational evidence that compact binary mergers are the progenitors of short GRBs was obtained recently with the joint observation of the gravitational wave GW 170817 with the short GRB 170817A resulting of the coalescence of 2 neutron stars with a total mass system of $\sim 2.8\ M_{\odot}$ [Abbott et al., 2017].
In the following we will only consider long GRB and the term GRB will refer to the long class type.

1.4. Host galaxies population

1.4.1. The early picture...

The first samples of long GRB host galaxies that were studied contained almost exclusively blue (UV-bright), low mass, irregular galaxies with active star formation and long GRBs were located close to the most UV bright regions [Fruchter et al., 1999 ; Le Floc'h et al., 2003 ; Berger et al., 2003 ; Christensen et al., 2004 ; Tanvir et al., 2004 ; Fruchter et al., 2006 ; Savaglio et al., 2009]. Lyman-α emission properties of the host galaxies indicated a preference for GRB progenitors to be metal-poor [J. P. Fynbo et al., 2003], and measurement of sub-solar metallicities [Prochaska et al., 2004 ; Sollerman et al., 2005 ; Gorosabel et al., 2005] further supported the predictions of the collapsar model. Whether this population of GRB host galaxies were representative of the general star-forming population was highly debated. As they are found on average bluer, less massive, fainter, younger and less less metal-rich than the general star-forming population several studies concluded that were biased tracers of star formation due to the lack of red, obscured and luminous galaxies [Fruchter et al., 1999 ; Le Floc'h et al., 2003 ; Berger et al., 2003 ; Christensen et al., 2004 ; Le Floc'h et al., 2006 ; Fruchter et al., 2006]. However, Savaglio et al., 2009 considered that blue, faint, and young galaxies are the most common galaxies that existed in the past, and did not find evidence that GRB host galaxies belonged to a special population using the largest sample at the time of 46 GRB hosts mostly at $z \lesssim 1.5$.

1.4.2. ... got dusty

In the late 1990s early 2000s the follow-up of GRB was not fully optimised and very often there was a long delay between the GRB detection at high energy and the beginning of the optical follow-up with ground telescopes. Moreover the follow-up was performed in the visible domain only and not in the NIR (see e.g. TAROT [Boer et al., 2003]). Consequently, there was a selection effect against high-z GRBs, that can only be detected in NIR, and dusty GRBs, whose flux is heavily extinguished by dust and falls below the instrument sensitivity more rapidly than non-extinguished GRBs (emitting the same amount of energy). In the mid 2000s early 2010s, the apparition of fully robotic telescope (e.g. REM [Zerbi et al., 2004] or semi-robotic telescopes (e.g. PAIRITEL [Butler et al., 2006], GROND [J. Greiner et al., 2008] and RATIR [Butler et al., 2012]) equipped with optical/NIR detectors and located at different latitudes, allowed a more systematic and rapid follow-up of the GRB alerts coming from the Swift Observatory. They allowed to detect many dusty GRB afterglows with visual extinction $A_V > 1$ mag (e.g. Krühler et al. 2008 ; D. A. Perley et al. 2009 ; J. Greiner et al. 2011) and detections of GRBs up to $z \sim$ 8-10 [Salvaterra et al., 2009 ; Tanvir et al., 2009 ; Cucchiara et al., 2011 ; Tanvir et al., 2018]. The host galaxy population associated to the dusty GRBs is more massive, suffering more dust attenuation, redder and more metal-rich than the host galaxy of bright GRB optical afterglow [Krühler et al., 2011 ;

Hjorth et al., 2012 ; Rossi et al., 2012 ; D. A. Perley et al., 2013]. The discovery of this new population different from the initial one along with spectroscopic measurements of solar or super-solar metallicty host environment [Levesque et al., 2010 ; Elliott et al., 2013 ; Schady et al., 2015] involved that GRB host galaxies are less biased tracers of star formation than initially thought. The determination of the fraction of GRBs whose optical afterglow is not detected because of intermediate to high dust extinction can give us an estimate of the fraction of this red, massive, metal-rich population in the total GRB host population. Defining dark bursts as bursts with an optical to X-ray slope β_{OX}<0.5 [Jakobsson et al., 2004], J. P. Fynbo et al., 2009 estimated the fraction of dark bursts to be between 25-42%. This estimation was confirmed by J. Greiner et al., 2011 who found a fraction of 25-40% depending on the definition of dark bursts, either β_{OX}<0.5 [Jakobsson et al., 2004] or $\beta_{OX} < \beta_X - 0.5$ with β_X the X-ray spectral index [van der Horst et al., 2009]. The darkness of an optical GRB afterglow can be either due to an intrinsic low luminosity of the afterglow, a large amount of extinction along the GRB line of sight or a burst located at high redshift and thus not detected in optical due to Ly-α blanketing and absorption in the intergalactic medium (IGM) [J. U. Fynbo et al., 2001]. J. Greiner et al., 2011 showed that $\sim$ 75% of these dark bursts are due to the amount of extinction along the GRB line of sight. Melandri et al., 2012 reached similar conclusions, they found a dark burst fraction of 20-36%, depending on the definition, mostly caused by dust extinction for a sample of GRBs selected with high-energy criteria. On a sample of 53 GRBs complete in redshift and selected from high-energy parameters of the prompt emission and therefore not biased against dusty lines of sight, Covino et al., 2013 estimated that half the GRBs have a visual extinction $A_V > 0.4$ mag and $\sim$25% above 1 mag. This suggests that the red population might account for approximately one quarter to one third of the overall GRB host galaxy population.

Currently, long GRB host galaxies have been found with stellar masses ranging from $\sim 10^8 M_\odot$ for optical bright GRBs up to $\sim 10^{11} M_\odot$ for dusty GRBs (e.g. Krühler et al. 2015 ; D. A. Perley et al. 2016b. They are generally sub-solar [Graham et Fruchter, 2013 ; Krühler et al., 2015 ; Japelj et al., 2016 ; Vergani et al., 2017] but solar and super-solar metallicities are also found (e.g. Krühler et al. 2012 ; Savaglio et al. 2012 ; Elliott et al. 2013 ; Krühler et al. 2015 ; Vergani et al. 2017). Because of the selection effects in optical, two X-ray selected samples were built to study properties of GRB host galaxies in a unbiased way : The Optically Unbiased GRB Host survey (TOUGH, Hjorth et al. 2012) and the Swift GRB Host Galaxy Legacy Survey (SHOALS, D. A. Perley et al. 2016a). They contain 69 and 119 GRBs respectively and SHOALS is the largest sample of GRB host galaxies up to now.

2. GRBs as probes of the high-redshift universe

2.1. Tracer of star formation

Due to their extreme luminosity, GRBs can be detected at very high distances and at present GRB 090423 is the farthest away GRB with a spectroscopic redshift measurement of $8.26^{+0.07}_{-0.08}$ [Salvaterra et al., 2009 ; Tanvir et al., 2009]. Their association with massive stars naturally implies that they offer a unique probe to study star formation up to very high redshift. The star formation activity of a galaxy can be inferred from its location on the main sequence of star-forming galaxies, typical star-forming galaxies exhibit a linear correlation between their star formation rate (SFR) and stellar masses, galaxies above the sequence are forming much more stars than expected for typical galaxies and galaxies below the sequence are only forming few to very few stars (see Figure I.6, e.g. Schreiber et al. 2015).

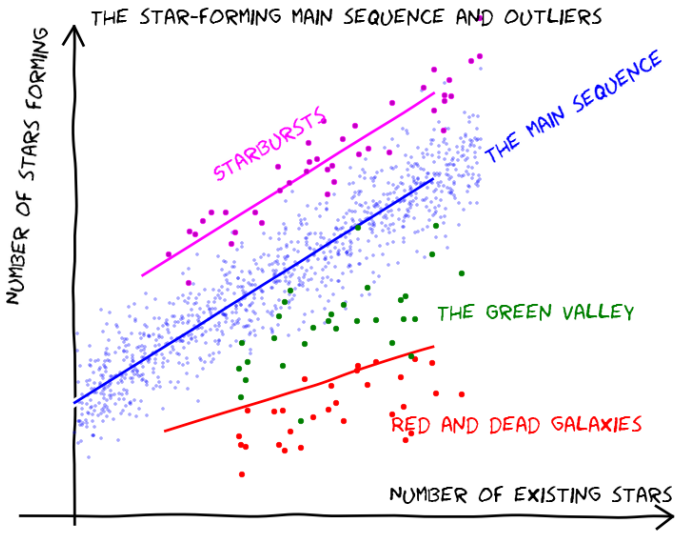

Figure I.6– Main sequence of star-forming galaxies. Normal galaxies are forming stars at a rate proportional to the number of stars they already formed (blue points). Galaxies forming stars at a higher rate are called starbursts (purple points). Galaxies that are forming few stars are located in the region called the "green valley" (green points). Galaxies that are not forming stars anymore are called quiescent galaxies (red points). (Credit : Cosmic Assembly Near-infrared Deep Extragalactic Legacy Survey (CANDELS))

As we already discussed, selection effects and low statistics are inherent to the study of long GRB host galaxies. Consequently, the question whether long GRBs are representative of normal star-forming galaxies is still debated (e.g. Le Floc'h et al. 2003; Michałowski et al. 2012; Schulze et al. 2015; Vergani et al. 2015; Japelj et al. 2016). The general picture is that GRB host galaxies at $z \lesssim$1-2 have in average lower stellar mass than normal star-forming galaxies, and sub-solar metallicities suggesting a high-metallicity aversion for long GRB host galaxies but without absolute threshold as some solar or even super-solar galaxies are found Graham et Fruchter, 2013; D. A. Perley et al., 2013; Boissier et al., 2013; Krühler et al., 2015; Vergani et al., 2017. A possible evidence of a metallicity threshold of $\sim 0.7\ Z_{\odot}$ has been found in Vergani et al., 2017. However, after the reinvestigation of stellar masses in Palmerio et al., soumis, derived from SED fitting instead of IRAC1 luminosities as previously, there was no evidence of a threshold anymore (see left panels of Figure I.7), although GRB hosts metallicities are still found lower than for field galaxies. The stellar mass-metallicity relation has also been discussed in Arabsalmani et al., 2018 where they found GRB host galaxies metallicities to be lower but still within the scatter observed for typical star-forming galaxies (see right panels of Figure I.7). Based on a sample of long GRBHs with dusty GRBs, L. K. Hunt et al., 2014 found that at $z \gtrsim 1$ GRBHs were unbiased tracers of star formation whereas at $z \lesssim 1$ GRBHs are biased towards lower stellar masses. Based on the largest sample of GRB host spectra observed with the X-shooter instrument [Vernet et al., 2011] at the Very Large Telescope in Paranal, Krühler et al., 2015 found that GRB host properties at low redshift ($z <$ 1-2) are influenced by the tendency of GRBs to avoid the most metal-rich environments. They concluded that given the decrease of metallicity with the redshift, normal star-forming galaxies are expected to have $Z \sim Z_{\odot}$ at $z \sim 3$ and thus GRBHs should probe most of the star formation at $z \gtrsim 3$, reaching similar conclusions as J. P. U. Fynbo et al., 2008; Schulze et al., 2015; Trenti et al., 2015.

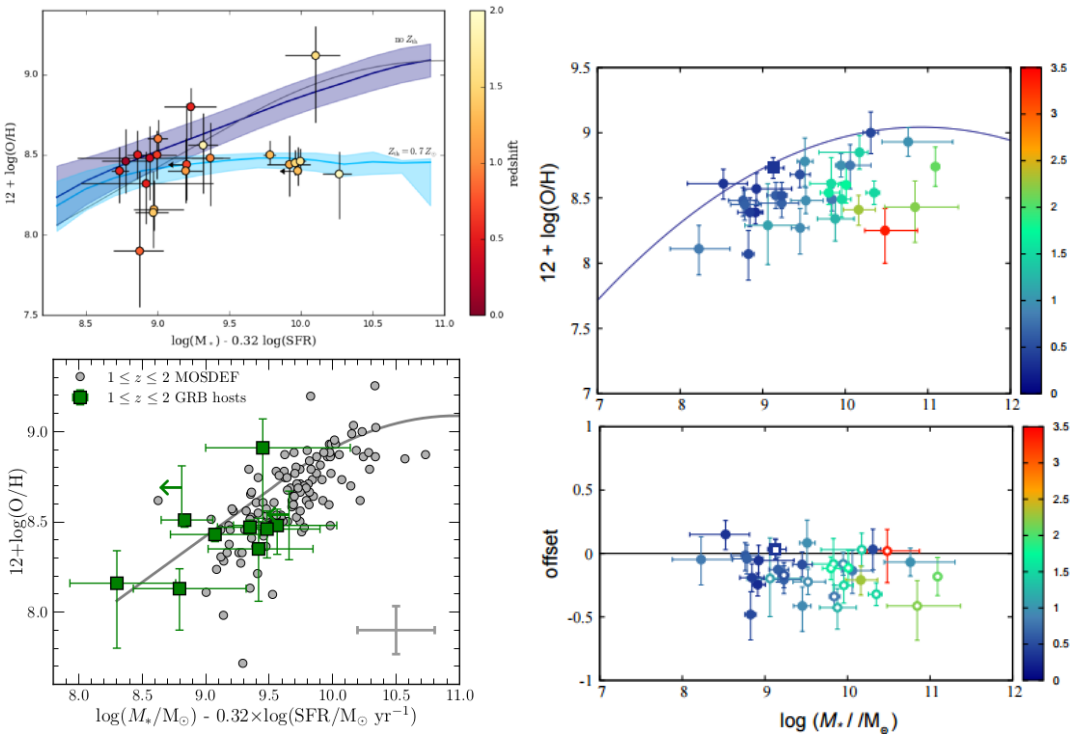

Figure I.7– ***Left :*** The fundamental metallicity relation(FMR) plane. *Top :* host galaxies of the Swift/BAT6 sample of LGRBs at z < 2 in Vergani et al., 2017. Metallicities are measured with the Maiolino et al., 2008 method, SFR measured from H_α luminosities [Krühler et al., 2015] and stellar masses are derived from IRAC1 luminosities [D. A. Perley et al., 2016b]. The gray line corresponds to the FMR found by Mannucci et al., 2010 ; Mannucci et al., 2011. The dark blue curve and area correspond to FMR relation and of its quartiles obtained using the simulation of Campisi et al., 2011 and the cyan curve and area correspond to the best-fit model results [Vergani et al., 2017]. *Bottom :* same sample as inVergani et al., 2017 with additional hosts between 1 < z < 2, metallicities and SFR are derived the same way as in Vergani et al., 2017 but stellar masses are derived from SED fitting [Palmerio et al., soumis]. ***Right :*** The stellar mass - metallicity (MZ) relation for 33 GRB hosts from Arabsalmani et al., 2018. Metallicities are derived with the Maiolino et al., 2008 method. In the upper panel, the solid line corresponds to the MZ relation at z = 0 from Maiolino et al., 2008. Lower panel shows the offsets between the metallicity measurements of GRB hosts and the MZ relation at the GRB redshift. (Credit : Vergani et al. 2017 ; Palmerio et al. soumis ; Arabsalmani et al. 2018)

GRBs are also used to study the cosmic star formation rate density. They are fainter galaxies than in typical galaxy surveys so they provide an insight of the contribution of faint galaxies to the cosmic SFR. Different studies found a larger SFR density at z > 4 compared to galaxy surveys, after a careful calibration at z < 4, suggesting the important role played by faint galaxies during reionization [Yüksel et al., 2008 ; Kistler et al., 2009 ; Trenti et al., 2012].

2.2. GRBs as probe of the ISM of distant star forming galaxies

Apart from being extremely luminous and indicating distant star-forming regions, GRB afterglows also provide a unique insight of the interstellar medium (ISM) of distant star-forming galaxies. Indeed, they can occur in very deep regions of the galaxies and their bright and featureless simple power-law spectrum can clearly imprint absorption features by intervening dust, gas and metals. Moreover, the afterglow fades rapidly allowing the study of the host galaxy once the afterglow does not contribute to the host galaxy luminosity anymore. The key point to study the ISM with GRBs is a rapid multi-wavelength follow-up to observe the afterglow in the first tens of minutes after the burst when it is very bright, permitting to collect valuable information from spectroscopic observations of the afterglow in only 1 or 2 hours observing time. Such an optimised observation strategy was possible for the time with the Neil Gehrels Swift observatory which could very rapidly provide arcsecond positions to the community thanks to a

rapid acquisition of optical and X-ray observations with UVOT and XRT. Then several ground facilities, such as GROND and X-shooter, were triggered to perform multi-wavelength observations of the early afterglow. The absorption imprint left on the GRB afterglow spectrum by intervening materials can be used to study the kinematics and ionization state of various intervening absorption systems (e.g. A. J. Fox et al. 2008 ; Thöne et al. 2010 ; Schady et al. 2011), chemical composition (e.g. Rau et al. 2010 ; Thöne et al. 2013 ; Cucchiara et al. 2015) and study the dust properties through the extinction curve measured along the GRB line of sight (e.g J. Greiner et al. 2011 ; Schady et al. 2012 ; Covino et al. 2013 ; Japelj et al. 2016 ; Zafar et al. 2011 ; Zafar et al. 2018b).
Sightlines of quasi stellar objects (QSOs) also provides information on the intervening material in the ISM of distant galaxies, but in a different manner : instead of probing the deep star-forming regions they rather cross the circumgalactic medium of intervening galaxies, and although these sightlines can be revisited at any time the intervening galaxies can not be observed without the contamination of the QSO emission unlike the GRB host galaxies at later time [Schady, 2017].
For a detailed review of the use of GRBs to probe the ISM of distant star-forming galaxies, I refer to Schady, 2017 and references therein. In the next section, we discuss the use of GRBs to derive extinction curves and infer dust properties.

3. Extinction curve

Dust particles interact with stellar light both through scattering and absorption. When a dust grain scatters a photon, it changes the direction of the photon but not its energy. When a dust grain absorbs a photon, the energy of the photon changes the internal structure of the grain, e.g. by breaking a molecular bond, moving one electron to a more excited state or even ionise the grain. The photon is then lost to us, but the dust grain will re-emit a photon at longer wavelength, typically in the infra-red (IR). Both interactions reduce the number of photons we can detect from the source and are wavelength dependent, ultra-violet (UV) photons are more likely to be absorbed or scattered by dust than optical and near infra-red (NIR) photons leading to a reddening of the observed stellar light emission.
In the case of point-like sources, such as individual stars or GRBs, the effects of dust are termed dust extinction and correspond to two processes :
- photons absorbed by dust
- photons scattered out of the line-of-sight by dust
For point-like sources, the amount of photons scattered into the line-of-sight to the star is negligible meaning that dust extinction is independent of the geometry and distribution of the dust in the ISM. Thus the dust extinction is only dependent on the dust composition and the dust size distribution.
The wavelength dependence of dust extinction is most commonly determined with the "pair method", first used by Bless et Savage, 1970 and used in many other works since then (see Valencic et al., 2004 and references therein). The method consists in the comparison of the spectra of two stars with the same spectral type, one with high extinction (target star) and the other one with little or no extinction (standard star). This method requires the accurate measurement of the spectral type of stars, which can be challenging for faint objects, and the availability of data for the standard star with the same spectral type as the target star. An alternative way of obtaining the extinction curve without referring to a standard star is by using a numerical code to fit the observed fluxes of the target star to a grid of synthetic SEDs with different stellar parameters (e.g. star's effective temperature, surface gravity or metallicity) and extinction amounts and shapes (e.g. Fitzpatrick et Massa 2005 ; Gordon et al. 2016). This method can be applied when the spectrum of individual stars can be obtained, which due to the

resolution of current instrument is only the case in the Local Group so far. Using this technique, extinction curves were obtained in four galaxies where stars can still be resolved : the Milky Way [MW ; Witt et al., 1984 ; Cardelli et al., 1989 ; Fitzpatrick et Massa, 1990 ; Fitzpatrick et Massa, 2007], the Small Magellanic Cloud [SMC ; Prevot et al., 1984 ; Gordon et Clayton, 1998 ; Gordon et al., 2003], the Large Magellanic Cloud [LMC ; Clayton et Martin, 1985 ; Fitzpatrick, 1985 ; Misselt et al., 1999], and M31 (Bianchi et al. 1996 ; Clayton et al. 2015). The extinction curve averaged over MW, LMC and SMC sightlines can be seen in Figure II.4. The strongest spectral feature is a prominent bump located at 2175 Å , whose strength decreases as one goes from MW to LMC to SMC. The extinction is rising from NIR to far UV (FUV), the SMC extinction curve has the steepest FUV slope and the MW has the flattest. These are general trends and regional variations are seen from one sightline to another in the same galaxy. In the following, the spectral feature at 2175 Å will be termed UV bump. Weingartner et Draine, 2001 showed that the MW, LMC, SMC extinction curves could be reproduced by models consisting of a combination of polycyclic aromatic hydrocarbons (PAHs), graphite and amorphous silicate, with only changes in the size distribution (and relative abundance of the 3 components) from sightline to sightline. As illustrated in the right panel of Figure II.4, the average Galactic extinction curve is well modelled by the three components model, the NIR and visible extinction up to $\sim 4\ \mu m^{-1}$ is dominated by large silicate and graphite grains of size $\gtrsim 250$ Å, the UV bump is well reproduced by PAHs and very small graphite grains of size $\lesssim 250$ Å, and the FUV rise is reproduced by very small grains of size $\lesssim 250$ Å . [Xiang et al., 2017]. I refer the reader to Draine, 2003 and references therein for a detailed review of interstellar dust.

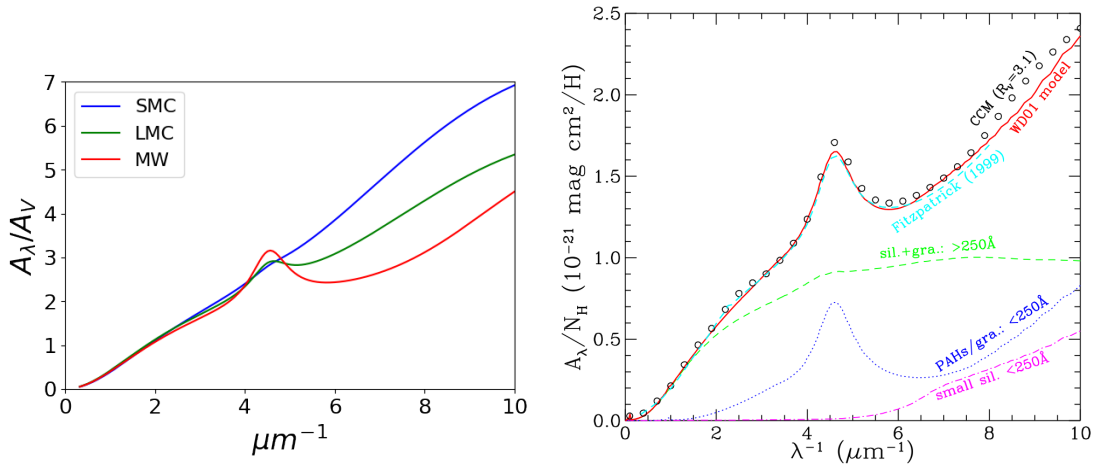

Figure I.8– ***Left :*** Mean SMC, LMC and MW extinction curves taken from Pei, 1992, only the MW and LMC exhibit a bump at 2175Å and the SMC has the steepest slope in UV. ***Right :*** Illustration of the different components in the extinction curve in terms of grains type and size. The Galactic average extinction is represented by the Cardelli et al., 1989 parametrization of R_V=3.1 (black open circles) and the Fitzpatrick, 1999 formula (cyan dashed line). The red line represents the extinction curve of the silicate-graphite-PAH model of Weingartner et Draine, 2001, which is a combination of three components : the extinction caused by silicate and graphite grains of radii > 250 Å(green dashed line), the extinction produced by PAHs or small graphitic grains of radii < 250 Å(blue dotted line), and the extinction arising from small silicate grains of radii < 250 Å(purple dashed-dotted line). (Credit : Xiang et al. 2017)

Beyond the Local Group, GRBs offer one of the only opportunity to study the dust extinction properties of distant star-forming galaxies due to their featureless simple power-law spectrum. The NIR-to-X-ray spectrum is usually modelled as a single power-law or a broken power-law to take into account a possible break in the synchrotron spectrum located between the X-ray and UV/optical/NIR domains at the time of observation. The intrinsic spectral shape of the GRB afterglow is well constrained by the barely

attenuated IR and X-ray wavelengths. Knowing the GRB intrinsic spectral shape, any difference with the observed spectrum is attributed to the interaction of photons with dust particles and allows to measure the wavelength dependence of this interaction, i.e. the extinction curve, along the GRB line-of-sight (e.g. Zafar et al. 2011; Zafar et al. 2012; Schady et al. 2012; Covino et al. 2013; Japelj et al. 2016; Bolmer et al. 2018; Zafar et al. 2018b). An example is showed in Figure I.9 where the observed spectrum of GRB 120119A is fitted with a single power law modelling the intrinsic emission spectrum from UV to X-rays (black dashed line) and an extinction curve similar to the one of the SMC. Most of the extinction curves derived from GRB sightlines are featureless but at present a UV bump has been spectroscopically measured in 5 GRBs such as GRB 070802 (see Figure I.9).

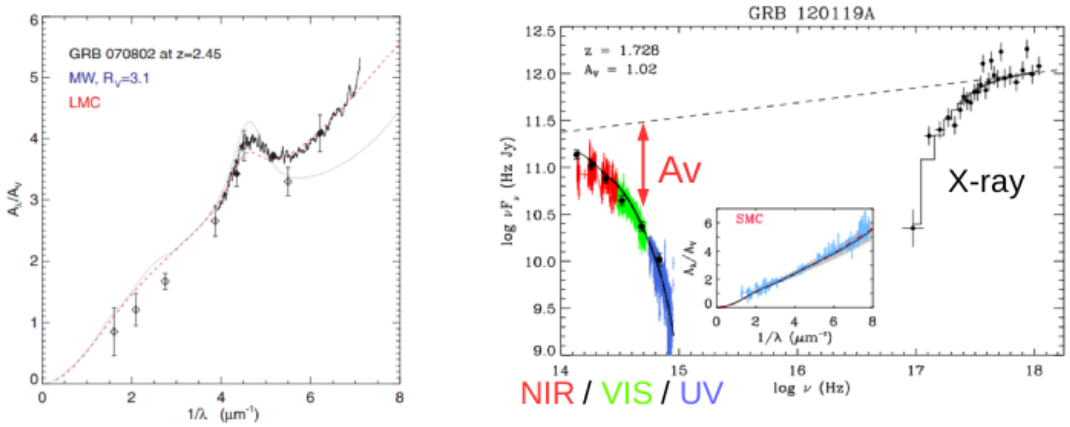

Figure I.9– ***Left :*** Extinction curve of GRB 070802 at z=2.45 [Elíasdóttir et al., 2009], the first spectroscopic detection of a UV bump in a GRB extinction curve. ***Right :*** Extinction curve of GRB 120119A [Zafar et al., 2018b]. The black points correspond to optical-NIR (left side) or Swift X-ray (right side) observations. The red, green and blue colors are for the UVB, VIS and NIR spectra obtained with VLT/X-shooter. The dashed and continuous lines represent the best fit intrinsic emission spectrum and extinguished spectrum respectively. The middle panel represents in blue the extinction curve derived from the GRB spectrum and the red dashed line corresponds to the SMC extinction curve, both are normalised to the amount of extinction in V band, A_V. (Credit : Elíasdóttir et al. 2009; Zafar et al. 2018b)

Most of the time the GRB afterglow is detected in a few photometric broad bands and the extinction curve is fitted using template extinction curves such as the mean MW, LMC and SMC ones. The extinction curve is only "really" measured when spectroscopic measurements of the afterglow are available. The common picture of GRB extinction curves is a relatively unextinguished ($A_V \sim 0.3$ mag) with a featureless shape well fitted by an SMC-like extinction law. The lack of UV bump implies the absence of very small graphitic and PAHs grains. These steep extinction curves are characteristics for a populations of small grains, either as the result of the destruction of large dust grains by the strong GRB UV radiation or of the young age and low metallicity environment for GRBs [Zafar et al., 2018b]. Only 10-15% of GRB extinction curves are found similar to the mean MW and LMC [J. Greiner et al., 2011; Zafar et al., 2011], most of them have large visual extinction ($A_V \gtrsim 1$ mag). The first spectroscopic detection of a UV bump was made for GRB 070802 (see Figure I.9) and so far only 4 others UV bumps were spectroscopically confirmed, they are the majority of firm detection of the UV bump outside the Local Group [Schady, 2017]. More detections are necessary to perform a statistical analysis of its properties, unfortunately highly extinguished GRB afterglows that are bright enough to obtain a decent signal-to-noise ratio spectrum are rare. To increase their detection rate, a very rapid localisation of the GRB and its multi-wavelength follow-up are required.

GRB extinction curves can also probe the dust production history across cosmic time. For example, Zafar et al., 2018c selected z $\gtrsim$ 3 GRB extinction curves spectroscopically observed by X-shooter and

found only low dust content above z > 3.5 while dusty GRB sightlines are found at z $\lesssim$ 3.5, suggesting a possible transition in the nature of dust producers. The increase of the dust content below z < 3.5 could arise from carbon production by the first carbon-rich AGB stars and possibly from iron production by the Type Ia SNe. The dust content being correlated with the stellar mass of the galaxy (e.g. Pannella et al. 2015 ; Álvarez-Márquez et al. 2016), the drop of high dust content above z > 3.5 could also be explained by low stellar masses of GRB host galaxies.

One advantage of the temporal decay of the GRB afterglow is that it permits to study the host galaxy when the afterglow has vanished, and thus to derive the attenuation curve of the host galaxy. The dust attenuation of light by dust for a whole galaxy is different from the dust extinction along one line of sight as it is not only dependent on the dust properties but also on the geometric distribution of dust and stars in the galaxy (e.g. Witt et Gordon 2000). As seen on the Figure I.10, the radiative transfer simulations of Witt et Gordon, 2000 showed that for a given extinction curve, i.e. dust properties, the attenuation curves resulting from different geometric distribution of dust and stars can exhibit very different shapes. A more detailed description of dust attenuation is given in Chapter IV. Consequently, if the extinction and attenuation curves are known for the same galaxy, one can derive dust grain properties from the extinction curve and try to infer information about the geometry of the ISM of this galaxy from the attenuation curve. GRBs offer the only possibility to measure both extinction and attenuation curves of distant galaxies but it is remained unexplored so far. This aspect is investigated mainly in the Section 3 of Chapter IV.

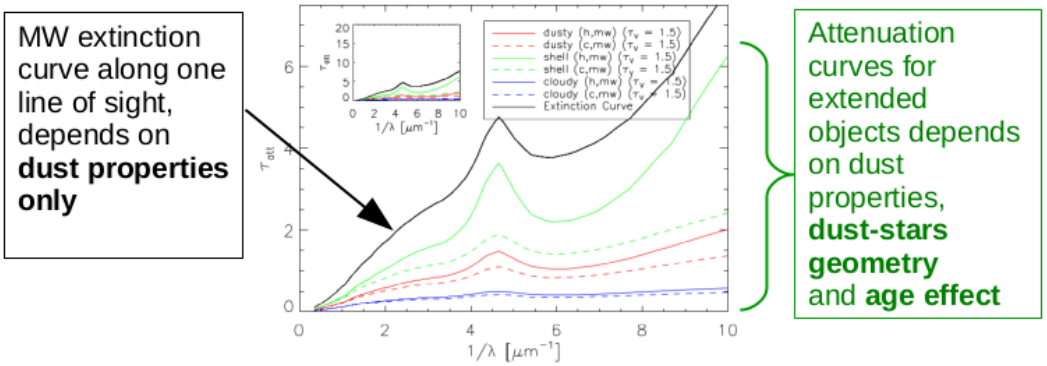

Figure I.10– Extinction vs attenuation curves with the radiative transfer model of Witt et Gordon, 2000. The black line represents a MW extinction curve, the various colored lines represent the attenuation curves resulting from various geometric distribution of stars and dust that are described in IV.(Credit : Witt et Gordon 2000)

4. SVOM, a space/ground multi-wavelength observatory

The Space Variable Object Monitor (SVOM) is a ground and space-based multi-wavelength observatory aiming at detecting GRBs and other transient phenomena. This mission is a collaboration between the french and chinese space agencies (CNES and CNSA) to be launched in 2021. It is the successor of the Neils Gehrels Swift Observatory launched by the NASA in 2004 [Gehrels, 2004]. The scientific objectives of the mission emphasize particularly on two categories of GRBs : faint / soft nearby GRBs to probe the nature of the progenitors and the physics of the GRB explosion ; and high-redshift GRBs at z > 5 which constitute exceptional probes of the early Universe. SVOM aims at providing fast, reliable GRB positions as well as to quickly identify the afterglows of detected GRBs in X-ray and visible/NIR domains, including high-redshift GRBs at z > 5.

The SVOM satellite will be equipped with four instruments (see Figure I.11), two wide field of view (FoV) high-energy instruments dedicated to the detection of the GRB and observation of the prompt

emission : a coded-mask γ-ray imager (ECLAIRs) operating in the 4-150 keV energy range with a FoV of 2 sr, and a γ-ray spectrometer (GRM) operating in the 15-5000keV energy range with a FoV of 2 sr ; and two narrow FoV telescopes aiming at providing a fast and reliable localisation of the GRB and at observing the afterglow : a Microchannel X-ray Telescope (MXT) operating in the 0.2-10 keV with a FoV of 64x64 arcmin^2 and a 40 cm Visible-band Telescope (VT) operating from 0.4 to 1μm with a FoV of 26x26 arcmin^2. The SVOM ground segment includes additional instruments : a wide angle optical camera (GWAC), composed of 36 cameras, each of them with an effective area of 18 cm for a total of FoV of 5400 square degrees, monitoring the ECLAIRs FoV in real-time aiming at the observation of the optical prompt emission ; and two 1-m-class robotic ground follow-up telescopes (the GFTs), one based in China and operating in the visible only and the other one based in Mexico operating in the visible/NIR.

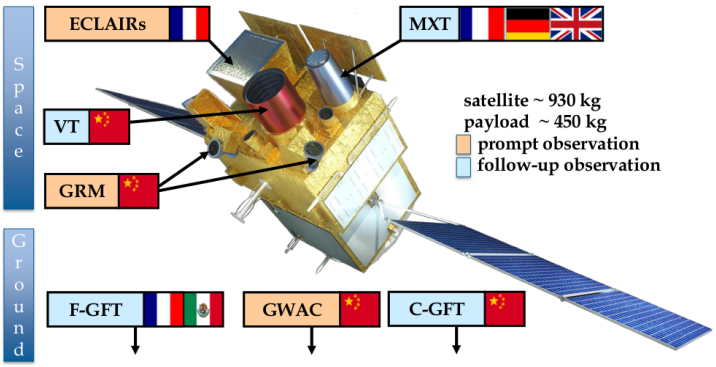

Figure I.11– View of the SVOM space-based and ground-based instruments. (Credit : Wei et al. 2016)

Most of the time, the SVOM satellite will point to a predefined direction [Cordier et al., 2008], waiting for a GRB. The observation strategy of a GRB is illustrated in Figure I.12 : when ECLAIRs detects a GRB with a localisation accuracy of $\sim$ 26 arcmin (in diameter), the position is communicated to the spacecraft which slews automatically in a few minutes to the GRB position in order to refine the localisation accuracy and perform rapid follow-up observations of the GRB afterglow emission with the narrow-FoV telescopes (MXT in X-rays and the VT in the visible). MXT and VT will have a sub-arcmin and sub-arcsec localisation accuracy respectively. The satellite stays pointed towards the source for about one day. The GRB position and its main characteristics determined by ECLAIRs are also quickly sent to the ground using the SVOM VHF emitter. Refined positions of the X-ray counterpart detected by MXT are also sent to the ground via VHF. The VHF signal is received by one of the 40 to 50 ground stations, distributed on Earth under the satellite track. The system design ensures that 65% of the alerts are received within 30 seconds at the Science Centers, which forward them via internet (using the GCN and VOEvent networks) to the SVOM ground instruments (GWAC and GFTs) and to the scientific community. The GFTs must provide first results, especially a sub-arcsec localisation, within 5 minutes of observations. Furthermore, thanks to its NIR coverage the F-GFT, also named COLIBRI (Catching OpticaL and Infrared BRight transIents), is expected to provide an information on the redshift after 5 minutes of observations.

The expected GRB rate is estimated to be around 60-70 per year [Wei et al., 2016], and SVOM will operate for a minimum of 3 years. I refer the reader to Wei et al., 2016 for a more detailed description of the instruments, observation strategy and scientific objectives of the mission.

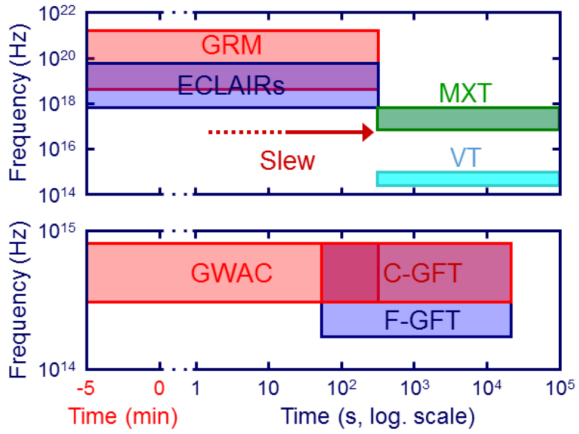

Figure I.12– Typical follow-up strategy of a GRB prompt emission with SVOM instruments. Upper panel represents the instruments on-board the satellite and the bottom panel the ground facilities. When the GRB is detected at t=0, the spacecraft starts to slew to align the narrow FoV telescopes (MXT and VT) with the GRB position and a VHF alert is sent to the ground follow-up telescopes (F-GFT and C-GFT) which start to observe approximately at t + 1 min and produce first results within 5 min. GWAC which is monitoring the ECLAIRs and GRM FoV will collect data from -5 to +15 min. Before the end of the (Credit : Wei et al. 2016)

The launch of SVOM will coincide with an era of time-domain multi-wavelength observatories. For example, the advent of the Square Kilometre Array (SKA) in radio, Large Synoptic Survey Telescope (LSST) in optical, Cherenkov Telescope Array (CTA) and High Altitude Water Cherenkov Experiment (HAWC) at very high energy will provide a large increase of rapidly available triggers for a wide variety of sources. Furthermore, the presence of three gravitational waves observatories : Advanced LIGO, Advanced Virgo and the Kamioka Gravitational Wave Detector (KAGRA) will provide localisations of 5-20 square degrees [Abbott et al., 2018], that SVOM can tile quickly and efficiently. The first phase of the new KM3NeT neutrino facility will complement IceCube and provide localisations that can be observed by SVOM MXT and VT telescopes in a single pointing and by the SVOM ground follow-up facilities (GFTs, GWAC) [Adrián-Martínez et al., 2016]. In order to contribute to this new era of time-domain astronomy scheduled for the next decade, the time allocated to the observation of targets of opportunity by SVOM will increase from 15% of the useful time of the mission at the beginning of the mission to 40% 3 years after the launch. The expected large number of triggers from sources of different nature provides a challenging scientific opportunity for SVOM which will have the capability to obtain multi-wavelength follow-up observations from its space and ground instruments.

1. COLIBRI overview

Simulations are an essential part of the development process of any instrumental project. During the project proposal and definition phases, they allow scientists to assess scientific performance of the mission by computing limiting magnitudes, images or spectra for instance. During later stages of the mission development, scientific simulations help to compare different instrument designs as they allow to assess how these designs affect the performance of the telescope.
Half of my PhD was dedicated to the implementation of software to assess the performances of COLIBRI (Catching OpticaL and Infrared BRight transIents), a future ground follow-up telescope of the SVOM mission. COLIBRI is a collaboration between France and Mexico, it will be installed at the Observatorio Astronómico Nacional in Mexico in 2020 which offers very good observing conditions (median seeing of 0.8 arcsec and about 85% of clear nights). This section aims at describing the requirements and optical design of COLIBRI, and afterwards the modelling of the telescope response. In Section 1.1 are summarised the main requirements for COLIBRI. In Section 1.2, the telescope optical design and filter transmission are is briefly described. In Section 2.1, we describe how GRBs are modelled. In Section 2.2, we present the Exposure Time Calculator (ETC) developed to assess the scientific performances of COLIBRI. We also present the limiting magnitudes as well as a comparison of COLIBRI sensitivity with a dataset of already detected GRB light curves. In Section 2.3 we present the Image Simulator (IS) developed to produce realistic images of COLIBRI to test the reduction pipeline.

1.1. Requirements

Gamma-Ray Bursts detection takes place in space because gamma rays are stopped by Earth's atmosphere. This task is devoted to the ECLAIRs telescope, in the X-/γ-ray energy range with a very large field of view, whose detection rate is estimated to be about 60-70 per year, with approximately 20% of very distant events with redshift greater than 6. An estimate of the event's position in the sky is then transmitted in $\sim$ 30 seconds to ground telescope for follow-up observations, transiting through a VHF alert network. COLIBRI is one of the two 1-m class telescopes included in the SVOM system. The other ground follow-up telescope will be based in China.
Their functions are summarized as follows :
- providing localisation and multi-wavelength GRB observations less than 5 minutes after the VHF alert reception. This is complementary to the slower on-board procedure as seen in Figure I.12, based on the chain : ECLAIRs => MXT (Microchannel X-ray telescope) => VT (Visible Telescope), which requires a repositioning of the spacecraft. It is also crucial for GRBs that cannot be observed quickly due to spacecraft constrains (estimated to about 20% of SVOM GRBs).
- providing an identification of low signal-to-noise triggers provided by ECLAIRs, for which the spacecraft slew is not requested. These triggers can be due to GRBs that are for example highly extinguished or located at very high redshift and have potentially a very strong scientific impact.
- localising and observing dark GRBs, i.e. events detected in gamma, x-ray domains, but not in the visible domain.
- providing an indication of the GRB redshift if possible, 5 minutes after the beginning of observations in order to trigger further observations with the SVOM satellite and the ground largest facilities (e.g. Nordic Optical Telescope, Very Large Telescope, ALMA, etc). A rapid and accurate localisation is essential for

a spectroscopic follow-up with the largest facilities.

The field of view is 26 arcminutes, corresponding to the typical ECLAIRs localisation uncertainty. In order to be able to observe the vast majority of the GRBs observed so far, the sensitivity must be able to observe targets with limiting magnitudes up to R = 19.2 and J = 18 for an exposure of 30s and R = 22 and J = 20 (AB system) for an exposure of 300s with SNR (Signal-to-Noise Ratio) = 10. This requirement imposes a diameter of at least 1 meter for the telescope.
The SVOM alert network has an intrinsic delay : about 65% of the alerts will arrive 30 seconds after the trigger [Wei et al., 2016], and so to allow COLIBRI to observe the optical prompt emission a requirement has been set to start observations within the 30 seconds following the alert reception. This will permit to study the optical prompt emission, the transition between the prompt and the afterglow emissions, the detection and characterization of the reverse shock with a temporal resolution of few to several seconds. One should keep in mind that GRB afterglows decay very quickly, typically like $t^{-\alpha}$ with $\alpha \sim 1$. Because of this intrinsic property, a longer exposure time cannot compensate for a late arrival as the gain in sensitivity is compensated by the reduction of the GRB brightness.
The main scientific requirements are summarised in Table II.1.

Table II.1– Summary of main scientific requirements

Observatory availability (without considering weather conditions)	90%
Field of View	26' in visible, 21.7' in NIR
Delay for pointing	$\lesssim$ 30 seconds (goal : 20s)
Precision of localisation	$< 0.5"$
Spectral coverage	400-1800 nm
Limiting magnitude	R=22, J=20 (300s, AB mag)
	R=19.2, J=18 (30s, AB mag)
Real-time data processing (localisation and redshift estimation)	$<$ 5 minutes

1.2. Optical design

COLIBRI has a primary mirror diameter of 1.3 meter and a secondary mirror diameter of 0.58 meter. The telescope will have 2 or 3 (goal) simultaneous channels : 1 (or 2) in the visible and 1 in the NIR domain. In the following we will only consider the goal optical design with 3 channels. The visible channels are equipped with DDRAGO-B and DDRAGO-R and the NIR channel with CAGIRE instruments. An overview of the telescope design is seen in Figure II.1. The main characteristics of the telescope instruments are summarised in Table II.2. CAGIRE will be equipped with the first sensor of a new serie developed for scientists by the SOFRADIR company with characteristics announced to be similar to the Teledyne sensors.
The global transmission curves for each filter band of COLIBRI is presented in Figure II.2.

Table II.2– Main characteristics of COLIBRI instruments.

	DDRAGO (B and R)	CAGIRE
Sensor	e2v	SOFRADIR
Wavelength coverage	400-1000 nm	1000-1800 nm
Number of pixels	4096x4096	2048x2048
Pixel size	15 μm	15 μm
Well capacity	350000 e^-	80000 e^-
Readout noise	8 e^-	<20 e^-
Operating temperature	170 K	100 K
Associated Dark current	<0.001 $e^-/pix/s$	~0.003 $e^-/pix/s$
Sky resolution	0.38 $arcsec/pix$	0.63 $arcsec/pix$
Field of View	26 $arcmin$	21.7 $arcmin$

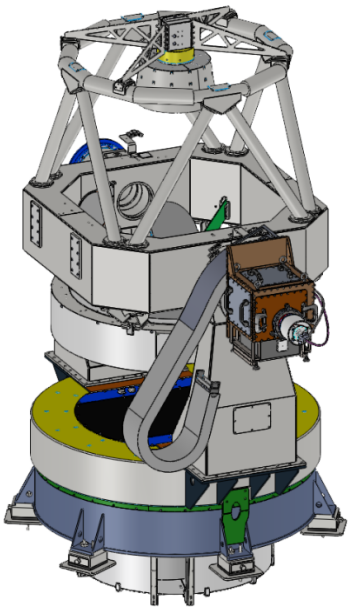

Figure II.1– The COLIBRI telescope and DDRAGO interim instrument.

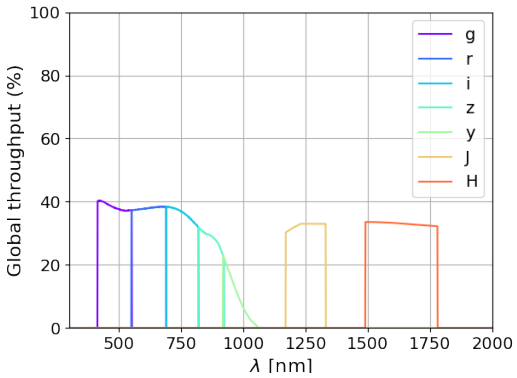

Figure II.2– Global transmission curves for the different filter bands of COLIBRI, including all optical elements and their coatings, and the detector quantum efficiency.

2. Modelling scientific performances of COLIBRI

In Section 2.1, we first describe how we model the object source, i.e. GRB light curve. In Section 2.2, we briefly describe the ETC we have developed to assess the scientific performance for a given optical design. In Section 2.3, we briefly describe the image simulator developed to provide realistic raw images of COLIBRI.

2.1. Modelling GRB afterglow SEDs

We start by describing how we modelled multi-wavelength GRB light curves. First we need to compute the intrinsic emission spectrum of the GRB, then we need to take into account the dust extinction in the host galaxy, the transmission in the IGM, and the Galactic dust extinction.

2.1.1. GRB emission

GRB afterglows are well described by synchrotron emission from accelerated electrons in a relativistic blast wave interacting with an external medium [Sari et al., 1998 ; Granot et Sari, 2002]. The observed synchrotron spectrum is composed of series of power-law segments joined at certain break frequencies (see Sari et al. 1998 ; Granot et Sari 2002). The NIR-to-X-ray spectrum is then usually modelled as a single power-law or a broken power-law to take into account a possible break in the synchrotron spectrum, most likely the cooling break, located between the X-ray and UV/optical/NIR.
For our simulations we have implemented two models, one empirical model assuming a single power law both in time and frequency and one theoretical based on the prescriptions of the standard synchrotron model of Granot et Sari, 2002.

2.1.1.a. Empirical model

For the purpose of our analysis, we first implemented a simple empirical model which simulates GRB afterglows with a power law in time and frequency as :

$$F_\nu(\lambda,\beta) \;=\; F_0 \times (\frac{\lambda}{\lambda_0})^\beta \times (\frac{t}{t_0})^{-\alpha} \tag{II.1}$$

where F_0 is the normalisation factor at λ_0 and t_0, λ is the wavelength and t the time since the trigger. Typical values are $\beta \sim 0.7$ and $\alpha \sim 1$ [Kann, 2010].

2.1.1.b. Standard synchrotron model

We have also used a theoretical model based on the standard synchrotron model following the prescriptions of Granot et Sari, 2002. The model used in this thesis, has been implemented by Alain Klotz and Damien Turpin at IRAP, and has been only translated into Python in this thesis and is now an open source package [1]. I refer the reader to Granot et Sari, 2002 ; Turpin, 2016 for a complete description of the model.
The Granot et Sari, 2002 model assumes that afterglows are well described by synchrotron emission from accelerated electrons in a relativistic blast wave interacting with an external medium. These electrons then cool both adiabatically and by emitting synchrotron and inverse Compton radiation. The resulting spectra is composed of several power-laws connected at three break frequencies : the self-absorption frequency, ν_{sa}, ν_m, the typical synchrotron frequency of the minimal electron in the power law, and ν_c , the synchrotron frequency of an electron whose cooling time equals the dynamical time of the system. For $\nu_c < \nu_m$, there is an additional break, ν_{ac}, due to the non-cooled electrons [Granot et al., 2000]. From the different possible ordering of the break frequencies, Granot et Sari, 2002 showed that the GRB afterglow can be described by five possible spectral regimes (see Figure II.3).
Here we briefly summarise the main assumptions of this model :
- Hydrodynamics is described by the Blandford et McKee, 1976 self-similar solution. This solution describes a spherical relativistic blast wave expanding into a cold medium whose density is described by a power law with radius $\rho(r)=Ar^{-k}$, k=0 corresponding to an interstellar medium of constant density and k=2 corresponding to a massive star progenitor surrounded by its pre-ejecta wind.
- The magnetic field gets a fixed fraction, ϵ_B , of the internal energy everywhere behind the shock.
- Electrons are assumed to acquire a power-law distribution of energies immediately behind the shock. The electrons get a fixed fraction, ϵ_e, of the internal energy everywhere behind the shock.

[1]. https://github.com/dcorre/pyGRBaglow

- Jet break due to lateral expansion is not considered.
- Only the forward shock is considered, (no reverse shock, nor flares, nor energy injection are considered).

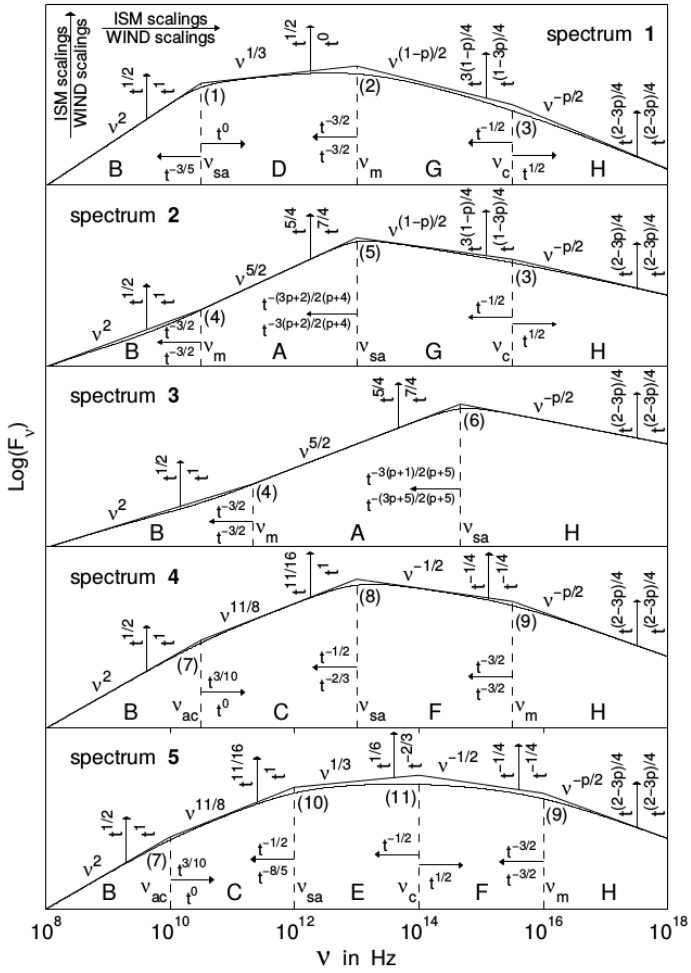

Figure II.3– Different possible broadband synchrotron spectra from the model of Granot et Sari, 2002, depending on the oredering of the break frequencies : spectra 1 and 2 correspond to slow cooling regime with $\nu_m < \nu_c$. Spectra 4 and 5 correspond to the fast cooling regime with $\nu_m > \nu_c$. Spectrum 3 corresponds to $\nu_{sa} > \nu_m$, ν_c. The temporal dependence of the break frequencies are given by the arrows. (Credit : Granot et Sari 2002)

This model is governed by 7 parameters describing the afterglow spectrum :
- z : GRB redshift - E_{52} : total energy in the shell (in $10^{52} ergs$).
- p : index of the electron power-law distribution.
- ϵ_B : fraction of shock energy converted to the magnetic fields energy.
- ϵ_e : fraction of shock energy used to accelerate the electrons.
- n_0 : particle density in the ambient medium (cm^{-3}).
- Y : Inverse Compton parameter, to take into account the Inverse Compton effects on the cooling of electrons. We set it to zero for all GRBs.

For the circumburst environment, we only simulate GRBs with a constant density profile, $\rho = n_0$, as very often it is the one returning the best fit to the data.

2.1.2. Extinction processes

2.1.2.a. Host galaxy dust reddening

The photons emitted by the GRB interact with dust particles along the GRB line of sigth. These photons can be absorbed or scattered out of the GRB line of sight, meaning that they are lost to us resulting in an attenuation of the emitted flux. This process occurs more efficiently at shorter wavelength leading to a reddening of the light, i.e. blue light is more attenuated than the red light. The wavelengths affected are primarily from the ultra-violet to the NIR. The wavelength dependence of the dust extinction is called extinction curve and denoted A_λ.

There are two methods to model A_λ. The first method consists in scaling the well defined extinction curves derived for the LMC, SMC, or MW to the GRB afterglow spectrum using A_V, the amount of extinction in the V band, as the scaling factor. The mean local extinction curves of Pei, 1992, normalised to the amount of extinction in the V band, A_V, are seen in Figure IV.23. This method has the advantage of introducing only one free parameter, A_V, to the SED fitting, but assumes that the wavelength dependence of dust extinction at high redshift is the same as the mean extinction in our local environment.

The second method uses more flexible formula to assess directly the wavelength dependence of dust extinction from the GRB spectrum. Usually this is performed using the prescriptions of Fitzpatrick et Massa, 1990 ; Fitzpatrick et Massa, 2007. This parametrisation offers more freedom to fit the actual shape of the extinction curve. However it has nine free parameters which leads to degeneracies between the parameters in the fitting process unless one has a finely-sampled SED. Consequently, this method is mainly used with spectroscopic measurements.

As COLIBRI does not have yet a spectrograph, we model the dust extinction in the host galaxy using the mean SMC, LMC and MW extinction curves of Pei, 1992. The MW extinction curve is characterised by a prominent UV bump at 2175 Å and a flat UV slope. The SMC extinction curve is featureless and has a steep UV slope. The LMC extinction curve also exhibits a UV bump but weaker than the MW and a UV slope intermediate between the MW and SMC ones.

The GRB spectrum attenuated by the dust in the host galaxy is given by :

$$\begin{aligned} F^{att}(\lambda,t) &= F^{em}(\lambda,t) \times exp\left[-\tau_{dust\ host}(\lambda/(1+z), A_V^{host})\right] \\ \tau_{dust\ host}(\lambda/(1+z)), A_V^{host}) &= 0.92 \cdot A_V^{host} \cdot \frac{A_{\lambda/(1+z)}}{A_V} \end{aligned} \tag{II.2}$$

with $F^{em}(\lambda,t)$ the intrinsic emission spectrum of the GRB (either modelled by the empiric or synchrotron model), and A_V^{host} the amount of visual extinction in the host galaxy, $\frac{A_{\lambda/(1+z)}}{A_V}$ the adopted extinction curve, and z the redshift of the GRB.

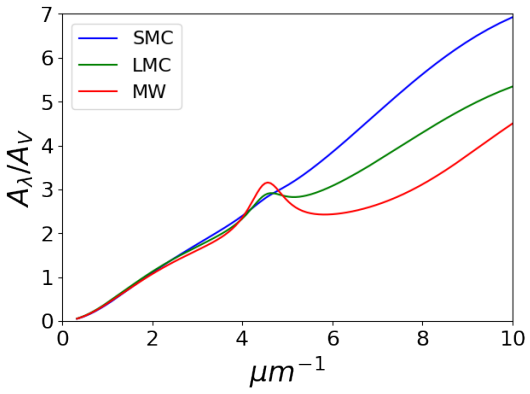

Figure II.4– Mean SMC, LMC and MW extinction curves of Pei, 1992 used in our analysis.

2.1.2.b. IGM transmission

Along the line of sight between the GRB and the observer, the photons emitted by the GRB interact with the gas in the intergalactic medium (IGM) mainly composed of hydrogen and helium. We model this attenuation with the prescriptions of Meiksin, 2006. The attenuation due to the intervening hydrogen in the IGM arises from two principal mechanisms : resonant scattering by Lyman transitions and photoelectric absorption. The blanketing by Lyman-series lines leads to an IGM transmission exhibiting a "staircase" shape (see Figure II.5) and the major contribution is due to Lyman-α at 1215 $\times(1+z)$ Å. The contribution due to photoelectric absorption is split into two parts, the contribution from systems optically thin at the Lyman edge and the contribution from Lyman Limit Systems. Madau, 1995 showed that the contributions of metals and He_I are negligible, and that He_{II} contributes only at wavelengths < 228 (1 + z) Å for a source at redshift z.

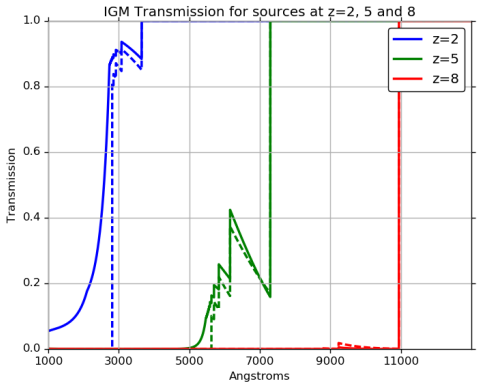

Figure II.5– IGM transmission for sources located at a redshift 2, 5 and 8 following Madau, 1995 (dashed lines) and Meiksin, 2006 (thick lines) prescriptions.

After the correction for the IGM transmission, the GRB spectrum is given by :

$$\begin{aligned} F^{att}(\lambda,t) &= F^{em}(\lambda,t) \times exp\left[-\tau_{dust\ host}(\lambda/(1+z), A_V^{host}) - \tau_{IGM}(z)\right] \\ \tau_{dust\ host}(\lambda/(1+z), A_V^{host}) &= 0.92 \cdot A_V^{host} \cdot \frac{A_{\lambda/(1+z)}}{A_V} \end{aligned} \tag{II.3}$$

with $\tau_{IGM}(z)$ the optical depth of the IGM following the prescriptions of Meiksin, 2006 and z the redshift of the GRB.

2.1.2.c. Galactic dust reddening

To model the galactic dust reddening, we use the mean extinction curve of the MW from Pei, 1992. In a similar way as for the extinction in the host galaxy we compute the GRB spectrum reaching the Earth as :

$$\begin{aligned} F^{att}(\lambda,t) &= F^{em}(\lambda,t) \times exp\left[-\tau_{dust\ host}(\lambda/(1+z), A_V^{host}) - \tau_{IGM}(z) - \tau_{dust\ gal}(\lambda, A_V^{gal})\right] \\ \tau_{dust\ host}(\lambda/(1+z), A_V^{host}) &= 0.92 \cdot A_V^{host} \cdot \frac{A_{\lambda/(1+z)}}{A_V} \\ \tau_{dust\ gal}(\lambda, A_V^{gal}) &= 0.92 \cdot A_V^{gal} \cdot \frac{A_\lambda^{MW}}{A_V} \end{aligned} \tag{II.4}$$

with A_V^{gal} the Galactic extinction in the V band and $\frac{A_\lambda^{MW}}{A_V}$ the MW mean extinction curve of Pei, 1992.

2.2. Exposure Time Calculator

The use of an Exposure Time Calculators (ETC) is a common practice in astronomy. Many observatories propose an ETC to observers to plan their observing plans as it allows them to estimate the exposure time required to reach the desired SNR for a given target or to estimate the SNR for a given target and exposure time. In the context of concept and design studies of new telescopes, an ETC is used to assess the scientific performances of a given optical design in order to check whether it meets the scientific requirements and to compare performances of different optical designs.

Usually, ETCs are specific to one instrument, however with the search for optical counterpart of cosmic events, astronomy is entering an era of complex follow-up strategy involving several facilities. Consequently, we have developed an ETC that can be used for different optical/NIR telescopes in order to be able to simulate an observation strategy involving several facilities. The characteristics of the telescope and the instrument are an input of the ETC in a hjson format. It takes into account the observation site characteristics (atmospheric transmission, seeing and sky background), the telescope characteristics (aperture, focal length, wavelength dependent transmission of each optical element, etc) and detector characteristics (quantum efficiency, dark current, readout noise, gain). The ETC allows to compare the scientific performance of designs with different number and kind of optical elements, coatings and detector characteristics. The ETC estimates the number of electrons produced by the different physical processes at stake (source signal, dark current, sky background, etc). An illustration of the output the ETC is seen on Figure II.6. This ETC is an open source Python package [2].

The limiting magnitudes in the different bands for a total exposure time of 30 seconds, 5 minutes and 1 hour are reported in Table II.3.

The sensitivity of COLIBRI is compared to a dataset of detected GRB light curves in Figure II.7. More than ∼95% of the GRBs dataset would have been detected by COLIBRI. As about ∼23% of the SVOM alerts will be immediately observable we performed the same analysis 12 hours after the trigger, and despite this long delay and decrease in the GRB brightness, COLIBRI has still sufficient sensitivity to allow the detection of ∼80% of the GRBs dataset in the NIR domain thanks to its 5σ limiting magnitude of 20.51 for a total exposure of 5min (10x30s) in the J band.

[2]. https://github.com/dcorre/pyETC

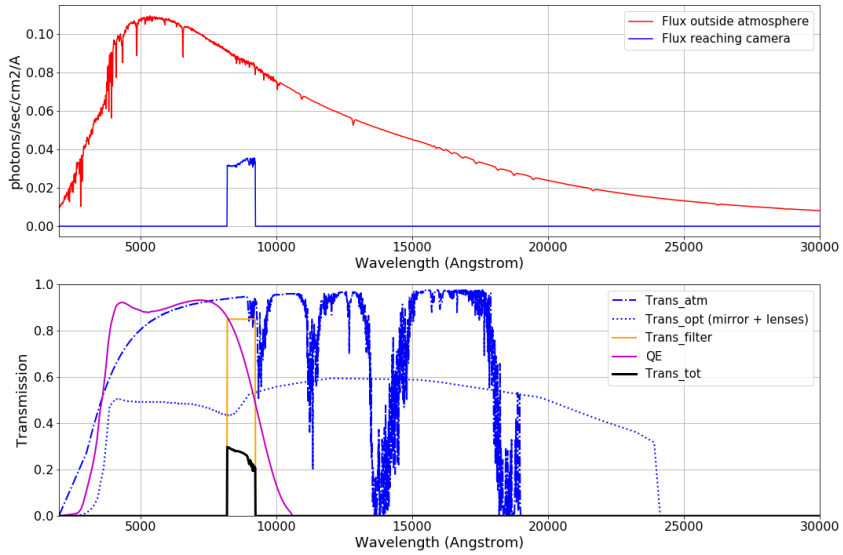


```
--------- Integrated over 7 pixels------------------

Photo-electrons created: brightest pix |  total of 7 pixels, 1 exposure(s) of 5.00 sec in z band
        by:
        - Object:          181236.95   |    907998.80   (electrons)
        - Sky:                73.21    |       512.44   (electrons)
        - Readout:             8.00    |        56.00   (electrons)
        - Dark current:        0.01    |         0.04   (electrons)
        - Digitization:        0.43    |         3.03   (electrons)

SNR: -central pixel: 425.56
     -integrated over 7 pixels: 952.39
```

Figure II.6– Example of ETC's outputs for the spectrum of HIP86443 for an exposure of 5 seconds in z band. *Top* : HIP86443 spectrum and COLIBRI's throughput. *Bottom* : extract of the results summarising the electrons generated and the reached SNR.

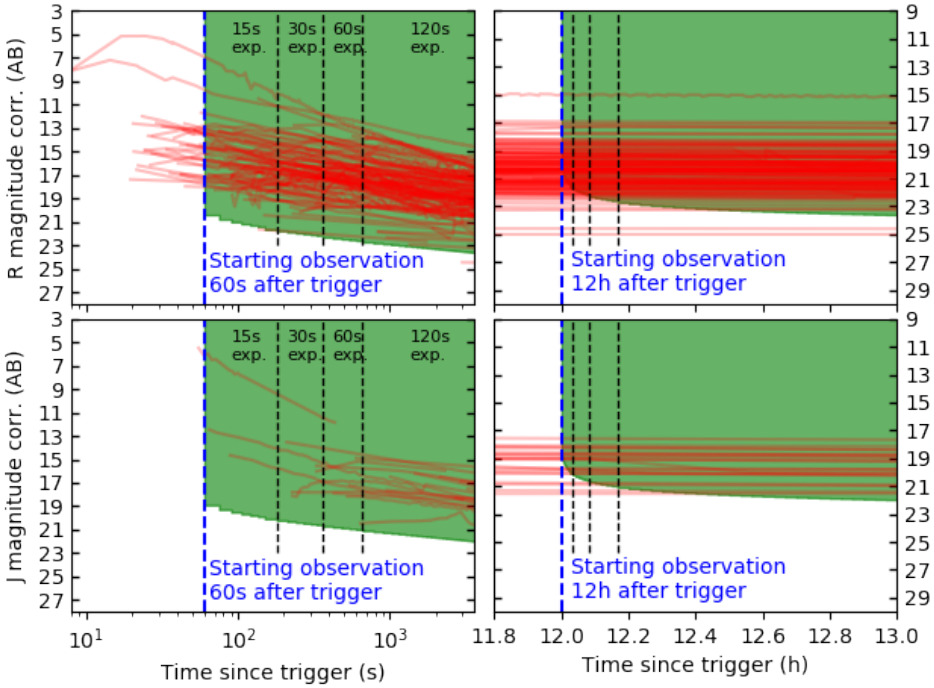

Figure II.7– *Top* : GRB light curves observed in the R band. *Bottom* : GRB light curves in the J band. *Left* : Light curves during the first hour after the trigger. *Right* : Light curves between 11.8 and 13 hours after the trigger. Red lines are the observed light curves, the green shaded area represents the sensitivity of COLIBRI. The observations consist in stack of 30s individual exposure with SNR=5, an airmass of 1.5 and 7 days after the new moon. The vertical black dashed lines correspond to 5, 10 and 30 minutes after the beginning of the observations.

Table II.3– Limiting AB magnitudes for different exposure time and SNR=5 with a seeing at zenith of 0.8", an airmass of 1.5. Dark stands for a sky brightness at the new moon and bright at full moon. The total exposure time of 5 minutes and 1 hour are stacks of 30s individual exposure.

band	30s		10min (20x30s)		1h (120x30s)	
	dark	bright	dark	bright	dark	bright
g	21.76	20.81	23.44	22.46	24.42	23.43
r	21.54	20.94	23.22	22.60	24.20	23.57
i	20.98	20.50	22.65	22.15	23.62	23.13
z	20.21	19.94	21.87	21.59	22.85	22.57
y	19.19	19.15	20.85	20.81	21.83	21.79
J	19.53		21.18		22.15	
H	18.79		20.42		21.39	
gri	22.12	21.36	23.77	23.00	24.75	23.98
zy	20.25	20.06	21.90	21.71	22.88	22.68
B	21.39	20.47	23.07	22.12	24.05	23.10

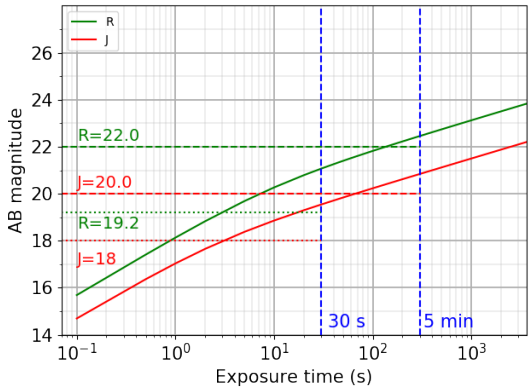

Figure II.8– 5σ limiting magnitudes of COLIBRI in the R and J bands. The requirement for a 30s and 300s exposure are represented by the dotted and dashed line respectively.

As seen from Figure II.8, the final optical design of COLIBRI leads to limiting magnitudes above the scientific requirements of R=19.2 and J=18 mag (AB) for a single exposure of 30s and R=22 and J=20 mag (AB) for a single exposure of 300s. Moreover, from Figure II.7, we see that the sensitivity of COLIBRI is about 2.5 magnitude deeper in R band at early times, $\sim$ 1 min after the trigger, and about 4-5 mag deeper in J band at early times. As very few GRB afterglows have been detected so far in NIR in the first minutes after the trigger, COLIBRI will extend the wavelength coverage from optical to NIR in the early times, which can be useful to study the transition from the prompt emission to the afterglow emission. These performances confirm that COLIBRI is designed to detect faint GRB afterglows, potentially at high-redshift and / or highly extinguished.

2.3. Image Simulator

An image simulator (IS) allows to compute realistic raw images in order to feed and test the detection/reduction pipeline. Stars and galaxies are simulated by convolving either point sources or galaxy model with the Point Spread Function (PSF). PSFs are either generated with Zemax for the adopted optical design or standard PSF profiles (Airy, Moffat, Gaussian), the seeing is modelled by a Moffat function. Realistic field views can be simulated by querying different astronomical catalogs such as Pan-

STARRS, 2MASS, NOMAD-1, etc. Different features such as pixel dependent gain, vignetting, cosmic rays can be taken into account by loading maps in fits format. The ability to reproduce observed images is an essential step in the validation of the image simulator. An example can be seen on Figure II.9, where we reproduce with our IS a real image of GRB170202a taken by Zadko Australia telescope. This image simulator is an open source Python package [3].

Figure II.9– *Left* : Image of GRB170202A taken with Zadko Australia telescope for an exposure of 30 seconds in a clear filter band. Field of view centered at RA, DEC = 152.518, 4.998 degrees (J2000). *Right* : Simulated image with Zadko telescope characteristics and observation site characteristics (sky background, seeing, atmosphere transmission), stars are simulated using the NOMAD-1 catalog.

2.3.1. Realistic case of GRB080607 : ability of COLIBRI to detect highly extinghished GRBs

An objective of COLIBRI end-to-end simulations is to use real GRB light curves and to study whether COLIBRI would have detected the GRB at a given time and to simulate the corresponding raw images in the desired bands. COLIBRI with its fast response time, good sensitivity and NIR spectral coverage is designed to detect dusty high redshift GRBs. We present here the case of GRB080607, a highly extinguished GRB (A_V=2.33 mag [Zafar et al., 2011]) at redshift 3.03. This kind of GRBs are among the most interesting ones to study the dust properties in the host galaxy, but only a few of them have been detected so far (see Chapter IV). This specific GRB is very interesting because a very early follow-up (less than 30s after the trigger in optical and less than 100s in the NIR) has been performed and thus a very well time sampling multi-wavelength light curve is available.

The multi-wavelength light curve of GRB080607 is seen on Figure II.10. Data are taken from a GRB database under construction, which compiled all GRB observations (Turpin, Klotz, Cordier, Gendre (in prep.)). Each band is interpolated using a spline interpolation. We define 4 periods at which observations start 100 seconds, 10 minutes, 30 minutes and 1 hour after the trigger. At a given time we fit the Spectral Energy Distribution (SED) with a power law, the same extinction law as in Zafar et al., 2011 and taking into account the transmission of the Inter Galactic Medium (IGM) using the prescriptions of Meiksin, 2006 :

$$F_\nu(\lambda, z, A_V, \beta, t_0) \;=\; F_0(t_0) \times (\frac{\lambda}{\lambda_0})^{\beta(t_0)} \times \;\cdot\; 10^{-0.4 A_\lambda} \times exp\left[-\tau_{IGM}(z)\right] \tag{II.5}$$

where F_0 and λ_0 are the flux and effective wavelength of the H band at a given time, t_0. β is the spectral slope, A_λ the extinction curve and $\tau_{IGM}(z)$ the transmission of the IGM for a source located at redshift z.

[3]. https://github.com/dcorre/ImSimpy

The SED is fitted at several times between the beginning and end of the observations : t_0 and $t_0 + t_{exp}$, with t_{exp} the exposure time. This allows to integrate the flux both in time and wavelength in order to simulate what would have seen COLIBRI at a given time, for a given exposure time and in a given filter band. The results are reported in Figure II.11. In the left panel all observations are performed with a single exposure of 30s, corresponding to the first image COLIBRI would have taken if observations start at 100s, 10min, 30min or 1h after the trigger. We see that the GRB is clearly detected up to 30 minutes after the trigger, whereas at 1 hour after the trigger it is only weakly detected in J and H bands. The right panel corresponds to the case where the GRB is detected at 100s after the trigger and later on the exposure time is adjusted : 2 exposures of 30s at 10min, 10 exposures of 30s at 30min and 20 exposures of 30s at 1h after the trigger. The GRB is clearly detected at all times in each band. These simulation results confirm the potential of COLIBRI to detect dusty GRBs even at high redshift.

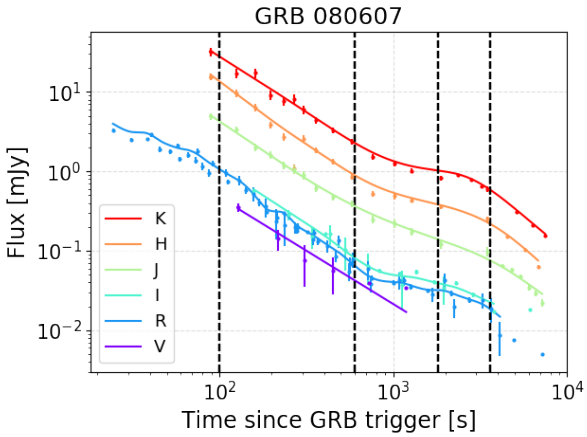

Figure II.10– Multi-wavelength light curve of GRB080607. Dots represent real observations and the solid line is a spline interpolation for each filter band. The black dashed line represent the time at which we extract the SED, from left to right : 100 seconds, 10 minutes, 30 minutes and 1 hour.

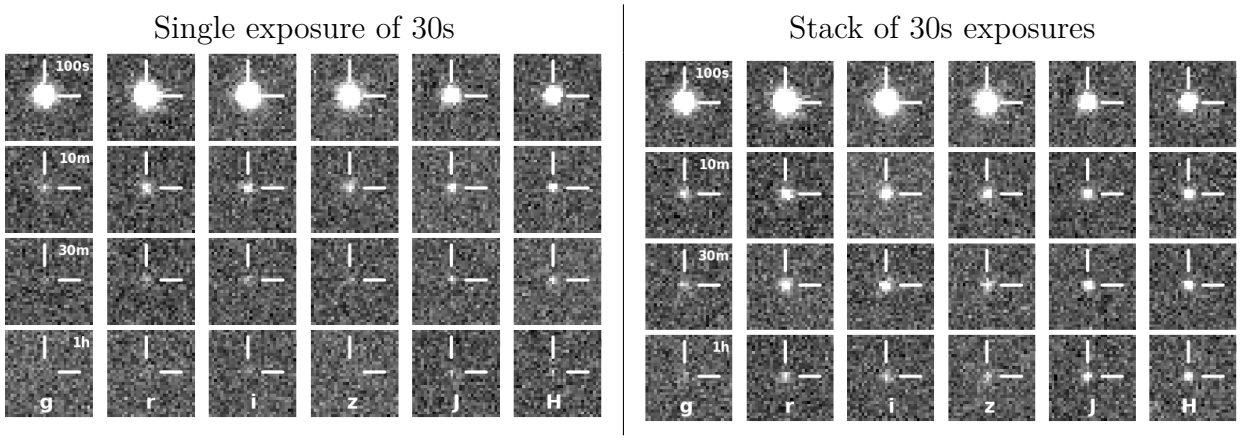

Figure II.11– *From top to bottom :* images of GRB080607 seen in each filter band of COLIBRI (g,r,i,z,J,H) starting at 100 seconds, 10 minutes, 30 minutes and 1 hour after the GRB trigger. *Left :* each image is a single exposure of 30 seconds. *Right :* Exposure time is adapted to the time at which the observations start : 30s exposure time at 100s, stack of 2x30s at 10min, stack of 10x30s at 30min and stack of 20x30s at 1h.

3. Conclusions

In order to estimate the scientific performances of COLIBRI, we have developed an ETC to estimate COLIBRI and an image simulator to provide realistic raw images. A code to model GRB light curves representative of what COLIBRI will observe is also available. All these codes are open sources and available to the community.

The ETC was used during the development of the optical design to check whether a given design was fulfilling the scientific requirements in terms of limiting magnitudes and to compare the scientific performances of two different designs. The image simulator is still in development and is currently modified to reproduce realistic images from the CAGIRE detector using a Teledyne detector. In the future, the ETC will be used on the COLIBRI website to allow astronomer to plan their observations and the image simulator will be used to provide raw images to feed the reduction pipeline. The ETC and image simulator are not specific to COLIBRI and so they can be used for any optical/NIR telescopes. This flexibility can be useful in the current and future era of time-domain astronomy where the research of optical counterpart of gravitational waves or fast radio bursts for instance requires a sophisticated observation strategy involving different telescopes.

One of the scientific requirement of COLIBRI is to provide a photometric redshift during the first minutes of observations of the GRBs by the SVOM mission, so in this Chapter we present an end-to-end simulation aiming at estimating the accuracy of the photometric redshift delivered by COLIBRI.
In Section 1 we describe the photometric redshift algorithm and its validation on observed optical GRB afterglows. In Section 2 we estimate the photometric redshift accuracy for COLIBRI based on different mock samples of GRBs.

1. Photometric redshift code

1.1. Method

The SED fitting procedure to obtain photometric redshifts is based on the fit of the overall shape of the spectra and on the detection of the strong spectral properties. Here only two prominent signatures can hint information about the redshift : the Lyman break at $912\times(1+z)$Åand the Lyman-α at $1216\times(1+z)$Å. The standard method is based on a standard χ^2 minimisation as used by SED-fitting codes such as Lephare or hyperz which compare the observed photometric SED to those obtained from a set of reference spectra. We decided to use a MCMC method of a standard χ^2 minimisation over a grid of parameters because of the better handling of local minima and it also offers more flexibility with the possible use of priors. To fully characterize the likelihood function over a broad range of parameter space and to obtain a Bayesian estimate for the posterior density function of the free parameters (leading to estimates for uncertainties in and correlations between the derived parameters), we carry out a Markov Chain Monte Carlo (MCMC) analysis using the Python-based code *emcee* (Foreman-Mackey et al., 2013). By implementing an affine-invariant MCMC ensemble sampler, *emcee* works well for both highly-anisotropic distributions, and distributions with localized regions of high likelihood (Goodman et Weare, 2010).

1.1.1. Compute the likelihood

To determine the best fit model we compute the likelihood function using a Gaussian error model. The likelihood function needs to account for both detections and non-detections, this is given by (e.g [Lawless, 2002 ; Laskar et al., 2014]) :

$$L = \prod p(e_i)^{\delta_i} F(e_i)^{1-\delta_i} \tag{III.1}$$

where $e_i = m_{obs,i} - m_{model,i}$ is the residuals, with $m_{obs,i}$ and $m_{model,i}$ the observed and computed magnitudes in a given filter i. δ_i is a 0/1 variable indicating whether an observation is a detection (1) or an upper limit (0), $p(e_i)$ is the probability density function (PDF) of the residuals and $F(e_i)$ the survival function also known as the complementary cumulative distribution function of the residuals. By definition $F(x)$ represents the probability of exceeding x, so here $F(e_i)$ represents the probability that $m_{model,i}$ exceeds $m_{obs,i}$.
For a Gaussian model error the PDF is given by :

$$p(e_i) = \frac{1}{\sqrt{2\pi\sigma_i}} \cdot e^{-e_i^2/2\sigma_i^2} \tag{III.2}$$

where σ_i are the measurement uncertainties.
The survival function is defined as :

$$F(e_i) = 1 - 0.5\left(1 + erf\left(\frac{e_i}{\sqrt{2}\sigma_i}\right)\right) \tag{III.3}$$

where $erf(x)$ is the error function.
In the code we compute the log-likelihood as :

$$lnL = \sum_i \delta_i \cdot \left(-0.5\frac{e_i^2}{\sigma_i^2}\right) + \ln\left(\frac{1}{\sqrt{2\pi}\sigma_i}\right) + (1-\delta_i) \cdot ln\left(1 - 0.5 \cdot \left(1 + erf\left(\frac{e_i}{\sqrt{2}\sigma_i}\right)\right)\right) \tag{III.4}$$

where i runs over the filters used and σ_i is the uncertainty on the measured magnitude in the i band.

1.1.2. Compute the model magnitude

We assume that the continuum spectrum of a GRB afterglow in the optical/NIR is well described as a single power law :

$$F_\nu(\lambda) \;=\; F_0 \times (\frac{\lambda}{\lambda_0})^\beta \tag{III.5}$$

where F_0 is the normalisation in μJy at λ_0.
F_0 is taken to be the flux in the filter band at the largest wavelength. Typically the H band for COLIBRI and sometimes Ks for some GRB afterglows observed by other telescopes. The reason is that the amount of the extinction in the host galaxy is lower in the NIR in comparison to the optical, thus the normalisation depends less of the dust extinction. λ_0 is the effective wavelength of the chosen band.
This spectrum has to be corrected from transmission of several processes such as dust reddening in the host galaxy and the IGM transmission. The observed magnitudes are assumed to be corrected for Galactic extinction before using the photometric redshift code. These processes are taken into account by adding corresponding optical depths, the final afterglow flux is then defined as :

$$F_\nu(\lambda, z, A_V, \beta) \;=\; norm \cdot F_0 \times (\frac{\lambda}{\lambda_0})^\beta \times exp\left[-\tau_{dust}(z, A_V) - \tau_{IGM}(z)\right] \tag{III.6}$$

where $\tau_{dust}(z, A_V^{host})$ and $\tau_{IGM}(z)$ are respectively the optical depth corresponding to the dust extinction in the host galaxy and the IGM transmission as defined in II.2.1.2.
Our model has thus 4 parameters : the redshift of the GRB z, the dust extinction A_V in the V band, the spectral index β and a $norm$ parameter used to adjust the scale of the flux.
The AB magnitude is computed by integrating the flux over the passband :

$$mag_{th} = -2.5 \cdot log_{10}\left(\frac{\int F_\nu(\lambda, z, A_V, \beta) \cdot T_\lambda \cdot \lambda^{-1}\,\mathrm{d}\lambda}{\int 3631 \cdot 10^6 \cdot T_\lambda \cdot \lambda^{-1}\,\mathrm{d}\lambda}\right) \tag{III.7}$$

where T_λ is the system throughput curve.

A GRB afterglow is simulated at different redshifts in Figure III.1 to illustrate the use of the spectral signature of Lyman-α as an indicator of the redshift the source.

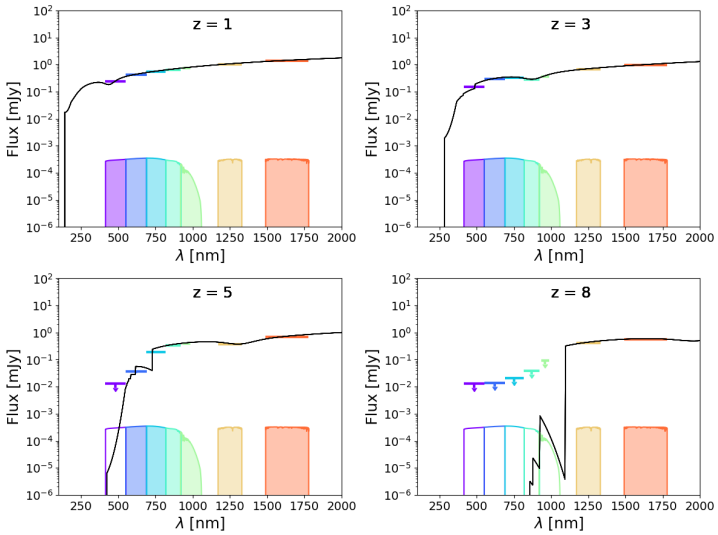

Figure III.1– GRB afterglow simulated with Equation III.6 at z=1, 3, 5 and 8 for F_0=1 mJy, $\beta = 0.8$, λ_0=6400Å and a LMC extinction curve with A_V=0.5mag. The global transmission curves of COLIBRI filters are represented with an arbitrary scales to illustrate which filters are affected by the IGM transmission at a given redshift.

1.1.3. The Posterior Probability Function

In Bayesian inference the posterior probability $p(\theta|x)$, where θ are the parameters of the models and x the measurements, is defined as :

$$p(\theta|x) = \frac{p(x|\theta) \cdot p(\theta)}{p(x)} \tag{III.8}$$

where :
- $p(x|\theta)$ is the likelihood, meaning how likely are the observed data given a set of parameters.
- $p(\theta)$ is the prior, the probability function on the model parameters. It is basically what we know of the parameters θ before "seeing" any data.
- $p(x)$ is the evidence, i.e. the evidence that the data were generated by this model.

The evidence is set equal to 1 so the posterior density function becomes : $p(\theta|x) = p(x|\theta) \cdot p(\theta)$
As we took the log-likelihood the log-posterior is the sum of the log-likelihood and the log-priors : $logp(\theta|x) = logp(x|\theta) + logp(\theta)$.
The log-likelihood, $logp(x|\theta)$, is defined above, and as we are using flat priors, meaning an equal probability over the defined range, $log(p(\theta)) = 0$. Consequently, the posterior probability function is equal to the likelihood.

1.1.4. Set up the MCMC

The initial values for the 4 parameters for each chain are drawn randomly in the prior intervals. So far only flat prior are used for the four parameters to fit, with the following intervals, chosen to account for low and high redshift, low and high visual extinction and representative of observed spectral slopes :
- redshift : $0 < z < 11$
- Host galaxy extinction : $0 < Av < 4$
- spectral slope : $0 < \beta < 2$
- Normalisation factor : $0 < norm < 5$

There are 2 possibilities to run the MCMC : a single run with possible multiple solutions, and a two-step

run aiming at avoiding secondary solutions. The two-step option first runs the MCMC for a given number of steps and then initialises the second run with the best fit values of the first run.
In the following, when we are dealing with hundreds of GRBs we use the two-step option in order to avoid secondary solutions and chain stocked outside the range defined by the priors. This allows to compute automatically the Bayesian estimation of the parameters for the main region of high likelihood only. The algorithm is first run for 300 steps, then the "production" run with 1000 steps is initialised with parameters values centered around the values with the highest likelihood in the first run, with a deviation of 10^{-2}. For the production run, we consider that the burn-in phase takes place during the first 300 steps. The statistics are performed on the remaining 700 steps (see Figure III.3). This configuration has been found to be a nice compromise between computational time and accuracy of the results.

1.1.5. The posterior distribution statistics

The posterior distribution frequently exhibits non Gaussian shapes, the uncertainties are then computed using the median of the distribution and the appropriate quantiles to compute either the 68%, 95% or 99.7% credible intervals around the median. The uncertainties are computed using 68%, 95% or 99.7% of points around the median value. The best fit values are also returned and plotted with the median values. Due to the specificity of the ensemble sampler, where the chains are not independent, Goodman et Weare, 2010 ; Foreman-Mackey et al., 2013 advised not to use standard convergence diagnostics to check whether a chain has converged but to use instead the integrated correlation time. However, most of the time a visual inspection of the evolution of the chains is sufficient to check whether chains have converged.

1.2. Validation test with observed GRB afterglows

In order to test the robustness of the algorithm, we need afterglows with and without detection(s), with high extinction, and GRB SEDs with one or two bands obviously off the trend. In total we selected 19 GRB afterglows with a spectroscopic redshift ranging from 0.34 to 8.26.The GRBs are mainly taken from the database of J. Greiner, database. The photometric data were obtained either by GROND or RATIR, and for GRB 050904 the photometry is a combination of several telescopes. The data can be seen in Appendix in Tables A.1 to A.3. All the magnitudes are expressed in the AB system and are not corrected for the Galactic reddening foreground. We used the dust map of Schlegel et al., 1998 to correct them before performing the MCMC analysis.
An example of best fit SED is shown in Figure III.2. The other SEDs are shown in the Appendix in Figures A.4 to A.6.

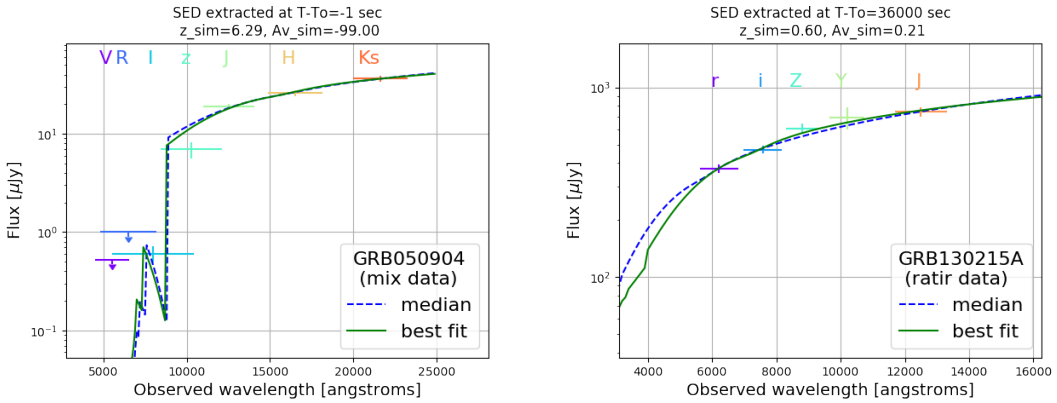

Figure III.2– Best fitted SED template for GRBs 050904 and 130215A in the left and right panel respectively. The photometric data are from different telescopes for GRB 050904 and only from RATIR telescope for GRB 130215A. The colored points represent the measurements, the blue dashed line the fit using the median values of z, A_V,β,$norm$ a posteriori distributions. The green line represents the best fit values.

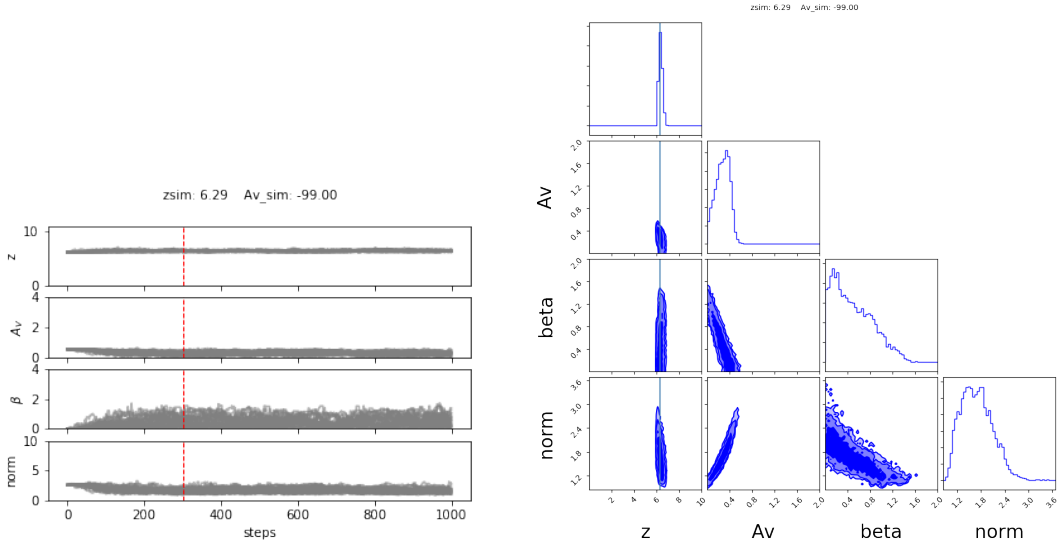

Figure III.3– Example of the outputs of the algorithm for GRB 050904 having a spectroscopic redshift of $z = 6.29$. *Left :* The evolution steps of each walker, i.e chain, for each parameter. The vertical red dashed line represents the burn-in phase, statistics are performed using only data on the right side of the red line. *Right :* one and two dimensional projections of the posterior probability distributions for all parameters. The vertical and horizontal blue lines represent the true value of the parameters.

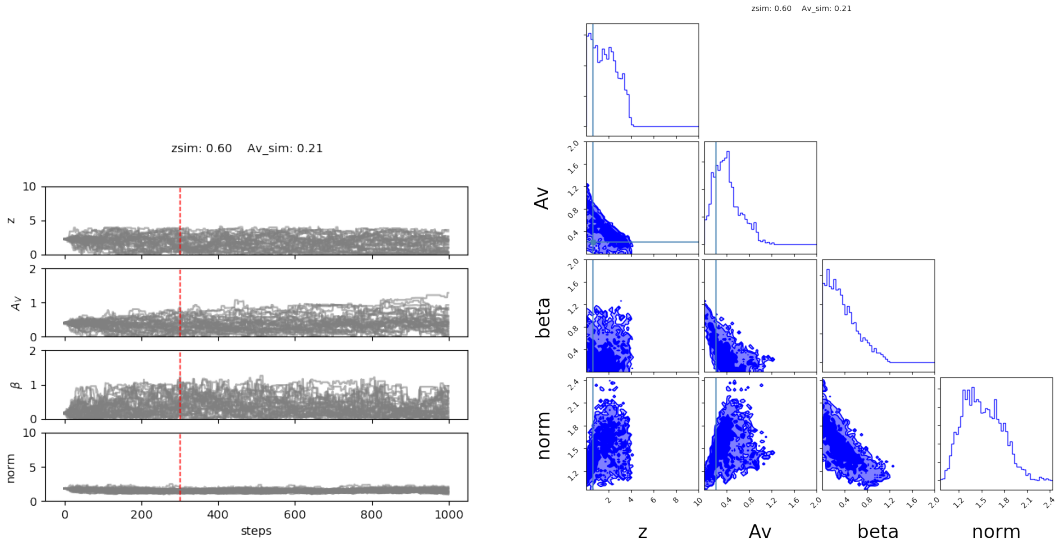

Figure III.4– Same as Figure III.3 but for GRB 130215A having a spectroscopic redshift of $z = 0.597$ and measured A_V=0.21 mag.

An example of a good redshift estimation is seen in Figure III.3 where the probability distribution function (PDF) is well peaked around the spectroscopic redshift. When there is no spectral signature in the GRB SED, like for GRB 130215A at z_{spec}=0.597 (see right panel of Figure III.2), the redshift is poorly constrained as seen by the broad and flat PDF of the redshift in Figure III.4 and only an upper limit can delivered by the code, as expected.
In addition to the redshift estimation, the code also estimates the visual extinction along the GRB sightline and the intrinsic spectral slope of the GRB afterglow as well as the correlation between these parameters. If the spectral slope has been estimated with X-ray observations, its estimation can be use as a prior to the redshift estimation.

The comparison of our photometric redshift estimates with the spectroscopic redshifts are reported in Figure III.5 and summarised in Table III.1. To quantify the quality of the agreement with the spectroscopic redshift we introduce two indicators : $\Delta z = z_{phot} - z_{spec}$ and $\eta z = \Delta z/(1 + z_{spec})$.
- The mean and standard deviation of Δz is -0.006 and 0.22 at z > 3 indicating no bias and a photometric redshift accuracy of $\sim$ 0.2.
- The mean and standard deviation of ηz is -0.003 and 0.034 at z > 3, meaning that there is no bias and a relative accuracy of 3%.
The agreement is then very good with spectroscopic measurements for $z > 3$. For $z < 3$, Lyman-α transition does not enter the optical filter band and as we do not have UV observations it results in larger uncertainties but the algorithm is able to give an upper limit for the redshift. More generally, this validation test showed that the non detection are well treated and that usually an SMC extinction law is able to reproduce the observed GRB SED (when using different extinction laws, the best fit returning the best χ^2 is picked).
We conclude that the algorithm is validated and sufficiently robust to be used by COLIBRI to estimate the photometric redshift within the first minutes of observations. The estimation of the photometric redshift accuracy delivered by COLIBRI is addressed in the next section. This photometric redshift code is publicly available as an open source Python package [1].

[1]. https://github.com/dcorre/pyGRBz

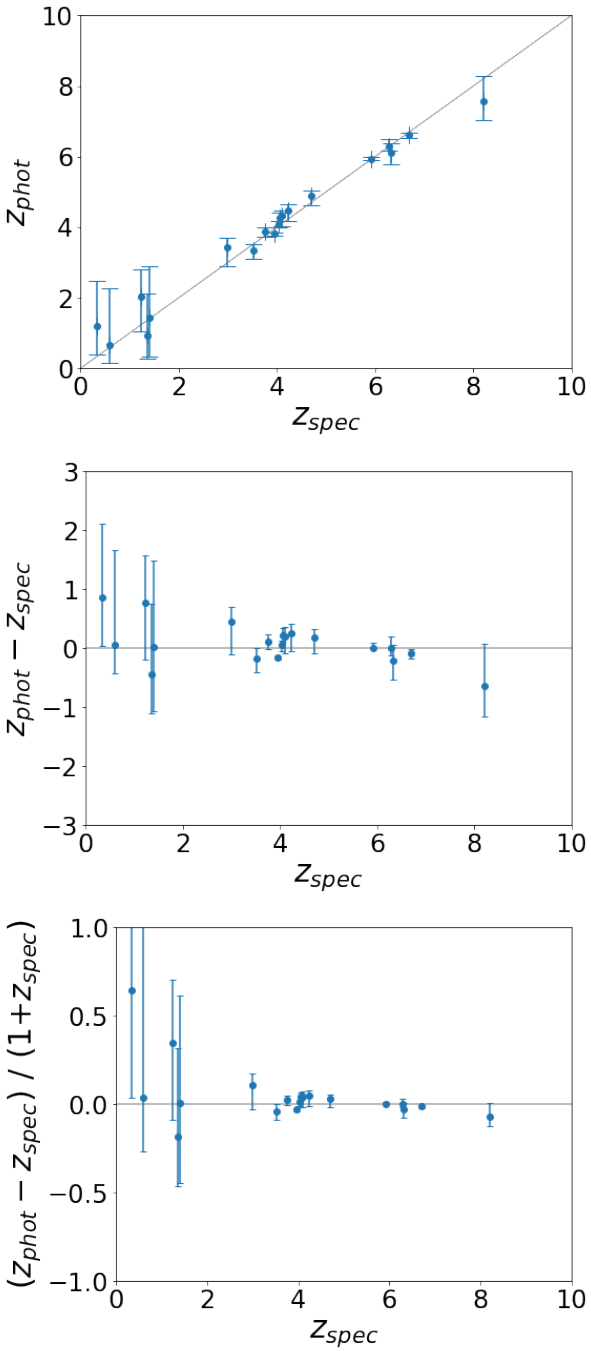

Figure III.5– Estimation of the photometric redshift and its 1σ uncertainty as a function of the spectroscopic redshift of observed GRBs. From top to bottom : z_{phot}, absolute accuracy $z_{phot} - z_{spec}$ and relative accuracy $(z_{phot} - z_{spec})/(1 + z_{spec})$ as a function of the spectroscopic redshift z_{spec}

Table III.1– Spectroscopic redshift measurements are taken from J. Greiner, database. The photometric redshift estimation and its 1σ uncertainty are given in the third column. All GRBs are fitted with an SMC extinction law except GRBs 130408A and 160203A fitted without dust.

GRB	z_{spec}	z_{phot}
050904	6.29	$6.29^{+0.20}_{-0.12}$
080913	6.695	$6.61^{+0.08}_{-0.08}$
090423	8.26	$7.63^{+0.63}_{-0.57}$
090516	4.109	$4.32^{+0.15}_{-0.29}$
130215A	0.597	$1.61^{+1.29}_{-1.15}$
130408A	3.757	$3.87^{+0.12}_{-0.13}$
130606A	5.913	$5.92^{+0.08}_{-0.06}$
130907A	1.238	$2.48^{+1.18}_{-0.96}$
130925A	0.347	$1.04^{+1.28}_{-0.69}$
131117A	4.042	$4.10^{+0.07}_{-0.11}$
140419A	3.956	$3.80^{+0.04}_{-0.04}$
140515A	6.32	$6.11^{+0.27}_{-0.32}$
140518A	4.707	$4.89^{+0.14}_{-0.25}$
140614A	4.233	$4.48^{+0.17}_{-0.29}$
141109A	2.993	$3.44^{+0.26}_{-0.55}$
150910A	1.359	$0.92^{+1.19}_{-0.66}$
151027B	4.063	$4.28^{+0.17}_{-0.11}$
160203A	3.52	$3.35^{+0.17}_{-0.24}$
160625B	1.406	$1.02^{+1.62}_{-0.86}$

2. Estimation of the photo-z accuracy on GRB mock samples

To study whether COLIBRI can meet the requirement of delivering a photometric redshift after 5 minutes of observations, we first built a sample of GRB using an empirical model based on optical observations at early times (few tens of second after the GRB trigger) in order to study GRB light curves representative of those COLIBRI will observe. As these observations are only valid for a given time interval and cannot be extrapolated to later times, we built a second sample based on the theoretical synchrotron model allowing to study the redshift estimation accuracy for the same GRB at different times, for instance at t_0+1min, t_0+12h and t_0+24h, with t_0 the GRB trigger.
In Section 2.1 we describe the 2 mock samples. In Section 2.2 we describe the observation strategy we used to define at what time after the GRB trigger COLIBRI is observing the GRB, in which filter and how long to expose. In Section 2.3 we present the resdshift accuracy of COLIBRI for the 2 mock samples.

2.1. Mock samples of GRB light curves

The objective is to simulate GRB afterglow light curves representative of what COLIBRI will observe. We consider 2 ways of simulating the afterglow spectrum, the first one is to use an empirical model which is model independent and reproduce most of the observations : the spectrum evolves as a power law both in time and frequency. However this model is only valid for a given time interval and it is not possible to extrapolate the observations at much later or sooner times (few hours). Consequently, we also considered a model based on the standard synchrotron model based on Granot et Sari, 2002.

2.1.1. Empirical model

As described in Section 2.1.2, empiric GRB light curves are modelled with a simple power law both in time and frequency :

$$F(\lambda, t, z, \beta, \alpha, A_V) \;=\; F_0 \times (\frac{\lambda}{\lambda_0})^{\beta} \times (\frac{t}{t_0})^{-\alpha} \times exp\left[-\tau_{dust}(z, A_V^{host}, \frac{\lambda}{1+z}) - \tau_{IGM}(z))\right] \qquad \text{(III.9)}$$

where F_0 is the normalisation factor at λ_0 and t_0.
λ is the observed wavelength, t the time since the trigger so $t = 0$ is the trigger time. $\tau_{dust}(z, A_V^{host}, \frac{\lambda}{1+z})$ and $\tau_{IGM}(z)$ are the optical depth corresponding to the dust extinction in the host galaxy and the IGM transmission respectively and are defined in II.2.1.2.
There are 5 parameters in this model : F_0, z, A_V^{host}, β and α.

2.1.1.a. Parameters distributions

The redshift distribution aims at probing the range 0 to 11 to study the behaviour of the photometric redshift algorithm at low-z, estimating the accuracy of the photometric redshift estimation within the range of interest (3<z<7), and to test the ability of COLIBRI to detect GRBs at high redshift (z>7). The distribution for the redshift is a Gaussian with mean 5.5 and a standard deviation of 3.5 truncated at 0 and 11 in order to especially probe the redshift range 3 to 9.
The F_0 distribution is taken from the distribution of R_C magnitude for GRB afterglows observed at $t_0 = 86.4$ seconds, transformed to a common redshift of $z = 1$ in Kann, 2010. λ_0 is set to the effective wavelength of the R_C filter, 6400 Åas defined in Bessell, 1979. The normalisation flux at $z = 1$ is equal to $F_{0,z=1} = 3080 \times 10^{-0.4 \times mag_{R_C}}$, with 3080 Jy being the zero magnitude flux for R_C [Bessell, 1979].

The flux at a redshift z is computed using the same prescriptions in Kann et al., 2006 :

$$F(\lambda, t, z, \beta, \alpha, A_V) = \frac{1+z}{1+1} \times F(\lambda \cdot \frac{1+1}{1+z}, t \cdot \frac{1+1}{1+z}, z = 1, \beta, \alpha, A_V) \times \left(\frac{D_{Lum}(z=1)}{D_{Lum}(z)}\right)^2 \times exp\left[-\tau_{dust}(z, A_V^{host}, \frac{\lambda}{1+z}) - \tau_{IGM}(z) + \tau_{IGM}(z=1)\right] \quad \text{(III.10)}$$

where $D_{Lum}(z)$ is the luminosity distance at a redshift z assuming a flat universe, using $H_0 = 67.8$ km/s/Mpc and $\Omega_m = 0.308$ from Planck Collaboration et Ade, 2015. As there is no information on the dust extinction for the flux at z=1 in Kann, 2010, we only corrected the flux at z from the IGM transmission at z=1.

The parameters for the distributions are summarised in Table III.2 and the distributions are plotted in Figure III.7. For A_V^{host} and β we used the values from Kann, 2010 to remain consistent with the magnitudes. For the α distribution we use the values from X.-G. Wang, 2015. The extinction law is randomly drawn between a SMC, LMC and MW with respectively 60%, 20% and 20% probability. 500 GRB afterglows are randomly drawn from these distributions. In order to incorporate a population of highly extinguished GRB afterglows accounting for 20% of the overall population, we added 125 GRB afterglows with a visual extinction randomly drawn from a Gaussian distribution of mean 1.3 mag and standard deviation of 1 mag within a redshift range randomly drawn from a Gaussian distribution of mean 2 and standard deviation of 1. The choice of these parameters was motivated by the work of Zafar et al., 2018c which found only low dust content at z $>$ 3.5 and maximum values of visual extinction at z $\sim$ 1.5-2. Similar results are found in Covino et al., 2013.

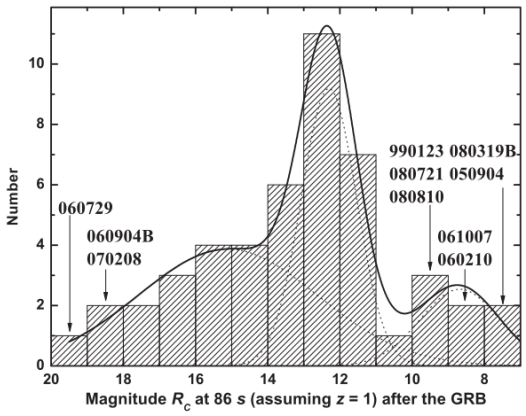

Figure III.6– Distribution of optical transient magnitudes at 86 s (10−3 days) after the GRB trigger in the observer frame, after shifting all afterglows to z = 1 [Kann, 2010]. (Credit : [Kann, 2010])

Table III.2– Parameter distributions for the empirical model. The distributions are modelled using a Gaussian with mean and standard deviation are given in the second and third columns.

	Mean	Standard deviation	limits	ref.
z	5.5	3.5	[0,11]	none
A_V	0.24	0.21	[0 , 2]	Kann, 2010
β	0.66	0.25	[0 , 2]	Kann, 2010
α	1.26	0.38	[-1 , 2.5]	X.-G. Wang, 2015
R_C mag at z=1		See Figure III.6		Kann, 2010

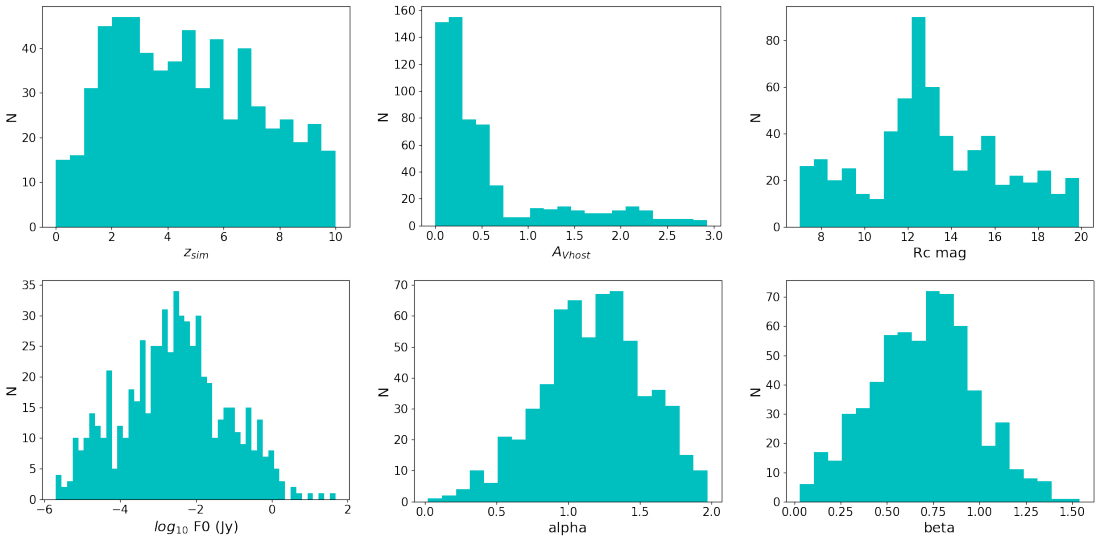

Figure III.7– Parameters distributions for the 625 GRBs.

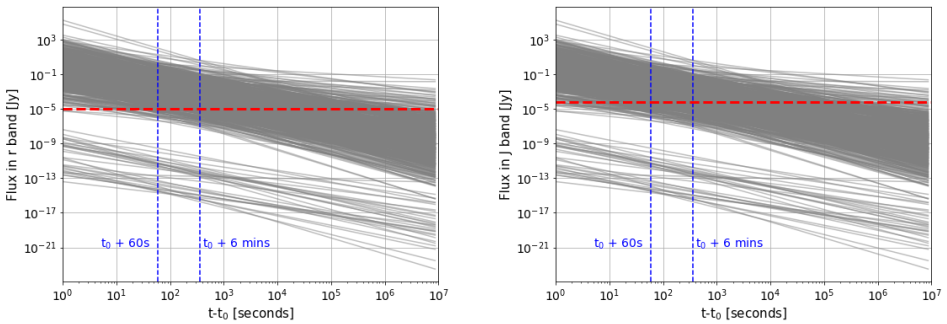

Figure III.8– Light curves in r (left) and J (right) band for the 625 samples for the empirical model. The blue dashed lines represents the time interval from 1 to 6 min after the trigger in which we observe these afterglows. The dashed red line represents the 5σ limiting magnitude for an exposure of 30s, an airmass of 1.5, a seeing at zenith of 0.8" and 7 days after the new moon. This corresponds to an AB magnitude of 21.27 and 19.53 in r and J bands respectively.

2.1.2. Standard synchrotron model

We model the standard synchrotron following the prescriptions of Granot et Sari, 2002. As seen in Section II.2.1.1.b, there are 6 parameters describing this model : E_{52} the total energy in the shell (in $10^{52} ergs$), p the index of the electron power-law distribution, ϵ_B the fraction of shock energy converted to the magnetic fields energy, ϵ_e the fraction of shock energy used to accelerate the electrons, n_0 particle

density in the ambient medium (cm^{-3}).

The redshift and A_V are drawn from the same distribution As for the empirical model. The extinction law is randomly drawn between a SMC, LMC and MW with respectively 60%, 20% and 20% probability. The parameters of the synchrotron model of Granot et Sari, 2002 are drawn from the distributions obtained in [Turpin, 2016] by fitting observed GRB light curves. There is one caveat by randomly drawing a parameter value from a distribution independently from the other distributions, i.e. not taking into account the correlation between parameters. Consequently it might sometimes results in a non realistic set of parameter values. This might explain the GRB afterglows with a rather long rise flux in the light curves in Figure III.10 which is not what is usually observed in GRB light curves. One solution would be to add some correlations between the parameters to the draw.

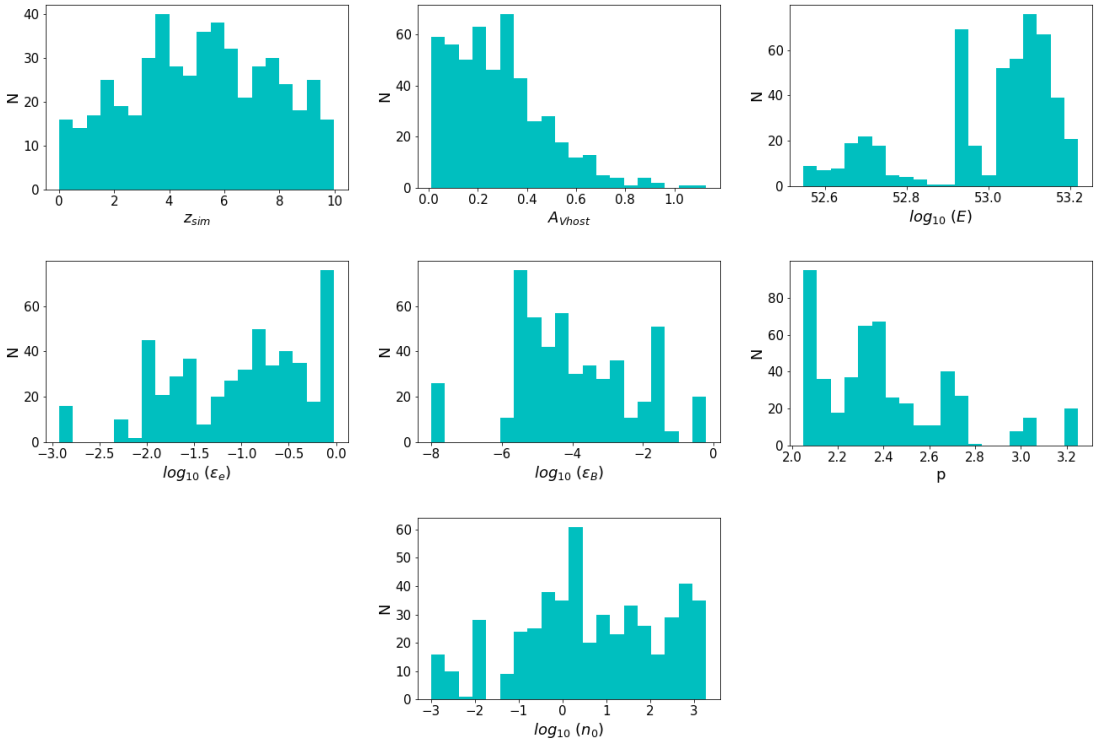

Figure III.9– Parameters distributions used to build the mock sample of 500 GRBs. z_{sim} is the redshift, A_{Vhost} the amount of attenuation in the host galaxy in the V band, E is the isotropic kinetic energy of the ejecta (in $ergs$), ϵ_B is the fraction of shock energy converted to the magnetic fields energy, ϵ_e is the fraction of shock energy used to accelerate the electrons, p is the index of the electron power-law distribution, and n_0 is the particle density in the ambient medium (cm^{-3}).

The GRB afterglow light curves of the 500 GRBs in the r and J bands are showed in Figure III.10.

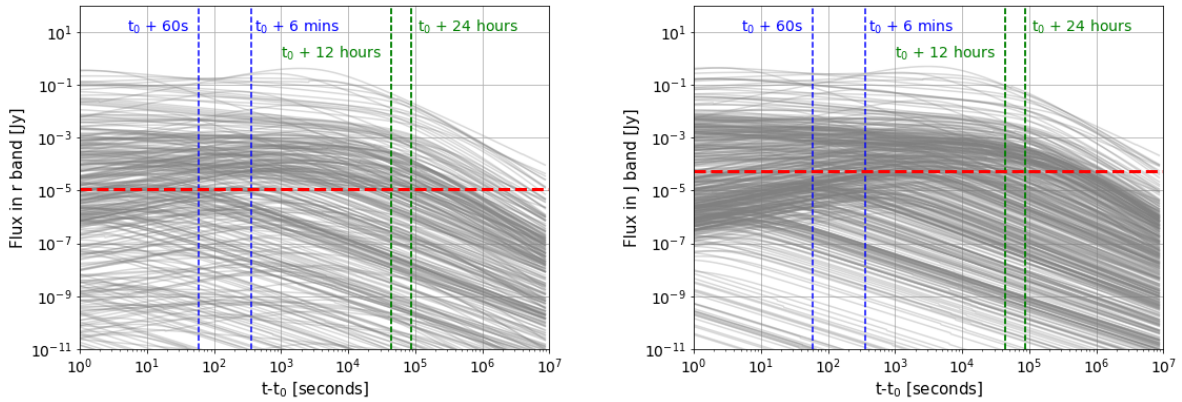

Figure III.10– Light curves in r (left) and J (right) bands of the 500 GRBs in our mock sample. The dashed red line represents the 5σ limiting magnitude for an exposure of 30s, an airmass of 1.5, a seeing at zenith of 0.8" and 7 days after the new moon. This corresponds to an AB magnitude of 21.27 and 19.53 in r and J bands respectively. The different time at which the observations are represented by the blue and green dashed lines.

2.2. Set up an observation strategy

Once the GRB light curves are simulated we need to set an observation strategy describing at what time after the GRB trigger COLIBRI is observing the GRB, in which filter and how long to expose. The main objective of the simulation is to study the first 5 minutes of observations imposed by SVOM requirements. We have selected 3 times at which the observations start : t_0+60s representing the most favourable case of a GRB observable as soon as the alert is received, t_0+12h representing the extreme case of a GRB exploding at dawn and t_0+24h to study the evolution of photometric redshift with time. A good photometric redshift estimation required a good spectral coverage to localise the wavelength at which Lyman-α or Lyman break occur. At the beginning of the observations, very large filters are used to optimise the detection of the GRB, *gri* and *zy* for the visible channels and J band in the NIR channel. As soon as the GRB is detected in one band, the filters are successively changing between g, r and i in the DDRAGO-B channel, between z and y in the DDRAGO-R channel and between J and H for the NIR channel in order to have a good spectral coverage. Each observation has an exposure time of 30s. An example of the observation strategy is given in Table III.3.

The simulated spectrum is then integrated at these times for the given exposure time through the Exposure Time Calculator to obtain the magnitude and its associated uncertainty in each filter band taking into account the different transmissions, the camera efficiency, the sky background, readout noise, thermal noise of COLIBRI.

For all GRBs we take an airmass of 1.5, the seeing at zenith to be 1" and the moon being 7 days from the new moon.

2.3. Photo-z accuracy for COLIBRI

2.3.1. Empirical model

To estimate the redshift, we extract the SED from the simulated light curves at the time where the flux in the reddest band is maximum, and perform the MCMC on the GRB SED at this time. The accuracy of the photometric redshift estimation for the 625 GRBs simulated with the empirical model is seen in Figure III.11 where the estimated photometric redshift, the absolute accuracy $\Delta z = z_{phot} - z_{sim}$ and relative accuracy $\eta z = \Delta z/(1 + z_{sim})$ are plotted. The redshift range can be split in 3 regions :

Table III.3– Observational strategy used in this study. In this example the GRB is detected in the first sequence with the very large filters. From the second sequence we switch to large filters and change the filter after each sequence to perform multi-wavelength observations.

Sequence	Time since burst s	Exposure time s	band
1	60	30	gri
1	60	30	zy
1	60	30	J
2	90	30	r
2	90	30	z
2	90	30	H
3	120	30	i
3	120	30	y
3	120	30	J
4	150	30	z
4	150	30	g
4	150	30	H
5	180	30	y
5	180	30	r
5	180	30	J
6	210	30	g
6	210	30	i
6	210	30	H
7	240	30	r
7	240	30	z
7	240	30	J
8	270	30	i
8	270	30	y
8	270	30	H
9	300	30	z
9	300	30	g
9	300	30	J
10	330	30	y
10	330	30	r
10	330	30	H

- $z < 3.5$ where the Lyman-α does not enter the g band.
- $3.5 < z < 8$ where there is a good spectral coverage thanks to the use of contiguous filter bands : g, r, i, z, y.
- $z > 8$ where a detection is only possible in the NIR bands (J, H).

The results are reported in Table III.4 and Figure III.11.

- There is large dispersion for $z < 3.5$ as expected, and COLIBRI will not be able to constrain accurately the redshift but will deliver an upper limit.
- In the range $3.5 < z < 8$, the dispersion is small meaning that COLIBRI will be able to derive robust estimate of photometric redshifts with a relative accuracy of 10%.
- For $z > 8$ COLIBRI will derive photometric redshift accuracy with a relative accuracy of $\sim$ 14%. However, as there are detections only in J and H, there is a degeneracy between the spectral slope, β, the redshift and the amount of extinction in the host galaxy that can only be broken with a high SNR. When the SNR is not sufficient, there is an under estimation of the redshift as it is estimated as the median of a flat and broad PDF distribution.
- Regarding the dusty GRB afterglows with $A_V > 1$ mag, 94 of the 125 dusty afterglow are detected.

Table III.4– Statistics summary of the photometric redshift estimation for the mock sample based on the empirical model. For the 3 redshift ranges the number of detected GRBs, mean and standard deviation of the absolute and relative accuracy are reported.

	nb of detections	Δz	ηz
z < 3.5	207 / 238 (87%)	-0.21 ± 1.11	0.0 ± 0.42
3 ≤ z ≤ 8	243 / 304 (80%)	-0.14 ± 0.49	-0.03 ± 0.10
z > 8	61 / 83 (73%)	-1.21 ± 1.32	-0.13 ± 0.14

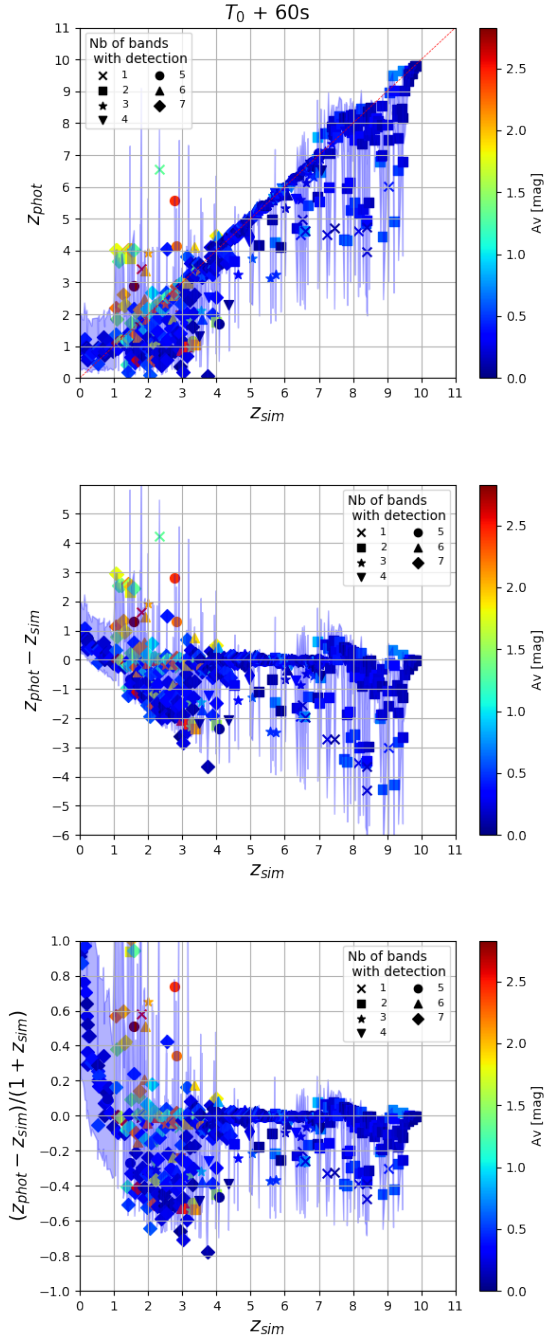

Figure III.11– Photometric redshift accuracy : results of the simulation of 625 GRB afterglow spectra samples with the empirical model. From top to bottom : z_{phot}, absolute difference $\Delta z = z_{phot} - z_{sim}$, relative difference $\eta z = \Delta z/(1 + z)$ versus the input redshift, i.e. z_{sim}. The points represents the z_{phot} values and the blue shaded area represents the uncertainty at 1σ level. The shape of the points represent the number of band with a SNR>3.

Table III.5– Statistics summary of the photometric redshift estimation for the mock sample based on the synchrotron model. For the three times and 3 redshift ranges the number of detected GRBs, mean and standard deviation of the absolute and relative accuracy are reported.

		nb of detections	Δz	ηz
t_0+60s	z < 3.5	97 / 138 (70%)	0.01 ± 0.89	0.11 ± 0.46
	3.5 ≤ z ≤ 8	137 / 279 (49%)	-0.07 ± 0.33	-0.01 ± 0.05
	z > 8	37 / 83 (23%)	-1.29 ± 1.31	-0.13 ± 0.13
t_0+12h	z < 3.5	63 / 138 (46%)	-0.11 ± 0.74	0.06 ± 0.48
	3.5 ≤ z ≤ 8	99 / 279 (35%)	-0.14 ± 0.45	-0.03 ± 0.09
	z > 8	11 / 83 (13%)	-1.10 ± 1.11	-0.11 ± 0.11
t_0+24h	z < 3.5	57 / 138 (41%)	-0.27 ± 0.79	-0.02 ± 0.34
	3.5 ≤ z ≤ 8	90 / 279 (32%)	-0.16 ± 0.36	-0.03 ± 0.07
	z > 8	10 / 83 (12%)	-1.21 ± 1.24	-0.12 ± 0.12

2.3.2. Synchrotron model

The accuracy of the photometric redshift estimation for the 500 GRBs simulated with the synchrotron model is seen in Figure III.13 where the estimated photometric redshift, the absolute and relative accuracy are plotted as a function of the input redshift for 5 minutes of observations starting 60s, 12h and 24h after t_0.

The results are reported in Table III.5 and Figure III.13, and conclusions are similar as for the mock sample based on the empirical model.

- For $z < 3.5$ COLIBRI will not be able to constrain accurately the redshift but will deliver an upper limit.
- For the range $3.5 < z < 8$ COLIBRI will be able to derive photometric redshifts with a relative accuracy of $\sim$ 5-10% at the 3 time periods.
- For $z > 8$ the relative accuracy is about 12% at each time period.
- We note that the number of GRB detected decreased more rapidly for the 12 first hours, from $\sim$ 54% to 35%, than for the next 12 hours, from $\sim$35% to 31%. This highlights the need of a rapid follow-up.

The need of a high SNR to break the degeneracy between the redshift and reddening at $z > 8$ is illustrated in Figure III.13 where at t_0+60s the z_{phot} of the 2 GRBs at $z \sim$9.5 are accurately estimated whereas at t_0+12h and t_0+24h it is not possible anymore to distinguish a high redshift GRB from a highly extinguished GRB because of the SNR decrease. This result in a broad and flat PDF for the redshift leading to an underestimation of the redshift with large uncertainties.

The fact that the mean of Δz and ηz is negative is mostly due to GRB afterglows with a weak SNR leading to a broad and unconstrained PDF for the redshift, and as the photometric redshift is estimated with the median of the PDF it usually underestimates the true value, nevertheless the true value is usually consistent with the photometric redshift estimate within the 1σ uncertainty (see example in Figure III.12).

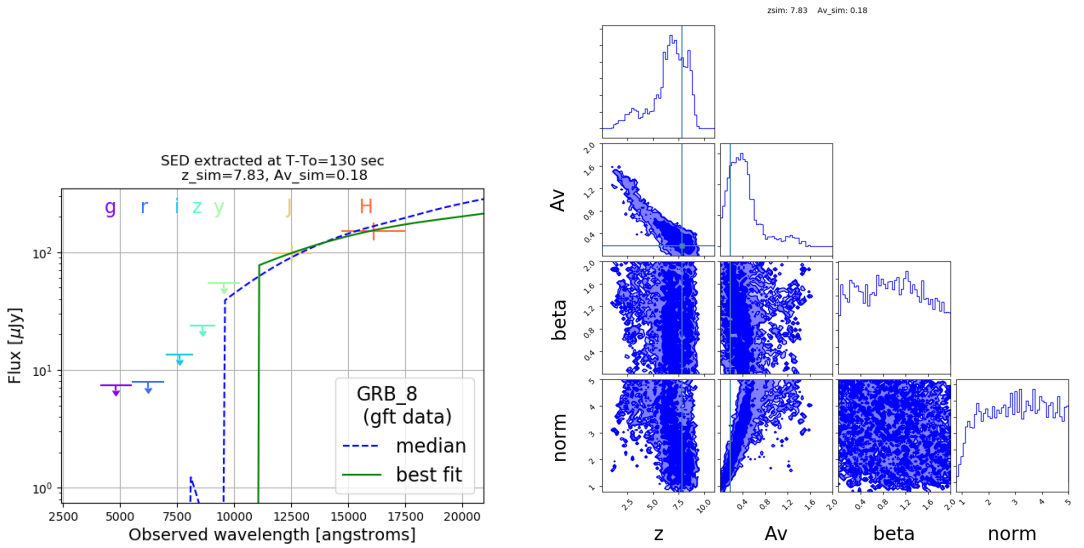

Figure III.12– Example of the outputs of the algorithm for a simulated GRB at z=7.83 with A_V=0.18 mag. The GRB is detected only in J and H with a SNR of 5.8 and 5.4 respectively. *Left :* Best SEDs using the best fit values (green line) and the median of the PDFs (dashed blue line). *Right :* one and two dimensional projections of the posterior PDFs for all parameters. The vertical and horizontal blue lines represent the true value of the parameters. The code returns a median value of z=6.81 with +1.42/-1.98 1σ uncertainty.

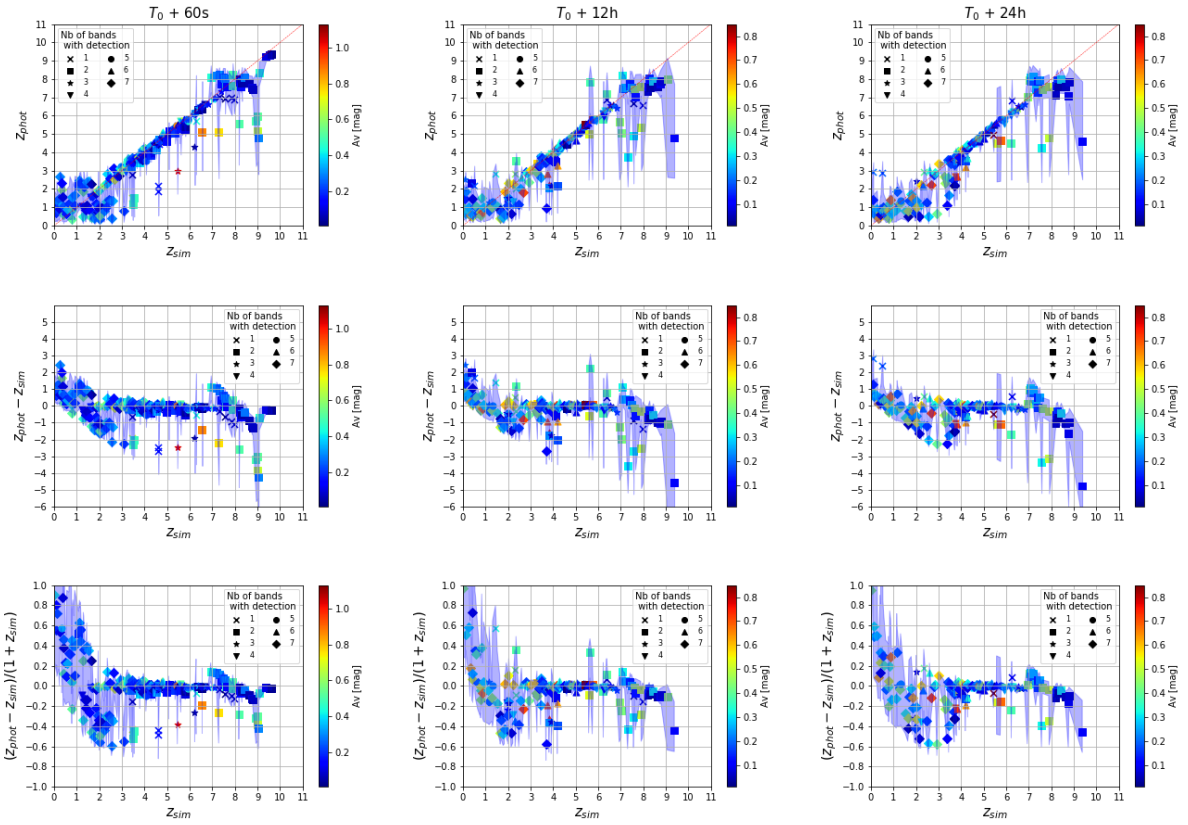

Figure III.13– Results of the estimation of z_{phot} for the 500 GRBs simulated with the synchrotron model and observed during 5 minutes starting at t_0+60s, t_0+12h and t_0+24h (from left to right). From top to bottom : z_{phot}, absolute difference $z_{phot} - z_{sim}$ and relative difference $(z_{phot} - z_{sim})/(1 + z_{sim})$ as a function of the input redshift z_{sim}. The colorbar encodes the amount of attenuation in the V band i the host galaxy. The symbols, located at the z_{phot} estimation, represents how many bands have a SNR>3. The blue shaded area represents the 1σ uncertainty associated to the photometric redshift estimation.

Table III.6– Statistics summary of the photometric redshift estimation with and without CAGIRE for the mock sample based on the empirical model. For the 3 redshift ranges, the number of detected GRBs, mean and standard deviation of the absolute and relative accuracy are reported.

		nb of detections	Δz	ηz
without CAGIRE	z < 3.5	190 / 238 (80%)	-0.15 ± 1.29	0.03 ± 0.51
	3.5 ≤ z ≤ 8	199 / 304 (65%)	-0.14 ± 0.61	-0.03 ± 0.12
	z > 8	1 / 83 (1%)	-	-
with CAGIRE	z < 3.5	207 / 238 (87%)	-0.21 ± 1.11	0.0 ± 0.42
	3 ≤ z ≤ 8	243 / 304 (80%)	-0.14 ± 0.49	-0.03 ± 0.10
	z > 8	61 / 83 (73%)	-1.21 ± 1.32	-0.13 ± 0.14

2.4. Importance of CAGIRE to detect high-z GRBs

As CAGIRE will be equipped with a new sensor developed by SOFRADIR, some delay in the delivery of the detector is unfortunately possible. Therefore, in this section we perform the same analysis as before but without a NIR detector, i.e. without J and H bands, using the same mock sample based on the empirical model. The results are reported in Table III.6 and Figure III.14.

- The accuracy on the photometric redshift is similar as with CAGIRE up to z $\sim$ 8 with a relative uncertainty of 12% within 3.5 <z< 8.

- For z > 8, there is only one GRB detected as the Lyman-α enters the J band around z = 8. Only 8% of the GRB are detected above z > 7.

- Without CAGIRE, the number of detected is slightly less for 3.5 <z< 8 as the faintest GRB afterglows can not be detected in the J and H bands anymore.

- The number of detected GRB afterglow with A_V > 1mag is now 75 over 125 instead of 94 with CAGIRE, which corresponds to a $\sim$15% decrease.

These results illustrate the importance of a NIR detector to detect faint and high-z GRBs, which are among the most interesting GRBs to study. If the follow-up starts in the first minutes after the GRB trigger, a large fraction of the dusty GRBs can be detected by COLIBRI. Moreover, without a NIR sensor GRBs can be detected up to z $\sim$ 8 with a relative accuracy of 12% on the photometric redshift estimation.

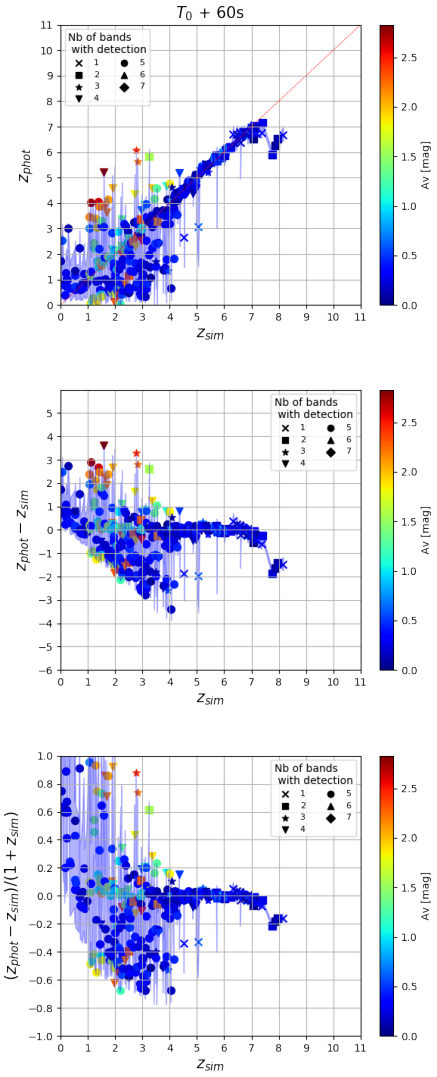

Figure III.14– Photometric redshift accuracy : results of the simulation of 625 GRB afterglow spectra samples with the empirical model without the NIR detector CAGIRE. From top to bottom : z_{phot}, absolute difference $\Delta z = z_{phot} - z_{sim}$, relative difference $\eta = \Delta z/(1+z)$ versus the input redshift, i.e. z_{sim}. The points represents the z_{phot} values and the blue shaded area represents the uncertainty at 1σ level. The shape of the points represent the number of band with a SNR>3.

3. Conclusions

We have implemented an algorithm which enables to determinate accurate photometric redshift for GRB afterglows. This algorithm has been tested successfully over a large sample of observed GRB afterglows with spectroscopic redshift. This algorithm takes either a light curve or a SED, not necessarily from the same instrument, as an input and derive the photometric redshift, the dust extinction coefficient in the V band in the host galaxy A_V, the spectral slope of the afterglow β and their correlation.
In order to study the SVOM requirement of delivering a redshift indication after 5 minutes of observations, we have built 2 different samples of GRB light curves using a realistic observation strategy to estimate the accuracy of the photometric redshift estimation delivered by COLIBRI. The relative accuracy is found to be about 10% for $3.5 < z < 8$ and $\sim$ 13-14% for $z > 8$. This study confirms the ability of COLIBRI to detect dusty and high-redshift GRBs and to reliably estimate their photometric redshift. Even without the NIR detector, CAGIRE, the relative accuracy remains on the same order, however less faint and high-z GRBs ($z \gtrsim 7$) are detected.

When COLIBRI will start to operate, this code will autonomously perform a quasi real-time photometric redshift estimation. As a by-product the visual extinction and optical spectral slope are also estimated and different extinction laws can be tested. A similar study for different observation strategies will allow to optimise the detection rate and photometric redshift estimation of COLIBRI.

Due to its sensitivity and very rapid follow-up, COLIBRI will detect GRBs suffering a high amount of visual extinction. These GRBs are preferentially found in dusty galaxies, and their detection is very important to assess whether GRB host galaxies can be used as tracers of star formation. In the second part of this thesis, I am interested in the characterisation of the dust properties inside these galaxies which are selected in a very different way as galaxies in field surveys.

GRBs : unique tools to probe dust properties and ISM structure of distant star-forming galaxies

This chapter aims at comparing the dust extinction and dust attenuation processes in GRB host galaxies. In Section 1 we define what is dust attenuation and how it differs from dust extinction. In Section 2 we describe different ways of modelling the dust attenuation either using attenuation laws or more complexed radiative transfer simulations. In Section 2.3, we study the ability of two attenuation laws to reproduce the variety of shapes observed in radiative transfer simulations. Finally, in Section 3 we study the dust extinction and attenuation processes in GRB host galaxies.

1. Dust attenuation is different from dust extinction

When considering observations of extended regions, such as a galaxy or a region of a galaxy, old and young stars are mixed within dust and are located at different optical depth. In addition to the two processes at stake for dust extinction described in Section I.3, two additional processes affect the intrinsic emission of an extended region :

- photons absorbed by dust (same as dust extinction)
- photons scattered out of the observer line-of-sight by dust (same as dust extinction)
- stars are located at different optical depth, i.e. embedded more and less deep in the galaxy (as seen from the observer)
- photons scattered into the observer line-of-sight by dust

The combination of these four processes is known as dust attenuation. Dust attenuation is thus different from dust extinction as it is highly dependent on the geometrical distribution of dust and stars in the galaxies. An illustrative sketch of these effects is seen in Figure IV.1. The modelling of the dust attenuation is discussed in the next section.

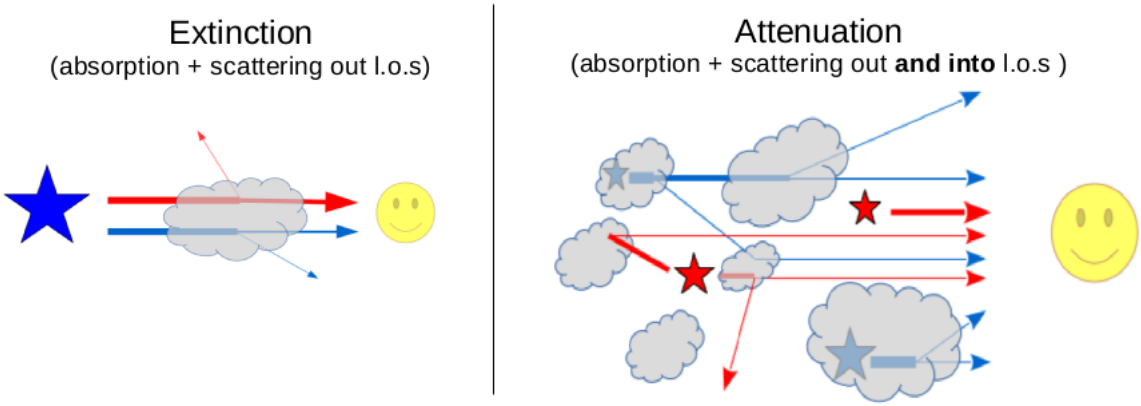

Figure IV.1– Sketch illustrating the dust effect of the dust extinction (left) and dust attenuation (right). *Left :* UV photons are preferentially absorbed compared to NIR photons and the scattering is rather forward oriented for UV photons while it is more isotropic for NIR photons. *Right :* For extended sources stars are located at different optical depth and young stars are preferentially found in their birth clouds while old stars had time to migrate outside [Charlot et Fall, 2000] and some photons can be scattered to the observer line of sight.

2. Modelling dust attenuation

The modelling of dust attenuation is not only important to study dust properties but also to study the star formation activity of a galaxy as young stars emit preferentially in UV. These UV photons are likely to interact with dust grains resulting in a decrease of the amount of UV photons that we can detect. An accurate modelling of the dust effects is thus crucial when interpreting the SEDs of galaxies, as illustrated in Figure IV.2 the dust effect impacts strongly the shape of a galaxy SED in the UV, less in the optical and has little influence to the stellar continuum in the NIR. The effect of dust attenuation depends on the combination of both the optical and physical properties of dust but also on the relative geometrical distribution of stars and dust leading to different shape of dust attenuation [Witt et Gordon, 2000; Seon et Draine, 2016]. So not only the amount of dust but also the shape of its wavelength dependence can vary from one galaxy, or region of a galaxy, to another. This makes an accurate correction of the dust effects challenging. Fortunately, most of the dust grains which absorbed UV photons will re-emit photons in the far-IR (FIR), providing an information on the amount of attenuation that took place in the UV. If FIR data are available the better constraint on the amount of dust allows for a more accurate measurement of the shape of the dust attenuation curve derived from UV to NIR data.

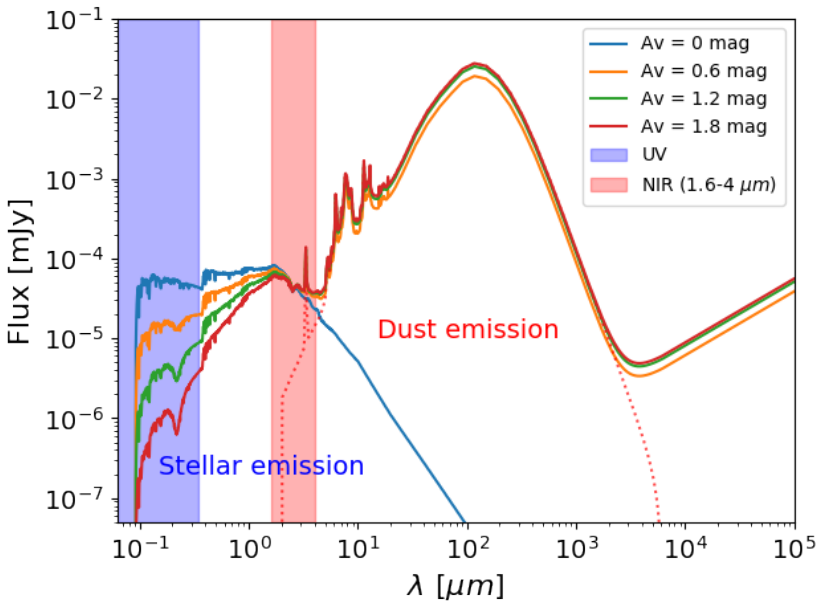

Figure IV.2– Spectral Energy Distribution of a galaxy simulated with CIGALE for different amount of attenuation : A_V= 0, 0.6, 1.2, 1.8 mag. The attenuation is modelled using the formulation of Noll et al., 2009 with δ=0, and a UV bump amplitude of 3. The galaxy is 1 Gyr old, with a solar metallicity, an initial mass function of Chabrier, 2003, and the dust emission in IR is modelled using Dale et al., 2014 templates. No nebular emission is used. The blue and red shaded area represents the UV and NIR (from 1.6 to 4 μm). The red dashed line represents the dust emission for A_V = 1.8 mag. The unattenuated stellar emission is visualised by the blue solid line corresponding to A_V = 0 mag.

The attenuation curve, in other words the dust effects occurring in the UV to NIR domain, can be modelled using different approaches. The most intuitive approach is to derive an attenuation law from observations, such as the attenuation law of Calzetti et al., 2000 derived using local starburst galaxies. However such an empirical law is only valid for the kind of galaxies that were observed. The second approach intends to reproduce a larger variety of attenuation curve shapes by using a more flexible parametric law. A popular formalism was proposed by Noll et al., 2009 consists in a modification of

the original starburst law of Calzetti et al., 2000 allowing for a varying shape and the possibility to introduce a UV bump. Finally, a most satisfying approach is to perform a radiative transfer simulation for a given geometry, dust/star distribution and dust grain properties [Silva et al., 1998; Witt et Gordon, 2000; Pierini et al., 2004; Tuffs et al., 2004; Seon et Draine, 2016]. These radiative models allow to reproduce the variety of attenuation curves but at the cost of consequent computational time. In the following we will group the first and second approaches under the term attenuation curve "recipes" and the third approach under the term radiative transfer (RT) attenuation curves.
In the sections 2.1 to 2.2 we will describe the different approaches. In section 2.3 we will study whether the recipes can fit accurately the more realistic attenuation curves from radiative transfer simulations.

2.1. Dust attenuation recipes

Following the method in Calzetti et al., 2000, one can recover the intrinsic wavelength dependence of the stellar emission from observations using :

$$f_{\rm int}(\lambda) = f_{\rm obs}(\lambda) 10^{0.4 k(\lambda) E(B-V)_{\rm star}} \tag{IV.1}$$

where $k(\lambda) = A(\lambda)/E(B-V)_{star}$ is the reddening curve to be applied to the observed stellar continuum SED, $f_{obs}(\lambda)$, of a galaxy in order to recover its intrinsic SED, $f_{int}(\lambda)$.
In the following, we will define the $k(\lambda)$ for the original starburst law of Calzetti et al., 2000 and the more flexible formalism of Noll et al., 2009.

2.1.1. Original starburst law

This attenuation law was calibrated on a sample of 39 nearby UV-bright starburst galaxies [Calzetti et al., 1994; Calzetti et al., 2000]. The normalised attenuation curve (see Figure IV.3) is characterised by a shallower slope in the UV than the 3 local extinction curves (SMC, LMC and MW). This is an effect of the more complex processes at stake for attenuation curves where the geometry and dust/stars distribution also shape the wavelength dependence of the attenuation which is not the case for the extinction curves. Its shape is fixed and only the amount of dust attenuation is a free parameter. This is the most currently used recipe and is also used at high redshift. This law is an average of 39 galaxies and so its usage for a single galaxy, even for one with similar characteristics as the sample used to construct the relation, brings intrinsic uncertainties as mentioned in Witt et Gordon, 2000. This law should be used only for correcting dust effects for a sample of galaxies that are experiencing an active star formation. In the following we will refer to it as the C00 law.

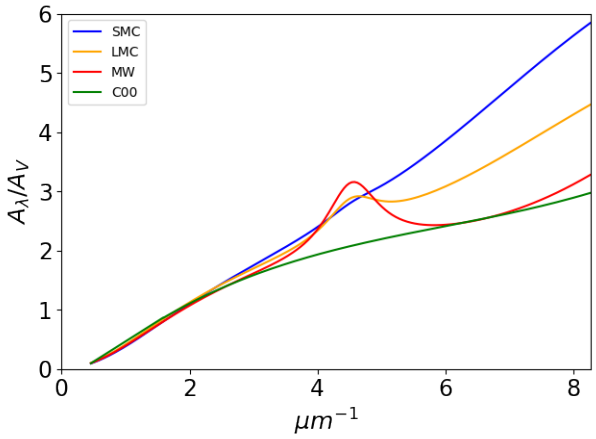

Figure IV.3– Attenuation curve from Calzetti et al., 2000 alongside the 3 local mean extinction curves from Pei, 1992.

The C00 recipe is parametrised as :

$$\begin{aligned} k_{\mathrm{C00}}(\lambda) &= 2.659 \times (-1.857 + 1.040/\lambda) + R_{\mathrm{V}} \\ (0.63\mu\mathrm{m} \leq \lambda \leq 2.20\mu\mathrm{m}) & \\ &= 2.659 \times (-2.156 + 1.509/\lambda - 0.198/\lambda^2 + 0.011/\lambda^3) + R_V \\ (0.12\mu\mathrm{m} \leq \lambda < 0.63\mu\mathrm{m}) & \end{aligned} \tag{IV.2}$$

with $R_{\mathrm{V}} = A_{\mathrm{V}}/E(B-V)_{star} = 4.05 \pm 0.80$.
The color excess of the stellar continuum, $E(B-V)_{star}$, is proportional to the color excess derived from the nebular emission lines : $E(B-V)_{star} = (0.44 \pm 0.03) \times E(B-V)_{lines}$.

2.1.2. Modified starburst law

The C00 starburst law only allows to fit the amount of attenuation in the V band, in other words it is a scaling relation as the shape is fixed by the equation IV.2. In order to provide more flexibility to the C00 law Noll et al., 2009 proposed a new formulation by adding the possibility to vary the steepness of the law in the UV-optical domain and to add a UV bump using a Lorentzian-Drude profile according to the following formalism :

$$\begin{aligned} k_{N09}(\lambda) = \frac{A(\lambda)}{E(B-V)_{star}} &= (k_{C00}(\lambda) + D_{\lambda_0,\gamma,E_{\mathrm{b}}}(\lambda)) \times \left(\frac{\lambda}{\lambda_{\mathrm{V}}}\right)^{\delta} \\ A(\lambda) = \frac{A_{\mathrm{V}}}{4.05}(k_{C00}(\lambda) + D_{\lambda_0,\gamma,E_{\mathrm{b}}}(\lambda)) &\times \left(\frac{\lambda}{\lambda_{\mathrm{V}}}\right)^{\delta} \end{aligned} \tag{IV.3}$$

where $\lambda_{\mathrm{V}} = 5500$ Å, k_{C00} is the C00 reddening curve, and $D_{\lambda_0,\gamma,E_{\mathrm{b}}}$ is the Lorentzian-like Drude profile defined as :

$$D_{\lambda_0,\gamma,E_{\mathrm{b}}}(\lambda) = \frac{E_{\mathrm{b}}\lambda^2\gamma^2}{(\lambda^2 - \lambda_0^2)^2 + \lambda^2\gamma^2}. \tag{IV.4}$$

with λ_0 the central wavelength of the bump, E_b the amplitude of the bump and γ the FWHM of the bump. The flexibility of this recipe is shown in Figure IV.4. In the following we will refer to this recipe as N09.

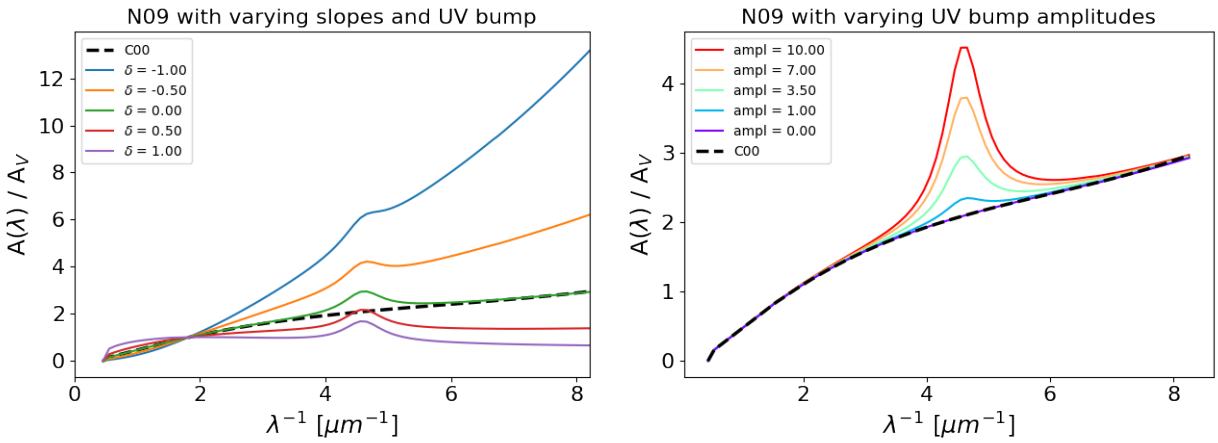

Figure IV.4– Attenuation curves modelled using the modified starburst law. *Left :* Using various slope and a UV bump amplitude of 3.5. *Right :* Using a slope of 0.0 and various UV bump amplitudes.

By definition the color excess is defined as $E(B-V) = A_B - A_V$, so to check whether Equation IV.3 respect this definition so we compute $A_B - A_V$ from Equation IV.3 :

$$\begin{aligned} A_B - A_V &= E(B-V) \times \left\{ [k_{C00}(B) + D_{\lambda_0,\gamma,E_b}(\lambda_B)] \left(\frac{\lambda_B}{\lambda_V}\right)^{\delta} - (k_{C00}(V) + D_{\lambda_0,\gamma,E_b}(\lambda_V)) \right\} \\ A_B - A_V &= E(B-V) \times \left\{ [1 + R_{V,C00} + D_{\lambda_0,\gamma,E_b}(\lambda_B)] \left(\frac{\lambda_B}{\lambda_V}\right)^{\delta} - (R_{V,C00} + D_{\lambda_0,\gamma,E_b}(\lambda_V)) \right\} \\ A_B - A_V &\simeq E(B-V) \times \left\{ [1 + R_{V,C00}] \left(\frac{\lambda_B}{\lambda_V}\right)^{\delta} - R_{V,C00} \right\} \end{aligned} \tag{IV.5}$$

To ensure $E(B-V) = A_B - A_V$, Equation IV.3 needs to be corrected by the additional term in Equation IV.6 :

$$\begin{aligned} k_{N09,corr}(\lambda) &= \frac{R_{V,N09}}{R_{V,C00}} \times (k_{C00}(\lambda) + D_{\lambda_0,\gamma,E_b}(\lambda)) \times \left(\frac{\lambda}{\lambda_V}\right)^{\delta} \\ R_{V,N09} &= \left[(1 + R_{V,C00}) \left(\frac{\lambda_B}{\lambda_V}\right)^{\delta} - R_{V,C00} \right]^{-1} \end{aligned} \tag{IV.6}$$

For the N09 recipe, the effective impact of the UV bump on the attenuation curve depends on the power law slope, meaning that for a given value of E_b the "real" amplitude measured on the attenuation curve will be different for different value of δ. The peak intensity of the UV bump relative to the linear component of the attenuation does not only depend on E_b but also on δ :

$$A_{N09}^{bump}(\lambda_0) - A_{N09}^{nobump}(\lambda_0) = A_V \cdot \frac{E_b}{R_{V,C00}} \cdot \left(\frac{\lambda_B}{\lambda_V}\right)^{\delta} \tag{IV.7}$$

where $A^{bump}(\lambda_0)$ and $A^{nobump}(\lambda_0)$ are the values of the attenuation estimated at the central wavelength of the bump, λ_0.

Salim et al., 2018 proposed to add the Lorentzian-like Drude profile after the correction due to the

power-law :

$$k_{SBL18}(\lambda) = k_{C00}(\lambda) \cdot \frac{R_{V,mod}}{R_{V,C00}} \cdot \left(\frac{\lambda}{\lambda_V}\right)^{\delta} + D_{\lambda_0,\gamma,E_b}(\lambda))$$
$$R_{V,mod} = \left[(1 + R_{V,C00})\left(\frac{\lambda_B}{\lambda_V}\right)^{\delta} - R_{V,C00}\right]^{-1} \quad \text{(IV.8)}$$

In the following, we will refer to this recipe as SBL18. This recipe is the one currently implemented in the CIGALE code.
Now the peak intensity of the UV bump is independent of δ and only proportional to E_b :

$$A^{bump}_{SBL18}(\lambda_0) - A^{nobump}_{SBL18}(\lambda_0) = A_V \cdot \frac{E_b}{R_{V,C00}} \quad \text{(IV.9)}$$

The Figure IV.5 illustrates the different meaning of E_b for the 2 recipes. For a given E_b, when the slope is negative (positive) the real UV bump amplitude is amplified (reduced) for the N09 recipe due to its dependence with δ. Apart from the difference on the UV bump strength this formalism is exactly the same as the N09 recipes. We will use the SBL18 recipe for the comparison with the radiative transfer models.

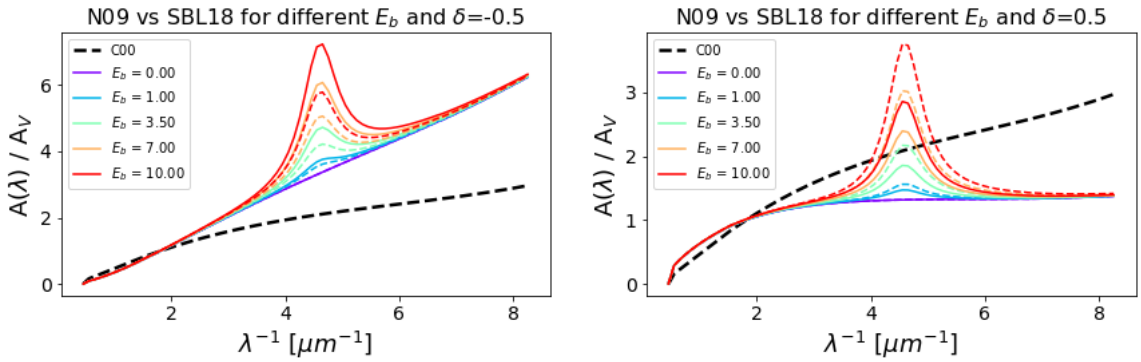

Figure IV.5– Illustration of the different meaning of E_b for the N09 and SBL18 recipes. *Left :* Attenuation curves modelled with various E_b and a slope of -0.5. *Right :* Attenuation curves modelled with various E_b and a slope of 0.5. The continuous and dashed lines correspond to the N09 and SBL18 recipes respectively.

2.2. Radiative transfer simulations

RT models allow the study of different dust grain properties, global geometry and local dust distribution. The interaction of photons with the dust grain are defined through the adopted wavelength dependence of the optical depth, τ, albedo, a and scattering phase g. Following the definition in Witt et Gordon, 2000, the optical depth defines where a photon of a given wavelength interacts with a dust particle, the albedo refers to the probability that this interaction results in scattering the photon and the scattering phase function defines the angle at which the photon scatters. The phase function is usually defined with the Henyey-Greenstein phase function. The global geometry defines how stars and dust are distributed and the local dust distribution defines whether the dust is homogeneously distributed or rather localised in clumps. In the following we will use the RT models of Seon et Draine, 2016 as our benchmark to compare our results because it provides RT simulations for 2 different dust model, one from Witt et Gordon, 2000 based on empirical grain properties for SMC and MW grain type and the other one based on theoretical model for LMC, SMC and MW grain type and different ISM structure. In this section, we briefly introduce the RT models of Witt et Gordon, 2000 and Seon et Draine, 2016.

2.2.1. Witt *et* Gordon, *2000 model*

This RT model is one of the reference work other works often compared to, and is described in details in Witt et al., 1992 ; Witt et Gordon, 1996 ; Witt et Gordon, 2000. The empirical dust grain model defined in this work is also used by the RT model of Seon et Draine, 2016. This model will denoted WG00 in the following.

2.2.1.a. Dust and stellar distribution

This model consists in a spherical geometry with 3 possible global dust/star distributions illustrated in Figure IV.6 :

- **The *Shell* geometry** has stars distributed up to 0.3 of the system radius and dust distributed from 0.3 to 1 of the system radius. Witt et al., 1992 justified the use of this geometry to model a dusty galactic nucleus. This is similar to the screen model but not identical because scattering effects are here taken into account. Calzetti et al., 1996 found evidence of foreground dust for 13 starburst galaxies with little dust in their central region, which they explained by supernovae explosions and hot star winds producing shock waves and mass outflows that can destroy or remove the internal dust of active star forming regions to the external dust.
- **The *Dusty* geometry** has dust and stars uniformly distributed over the system radius. This is one of the most efficient geometry to convert stellar photons into IR thermal emission. Witt et al., 1992 justified the use of this geometry to model dusty portions of normal-late type galaxies or badly disrupted merging ISM-rich galaxies, for instance ultraluminous starburst galaxies where the disrupted dusty ISM would be very efficient at absorbing starlight so that an abundant old stellar population may significantly contribute to the heating of dust grains.
- **The *Cloudy* geometry** has stars distributed to the system radius and dust distributed up to 0.69 to the system radius. Witt et al., 1992 justified the use of this geometry to model undisturbed disk geometries where the ISM occupies only a modest fraction of the volume filled with stars.

The local dust distribution can be either homogeneous or clumpy. The clumpy distribution is defined with a filling factor of 0.15 and a low to high density ratio of 0.01 (see Witt et Gordon, 1996 ; Witt et Gordon, 2000 for more details). The optical depth takes discrete values from 0.25 to 50.

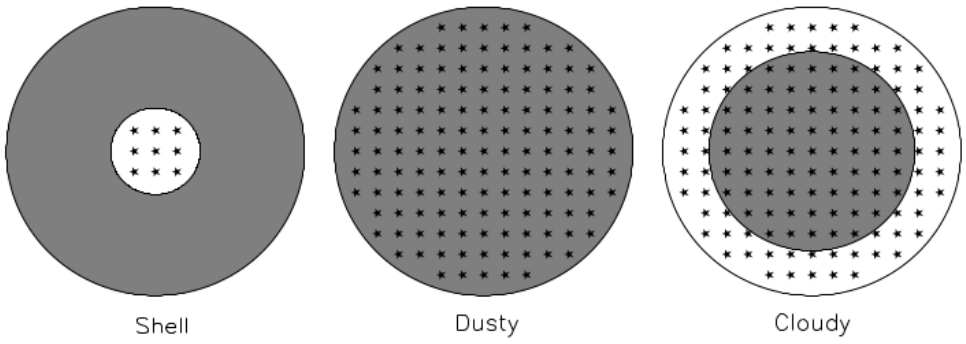

Figure IV.6– Illustration of the 3 geometries adopted in WG00. The star symbols represent the stellar distribution and the grey shaded area represents the dust distribution. Figure taken from WG00.

2.2.1.b. Dust grain characteristics

This model provides 2 types of dust grains, one for the MW and the other one for the SMC, both empirically determined. For the MW, the optical depth, τ, is determined using the extinction curve of Cardelli et al., 1989 with R_V=3.1, the albedo and scattering phase function are empirically determined from reflection nebulae (see Figure IV.7). For the SMC dust grains, the optical depth is computed as the average of the 3 extinction curves of the SMC Bar in Gordon et Clayton, 1998. The albedo values are based on those of the MW with a modification to reproduce the lack of 2175 Å feature (hereafter we will refer to this feature as the UV bump). The scattering phase function is taken to be identical to the one of the MW. On the right panel of Figure IV.7 we see that the scattering phase function is about 0.7-0.8 for UV photons and about 0.5 for NIR photons, meaning that UV photons are more forward scattered whereas the NIR photons are more isotropically scattered. It is important to stress that the UV bump is treated as an absorption feature only (see Figure IV.11).

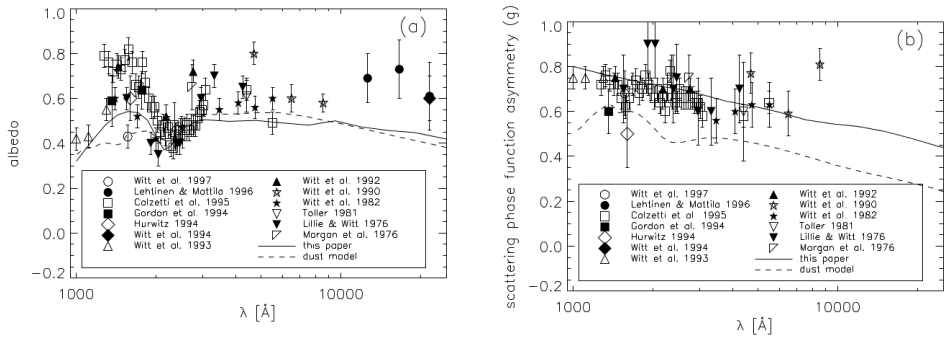

Figure IV.7– The continuous line represents the albedo (left) and scattering phase function (right) as a function of wavelength for the MW dust adopted in WG00. The points are measurements and the dashed line is the dust grain model of Kim et al., 1994. Figure taken from WG00.

2.2.1.c. What influences the shape of the attenuation curve ?

The influence of the optical depth can be seen on the left panel of Figure IV.8 where low optical depths lead to attenuation curves with a similar shape as the extinction curve and high optical depths lead to grey attenuation curves. It is then obvious that the amount of dust plays an important role in shaping the attenuation curve. The middle panel of Figure IV.8 shows the influence of the global geometry on the shape of the attenuation curve for a local clumpy dust distribution with τ_V=1. All geometries have shallower shape than the extinction curve which is due to the effect of scattering. The *Shell* geometry suffers the more attenuation, the *Dusty* geometry suffers just slightly less attenuation with a similar shape as the *Shell* one, and the *Cloudy* geometry leads to a greyer attenuation curve because more stellar light are not affected by dust as in the outskirts of the system more stars are not, or lightly, embedded in the dust. The right panel of Figure IV.8 shows the influence of the local dust distribution with a *Shell* geometry and τ_V=1, and a clumpy distribution of MW dust leads to less attenuation than homogeneous distribution as some stars are more lightly embedded in the dust.

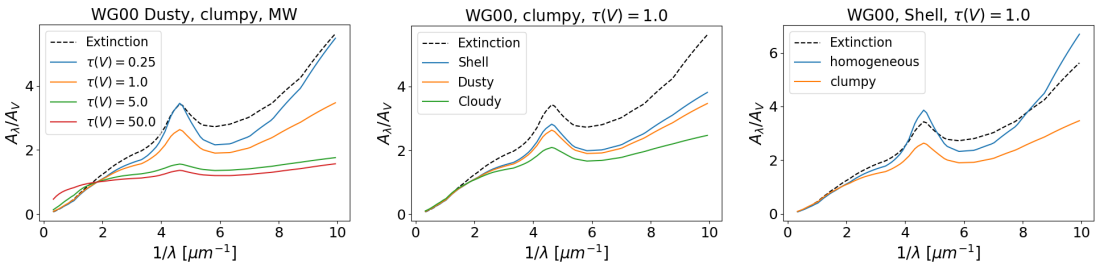

Figure IV.8– Attenuation curves normalised to A_V computed with the model of WG00 for different dust model and types using the python package *dust_attenuation* [1] . *Left :* influence of the optical depth with the other parameters fixed to the *Dusty* geometry with a MW dust type and a clumpy dust distribution . *Middle :* influence of the global geometry with the others parameters fixed to a clumpy distribution of MW dust type and optical depth of 1. *Right :* influence of the local dust distribution with the others parameters fixed to a *Shell* geometry with MW dust type and optical depth of 1.

Using the python package *dust_attenuation*, to which I contributed significantly to, we fitted all the possible configuration of the WG00 RT models to the C00 starburst law. As it can be seen on the Figure IV.9 the C00 starburst law is best fitted with either a *Shell* geometry with a clumpy local distribution of SMC dust or a *Dusty* geometry with a local homogeneous distribution of SMC dust with higher amount of dust. Using additional diagnostics, such as the ratio of FIR to F160BW fluxes as a function of the change in UV spectral index, $\Delta\beta$, and the (F170W -F218W) vs. (B-V) color diagram, the clumpy Shell geometry is favored in WG00.

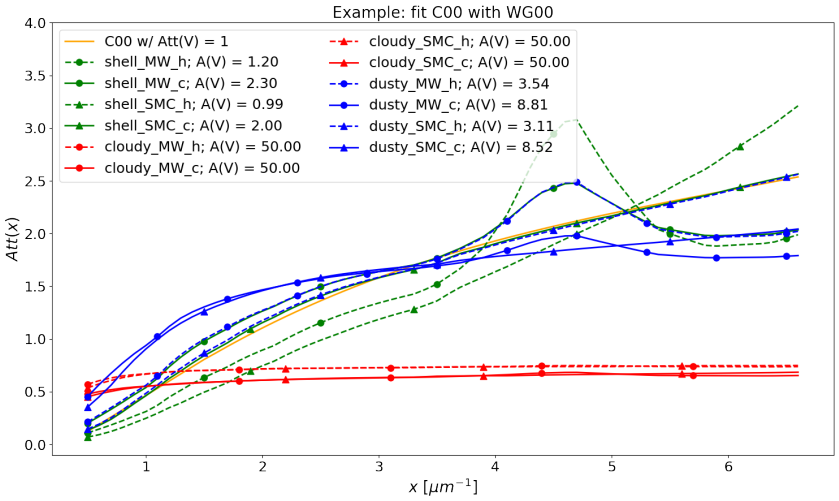

Figure IV.9– The C00 law with A_V=1mag is represented with the orange line. The best fit for each geometry, local dust distribution and dust type are reported. Green, red and blue colors refer to the *Shell*, *Cloudy* and *Dusty* geometries respectively. Circle and triangle symbols refer to MW and SMC dust types respectively. Lines and dashed lines refer to a clumpy and homogeneous local dust distribution respectively. The best fit A_V value is reported in the legend.

2.2.2. Seon *et* Draine, *2016 model*

In the more recent work of Seon et Draine, 2016 the dust and stars are also spherically distributed. In comparison to the WG00 model this model provides more values to quantify the clumpiness of the ISM as well as the dust/star geometry. This model will be denoted SD16 in the following.

2.2.2.a. Dust and stellar distribution

Dust and stars are distributed in a sphere of radius R_d and R_s respectively. The distribution of stars can extend up to the dust distribution radius, i.e the ratio R_s/R_d lies between 0 and 1, 0 representing a

[1]. http ://dust-attenuation.readthedocs.io/

compact OB association surrounded by a dust cloud and 1 corresponds to the *Dusty* geometry of WG00, and the *Shell* geometry of WG00 corresponds to $R_s/R_d = 0.3$. On the contrary of the WG00 RT model with the *Cloudy* geometry, there is no publicly available data for a geometry where stars are distributed beyond the dust radius. The local dust distribution is set by the sonic Mach number, M_s, governing the turbulence and variance of the ISM density field, in other words, it quantifies the clumpiness of the ISM. It takes discrete values between 0 and 20. $M_s = 0$ corresponds to a homogeneous ISM and $M_s = 20$ to a very clumpy ISM. The illustration of different M_s values can be seen on Figure IV.10.

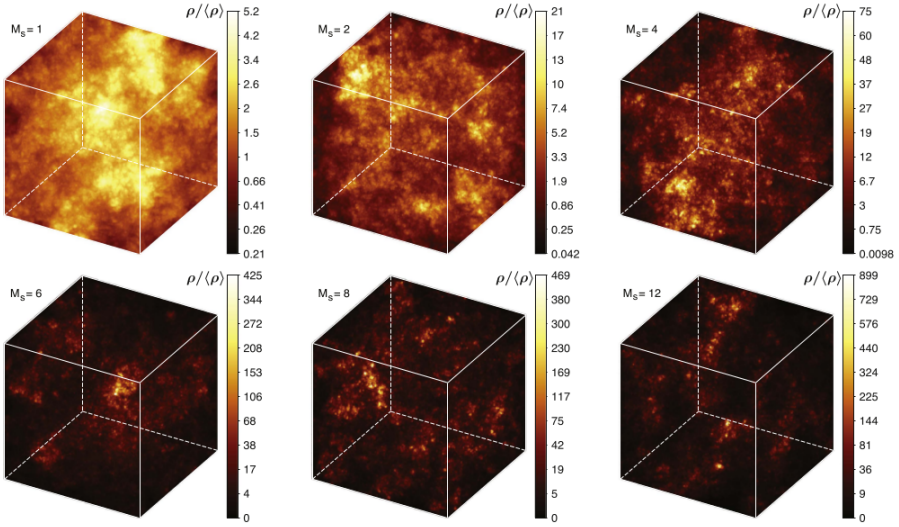

Figure IV.10– Illustration of the lognormal density fields computed for sonic Mach numbers of 1, 2, 4, 6, 8, and 12. The color bars show the ratio of density over the mean density. The density field evolves from being almost homogeneous for Ms=1 to very clumpy for M_s=12. Figure taken from SD16.

2.2.2.b. Dust grain characteristics

One of the most important difference with the WG00 RT model lies in the adopted dust grain properties. While empirically determined values are used in WG00, theoretical values from Weingartner et Draine, 2001 ; Draine, 2003 are used for the extinction and albedo in SD16. The extinction is very similar for both works, however the albedo exhibits different shapes (see Figure IV.11). The albedo adopted in WG00 is relatively constant with wavelength apart for the FUV part for both MW and SMC dust model and the region around the UV bump for the MW dust model. In SD16 the albedo is rising from NIR to optical domain and then continuously decreasing in the UV for MW and LMC dust models. For the SMC dust model, the albedo is also first rising from NIR to optical, then is constant from optical to NUV and then decreases in the FUV.

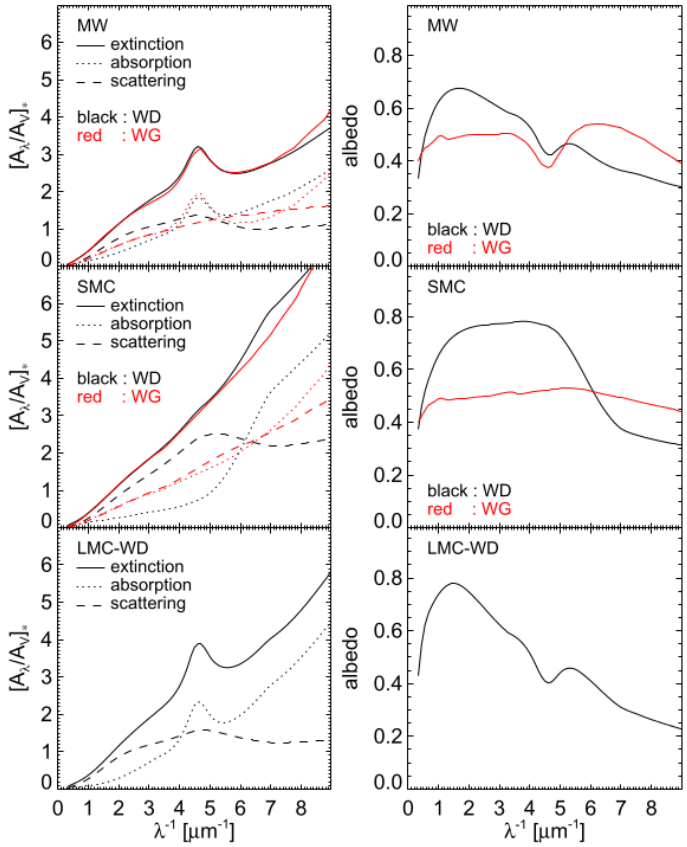

Figure IV.11– Comparison of the extinction and albedo curves of Weingartner et Draine, 2001 and Witt et Gordon, 2000. In the left panels, the extinction, absorption, and scattering curves are denoted as solid, dotted, and dashed lines, respectively. In the top and middle panels, the MW and SMC curves of Weingartner et Draine, 2001 and Witt et Gordon, 2000 are denoted as black and red lines, respectively. The LMC curves of Weingartner et Draine, 2001 are also shown in the bottom panels. Figure and caption taken from SD16

2.2.2.c. What influences the shape of the attenuation curve ?

We compare the 5 dust models with the same geometry (τ_V=1, M_s=8, R_s/R_d=0.6) on the top panel of Figure IV.12. On the left panel we see that the attenuation curves for the WD-MW and WG-MW exhibit different shape with the WD-MW suffering less attenuation in the optical and NIR and more in the NUV-FUV due the difference in the adopted albedo (see top right panel of Figure IV.11). The UV bumps are very similar in amplitude and width. The WD-SMC and WG-SMC exhibit very different shape, with the WG-SMC following a simple power law while the WD-SMC is a series of 3 power-law segments. The WD-SMC dust model suffers less attenuation from NIR to NUV and more attenuation in FUV than the WG-SMC. This difference is again due to the different prescription used for the albedo. The WD-LMC suffers less attenuation in the NIR-optical than the MW models and similar attenuation to the WG-SMC in the NUV and FUV. In general, the WD dust models suffer less attenuation in the optical than their WG counterpart, due to the higher adopted albedo meaning that more optical photons are scattered to the observer line of sight, and so when normalising the attenuation curves to A_V the WD models are steeper than the WG ones, as seen on the top right panel of Figure IV.12. The WD-SMC has the steepest slope in the UV, closely followed by the WD-LMC, the WD-MW is as steep as the WG-SMC model in the FUV and the WG-MW is greyer than the WD-MW.

To understand the influence of the parameters on the shape of the attenuation curves we chose a WD-LMC dust model and let vary only one the parameter at a time. The bottom left panel of Figure IV.12 shows that the more amount of dust there is, the greyer the attenuation curve is almost suppressing the

UV bump. The bottom middle panel of Figure IV.12 shows that the amount of attenuation scales with R_s/R_d, with a system where stars are uniformly distributed up to the dust distribution radius (R_s/R_d=1) suffering less attenuation than systems where stars are surrounded by a "dust cloud" (R_s/R_d<1). This is explained by the fact that more stars will be lightly embedded in the dust and thus less affected by dust in a system with R_s/R_d=1 than in a system with R_s/R_d<1. Finally the bottom right panel of Figure IV.12 shows that the more clumpy the system is (higher M_s) the less attenuation it suffers and the greyer is the attenuation curve. We find the same influence of the parameters as for the WG00 RT model. More generally the WG00 and SD16 RT simulations show that the amount of dust influences the more the shape of the attenuation curve with higher optical depth leading to greyer attenuation curves (see also the compilation of RT simulations results in Chevallard et al., 2013).

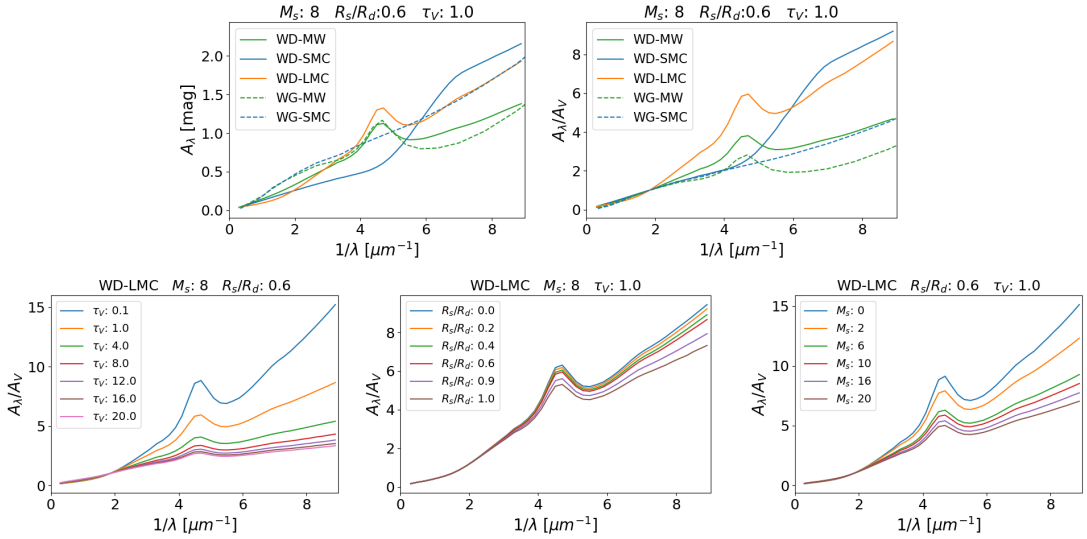

Figure IV.12– *Top left :* Attenuation curves computed with the model of SD16 for the different dust models and same geometry (τ_V=1, M_s=8, R_s/R_d=0.6). *Top right :* Attenuation curves normalised to A_V computed with the model of SD16 for the different dust models and same geometry (τ_V=1, M_s=8, R_s/R_d=0.6). *Bottom :* attenuation curves normalised to A_V for the WD-LMC dust type, from left to right only τ_V, R_s/R_d and M_s are varied while the other 2 parameters are fixed.

The WG00 and SD16 RT models both adopt a spherical geometry that is obviously not able to accurately model galaxies. However, the extinction curve along the GRB line of sight provides information about the type of dust in the host galaxies and so we required radiative transfer models with publicly available data for different type of dusts. Most of the time, for studies using more complex modelling of the bulge and disk of galaxies such as in the work of Tuffs et al., 2004 ; Pierini et al., 2004 only one type of dust is considered.

In a future study, we could further investigate whether the SBL18 recipe can fit accurately attenuation curves from RT models with a more complex modelling of the bulge and disk of galaxies for a given type of dust.

2.3. Fitting RT attenuation curves with analytical recipes

The RT attenuation curves are considered as the most satisfying modelling of the effect of dust on stellar light and as we have seen in Section 2.2 their shape exhibits a great variety depending on the distribution of dust and stars in the galaxy, the local dust distribution and optical depth. This non-universality of the attenuation curve has already been found and discussed in many works [Buat et al., 2011 ; Buat et al., 2012 ; Buat et al., 2018 ; Wild et al., 2011 ; Kriek et Conroy, 2013 ; Reddy et al., 2015 ; Reddy et al., 2016 ; Salmon et al., 2016 ; Battisti et al., 2016 ; Battisti et al., 2017 ; Salim et al., 2018], however no

work has been performed to my knowledge to ensure that the common attenuation curve recipes are able to reproduce the variety of the RT attenuation curves. This section aims at studying how accurately the commonly used C00 and the N09 recipes are able to fit the RT attenuation curves. As already mentioned in Section 2.1.2, instead of the original N09 formalism we will rather use the modified version provided by Salim et al., 2018 where the strength of the UV bump is not affected by the power-law slope. Apart from the UV bump amplitude, the same conclusions can be drawn for the N09 recipe.

For this purpose, we use the radiative transfer model of SD16 which offers the possibility to choose between three theoretical dust models adopted from Weingartner et Draine, 2001 and Draine, 2003 for the MW, LMC, and SMC-bar, and two empirical models for the MW and SMC from WG00. The former dust models are noted WD-MW, WD-LMC and WD-SMC and the later WG-LMC and WG-SMC. The attenuation curves computed with the radiative transfer model of SD16 are defined with three parameters : τ_V, R_s/R_d and M_s taking discrete values from 0.1 to 20, 0 to 1 and 0 to 20 respectively [2]In total there are 910 attenuation curves computed for each dust model.

For each dust model and values of τ_V, $\frac{R_s}{R_d}$, M_s, we fitted the RT attenuation curves with our 2 recipes : C00 and SBL18. We restricted the fit between $0.11\mu m$ to $2.2\mu m$ which corresponds to the wavelength range where the formalism of C00 with the modification of Leitherer et al., 2002 applies. The fit is performed using an MCMC algorithm with the Ensemble Sampler of the python package emcee [Foreman-Mackey et al., 2013], using 100 walkers and 1000 steps. The parameters range are defined as follows : $0 \leq E(B-V) \leq 10$, $-3 \leq \delta \leq 3$, $0 \leq E_b \leq 50$ and $25 \leq \gamma \leq 45$.

In Section 2.3.1 we first consider the total amount of attenuation by fitting A_λ of the RT models. Then, in Section 2.3.2 we fix A_V of the recipes to be equal to the one of the RT models in order to consider only the shape of the attenuation.

2.3.1. Fitting total attenuation, A_λ

In this section we fit the total amount of attenuation by comparing A_λ^{recipe} to A_λ^{RT} using the following χ^2 :

$$\chi^2(params) = \sum_{i=1}^{N_{data}} \left(A_{\lambda,i}^{recipe}(params) - A_{\lambda,i}^{RT} \right)^2 \tag{IV.10}$$

with $A_{\lambda,i}^{RT}$ the amount of attenuation from the SD16 RT model, $A_{\lambda,i}^{recipe}$ the amount of attenuation for the corresponding recipe and its parameters. The N_{data} wavelengths are defined between 0.11 and 2.2 microns. *params* refer to the parameters of each recipe defined in 2.1.

To compute the accuracy of a given recipe to retrieve the wavelength dependence of all the RT attenuation curves, we compute the absolute and relative difference between the recipe, estimated with the parameters returning the best χ^2 of the MCMC run, and the RT attenuation curves for each value of τ_V, $\frac{R_s}{R_d}$, M_s values :

$$\begin{aligned}
f(\lambda, \tau_V, \frac{R_s}{R_d}, M_s) &= A_\lambda^{recipe}/A_V^{recipe} - A_\lambda^{RT}/A_V^{RT} \\
g(\lambda, \tau_V, \frac{R_s}{R_d}, M_s) &= \frac{A_\lambda^{recipe}/A_V^{recipe} - A_\lambda^{RT}/A_V^{RT}}{A_\lambda^{RT}/A_V^{RT}} \\
f_{abs}(\lambda, \tau_V, \frac{R_s}{R_d}, M_s) &= |A_\lambda^{recipe}/A_V^{recipe} - A_\lambda^{RT}/A_V^{RT}| \\
g_{abs}(\lambda, \tau_V, \frac{R_s}{R_d}, M_s) &= |\frac{A_\lambda^{recipe}/A_V^{recipe} - A_\lambda^{RT}/A_V^{RT}}{A_\lambda^{RT}/A_V^{RT}}|
\end{aligned} \tag{IV.11}$$

[2]. https ://seoncafe.github.io/MoCafe.html

where A_V^{recipe} is the value of A_λ^{recipe} estimated at 550nm, A_V^{RT} the value from RT models. f represents the deviation between the recipe and the RT attenuation curves, g represents the deviation between the recipe and the RT attenuation curves normalised to the RT attenuation curve. f_{abs} and g_{abs} represents the absolute values of f and g. For these 4 functions we compute the mean and standard deviation at each wavelength for the 910 attenuation curves of a given dust model. For instance for f (and similarly for the 3 other functions), the mean and standard deviation are computed as :

$$\overline{f(\lambda)} = \frac{1}{N_{tot}} \sum_{i}^{\tau_V} \sum_{j}^{\frac{R_s}{R_d}} \sum_{k}^{M_s} f(\lambda, i, j, k) \tag{IV.12}$$

$$\sigma_f = \sqrt{\frac{1}{N_{tot}} \sum_{i}^{\tau_V} \sum_{j}^{\frac{R_s}{R_d}} \sum_{k}^{M_s} f(\lambda, i, j, k) - \overline{f(\lambda)}} \tag{IV.13}$$

The results for each dust model can be seen on Figure IV.13 for the WD dust models and IV.14 for the WG dust models. The top panels represent the averaged deviation between the recipe and the RT attenuation curves and inform us about a global tendency of the recipe to over- or underestimate the attenuation at a given wavelength. The middle-top panels represent the same deviation but normalised to the RT attenuation curve normalised to A_V which gives us the percentage of deviation at a given wavelength. As averaging negative with positive values can strongly biased our analysis of the averaged curves, the next 2 panels below represent the same quantities but using the absolute difference this time. For all the dust models it is clear that the C00 recipe is not able to reproduce the variety of shapes as we expected. Looking at the bottom panel of Figures IV.13 and IV.14 we see that the absolute mean deviation of the SBL18 recipe compared to SD16 RT models is between about 0% and 10% from the optical to the FUV for WD-MW and WD-LMC dust models. The WG-MW dust model is well fitted by the SBL18 recipe with an absolute mean deviation lower than 10% except in the FUV region from 5 to 6-7 μm^{-1} where the mean deviation goes up to 20%. The WG-SMC dust model is not well fitted by the SBL18 recipe with an absolute mean deviation of about 20% in the UV with a large dispersion around the mean value. The WD-SMC is badly fitted with the SBL18 recipe with an absolute mean deviation almost always higher than 50% with a maximum of 100% deviation around 5 μm^{-1}. However the shape of the WD-SMC is rather uncommon with 2 spectral breaks (see Figure IV.12) and to my knowledge such a shape has not been observed so far. For the 3 WD dust models the NIR domain is badly fitted with a tendency of the recipe to underestimate the amount of dust (see first 2 top panels of Figure IV.13). This is also true for the WG dust models even if the deviation is lower than for the WD dust models.
An other point to stress is that the UV bump is usually very well reproduced by the SBL18 recipe. The WG-MW model in the FUV region from 5 to 6-7 μm^{-1} exhibits a depression in attenuation that is not well reproduced by the SBL18 recipe. In that case a more flexible recipe, such as the one of Fitzpatrick et Massa, 2007 adopted for deriving extinction curves, should be more capable of reproducing a wider variety of shapes but at the cost of more free parameters.

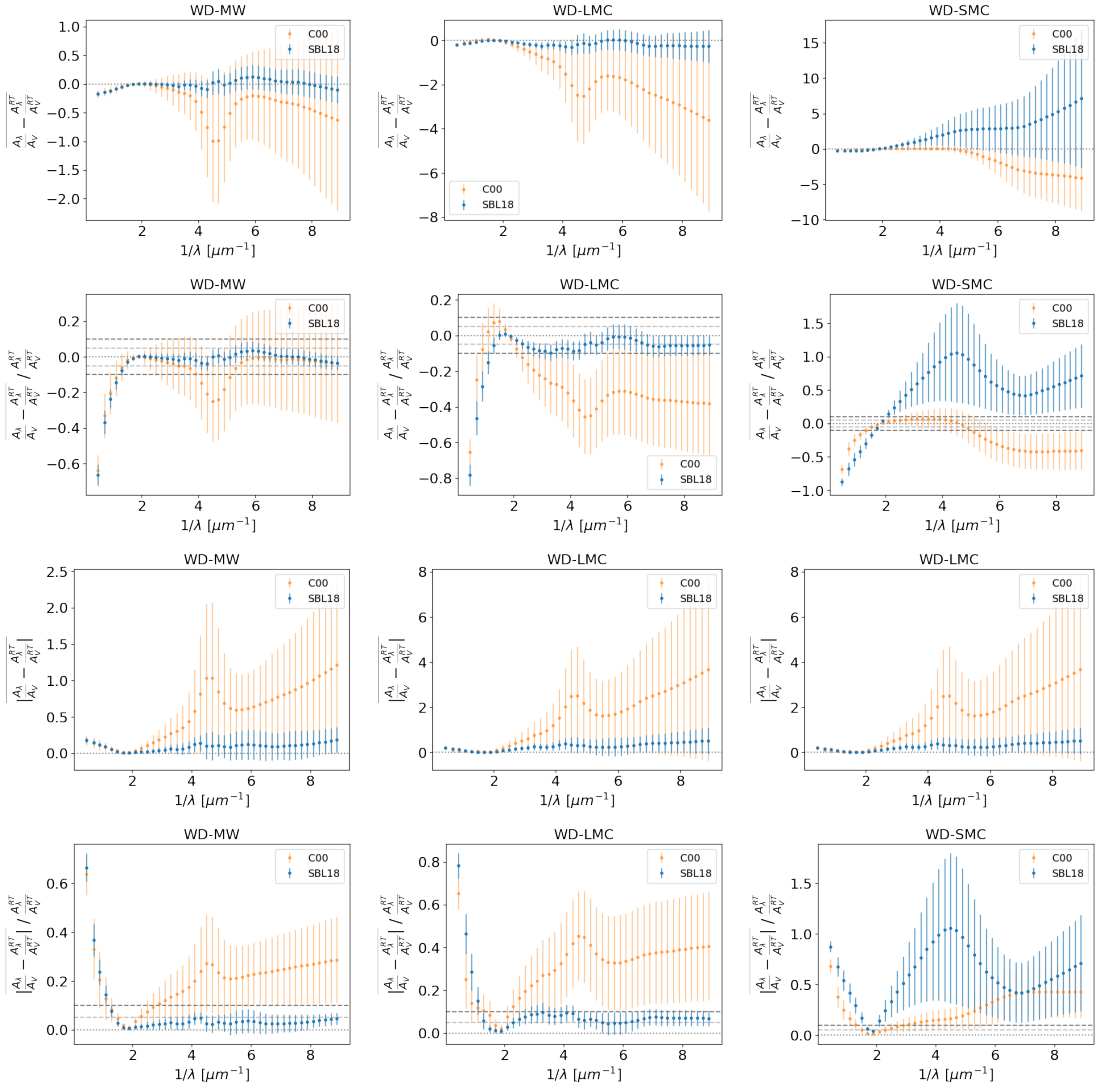

Figure IV.13– Absolute and relative difference of the best fit of RT attenuation curves adopting the WD dust models with different attenuation recipes : C00 (orange points), SBL18 (blue points). *From left to right :* WD-MW, WD-LMC and WD-SMC dust types. *From top to bottom :* absolute difference between the intrinsic shape of RT attenuation curve, i.e. A_λ^{RT}/A_V^{RT}, and the intrinsic shape of the best fit for a given recipe, i.e, $A_\lambda^{recipe}/A_V^{recipe}$, relative difference, absolute values of the absolute difference, and the absolute values of the relative difference. The dotted grey line represents no deviation, the light and dark grey dashed lines represent a deviation of 5 and 10 % respectively.

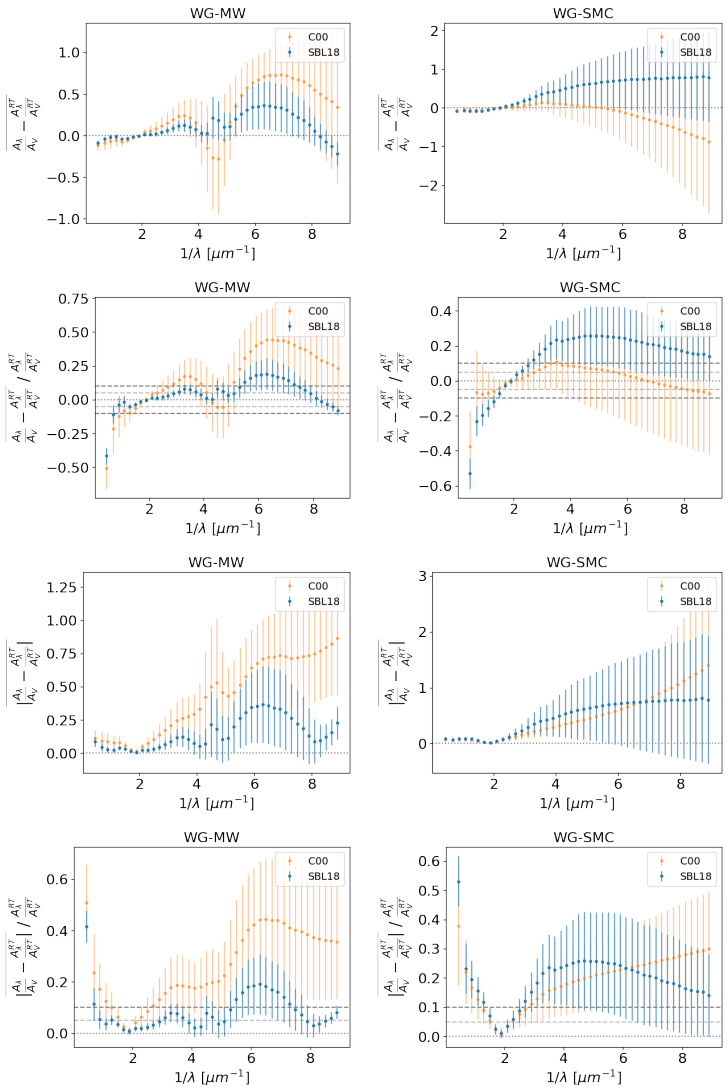

Figure IV.14– Same as Figure IV.13 but for the WG dust models.

The results are normalised to A_V and so a bad estimation of this parameter can bias our conclusion on the ability of the recipes to correctly fit the attenuation curves of RT models whose shape depends on A_V. In Figure IV.15 we plot the A_V values from the RT models against the value found for the best model of our fit. There is a large dispersion on the estimated values of A_V for the C00 recipe for all the dust models. The C00 attenuation law has a flat UV slope and so it must suffer more (less) attenuation to fit attenuation curves with steeper (shallower) UV slopes explaining the bad estimation of A_V for the C00 recipe. The C00 recipe is usually overestimating the amount of attenuation. The SBL18 recipe allows for a reliable estimation of A_V for the WD-LMC, WD-MW and WG-MW dust models and underestimates it for the WD-SMC and WG-SMC dust models. In the next section we will perform the fit again but this time with A_V^{recipe} fixed to A_V^{RT} in order to consider only the shape of the attenuation curve.

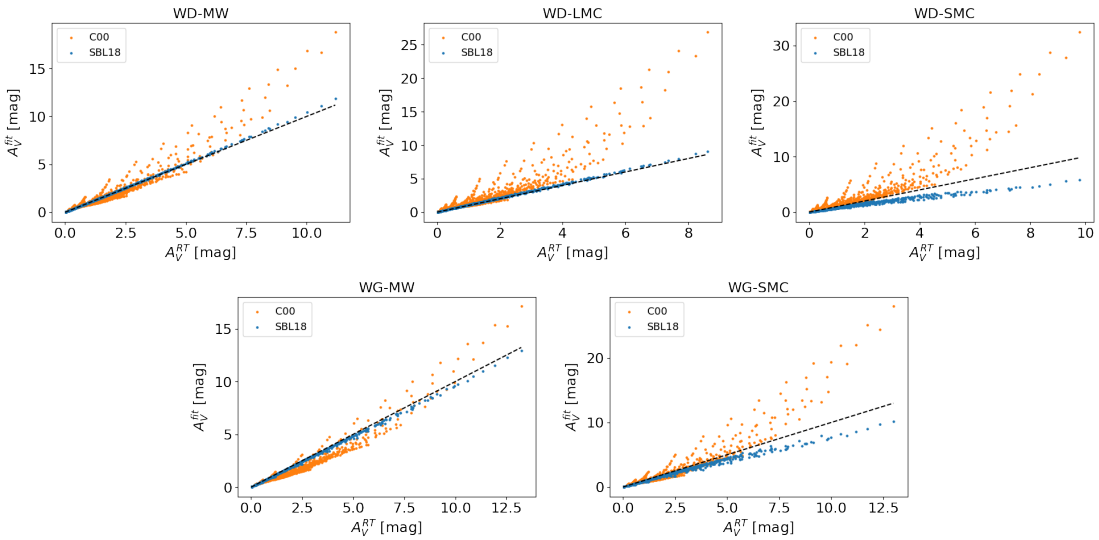

Figure IV.15– A_V^{recipe} as a function of the input A_V^{RT} for WD-MW, WD-LMC, WD-SMC, WG-MW and WG-SMC dust models. The orange and blue points are the results obtained with the C00 and SBL18 recipes respectively. The dashed line represents the 1 :1 relation.

2.3.2. Fitting normalised attenuation, A_λ with fixed A_V

We have just seen that the shape of the attenuation curves can be reasonably well fitted by the SBL18 recipe, however A_V^{recipe} is not always consistent with A_V^{RT}. In order to be fully consistent with the RT models, we perform the fit using the same χ^2 as before but this time setting $A_V^{recipe} = A_V^{RT}$. In other words we now only consider the shape, i.e A_λ/A_V, of the attenuation curves.

Again for all the dust models the C00 recipe is not able to reproduce the variety of shapes as we expected, and in this section we only plot results for the SBL18 recipe. The results for the C00 recipe can be seen in Appendix C. Looking at the bottom panel of Figures IV.16 and IV.17 we see that now the absolute mean deviation of the SBL18 recipe compared to SD16 RT models is between 0% and about 10% from the optical to the FUV for all the dust models except the WD-SMC. The WD-SMC dust model is better fitted than previously with an absolute mean deviation of about 0 to 10% above 6 μm^{-1} but still a larger deviation up to 40% from 2 to 6 μm^{-1}. The recipes still underestimate the amount of dust in the NIR domain for all dust models although it is more pronounced for the WD dust models. The UV bump is still well reproduced, but the depression in attenuation in the FUV of the WG-MW not well reproduced by the SBL18 recipe.

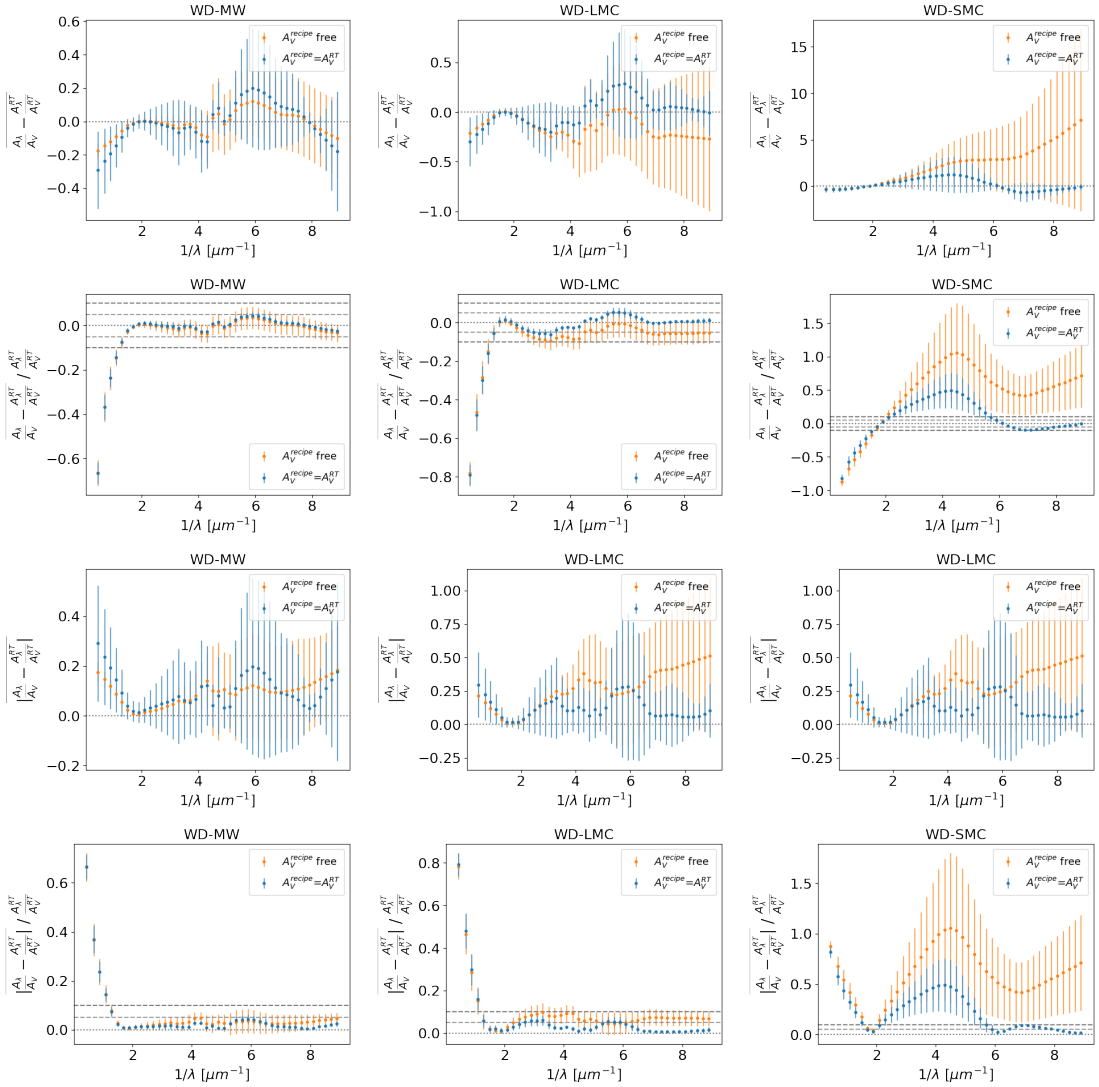

Figure IV.16– Same as Figure IV.13 but this time A_V^{recipe} is fixed to A_V^{RT} and only the SBL18 is considered.

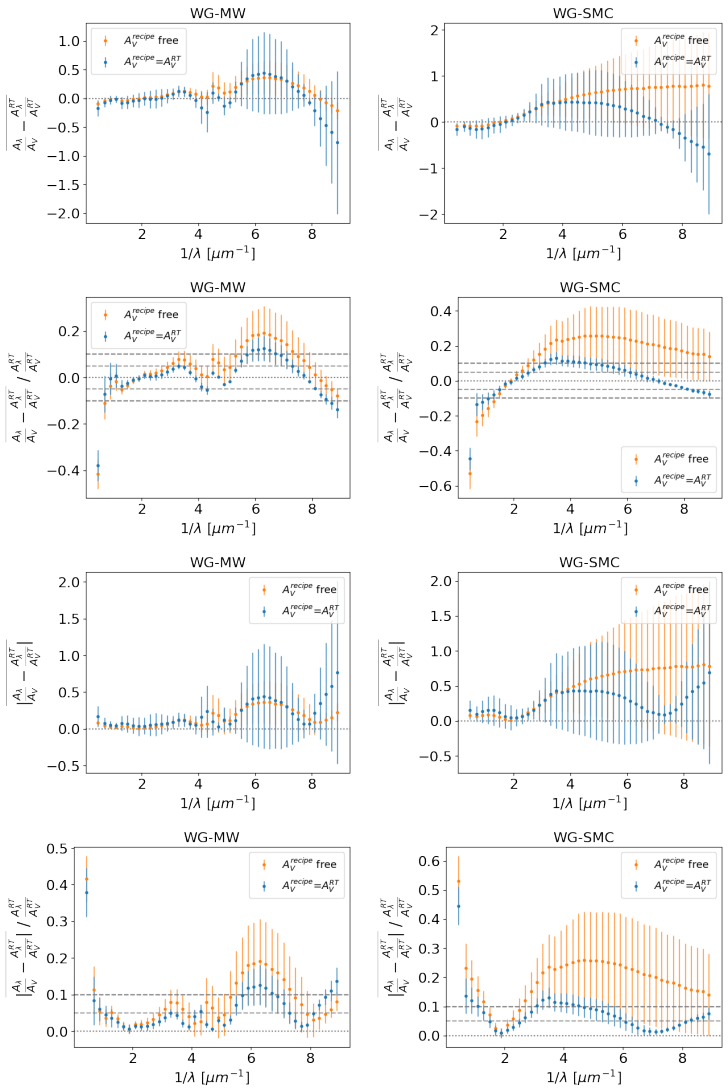

Figure IV.17– Same as Figure IV.16 but for the WG dust models.

The results presented in Figures IV.16 and IV.17 are averaged over the 910 attenuation curves of the SD16 RT model, and for a better illustration we present the best fit for one configuration of the SD16 RT model (τ_V=1, R_S/R_d=0.6, M_s=8) and each dust model in the Figure IV.18. We see that attenuation curves for WD-MW, WD-LMC and WG-SMC are well fitted by the SBL18 recipe. The WD-SMC can clearly not be reproduced by a simple power law and the WG-MW is well fitted up to $5\mu m^{-1}$ but not above where the slope of the SBL18 fit is too flat compared to the RT curve. We tried to reproduce a UV slope as steep as the one from the RT model for the WG-MW model by varying the slope of the SBL18 while keeping the other parameters to their best fit values. In the top panel of Figure IV.19, we see that similar UV slopes (blue-purple lines) with the SBL18 recipe have steeper slopes in the NIR domain which does not match the RT model. The SBL18 recipe matches the SD16 RT model in the NIR only for very flat attenuation curves in the UV (yellow lines) which does not match the RT curve in the UV. We conclude that the shape of the WG-MW attenuation curves can not be reproduced by a simple power law.

In the bottom panel of the same Figure we did the same with the WD-MW model, and we see that the NIR part of the SD16 RT attenuation curve can not be reproduced by the SBL18 recipe for any of the slope. It illustrates that the NIR attenuation of WD models are more underestimated when fitted by the

SBL18 recipe than the WG models.

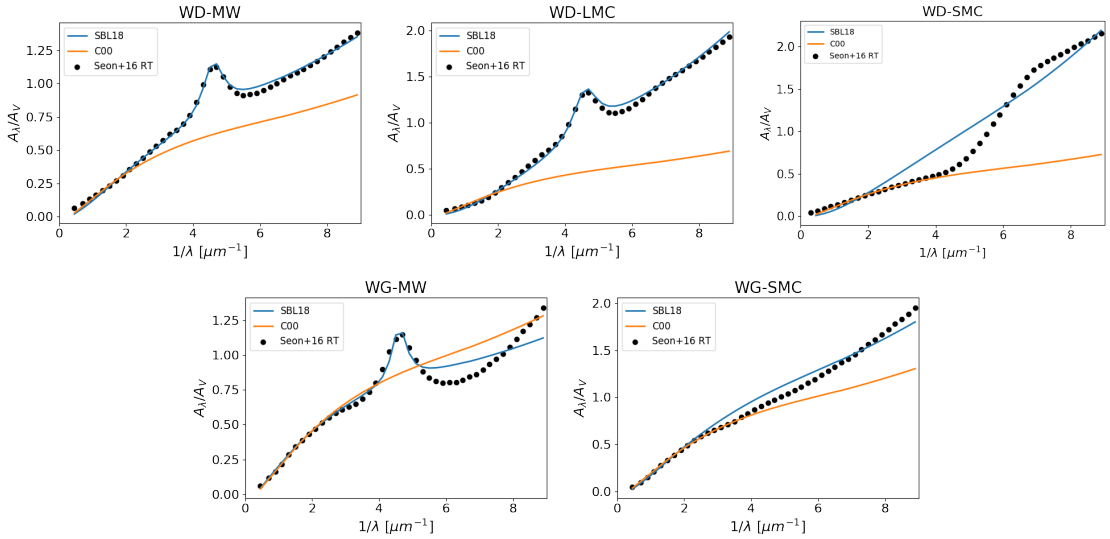

Figure IV.18– Illustration of the best fit of one RT attenuation curve (τ_V=1, R_S/R_d=0.6, M_s=8) with the C00 (orange) and SBL18 (blue) recipes with A_V^{recipe} set to A_V^{RT}.

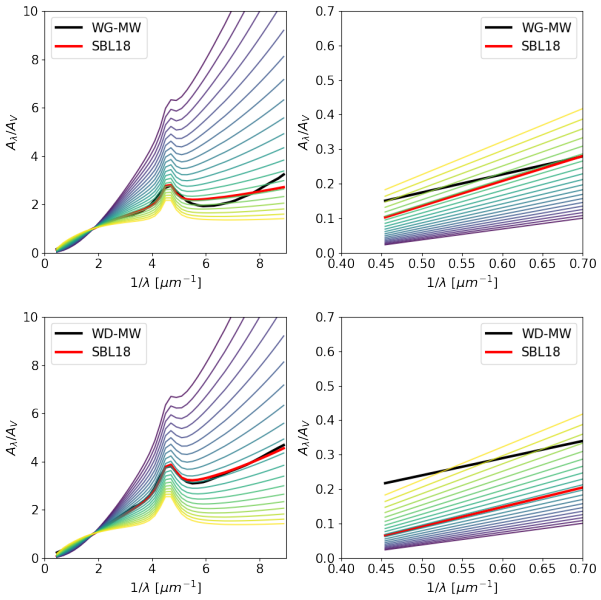

Figure IV.19– *Top :* the black line correspond to the SD16 RT attenuation curve with τ_V=1, R_S/R_d=0.6, M_s=8 for the WG-MW dust, the red line correspond to its best fit with the SBL18 recipe. The multi color lines correspond to the SBL18 best fit where the slope δ is varied from -1 (purple) to 0.5 (yellow). The right panel is a zoom in of the NIR domain. *Bottom :* Same as for the top panel but for the WD-MW dust model.

We conclude that the SBL18 formulation is able to reproduce the shape of the WD-MW, WD-LMC and WG-SMC dust models with an absolute mean deviation less than 10%. The UV bump is also nicely reproduced. The WD-SMC and WG-MW dust models are not accurately fitted with the SBL18 recipe. On the contrary, the C00 recipe is not able to reproduce accurately any of the dust model attenuation curve shape. The attenuation in the NIR domain is usually underestimated with both recipes which will result in an underestimation of the NIR fluxes corresponding to the emission of the old stellar population.

2.3.3. Parameters range and correlations

In this section we intend to study the parameter range and possible correlations between parameters. Most of the correlations have been discussed in details in Seon et Draine, 2016, our aim here is to study whether some combination of values for the SBL18 parameters are only possible for some of the dust models and thus help to distinguish between dust models in distant galaxies. In this section we did not consider the WD-SMC and WG-MW dust models as the SBL18 recipe is not able to reproduce their attenuation curves as seen in the previous section. The distributions of the best-fit parameters of the SBL18 recipe for all dust models are shown along the diagonal of the Figure IV.20. The distribution of the slope of the attenuation curve covers a broad range from ∼-1.1 to 0.5 and is peaking around 0.1, and most of the attenuation curves have a slope δ between -0.6 and 0.3. We recall that the slope for the SMC extinction curve is ∼ -0.5 and the starburst law C00 has a slope of 0. The color excess, $E(B-V)$, is exponentially decreasing from 0 to ∼2 with most of the values found within the range 0 to 1. Most of the UV bump amplitudes are found within the range 1 to 8 with a peak at ∼2.5. The FWHM of the UV bump was allowed to vary from 25 to 45 nm and two peaks are seen, one at 34-35nm and a second one at 44-45nm. The peak around 35nm is representative of the WD-MW model and this is what we expect from [Noll et al., 2009], the second peak is due to the WD-LMC model and at least partly due to the limits we set for the fit.

To search for possible correlations between the parameters we plotted the 2D distributions of the SBL18 recipe parameters in Figure IV.20. Apart from the obvious correlation between $E(B-V)$ and A_V, the most clear correlation is found between the UV bump amplitude, E_b, and the slope of the attenuation curve, δ, with large (small) amplitude associated to steep (shallow) slopes. This relation has been observationally confirmed in Kriek et Conroy, 2013 and discussed in details in Seon et Draine, 2016. From the δ-A_V plot we see that steepest (shallowest) slope, i.e. more negative (positive) values of δ are associated to low (high) A_V. The same trend is seen on the $E(B-V)$-δ plot.

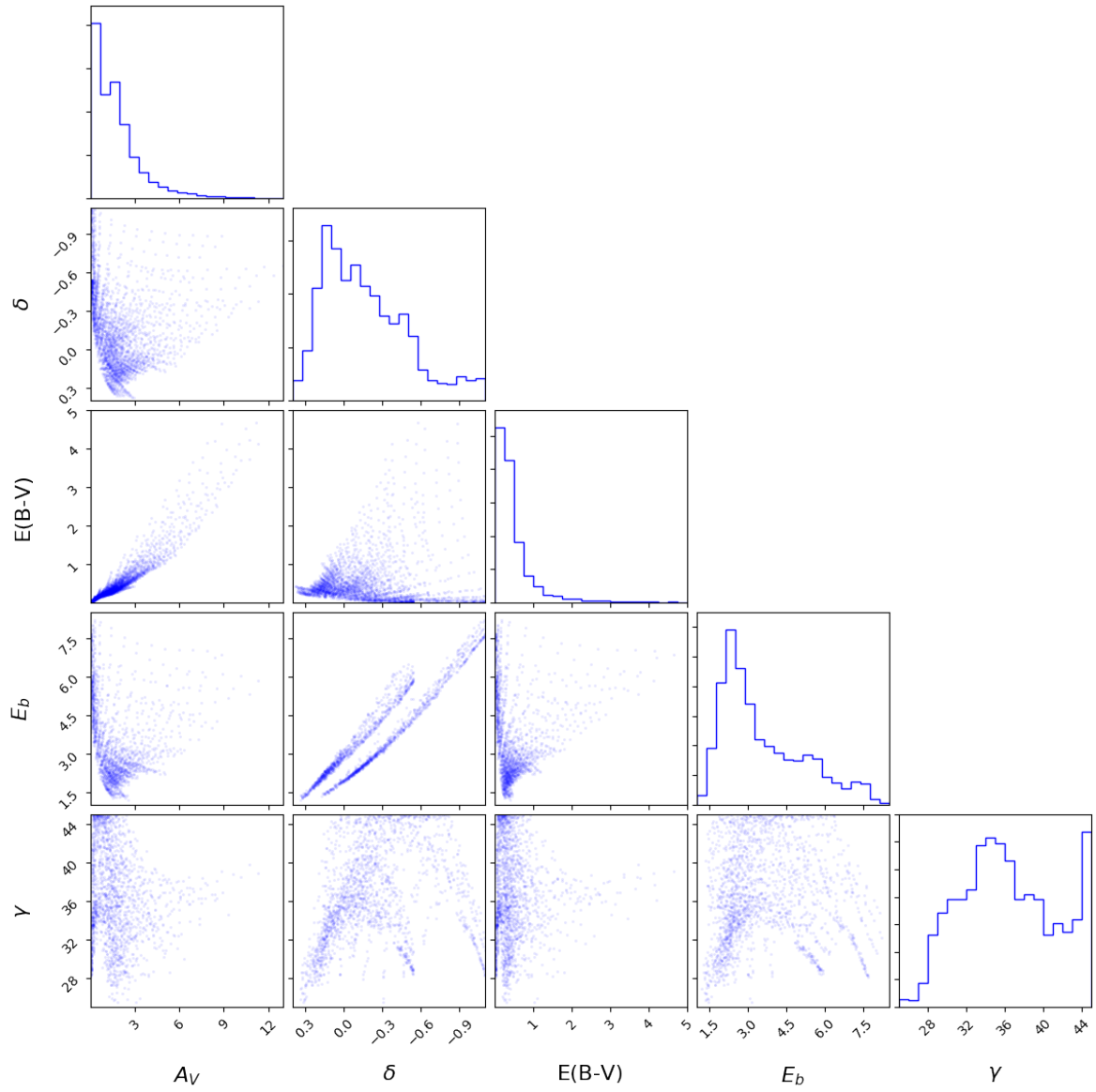

Figure IV.20– 2D distributions of the best-fit parameters of the SBL18 recipe for the WG-SMC, WD-MW and WD-LMC dust models. The 1D distribution of the individual parameters are shown along the diagonal.

These trends are better illustrated in Figure IV.21 where we plotted δ as a function of A_V and $E(B-V)$ for each dust model. We binned A_V and $E(B-V)$ in 20 bins and computed the mean and standard deviation of δ for each dust model. For all dust models δ correlates with A_V, with the WD-LMC exhibiting the steepest slopes, the WD-MW and WG-SMC exhibit similar slopes. The trend to have steeper (shallower) attenuation curves at low (high) optical depth has already been discussed in many in radiative transfer studies [Witt et Gordon, 2000 ; Chevallard et al., 2013 ; Seon et Draine, 2016] and has been observationally confirmed by Salmon et al., 2016 ; Salim et al., 2018. For increasing values of $E(B-V)$ up to 0.3 mag, δ is increasing before exhibiting a shallow decrease from 0.3 to 1.5 mag. This trend is not in agreement with the works of Salmon et al., 2016 where δ is increasing with $E(B-V)$ in a similar manner as it does with A_V. The value of $E(B-V)$ in their work is not equal to $A_B - A_V$ as the introduction of a varying slope to the original C00 law modifies the original $R_V = A_V/E(B-V)$ as explained in Section 2.1.2. However in our analysis, $E(B-V)$ is corrected to impose $E(B-V) \equiv A_B - A_V$. So we corrected the $E(B-V)$ values given in Salmon et al., 2016 which is represented by the grey line in the middle

panel of Figure IV.21 and our results are still not in agreement for values of $E(B-V)$ higher than $\sim$0.3 mag. We then decided to reproduce the Figure 13 of Salmon et al., 2016 where their relation is well fitted by the *Shell* clumpy geometry of WG00 with SMC dust. In the bottom right panel of Figure IV.21 we plotted only the SD16 RT attenuation curves with $8 \leqslant M_s \leqslant 12$ to reproduce a clumpy ISM and $0.2 \leqslant R_s/R_d \leqslant 0.4$ to reproduce the *Shell* geometry (defined with R_s/R_d=0.3 in WG00, but this value is not publicly available for the SD16 model). We see that the corrected relation of Salmon et al., 2016 is now in very good agreement with our best fits for the WG-SMC. This seems to indicate that their result is representative for a given dust model and geometry but is not universal. Indeed, as seen in the middle panel of Figure IV.22 the highest $E(B-V)$, for which the disagreement is stronger, are found in more homogeneous ISM (i.e small M_s) and at higher optical depths. We also remark that a value of $E(B-V)$ higher than $\sim$ 1 mag is associated to a $M_s \leqslant 2$ corresponding to an homogeneous local dust distribution and for $M_s > 8$, corresponding to clumpy dust distribtuion,$E(B-V)$ is in average $\sim$ 0.3 mag. In the work of Witt et Gordon, 2000, we can see from their Figure 4 that $E(B-V)$ is saturating at $\sim$0.25 and 0.3 mag for the MW and SMC dust model respectively. Higher values of $E(B-V)$ are found only with their *Shell* geometry and only in the case of an homogeneous local dust distribution is $E(B-V)$ higher than 1 mag. Interestingly, as seen in Figure IV.21 a given value of $E(B-V)$ leads to different values of δ depending on the adopted dust model. Consequently, the δ-$E(B-V)$ plot might be used to distinguish among different dust model and even to give an indication of the local dust distribution in distant galaxies.

An other conclusion is that both δ-A_V and δ-$E(B-V)$) trends are mainly explained by a dependence to the optical depth as seen in the upper left panel in Figure IV.22.

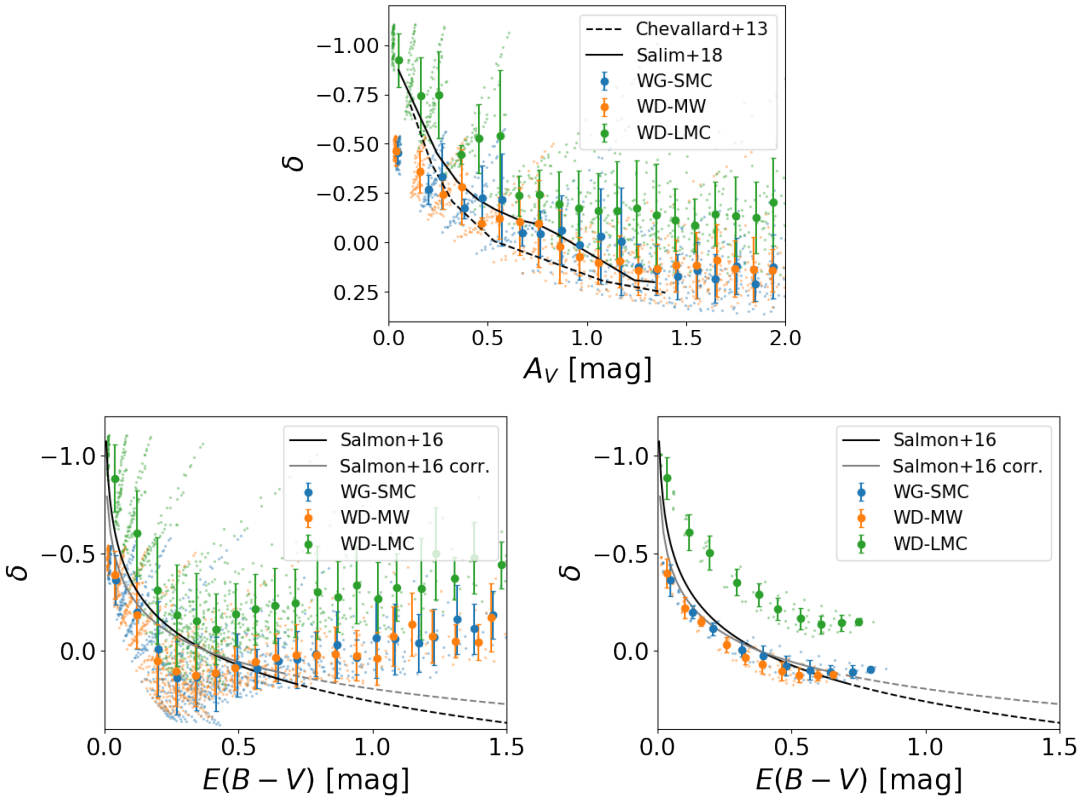

Figure IV.21– *Top :* Slope of the attenuation curve, δ, as a function of A_V. The black dashed line represents the relation found from a compilation of radiative transfer simulations in Chevallard et al., 2013. The black line represents the mean relation based on the observations of 230000 local galaxies in Salim et al., 2018. *Bottom left :* Slope of the attenuation curve, δ, as a function of the color excess, $E(B-V)$. The black line represents the relation based on galaxies at z∼1.5-3 from CANDELS in Salmon et al., 2016. The grey line represents the relation of Salmon et al., 2016 corrected to impose $E(B-V) \equiv A_B - A_V$ when using the N09 recipe. The dashed line are extrapolation of these relations at higher $E(B-V)$. *Bottom right :* Same as the middle panel except that we selected only attenuation curves with $8 \leqslant M_s \leqslant 12$ and $0.2 \leqslant R_s/R_d \leqslant 0.4$ to model a clumpy shell geometry as in Salmon et al., 2016. The colors encode different dust models. Each point represents the best-fit values for one configuration (τ_V, R_S/R_d, M_s) of SD16. The error bar represent the mean and standard deviation of δ for each bin in A_V and $E(B-V)$.

In the Figure IV.22 we study the influence of the parameters of the RT model (τ_V, R_S/R_d, M_s) on the parameters of the SBL18 recipe (δ, $E(B-V)$, A_V, E_b, γ). We see that the optical depth is the parameter influencing the most the shape of the attenuation curve with steep (shallow) attenuation curves associated to low (high) optical depth, large (small) UV bump amplitude associated to low (high) optical depth. The UV bump width is first increasing with optical depth up to $\tau_V \sim 2-4$ and afterwards monotonically decreases with optical depth. A similar trend between A_V and the bump amplitude has been found on a sample of 230 000 local galaxies in Salim et al., 2018 where the strongest UV bump are found for low A_V and low mass galaxies. Similarly, Hagen et al., 2017 found that in star-forming regions of the SMC the strength of the UV bump decreases with A_V.

The degree of clumpiness, i.e. M_s, influences the slope and the UV bump amplitude with steeper (shallower) slopes associated to low (high) M_s and large (small) E_b associated to low (high) M_s. This is due to the fact that more homogeneous ISM results in higher A_V, which explains the similar trend as the one with the optical depth. The ratio R_s/R_d has a smaller influence on δ and E_b with steeper (shallower) slopes associated to small (high) R_s/R_d and large (small) E_b associated to small (high) R_s/R_d.

Regarding the dust models, we see that the WD dust models exhibit steeper slopes as the WG dust models. The WD-LMC dust model even exhibits steeper slopes (up to $\delta \sim -1$) than the WG-SMC dust model (only up to $\delta \sim -0.5$) and stronger UV bumps (up to $E_b \sim 8$) than the WD-MW dust model (only

up to $E_b \sim 7$). This is a consequence of the adopted extinction curves (see Figure IV.11).

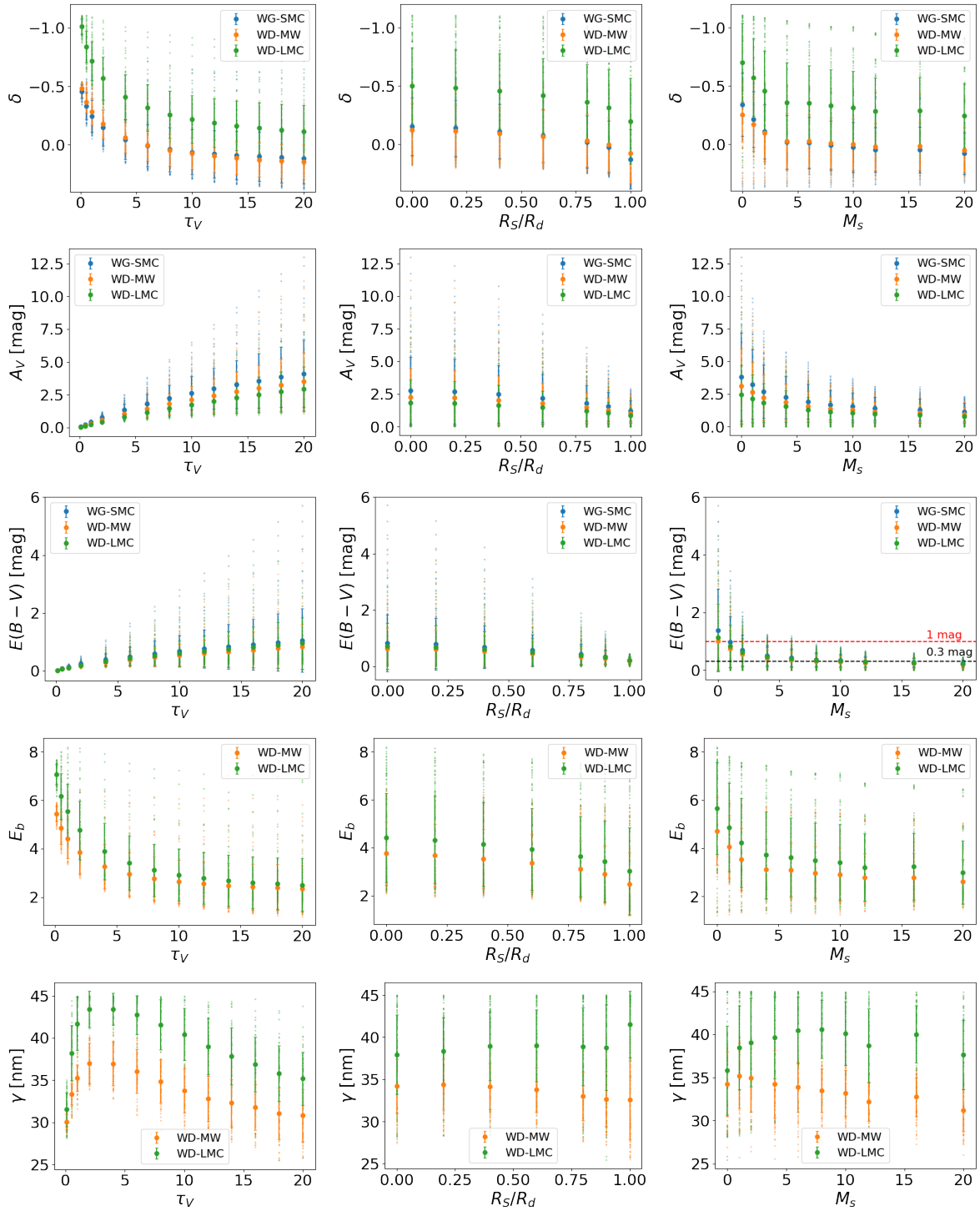

Figure IV.22– Dependence of the SBL18 recipe parameters to the optical depth (τ_V), ratio of stellar over dust distribution (R_s/R_d) and degree of clumpiness (M_s of the SD16 RT model. *From top to bottom :* Dependence of the attenuation slope (δ), the amount of dust in V band (A_V), the color excess ($E(B-V)$), the UV bump amplitude (E_b) and the UV bump width (γ) to τ_V, R_s/R_d and M_s from left to right. The colors encode the different dust models. Each point represents the best-fit values for one configuration (τ_V, R_S/R_d, M_s) of SD16. The error bar represent the mean and standard deviation of δ for each bin of the considered SBL18 parameter.

3. Comparison of observed extinction and attenuation curves in GRB hosts

3.1. Investigation of dust attenuation and star formation activity in galaxies hosting GRBs

We have seen in the previous section that for a given dust model, i.e. extinction curve, different geometries can lead to very different attenuation curves. If the extinction and attenuation curves are known for the same galaxy, one can derive dust grain properties from the extinction curve and try to infer information about the geometry of the ISM of this galaxy from the attenuation curve. Unfortunately, extinction curves are mostly derived on local galaxies (Milky Way, the Large and Small Magellanic Clouds and Andromeda) for which it is very difficult to derive the attenuation curve of the whole galaxy as these galaxies have large angular sizes requiring to build a mosaic of images to cover the whole galaxy. This has been done for M31 by Viaene et al., 2017 who used a radiative transfer model to compute the attenuation curve of M31. At larger distances, the attenuation curve can be more easily derived as galaxies have smaller angular size, however extinction curves can not be measured with the pair method as stars are not resolved anymore.

Several techniques have been developed to derive the dust extinction curve for extragalactic sources, providing that the intrinsic SEDs of these sources are well characterised (see a more detailed review in Draine 2003). One of the technique uses QSO sightlines, where the extinction curve is derived by comparing composite spectra of reddened and un-reddened quasars (Richards et al. 2003; Hopkins et al. 2004; Zafar et al. 2015) and it is found that featureless SMC-like extinction curves are the most common along QSO sightlines. However, the emission of the AGN powering the QSO can contaminate the emission of the galaxy. An other technique measures extinction curves along GRB line of sight as their intrinsic emission is well modelled by a synchrotron emission [Sari et al., 1998; Granot et Sari, 2002]. What makes GRBs excellent probes for studying both extinction and attenuation curves is that their luminosity is fading rather rapidly with time, within a few days to weeks in the optical/NIR domain usually and up to months or even years for the radio emission. The measurement of the extinction curve is performed during a few minutes to hours after the GRB explosion when its luminosity is bright enough. After some months to years, when the contribution of the GRB luminosity to the host galaxy luminosity becomes negligible, the attenuation curve of the host galaxy can be derived.

In the paper entitled "Investigation of dust attenuation and star formation activity in galaxies hosting GRBs.", we investigated the use of GRBs to derive dust attenuation curves of distant star-forming galaxies and obtain information about the dust properties and the ISM structure of these galaxies by comparing their attenuation curves to the extinction curves derived along the GRB line of sight.

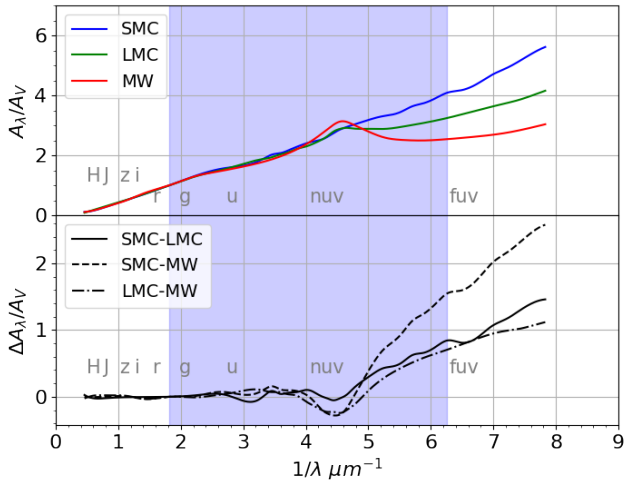

Figure IV.23– *Top* : Mean local extinction curves using data of Table 1 in Pei, 1992, normalised to A_V. *Bottom* : Difference between the mean local extinction curves, normalised to A_V. They start to differ significantly in the FUV. The blue shaded area represents the minimum rest-frame spectral coverage we require, that is, 1600Å to 5500Å .

As seen in Figure IV.23 (same as Figure 1 of the paper) the shape of extinction curves differs substantially in the UV domain only. Consequently, we first selected 30 GRB extinction curves having a UV rest-frame coverage. Then we compiled some properties their GRB host galaxies (GRBH) such as the stellar mass and the Star Formation Rate (SFR) to study whether dust properties along the GRB line of sight correlates with some physical properties of the host galaxies. We found that the GRB extinction curves having a spectroscopically confirmed UV bump are preferentially located in dusty massive galaxies (see Figure 3 of the paper) as already mentioned in Krühler et al., 2011. We also found that a rapid follow-up is required in order to catch these extinction curves (see Figure 2 of the paper) due to the higher amount of attenuation associated to extinction curves exhibiting a UV bump and the fading of the GRB luminosity with time. Interestingly, we do not find SMC-like extinction curves to be predominant when a rapid follow-up was achieved (within 3 hours since the GRB trigger) whereas we only find SMC-like extinction curves when the follow-up was achieved more than 3 hours after the GRB trigger. This might indicate an observational bias towards SMC-like extinction curves.

Then, From these 30 GRB selected galaxies we selected only the 7 galaxies having photometric measurements in at least 6 bands from UV to NIR in order to derive their attenuation curves and other physical parameters (SFR, stellar mass, etc) using the SED fitting CIGALE code [Noll et al., 2009]. We used the H_α measurements to check that our estimates of the SFR and amount of dust attenuation are compatible with the SFR derived with H_α luminosities and the Balmer decrement. This compatibility is very important to ensure that the amount of attenuation is well constrained as we do not have IR data, except for 1 galaxy.

In CIGALE we chose to model the attenuation curve using the SBL18 recipe, we proved to be a flexible enough recipe to catch various shapes of the attenuation curves. The results, described in Section 5.4 of the paper show a great variety of shape, from flat attenuation curves compatible to the C00 starburst law to attenuation curves as steep as the SMC extinction curve (see Figure IV.24). The comparison of these attenuation curves with the SD16 RT model in Section 5.5 shows that there is not a single dust/star geometry that can reproduce all the data. A clumpy to very clumpy local dust distribution is found to reproduce all the cases. For the two steepest attenuation curves two configurations are found to reproduce almost as likely the data, either a *Dusty* geometry associated with dust homogeneously distributed or a

Shell geometry associated with dust distributed in clumps.
As a by-product of our analysis we found that 5 out of 7 GRBHs require a recent burst of star formation to fit the data. As a consequence of these recent bursts of star formation, our estimation of the stellar mass is found lower than the stellar masses derived for the Swift GRB Host Galaxy Legacy Survey (SHOALS) [D. A. Perley et al., 2016b] using a mass-to-luminosity ratio using IRAC1 luminosities.

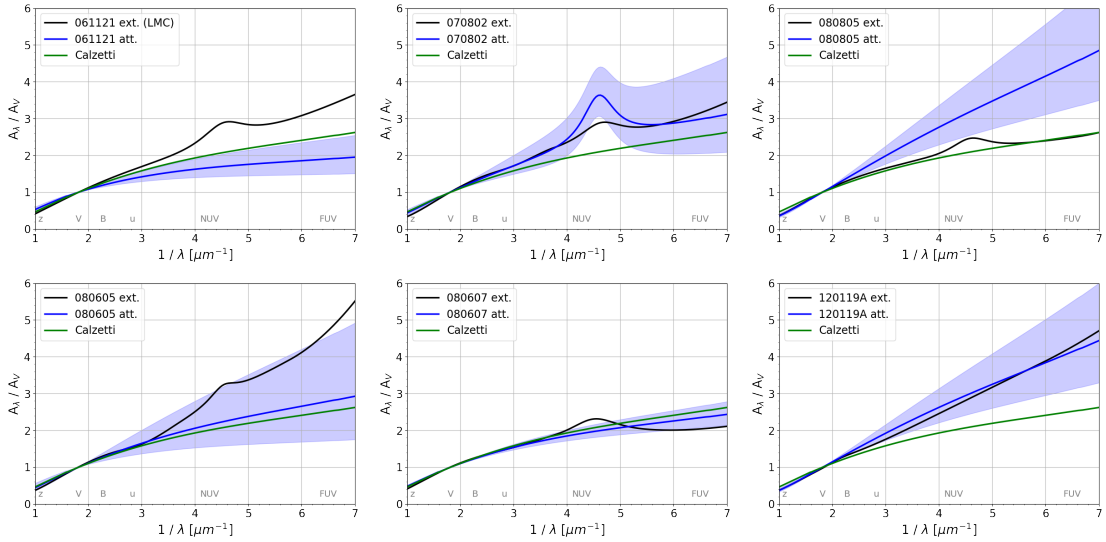

Figure IV.24– *Top* : GRBH 061121, GRBH 070802 and GRBH 080805, *Bottom* : GRBH 080605, GRBH 080607 and GRBH 120119. The solid black line is the extinction curve normalised to A_V^{grb}, the blue one is the attenuation curve normalised to A_V^{stars} and the green one is the normalised Calzetti law. The blue shaded area represents the 1σ uncertainty on the attenuation curve.

.

Unfortunately the use of wide filter bands did not allow to confirm the presence of the UV bump in the attenuation curves. In the future, it would be very interesting to obtain spectroscopy or narrow band observations of the GRBHs where a UV bump was spectroscopically detected in the extinction curve.
Since the publication of the article, an another UV bump has been spectroscopically measured in the extinction curve of GRB180325A at z=2.2 [Zafar et al., 2018a]. There are now 5 GRBs with an unambiguously spectroscopically confirmed UV bump. Though the time limit of 3 hours is arbitrary and must be only used as a rough estimate of a good follow-up response time, we note that the GRB spectrum was acquired less than 3 hours after the trigger. The large amount of extinction along the GRB line of sigth with $A_V^{grb} \sim 1.5$ mag is similar to the other GRBs with a UV bump. Using dust corrected H_α luminosities they derived a SFR of 46±4 $M_\odot.yr^{-1}$ from the calibration of Kennicutt, 1998. The stellar mass of $10^{9.3\pm0.4}$ $M_\odot$ they derived using the correlation between stellar mass and velocity width of the H_α line derived for GRBHs in Arabsalmani et al., 2018. Both SFR and stellar mass are comparable within uncertainty with the GRBHs of our sample. It will be interesting to perform a multi-wavelength observation of the galaxy to derive the attenuation curve and a more precise estimation of the stellar mass using a SED fitting.

A&A 617, A141 (2018)
https://doi.org/10.1051/0004-6361/201832926

Astronomy & Astrophysics

Investigation of dust attenuation and star formation activity in galaxies hosting GRBs

D. Corre[1], V. Buat[1], S. Basa[1], S. Boissier[1], J. Japelj[2], J. Palmerio[3], R. Salvaterra[4], S. D. Vergani[5], and T. Zafar[6]

[1] Aix-Marseille Univ, CNRS, CNES, LAM, Marseille, France
e-mail: david.corre@lam.fr, veronique.buat@lam.fr
[2] Anton Pannekoek Institute for Astronomy, University of Amsterdam, Science Park 904, 1098 XH Amsterdam, The Netherlands
[3] Institut d'Astrophysique de Paris, Université Paris 6-CNRS, UMR7095, 98bis Boulevard Arago, 75014 Paris, France
[4] INAF–IASF Milano, via E. Bassini 15, 20133 Milano, Italy
[5] GEPI, Observatoire de Paris, PSL University, CNRS, 5 Place Jules Janssen, 92190 Meudon, France
[6] Australian Astronomical Observatory, PO Box 915, North Ryde, NSW1670, Australia

Received 28 February 2018 / Accepted 16 June 2018

ABSTRACT

Context. The gamma-ray bursts hosts (GRBHs) are excellent targets to study the extinction properties of dust and its effects on the global emission of distant galaxies. The dust extinction curve is measured along the GRB afterglow line of sight and the analysis of the spectral energy distribution (SED) of the host galaxy gives access to the global dust attenuation of the stellar light.
Aims. In this pilot study we gather information on dust extinction in GRBHs to compare the properties of the extinction curve to those of the dust obscuration affecting the total stellar light of the host galaxy. Assuming the extinction curve to be representative of the dust properties, we aim to investigate which dust-stars geometries and local dust distribution in the inter stellar medium (ISM) can reproduce the observed attenuation curve.
Methods. We selected a sample of 30 GRBs for which the extinction curve along the GRB afterglow line-of-sight (l.o.s.) is measured in the rest-frame ultraviolet (UV) up to optical and we analysed the properties of the extinction curve as a function of the host galaxy properties. From these 30 GRBs, we selected seven GRBHs with a good rest-frame UV to near-infrared (NIR) spectral coverage for the host. The attenuation curve was derived by fitting the SEDs of the GRBH sample with the CIGALE SED fitting code. Different star formation histories (SFH) were studied to recover the star formation rates (SFR) derived using H_α luminosities. Implications for the dust-stars geometries in the ISM are inferred by a comparison with radiative transfer simulations.
Results. The most extinguished GRBs are preferentially found in the more massive hosts and the UV bump is preferentially found in the most extinguished GRB l.o.s. Five out of seven hosts are best fitted with a recent burst of star formation, leading to lower stellar mass estimates than previously found. The average attenuation in the host galaxies is about 70% of the amount of extinction along the GRB l.o.s. We find a great variety in the derived attenuation curves of GRBHs, the UV slope can be similar, flatter or even steeper than the extinction curve slope. Half of the attenuation curves are consistent with the Calzetti attenuation law and there is evidence of a UV bump in only one GRBH. We find that the flatter (steeper) attenuation curves are found in galaxies with the highest (lowest) SFR and stellar masses. The comparison of our results with radiative transfer simulations leads to a uniform distribution of dust and stars in a very clumpy ISM for half the GRBHs and various dust-stars geometries for the second half of the sample.

Key words. gamma-ray burst: general – dust, extinction – galaxies: starburst – galaxies: star formation – galaxies: high-redshift – galaxies: ISM

1. Introduction

Stellar light in galaxies is absorbed and scattered in the interstellar medium by dust grains. Dust effects are particularly strong in the ultraviolet (UV), where photons are preferentially absorbed and scattered by interstellar dust. Moreover the UV light is emitted by young stars and is a tracer of the recent star formation. It is thus of the utmost importance to well quantify the interaction between the dust and the stellar light in the UV to study the dust properties and to measure accurately the star formation activity inside a galaxy.

Dust attenuation for extended objects should be distinguished from the extinction for point sources. In the case of a point source, the extinction quantifies how many photons are absorbed and scattered out of the line of sight (l.o.s.) and is thus directly linked to dust properties. For extended objects, such as galaxies, dust and stars are mixed and the attenuation does not only quantify how many photons are absorbed and scattered by dust out of the l.o.s. but also how many photons are scattered into the l.o.s. This means that it does not only depend on dust properties but also on the dust-stars geometry in the ISM.

The extinction curve can be directly measured along sight-lines where the spectrum of individual stars can be obtained, which due to resolution is only the case in the Local Group so far. Using this technique, extinction curves were obtained in four galaxies where stars can still be resolved: the Milky Way (MW; Witt et al. 1984; Fitzpatrick & Massa 1990, 2007), the Small Magellanic Cloud (SMC; Prevot et al. 1984; Gordon & Clayton 1998; Gordon et al. 2003), the Large Magellanic Cloud (LMC; Clayton & Martin 1985; Fitzpatrick 1985; Misselt et al. 1999), and M 31 (Bianchi et al. 1996; Clayton et al. 2015).

Beyond the Local Group, where individual stars cannot be resolved, several techniques have been developed to derive the dust extinction in extragalactic sources, provided that the

intrinsic SEDs of these sources are well characterised (see a more detailed review in Draine 2003). Most of these techniques assume the sources to be point-like which is not the case and therefore geometrical effects are included in the extinction curve. The importance of these effects are discussed by Krügel (2009) and Scicluna & Siebenmorgen (2015). For example, the dust extinction curve can be derived from QSO sightlines by comparing composite spectra of reddened and un-reddened quasars (Richards et al. 2003; Hopkins et al. 2004; Zafar et al. 2015) and it is found that featureless SMC-like extinction curves are the most common along QSO sightlines.

The attenuation curve of a whole galaxy can be derived from observations using UV-optical spectra or multi-band photometric data. For local UV-bright starburst galaxies, Calzetti et al. (1994, 2000) derive a mean attenuation curve characterised by a flatter slope than for mean local extinction curves and by a lack of the 2175 Å absorption feature (UV bump). After Calzetti's work the topic was reinvestigated at low and high redshift (e.g. Buat et al. 2010, 2011, 2012; Wild et al. 2011; Kriek & Conroy 2013; Reddy et al. 2015, 2016; Salmon et al. 2016; Battisti et al. 2016, 2017) leading to a non-universality of the dust attenuation law. Using a similar method as the one of Calzetti et al. (2000; hereafter C00) on a larger sample of about 10 000 local ($z \lesssim 0.1$) star forming galaxies, Battisti et al. (2016, 2017) derive a mean attenuation curve similar to C00 one though a bit shallower in the UV. Reddy et al. (2015) also applied a similar method to the C00 one to estimate the attenuation curve of 224 star forming galaxies at $z \sim 2$. They find that the mean attenuation curve shape is again similar to the one of C00 in the UV but with a lower normalisation and similar to the mean SMC extinction curve at larger wavelength. Based on the NOAO Extremely Wide Field Infrared Mosaic (NEWFIRM) Medium-Band Survey, Kriek & Conroy (2013) constrain the dust attenuation of $0.5 < z < 2$ galaxies. They find that a MW and Calzetti law provide poor fits at UV wavelengths, and that steeper laws have stronger UV bumps together with more active galaxies having flatter attenuation curves and weaker UV bumps. Using galaxies from the Cosmic Assembly Near-infrared Deep Extragalactic Legacy Survey (CANDELS) at $z \sim 1.5{-}3$, Salmon et al. (2016) find a correlation between the colour excess $E(B-V)$ and the slope of the attenuation law: galaxies with high colour excess have shallower attenuation curves and those with low colour excess have steeper attenuation curves.

The attenuation curve of galaxies is also studied using radiative transfer models with various dust physical properties and geometrical distribution of stars and dust. In general, shallower attenuation curves correspond to larger optical depths and mixed star-dust geometries (e.g. Witt & Gordon 2000; Pierini et al. 2004; Tuffs et al. 2004; Panuzzo et al. 2007; Chevallard et al. 2013). Applying radiative transfer models to M 31 and M 51, Viaene et al. (2017) and De Looze et al. (2014) respectively derived very steep attenuation curves with the presence of a UV bump. Most of the numerical simulations using radiative transfer models use the extinction law of local galaxies to characterise the dust properties and compute the attenuation curve one would observe for a given dust-stars geometry (e.g. Witt & Gordon 2000; Pierini et al. 2004; Seon & Draine 2016).

Gamma-ray bursts (GRBs) with their featureless power-law like spectrum shape of their afterglows are excellent probes of dust extinction in their host galaxies (Zafar et al. 2011, 2018; Schady et al. 2012; Covino et al. 2013; Japelj et al. 2015). Thanks to their extremely high luminosity (up to $\sim 10^{53}$ erg s^{-1}) such studies can be extended to very high redshift. In this work, we take advantage of the fact that both the extinction and attenuation curves can be measured for the same galaxy. The observed difference between attenuation and extinction curves contains information about the GRBH ISM structure. The extinction curves measured along the GRB l.o.s. are taken from the literature. The global dust attenuation in the GRBH galaxies is obtained by deriving the attenuation curve from SED fitting. Assuming GRB extinction curves are representative of the dust properties of their hosts, we compared our results to radiative transfer simulations in order to put some constraint on the dust-stars geometry and local distribution of dust in the ISM. As a by-product of the SED fitting we also derive robust stellar masses and SFR for the GRBHs.

The paper is organised as follows: in Sect. 2, we explain the selection of the GRB extinction curves and later the selection of the GRB host galaxies. In Sect. 3 we will search for correlations between the GRB l.o.s. and the host galaxy properties. In Sect. 4, we derive the attenuation curves of the selected host galaxies using the CIGALE SED fitting algorithm as well as the stellar mass and SFR of the galaxies. In Sect. 5, the extinction curves are compared to the derived attenuation curves and we compare our results with radiative transfer simulations.

2. Selection of the targets

Our strategy was to find reliable GRB extinction curves in the literature and then select the host galaxies for which we were able to derive the attenuation curves. In this section, we briefly explain the methods to measure the extinction curve along GRB afterglow l.o.s. in order and we define selection criteria to select the GRB extinction curves. The last step is the selection of the host galaxies.

2.1. GRB selection

2.1.1. SED of GRB afterglows

GRB afterglows are well described by synchrotron emission from accelerated electrons in a relativistic blast wave interacting with an external medium (Sari et al. 1998; Granot & Sari 2002). The observed synchrotron spectrum is composed of series of power-law segments joined at certain break frequencies (see Sari et al. 1998; Granot & Sari 2002). The NIR-to-X-ray spectrum is then usually modelled as a single power-law or a broken power-law to take into account a possible break in the synchrotron spectrum, most likely the cooling break, located between the X-ray and UV/optical/NIR ranges at the time of observation. Knowing the intrinsic spectral shape, the comparison of the observed spectrum with an expected one gives a direct access to the extinction curve. The non-attenuated intrinsic GRB afterglow SED is modelled by

$$F_\nu = \begin{cases} F_0 \cdot \nu^{-\beta_O} & \nu \leq \nu_{break} \\ F_0 \cdot \nu_{break}^{\beta_X - \beta_O} \cdot \nu^{-\beta_X} & \nu > \nu_{break} \end{cases} \quad (1)$$

where F_0 is the flux normalisation, ν the frequency, ν_{break} the break frequency, β_O and β_X are the spectral slopes of the UV/optical/NIR and X-ray segments respectively. The free parameters are F_0, β_O and β_X. At sufficiently late times the synchrotron emission is expected to radiate in the slow cooling regime, where $\beta_O = \beta_X + 0.5$ (Sari et al. 1998; Zafar et al. 2011). This emitted flux is then attenuated by dust absorption and scattering and photoelectric absorption of soft X-rays in the the host galaxy. The attenuated flux is given by

$$F_\nu^{obs} = F_\nu \cdot 10^{-0.4 A_\lambda} \cdot e^{-N_{H,X}\sigma(\nu)} \quad (2)$$

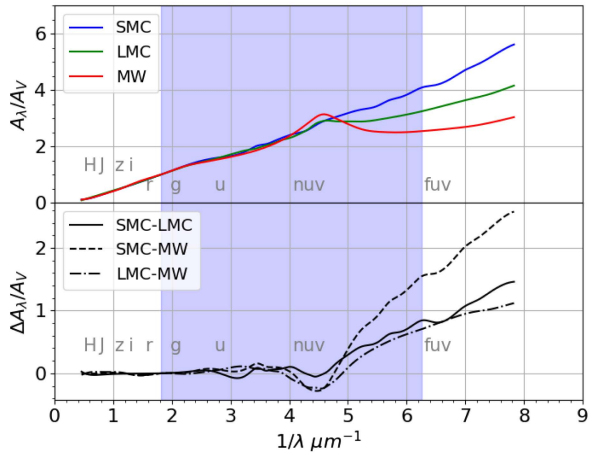

Fig. 1. *Top*: mean local extinction curves using data of Table 1 in Pei (1992), normalised to A_V. *Bottom*: difference between the mean local extinction curves, normalised to A_V. They start to differ significantly in the FUV. The blue shaded area represents the minimum rest-frame spectral coverage we require, that is, 1600 Å–5500 Å.

where A_λ is the wavelength dependent extinction in the host galaxy, $N_{H,X}$ is the equivalent neutral hydrogen column density derived from the soft X-ray absorption along the GRB l.o.s. in the host galaxy and is a free parameter. $\sigma(\nu)$ is the cross-section for the photoelectric absorption from the gas in the host galaxy.

2.1.2. Modelling extinction processes

There are two methods to assess A_λ, in other words, the extinction curve. The first method consists in scaling the well defined extinction curves derived for the LMC, SMC, or MW to the data. The mean local extinction curves of Pei (1992), normalised to the amount of extinction in the V band, A_V, are seen on top panel of Fig. 1. These local laws are scaled to the GRB afterglow spectrum using A_V as the scaling factor. This method has the advantage of introducing only one free parameter, A_V, to the SED fitting, but assumes that the wavelength dependence of dust extinction at high redshift is the same as the mean extinction in our local environment. Recently, Zafar et al. (2018) suggested avoiding use of the canonical Pei (1992) SMC curve to fit GRB data and to use the SMC-bar extinction curve from Gordon et al. (2003).

The second method is to perform a fit to assess directly the wavelength dependence of dust extinction. Usually the fit is performed using the prescriptions of Fitzpatrick & Massa (2007; hereafter FM07) which parametrises the extinction curve as

$$A_\lambda = A_V\left(\frac{1}{R_V}k(\lambda - V) + 1\right) \tag{3}$$

where $R_V = A_V/E(B-V)$ is the ratio of absolute-to-selective extinction.
In the UV wavelength range ($\lambda < 2700$ Å):

$$k(\lambda - V) = \begin{cases} c_1 + c_2 x + c_3 D(x, x_0, \gamma) & x \le c_5 \\ c_1 + c_2 x + c_3 D(x, x_0, \gamma) + c_4 (x - c_5)^2 & x > c_5 \end{cases} \tag{4}$$

where $x \equiv \lambda^{-1}$ in units of μm^{-1}, c_1 and c_2 represents the UV linear component, c_3 represents the bump strength, c_4 and c_5 the FUV curvature, and the Drude profile modelling the 2175 Å bump is expressed as

$$D(x, x_0, \gamma) = \frac{x^2}{(x^2 - x_0^2)^2 + x^2\gamma^2} \tag{5}$$

where x_0 is the central wavelength number and γ is the width of the bump. In the optical and NIR a spline interpolation is used to estimate the extinction curve. The FM07 parametrisation offers more freedom to fit the actual shape of the extinction curve. However it has nine free parameters which leads to degeneracies between the parameters in the fitting process unless one has a finely-sampled SED. Consequently, this method is mainly used with spectroscopic measurements, as with photometric measurements only one has to fix some of the parameters, such as intrinsic spectral slope. Moreover, photometric observations affected by the IGM absorption are usually not used which further limits the number of data.

2.1.3. Selection criteria for GRB extinction curves

For our study purpose, it is essential to have a well characterised extinction curve. The three local extinction curves (MW, LMC, and SMC) have a very similar shape in the rest-frame NIR and optical and start to differ significantly in the rest-frame FUV (Fig. 1). To be able to distinguish them, observations in the rest-frame UV bluewards of 2000 Å are needed. The lower panel of Fig. 1 shows the difference between the local extinction curves normalised to A_V. We can see that for low to moderate A_V the difference in magnitudes between the local extinction curves may be below a standard photometric accuracy. A typical amount of extinction in the V band of 0.2 mag leads to a difference between the different local extinction curves higher than 0.15 mag only at 1600 Å in the rest-frame. It increases to at least 0.75 mag with $A_V = 1$ mag. In the following, the amount of extinction in the V band along the GRB l.o.s. will be denoted A_V^{grb}. We started by considering only GRB extinction curves derived using the FM07 formula with at least observations between 1600 Å and 5500 Å in the rest-frame. We used the largest sample of GRB extinction curves derived from spectroscopic measurements of the afterglow from Zafar et al. (2011) and the updated results in Zafar et al. (2012). From the 42 GRBs of this sample, we kept the 31 GRBs with evidence of dust extinction along the GRB l.o.s., that is, A_V^{grb} not consistent with 0 mag within 1σ uncertainty. After applying the minimum wavelength coverage defined above we are left with a sample of eight GRBs: five with an SMC-like extinction curve and three exhibiting a 2175 Å bump (see Table A.1). Initially, GRB 080805 is not part of our sample due to the scarcity of optical data which can not safely constrain the extinction curve slope. However, the spectroscopic confirmation of the presence of a UV bump is an interesting information about the dust inside the galaxy and we decide to include GRB 080805 in our sample. To our knowledge there are only four GRBs with a spectroscopically confirmed UV bump (GRB 070802, GRB 080605, GRB 080607, GRB 080805) and they are all in our sample.

In order to increase our sample we also considered GRB extinction curves derived using the scaling method. We started with the sample of Japelj et al. (2015) based on spectroscopic measurement of the afterglow. It consists of nine GRBs observed within the X-shooter GRB GTO programme between 2009 and 2014. For the scaling method, the slope of the extinction curve is fixed, therefore we apply a relaxed minimum wavelength coverage going from 1600 to 3500 Å in the rest-frame. We kept

Table 1. GRB hosts in our Golden sample.

Name	Redshift	Ext. curve	Host data
061121[a]	1.31	LMC	10 bands (incl. VLA)
070802	2.45	Relatively steep + UV bump	7 bands
080605	1.64	Steep + UV bump	8 bands
080607	3.04	Flat + UV bump	9 bands (incl. ALMA)
100814	1.44	SMC-like	6 bands
120119	1.72	SMC-like	6 bands
080805	1.51	Flat + UV bump	6 bands

Notes. The only host which does not meet our selection criteria of minimum wavelength coverage is listed at the bottom. [(a)] GRB 061121 is the only afterglow for which the extinction curve is derived with photometric data only.

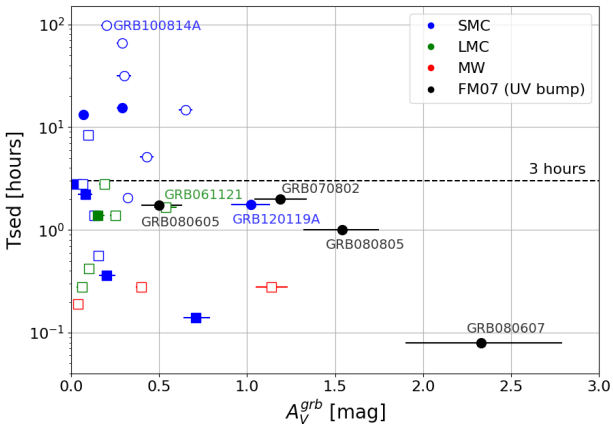

Fig. 2. Time, since the GRB trigger, at which the SED were evaluated as a function of the extinction along the GRB l.o.s., A_V^{grb}. The blue, green and red colours represent which local extinction curve (SMC, LMC, MW) scaled the best to the data. The black colour means that the extinction curve was fitted with the FM07 and has a spectroscopically confirmed UV bump. The circles represent the afterglows with spectroscopic measurement and the squares the ones with photometric measurement only. The filled symbols represent SEDs best fitted with a single power law, the empty ones represent SEDs best fitted by a broken power law. Only the names of the GRB in our Golden sample are indicated.

the eight GRBs with evidence of dust and after applying our wavelength coverage criterion we are left with four GRBs. GRB 120119A is best fitted with an LMC extinction curve, however Japelj et al. (2015) reported that it overpredicts the strength of the UV bump and that none of the mean LMC, SMC and MW is able to accurately match the the binned spectrum of GRB 120119A. Using the afterglow spectrum observed by the X-shooter and with the same data analysis as in Zafar et al. (2011, 2018) find an SMC-like extinction curve using the FM07 formula. In the following we therefore consider the extinction curve to be SMC-like. We are left with 4 GRBs with an SMC-like extinction law. We also considered the sample of Schady et al. (2012) based on broad-band photometry measurement of the afterglow since they required at least one detection at a rest-frame wavelength below 2000 Å. It consists of 49 GRBs. We kept the 36 GRBs with evidence of dust extinction and after applying our relaxed wavelength criterion we were left with 17 GRB extinction curves: eight consistent with an SMC extinction curve, six with an LMC one, and three with an MW one (see Table A.1). At the end we have a sample of 30 GRB extinction curves: 17 with an SMC-like curve, six with an LMC-like, three with an MW-like, and four with a spectroscopically confirmed bump exhibiting various slopes.

2.2. GRB host galaxies selection

Now that we have selected the extinction curves of 30 GRBs, we first compile some properties of their host galaxies, such as the SFR, stellar mass, and amount of attenuation in order to search for a correlation between the dust properties along the GRB l.o.s. and inside the host galaxy. For the second part of our study we selected only the host galaxies for which we can derive the attenuation curves from SED fitting.

2.2.1. GRB host galaxy properties

The SFR derived from the dust corrected H_α luminosity (Kennicutt 1998) is considered as one of the most robust tracers of recent star formation, in the following it will be denoted SFR_{H_α}. The extinction of emission lines derived from the Balmer decrement is an indicator of the dust extinction towards the HII regions. In the following, the amount of attenuation in the V band in the host derived from the Balmer decrement will be denoted A_V^{lines}. For homogeneity, these two quantities are exclusively taken from Krühler et al. (2015), with the exception of GRBH 061121 for which the SFR_{H_α} is taken from Vergani et al. (2017) and A_V^{lines} is computed from the H_α and H_β fluxes in Vergani et al. (2017) using the same prescriptions as in Krühler et al. (2015). The metallicities were measured using the calibration of Maiolino et al. (2008), and taken from Krühler et al. (2015), Japelj et al. (2016) and Vergani et al. (2017). The stellar masses are taken from Perley et al. (2016).

2.2.2. Golden sample for deriving GRBH attenuation curves

The characterisation of the dust effects is crucial in the UV. From the 30 GRB host galaxies selected with robust GRB extinction curves we select only targets with photometric measurements of the UV rest-frame emission of the host and a UV-to-NIR spectrum reasonably well sampled (with at least six bands) in order to measure physical parameters. After a careful inspection of the photometric and spectroscopic data of the host galaxies of GRBs selected in Sect. 2.2.1, we select seven galaxies with good photometric data on at least six bands, including a detection with the *Spitzer* Infrared Array Camera at 3.6 μm (IRAC1) and hydrogen recombination lines (except for GRBH 080607 at $z = 3.04$) allowing a measure of SFR_{H_α} and of the Balmer decrement. The photometric data collected for each target are described in Appendix B. The data are corrected for the foreground Galactic extinction using Schlafly & Finkbeiner (2011). The seven hosts are gathered in Table 1.

3. GRB and host properties

Before comparing the extinction curve derived from the GRB l.o.s. with the attenuation curve derived for the host galaxy we are searching for some correlations between properties derived along the GRB l.o.s. and for the whole galaxy to check whether GRB l.o.s. are representative for the dust properties of the hosts.

3.1. Importance of a rapid follow-up

As GRB afterglows fade rather rapidly, we first check whether the time at which the GRB SED is extracted has an influence on the study of GRB extinction curves. Figure 2 represents the time, after the GRB trigger, at which the GRB SED is extracted as a function of A_V^{grb} for different types of extinction curves. We see that at early times, below roughly three hours, GRB afterglows exhibit all type of extinction curves from low to high extinction whereas after three hours only SMC-like extinction curves with low to moderate extinction are found. There are two ways to explain this trend, either as a bias against highly extinguished afterglows or a time dependent dust composition modification. A temporal evolution of the dust properties is expected from theoretical simulations (Waxman & Draine 2000; Fruchter et al. 2001; Perna et al. 2003) where a strong X-ray/UV radiation field can deeply modify the dust properties in the close environment (∼10−100 pc) of the source. Dust sublimation is predicted to affect primarily the smaller grains, and the silicates are preferentially destroyed compared to graphite, leading to featureless and shallow extinction curves. A possible early colour variation has been studied in Morgan et al. (2014). However, these processes mainly take place during the first seconds or minutes after the burst and not a few hours after the burst.

The other explanation is a bias against highly extinguished afterglows due to instrument sensitivity and fast decay of the GRB afterglow brightness. Indeed, if we consider that GRBs in dusty galaxies are not intrinsically brighter than those in galaxies with low dust content, they will be below instrument sensitivities very rapidly, with the exception of extremely bright afterglows. As mentioned in Zafar et al. (2011), where the afterglows in their sample have an average magnitude of 21.1 ± 1.7, a MW-like extinction curve with a rest-frame visual extinction of $A_V^{grb} = 1$ mag will yield roughly 2–3.5 magnitudes of extinction in the optical at $z = 2$. Therefore GRB afterglows with $A_V^{grb} > 1$ mag are unlikely to be detected with current instrument sensitivity except for the few brightest ones and those with a follow-up within the first minutes after the GRB trigger. The fraction of dark bursts has been estimated between 25 and 42% in Fynbo et al. (2009) and using the complete BAT6 sample, Melandri et al. (2012) derived a 25–35% fraction of genuine optically dark bursts. Using systematic follow-up observations from GROND, Greiner et al. (2011) show that at moderate redshift, the main contribution to dark bursts is a moderate extinction. We conclude that the trend observed in Fig. 2 is very likely driven by the observed GRB brightness and not due to a temporal evolution of dust properties. In Fig. 2, we also see that extinction curves exhibiting a 2175 Å bump are preferentially found in the most extinguished l.o.s. as previously found in (Zafar et al. 2011; Greiner et al. 2011; Krühler et al. 2011). They are therefore more easily detected at early times. It follows that there is an observational bias towards SMC-like extinction curves.

The forthcoming French Ground Follow-up Telescope (F-GFT), a 1.3 m optical/NIR robotic telescope for the Space Variable Object Monitor mission (Wei et al. 2016), with its extremely fast response time of less than 20 s after receiving an alert, should significantly increase the detection of extinguished bursts. It should also be able to observe at early times the rapid afterglow colour change characteristic of a temporal variation of dust properties under the influence of intense X-ray/UV radiation field[1].

[1] For GRBs from Zafar et al. (2011, 2012) and Schady et al. (2012) this is the time at which the SED is extracted, and for those from Japelj et al. (2015) the time corresponds to the mid-time of the X-shooter observations.

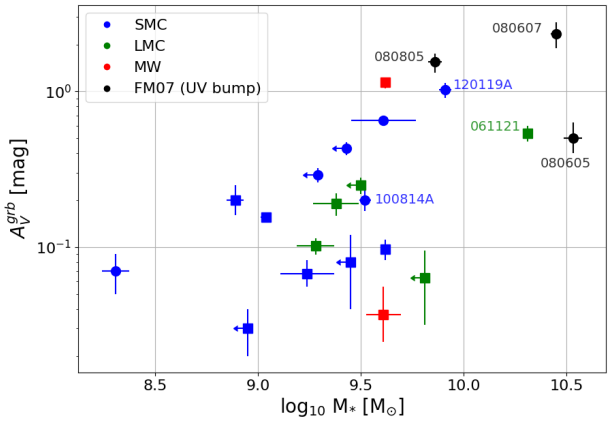

Fig. 3. Extinction along the GRB l.o.s. as a function of the host galaxy stellar mass, the latter taken from Perley et al. (2016). Same colours and symbols as in Fig. 2.

3.2. Dust extinction along GRB l.o.s. as a function of GRBH stellar mass

Figure 3 represents A_V^{grb} as a function of the GRBH stellar mass for different types of extinction curves. It shows that highly extinguished GRB l.o.s. are preferentially found in the most massive host galaxies. Previous studies (e.g. Zahid et al. 2013; Heinis et al. 2014) showed that the amount of dust attenuation in a galaxy is correlated with the stellar mass of the galaxy. Vijh et al. (2003) found a similar relation between the UV attenuation and UV luminosity of Lyman break galaxies. This relation holds if the GRB afterglow probes not only the dust capable to survive the intense radiation of the afterglow in the surrounding environment of the GRB progenitor but also the dust located at sufficiently large distances to be representative of the whole galaxy. Interestingly, this figure also shows that GRB extinction curves exhibiting a UV bump are preferentially found in the most massive host galaxies as already noticed in Krühler et al. (2011). Noll et al. (2009b) find that galaxies with evidence of a UV bump have a more evolved stellar population than galaxies lacking this feature.

4. Fitting the SED of the hosts

For the seven GRBHs in our Golden sample defined in Table 1 we perform SED fitting to derive the attenuation curve. The method and the models are first described, then we discuss the SED fitting analysis of each GRB host galaxy. In the last part of this section we discuss the star formation activity of these seven GRBHs.

4.1. SED fitting method

The SED fitting is performed with the version v0.11 of the CIGALE code (Code Investigating GALaxy Emission)[2]. CIGALE combines a UV-optical stellar SED with a dust component emitting in the IR and fully conserves the energy balance between dust absorbed emission and its re-emission in the IR. Star formation histories as well as dust attenuation characteristics, including the attenuation law, are input parameters that can

[2] http://cigale.lam.fr

Table 2. Input parameters for SED fitting with CIGALE.

Parameter	Symbol	Range
Colour excess[a]	$E(B-V)_s$	0.01, 0.05, 0.1, 0.25, 0.5, 0.75, 1.0, ... 1.25, 1.5, 1.75, 2.0, 2.25, 2.5, 3.0, 4.0 mag
Attenuation curve[b]	δ	[−1: + 0.7] per bin of 0.1
Delayed star formation history + recent burst		
Age of the main stellar population	t_0	1000, 2000, 3500 Myr
Peak of the star formation (delayed SFH)	τ	1000, 2000, 3000, 5000, 7000, 10 000 Myr
Age of the burst	t_b	20, 50, 100 Myr
Stellar mass fraction due to the burst	f_b	[0:0.5] per bin of 0.05
Metallicity[c]	Z	0.008, 0.02

Notes. Values of input parameters used for the SED fitting with CIGALE. [(a)] $E(B-V)_s$ is the colour excess between the B and V bands applied on the stellar continuum. [(b)] Defined in Eq. (6). [(c)] The metallicity is set to one of the 2 values ($Z = 0.02$ being the solar metallicity).

be either taken free or fixed according to the available data or the specific aims. The main characteristics of the code are described in Noll et al. (2009a). We refer to Boquien et al. 2017 (in prep.) for a detailed description of the new version of the code and to the online information to use the code. Here we only describe the assumptions and choices specific to the current study. The main parameters and range of input values are reported in Table 2. The output values of the parameters are estimated by building the probability distribution function (PDF) and by taking its mean and standard deviation. To assess the quality of the fit we compare the results to the SFR derived from the dust corrected H_α luminosity and the amount of dust attenuation derived from the Balmer decrement.

Different scenarios of star formation history are implemented in CIGALE. In this work, we have adopted a delayed star formation rate ($SFR \propto t \cdot e^{-t/\tau}$) on which we add a young burst of constant star formation with a free age and amplitude. This scenario aims at reproducing both the general star formation history of distant galaxies (i.e. Lee et al. 2010; Maraston et al. 2010; Pforr et al. 2012) and a possible recent burst of star formation. The hosts of GRBs are known to be active in star formation (Savaglio et al. 2009; Perley et al. 2013; Hunt et al. 2014; Japelj et al. 2016). As rest-frame UV photometric data can probe down to the last 20 Myr of star formation history (Boquien et al. 2014), the age of the burst is allowed to vary from 20 Myr–100 Myr. The fraction of stellar mass in the recent burst is allowed to vary from 0 to 50% of the main stellar population.

The initial mass function of Chabrier (2003) is adopted with the stellar synthesis models of Bruzual & Charlot (2003). The nebular emission is included with standard parameters. The metallicity is fixed and chosen to be the closest value to the measurements between $Z = 0.008$ and 0.02 (solar value).

To model the attenuation by dust, we used a modified version of the attenuation law of C00, which offers the possibility of varying the steepness of this law and adding a bump centred at 2175 Å. We refer to Noll et al. (2009a) for a complete description of the dust attenuation prescription, which still holds in the new version of the code. In brief, the dust attenuation is described as

$$A_\lambda = E(B-V)_s \left[k'(\lambda) \left(\frac{\lambda}{\lambda_V} \right)^\delta + D_{\lambda_0,\gamma,E_b}(\lambda) \right] \quad (6)$$

where $\lambda_V = 5500$ Å, $k'(\lambda)$ comes from C00. $D_{\lambda_0,\gamma,E_b}(\lambda)$, the Lorentzian-like Drude profile commonly used to describe the UV bump (Fitzpatrick & Massa 1990), is defined as

$$D_{\lambda_0,\gamma,E_b} = \frac{E_b \lambda^2 \gamma^2}{(\lambda^2 - \lambda_0^2)^2 + \lambda^2 \gamma^2} \quad (7)$$

with $\lambda_0 = 2175$ Å. An extinction curve as steep as the SMC corresponds to $\delta \simeq -0.5$ and the bump amplitude found in the average extinction curve of the MW corresponds to $E_b = 3.5$. For a sample of UV selected galaxies at intermediate redshift Buat et al. (2012) find $E_b = 1.6$ and $\delta = -0.27$, which is close to the shape of the LMC2 extinction curve with a UV bump of moderate amplitude.

The photometric data partially overlap the bump for GRBHs 061121, 070802, 080605, 080805, 100814A and 120119A. For these six sources the bump will be fixed at $\lambda_0 = 2175$ Å with a width $\gamma = 350$ Å and the amplitude is taken free. Because of the lack of wavelength coverage the other fits are performed without adding any bump in the attenuation curve and only varying its slope (δ).

The stellar emission absorbed by dust is re-emitted in the IR. The IR templates used in this work are from (Dale et al. 2014; without the AGN component) which are parametrised with a single parameter α corresponding to the exponent of the distribution of heating intensity over dust mass. A single template ($\alpha = 2$) is used except for the only galaxy detected in IR, GRBH 080607, for which different α of between 1 and 2 are tested to cover the range of values found from quiescent to active star-forming galaxies (Dale & Helou 2002).

The attenuation of the continuum obtained from the SED fitting will be denoted A_V^{stars}.

4.2. Analysis of the sources

4.2.1. GRBH 061121

From H_α measurements, Vergani et al. (2017) derived a SFR_{H_α} of $44.2^{+19}_{-10}\,M_\odot\,yr^{-1}$. Using the Balmer lines measurements by Vergani et al. (2017), we computed $E(B-V)_g = 0.53^{+0.19}_{-0.19}$ mag corresponding to $A_V^{lines} = 1.66^{+0.60}_{-0.60}$ mag (using $R_V = 3.08$ as in Krühler et al. 2015). From IRAC1 measurement Perley et al. (2016) derived a stellar mass of $2 \times 10^{10}\,M_\odot$.

The radio component is added to the fit with standard parameters (a FIR/radio correlation coefficient of 2.58 and a slope of 0.8 for the power-law synchrotron emission). The best model is obtained for $Z = 0.008$ and shown in Fig. 4. No evidence of a UV bump is found. The SFR is found equal to $62 \pm 26\,M_\odot\,yr^{-1}$ consistent with SFR_{H_α}. A strong burst involving $29 \pm 14\%$ of the total mass with an intermediate age of

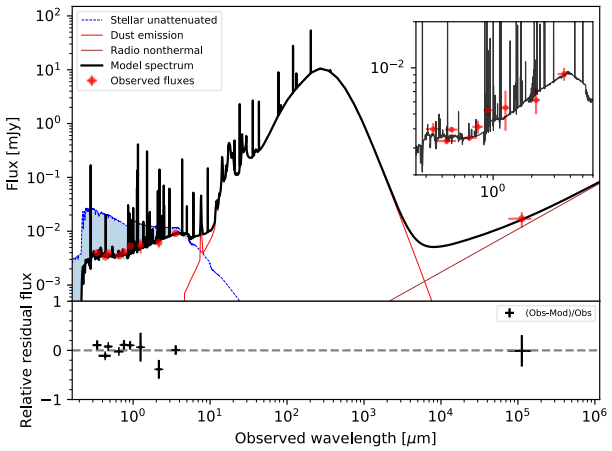

Fig. 4. Best-fitted SED for GRBH 061121. Red points are the observed fluxes with their uncertainties. The black line represents the best fitted spectrum composed of attenuated stellar emission, dust emission, non-thermal radio emission and nebular lines. The dashed blue line represents the unattenuated stellar emission and the blue shaded area indicates the amount dust attenuation. The *lower panel* shows the relative residual. The *upper right panel* is an enlargement of the UV/optical/NIR domain.

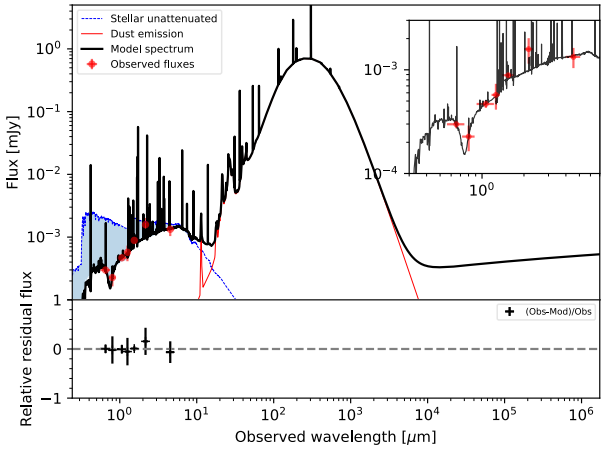

Fig. 5. Best-fitted SED for GRBH 070802. Colour and symbols convention as in Fig. 4.

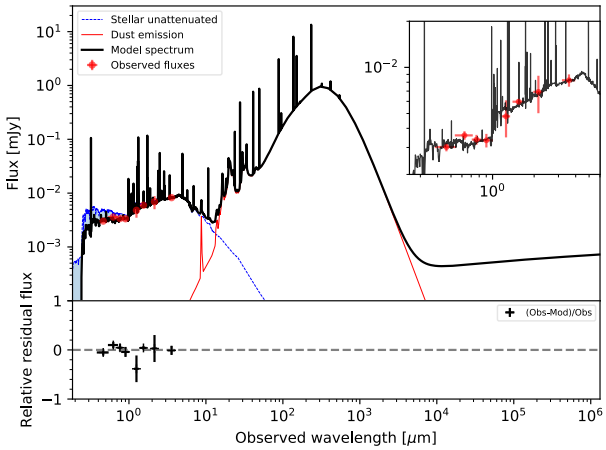

Fig. 6. Best-fitted SED for GRBH 080605. Colour and symbols convention as in Fig. 4.

58 ± 31 Myr is needed to reproduce the SED. The stellar mass is $M_\star = 6.9 \pm 2.4 \times 10^9\,M_\odot$ a factor 3 lower than the one measured by Perley et al. (2016). The resulting specific SFR, defined as $\mathrm{sSFR} = \mathrm{SFR}/M_\star$ is equal to $9\,\mathrm{Gyr}^{-1}$. The dust attenuation is found moderate with $E(B-V)_\mathrm{s} = 0.15 \pm 0.04$ mag, with a flat attenuation law ($\delta = 0.22 \pm 0.2$) marginally consistent with the starburst law of C00. The resulting amount of visual extinction is $A_\mathrm{V}^\mathrm{stars} = 0.88 \pm 0.30$ mag. A metallicity of $Z = 0.02$ returned a slightly higher χ^2 with similar values for the SFR, the stellar mass, δ and $A_\mathrm{V}^\mathrm{stars}$.

4.2.2. GRBH 070802

The Balmer lines are measured by Krühler et al. (2015), corresponding to a moderate attenuation with $E(B-V)_\mathrm{g} = 0.31^{+0.12}_{-0.12}$ mag corresponding to $A_\mathrm{V}^\mathrm{lines} = 0.95^{+0.37}_{-0.37}$ mag and $\mathrm{SFR}_{\mathrm{H}_\alpha} = 24^{+11}_{-8}\,M_\odot\,\mathrm{yr}^{-1}$.

The best model is obtained for $Z = 0.008$ and shown in Fig. 5. The SFR is found equal to $32.2 \pm 17.8\,M_\odot\,\mathrm{yr}^{-1}$ consistent with $\mathrm{SFR}_{\mathrm{H}_\alpha}$. A strong burst involving $26 \pm 15\%$ of the total mass with an intermediate age of 55 ± 32 Myr is needed to reproduce the SED. The stellar mass is $M_\star = 3.7 \pm 1.6 \times 10^9\,M_\odot$.

The dust attenuation is found moderate with $E(B-V)_\mathrm{s} = 0.21 \pm 0.05$ mag, with a relatively steep attenuation law ($\delta = -0.12 \pm 0.30$) consistent within 1σ uncertainty with the starburst law of C00. The resulting amount of visual extinction is $A_\mathrm{V}^\mathrm{stars} = 0.86 \pm 0.35$ mag. Letting the UV bump amplitude vary between 0 and 6, as observed in MW sighlines, a significant bump is found with $E_\mathrm{b} = 3.6 \pm 1.7$. This detection is due to the flux drop observed in the i' band, the large uncertainty does not allow to tightly constrain the bump amplitude ($i' = 25.5 \pm 0.3$ mag). As the PDF of the bump amplitude is cut close to the peak of the PDF, we have performed the fit again by letting the bump amplitude to vary between 0 and 10 and it results in $E_\mathrm{b} = 5.3 \pm 2.6$ with a better defined PDF, while the χ^2 and estimations for the other output parameters remain unchanged. We also performed the fit without bump and the estimation of the SFR, $M_\star$ and $E(B-V)_\mathrm{s}$ remain unchanged while the slope of the attenuation curve becomes steeper with $\delta = -0.31 \pm 0.26$.

with a higher χ^2. A metallicity of $Z = 0.02$ returned a slightly higher χ^2 with similar values for the SFR, the stellar mass, δ and $A_\mathrm{V}^\mathrm{stars}$.

4.2.3. GRBH 080605

The Balmer lines are measured by Krühler et al. (2015), corresponding to a moderate attenuation with $E(B-V)_\mathrm{g} = 0.26^{+0.11}_{-0.10}$ mag and $A_\mathrm{V}^\mathrm{lines} = 0.8^{+0.31}_{-0.34}$ mag with an intense star formation: $\mathrm{SFR}_{\mathrm{H}_\alpha} = 47^{+17}_{-12}\,M_\odot\,\mathrm{yr}^{-1}$. From IRAC1 measurement, Perley et al. (2016) derive a stellar mass of $3.4 \times 10^{10}\,M_\odot$.

The best model is obtained for $Z = 0.02$ and shown in Fig. 6.

The SFR found equal to $44.9 \pm 22.9\,M_\odot\,\mathrm{yr}^{-1}$ is in very good agreement with the one measured with the H_α flux. A recent burst of star formation is found with an amplitude of $15 \pm 14\%$ of the total mass and an age of 75 ± 31 Myr. The stellar mass is $M_\star = 12.3 \pm 4.2 \times 10^9\,M_\odot$ a factor 2.8 lower than the one measured by Perley et al. (2016). We estimate a sSFR for this starbursting galaxy of $3.6\,\mathrm{Gyr}^{-1}$.

Dust attenuation is characterised by a colour excess $E(B-V)_\mathrm{s} = 0.09 \pm 0.05$ mag and a shallow attenuation curve consistent with C00 ($\delta = -0.08 \pm 0.38$). This results in a modest amount of visual extinction of $A_\mathrm{V}^\mathrm{stars} = 0.41 \pm 0.29$ mag. No evidence for a UV bump is found. A metallicity of $Z = 0.008$

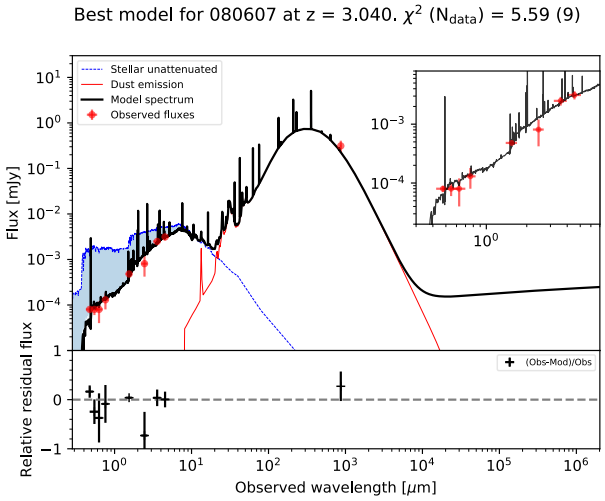

Fig. 7. Best-fitted SED for GRBH 080607. Colour and symbols convention as in Fig. 4.

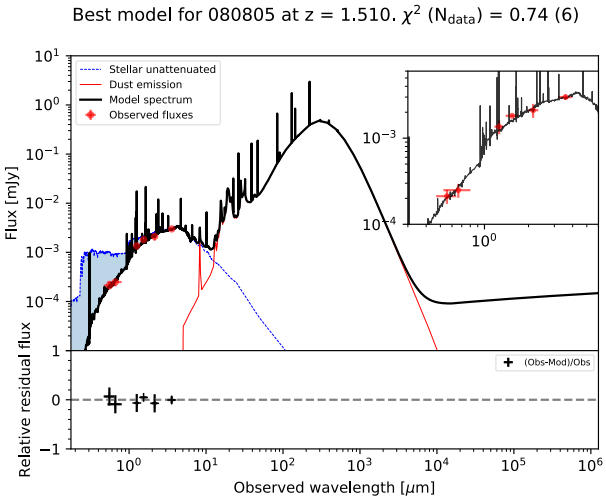

Fig. 8. Best-fitted SED for GRBH 080805. Colour and symbols convention as in Fig. 4.

returned a higher χ^2 with similar values for the SFR, the stellar mass, δ and A_V^{stars}.

4.2.4. GRBH 080607

The stellar mass is measured with IRAC1 data by Perley et al. (2016): $M_\star = 2.8 \times 10^{10}\,M_\odot$. No measure of the Balmer lines is available.

We adopted a solar metallicity ($Z = 0.02$) as measured for the host ISM from afterglow absorption-line observations (Prochaska et al. 2009). With only one measurement for the dust emission, we cannot run CIGALE with a free dust component. Instead we performed several runs varying the α parameter ($\alpha = 1$, 1.5 and 2), the quality of the fits are similar. Varying α changes the dust temperature and the position of the peak of the dust component. The IR luminosity, SFR, stellar mass and attenuation vary accordingly: L_{IR}, SFR, $M_\star$ and A_V^{stars} decrease from $\sim 7.2 \times 10^{11}\,L_\odot$, $\sim 70\,M_\odot\,yr^{-1}$, $\sim 3.4 \times 10^{10}\,M_\odot$ and ~ 2 mag to $\sim 1.9 \times 10^{11}\,L_\odot$, $\sim 20\,M_\odot\,yr^{-1}$, $\sim 2.1 \times 10^{10}\,M_\odot$ and ~ 1 mag when α increases from 1 to 2. As expected the stellar mass remains similar. Taking in mind this uncertainty we fix $\alpha = 1.5$, describing a galaxy extremely active in star formation. The best fit is shown in Fig. 7.

The stellar mass fraction due to the recent burst is $8 \pm 11\%$, consistent with no burst, consequently we decide to report the results without any recent burst. The total IR luminosity of the galaxy is $L_{IR} = 3.6 \pm 1.4 \times 10^{11}\,L_\odot$ with a SFR equal to $35.2 \pm 13.9\,M_\odot\,yr^{-1}$. The stellar mass, $M_\star = 2.75 \pm 0.8 \times 10^{10}\,M_\odot$ is in very good agreement with the one measured by Perley et al. (2016). The sSFR is equal to $1.3\,Gyr^{-1}$. The dust attenuation is characterised by a colour excess of $E(B-V)_s = 0.31 \pm 0.04$ mag and a flat attenuation curve ($\delta = 0.05 \pm 0.10$) consistent with C00. The resulting amount of visual extinction is $A_V^{stars} = 1.39 \pm 0.29$ mag.

The fit with a recent burst gives a slightly higher SFR of $49.7 \pm 14\,M_\odot\,yr^{-1}$, a slightly lower stellar mass, $M_\star = 2.3 \pm 1 \times 10^{10}\,M_\odot$, and similar colour excess and slope for the dust attenuation.

4.2.5. GRBH 080805

The Balmer lines are measured by Krühler et al. (2015). They derive a high colour excess although with a large uncertainty, $E(B-V)_g = 0.78^{+0.39}_{-0.31}$ mag corresponding to an attenuation A_V^{lines} of $2.4^{+1.2}_{-0.9}$ mag, and a highly uncertain star formation rate, $SFR_{H_\alpha} = 45^{+79}_{-26}\,M_\odot\,yr^{-1}$. The stellar mass derived from IRAC1 measurement by Perley et al. (2016) is $M_\star = 7.2 \times 10^9\,M_\odot$.

The best model is obtained for $Z = 0.02$ and shown in Fig. 8. The SFR is found equal to $20.6 \pm 12\,M_\odot\,yr^{-1}$ is in agreement with the one measured with the H_α flux within errorbars. A burst of star formation is found with an amplitude of $22 \pm 16\%$ of the total mass and an age of 60 ± 33 Myr. The stellar mass is $M_\star = 3.4 \pm 1.7 \times 10^9\,M_\odot$. We estimate a sSFR for this galaxy of $6\,Gyr^{-1}$. The dust attenuation is characterised by a colour excess $E(B-V)_s = 0.37 \pm 0.07$ mag and a steep attenuation curve, similar to that of the SMC ($\delta = -0.45 \pm 0.24$). This results in an amount of visual extinction of $A_V^{stars} = 1.06 \pm 0.34$ mag. No evidence for a UV bump is found. A metallicity of $Z = 0.008$ returns a worse χ^2 with similar values for the SFR and stellar mass but different values for the dust attenuation: δ (-0.19 ± 0.23) and A_V^{stars} (1.38 ± 0.47 mag).

In order to improve the agreement between the SFR found from the SED and from H_α measurements, we checked whether the presence of a very young starburst could enhance the current star formation rate. We ran again CIGALE with a recent burst taking place within the last 10–20 Myr. The SFR increases to $48.2 \pm 29.9\,M_\odot\,yr^{-1}$, in very good agreement with the H_α measurements. The burst of star formation is found with an amplitude of $22 \pm 16\%$ of the total mass and an age of 15 ± 4 Myr. As expected, the stellar mass is reduced to $M_\star = 2.9 \pm 1.6 \times 10^9\,M_\odot$. The attenuation curve becomes shallower, but still steeper than the one of C00, with $\delta = -0.25 \pm 0.24$ and the amount of attenuation in the optical increases to $A_V^{stars} = 1.53 \pm 0.5$ mag. This indirect use of the H_α emission line indicates that a very recent episode of star formation can explain the measured SFR_{H_α}. In a future work, taking into account the emission lines in the fit would allow to probe star formation at timescales lower than 20 Myr. We retain the result with a burst age older than 20 Myr as the reference.

4.2.6. GRBH 100814A

The Balmer lines are measured by Krühler et al. (2015), they derive a colour excess of $E(B-V)_g = 0.08^{+0.26}_{-0.08}$ mag corresponding to an attenuation of $A_V^{lines} = 0.24^{+0.8}_{-0.24}$ mag, and the lowest SFR

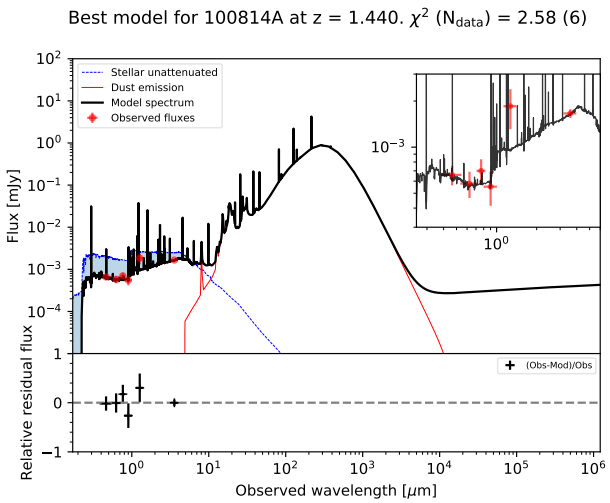

Fig. 9. Best-fitted SED for GRBH 100814A. Colour and symbols convention as in Fig. 4.

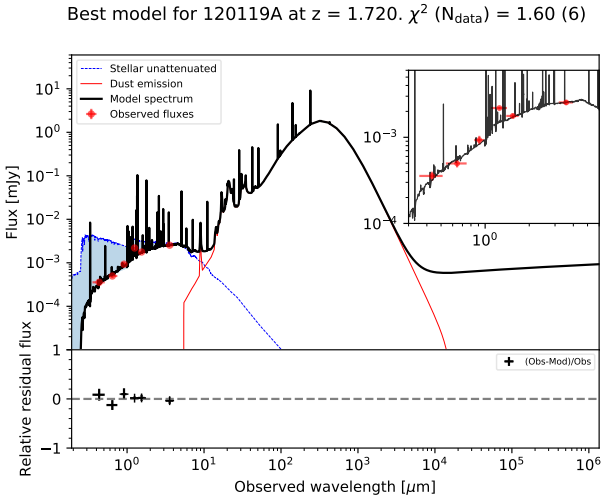

Fig. 10. Best-fitted SED for GRBH 120119A. Colour and symbols convention as in Fig. 4.

of our sample with $\mathrm{SFR}_{\mathrm{H}_\alpha} = 3.2^{+2.9}_{-0.7}\,M_\odot\,\mathrm{yr}^{-1}$. The stellar mass measured from the IRAC1 measurement in Perley et al. (2016) is $M_\star = 3.3 \times 10^9\,M_\odot$.

The best model is obtained for $Z = 0.008$ and shown in Fig. 9. No recent burst of star formation is added to the SFH. The SFR is equal to $4 \pm 2.3\,M_\odot\,\mathrm{yr}^{-1}$ which is in good agreement with the one measured with the H_α flux. The stellar mass is $M_\star = 2.9 \pm 0.8 \times 10^9\,M_\odot$ in agreement with the one measured by Perley et al. (2016). We estimate a sSFR of $1.4\,\mathrm{Gyr}^{-1}$.

The dust attenuation is characterised by a colour excess $E(B-V)_\mathrm{s} = 0.05 \pm 0.04$ mag and a flat attenuation curve ($\delta = 0.09 \pm 0.51$). This results in an amount of visual extinction of $A_\mathrm{V}^\mathrm{stars} = 0.35 \pm 0.4$ mag. No evidence for a UV bump is found. A metallicity of $Z = 0.02$ returned an equivalently good fit with very similar values for the SFR, the stellar mass, δ and $A_\mathrm{V}^\mathrm{stars}$. A recent burst in the SFH leads to an SFR estimation of $17.2 \pm 14.2\,M_\odot\,\mathrm{yr}^{-1}$ and a colour excess of 0.16 ± 0.07 mag which are not in agreement with the $\mathrm{SFR}_{\mathrm{H}_\alpha}$ and the colour excess derived from the Balmer lines Krühler et al. (2015). For this reason, we keep the results without any recent burst in the SFH as the reference.

4.2.7. GRBH 120119A

The Balmer lines are measured by Krühler et al. (2015), they derive a colour excess for the emission lines of $E(B-V)_\mathrm{g} = 0.35^{+0.16}_{-0.14}$ mag corresponding to a visual attenuation of $A_\mathrm{V}^\mathrm{lines} = 1.07^{+0.49}_{-0.43}$ mag, and a $\mathrm{SFR}_{\mathrm{H}_\alpha}$ of $43^{+24}_{-14}\,M_\odot\,\mathrm{yr}^{-1}$. The stellar mass measured from the IRAC1 measurement in Perley et al. (2016) is $8 \times 10^9\,M_\odot$.

The best model is obtained for $Z = 0.008$ and shown in Fig. 10. The SFR is found equal to $25.5 \pm 14.1\,M_\odot\mathrm{yr}^{-1}$ marginally consistent with the one measured with the H_α flux. A burst of star formation is found with an amplitude of $23 \pm 15\%$ of the total mass and an age of 64 ± 33 Myr. The stellar mass is $M_\star = 3.8 \pm 1.2 \times 10^9\,M_\odot$ a factor of 2.1 lower than the one measured by Perley et al. (2016). We estimate a sSFR for this starbursting galaxy of $6.7\,\mathrm{Gyr}^{-1}$. The dust attenuation is characterised by a colour excess $E(B-V)_\mathrm{s} = 0.24 \pm 0.06$ mag and a attenuation curve steeper than the one of C00 ($\delta = -0.39 \pm 0.22$). This results in an amount of visual extinction of $A_\mathrm{V}^\mathrm{stars} = 0.74 \pm 0.28$ mag. No evidence for a UV bump is found. A metallicity of 0.02 returned a slightly worse χ^2 with similar values for the SFR, stellar mass, δ and $A_\mathrm{V}^\mathrm{stars}$.

As for GRBH 080805, in order to improve the agreement between the SFR found from the SED and from H_α measurements, we checked whether the presence of a very young starburst could enhance the current star formation rate. We ran again CIGALE with a recent burst taking place within the last 10–20 Myr. The resulting fit is slightly better with a lower χ^2. The SFR increases to $44.4 \pm 26.6\,M_\odot\,\mathrm{yr}^{-1}$, in very good agreement with the H_α measurements. The burst of star formation is found with an amplitude of $16 \pm 15\%$ of the total mass and an age of 15 ± 4 Myr. The stellar mass is only reduced to $M_\star = 3.6 \pm 1.4 \times 10^9\,M_\odot$. The attenuation curve becomes shallower with $\delta = -0.29 \pm 0.24$. The amount of attenuation is $A_\mathrm{V}^\mathrm{stars} = 0.95 \pm 0.39$ mag. We keep the result with a burst age older than 20 Myr as the reference.

4.3. Star formation activity and SFR-$M_\star$ comparison

The results of the SED fitting are reported in Table 3. The scenario with a recent burst on top of a delayed star formation history is favoured over a delayed only SFH for five of our seven GRB host galaxies. Generally, our stellar mass estimates are lower than in Perley et al. (2016) where stellar masses are derived from the IRAC 3.6 μm luminosities using a continuous SFH. In order to check whether this difference is due to the SED fitting algorithm or to the adopted SFH we perform our fits with a constant SFR over 1–3.5 Gyr similarly to the method in Perley et al. (2016). However, we are using all the photometry data and not only the IRAC1 detection, and the stellar population age was fixed according to the stellar mass in Perley et al. (2016) which is not the case in our method. In the right panel of Fig. 11 we compare the SFR derived with a continuous SFH and our results to the $\mathrm{SFR}_{\mathrm{H}_\alpha}$ derived in Krühler et al. (2015). The continuous SFH leads to lower SFR estimates that are not consistent with the $\mathrm{SFR}_{\mathrm{H}_\alpha}$ except for GRBHs 080607 and 100814A where a recent burst is not required. On the contrary, the SFRs we derive with the delayed or delayed + burst SFH are always found in agreement with the $\mathrm{SFR}_{\mathrm{H}_\alpha}$. As shown in the left panel of Fig. 11, the assumption of a constant SFR also impacts the mass measurements and our stellar mass estimates are lower (up to a factor three) than the ones in Perley et al. (2016) except for GRBHs 080607 and 100814A. The fact that we include all observations instead of just the IRAC1 measurement might partly

Table 3. Results of the SED fitting.

Ident GRBH	z	SFR $M_\odot\,\mathrm{yr}^{-1}$	$M_\star$ $10^9\,M_\odot$	A_V^{stars} mag	$\frac{E(B-V)_s}{E(B-V)_g}$	δ slope	sSFR Gyr^{-1}	Recent burst y/n
061121	1.31	62.0 ± 25.7	6.9 ± 2.4	0.88 ± 0.30	0.28	0.22 ± 0.2	9.0 ± 4.9	y
070802	2.45	32.2 ± 17.8	3.7 ± 1.6	0.86 ± 0.35	0.71	-0.12 ± 0.30	8.7 ± 6.1	y
080605	1.64	44.9 ± 22.9	12.3 ± 4.2	0.41 ± 0.29	0.35	-0.08 ± 0.38	3.6 ± 2.2	y
080607	3.04	35.2 ± 13.9	27.5 ± 8.2	1.39 ± 0.29	–	0.05 ± 0.10	1.3 ± 0.6	n
080805	1.5	20.6 ± 12	3.4 ± 1.7	1.06 ± 0.34	0.47	-0.45 ± 0.24	6.1 ± 4.6	y
100814A	1.44	4 ± 2.3	2.9 ± 0.8	0.35 ± 0.4	0.6	0.09 ± 0.51	1.4 ± 0.9	n
120119A	1.73	25.5 ± 14.1	3.8 ± 1.2	0.74 ± 0.28	0.68	-0.39 ± 0.22	6.7 ± 4.3	y

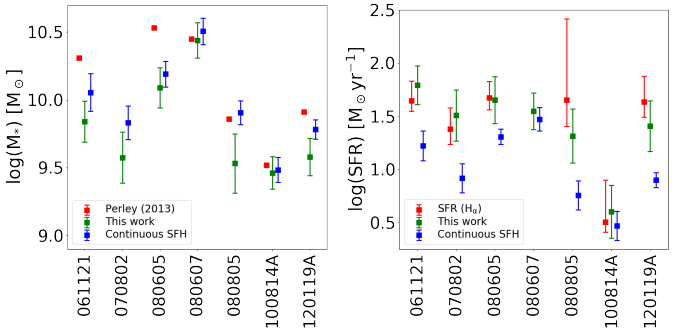

Fig. 11. *Left*: stellar masses estimated from: IRAC1 measurement in Perley et al. (2016, red), this work with either a delayed or delayed + burst SFH (green), CIGALE using same configuration as in Table 2 but with a continuous SFH with a main stellar population age between 1 and 3.5 Gyr (blue). *Right*: SFR estimated from: H_α measurement from Krühler et al. (2015) and Vergani et al. (2017, red) this work using either a delayed or delayed + burst SFH (green), CIGALE using same configuration as in Table 2 but with a continuous SFH with a main stellar population age between 1 and 3.5 Gyr (blue).

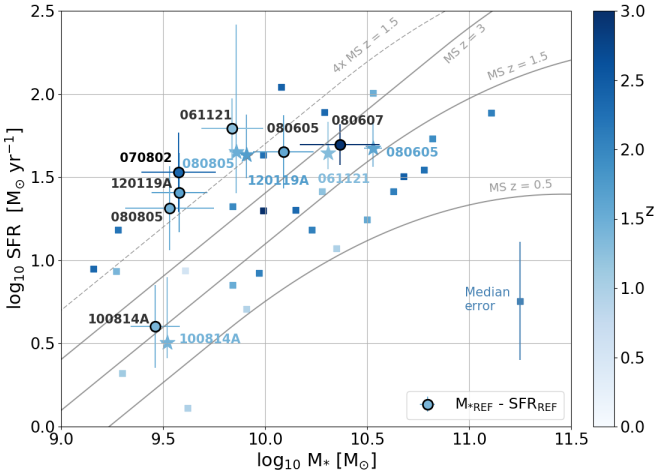

Fig. 12. SFR-stellar mass relation. Blue points represent stellar masses from Perley et al. (2016) and SFR from Krühler et al. (2015) where we highlighted the GRBHs in our sample using a star symbol and the corresponding name. The colour map encodes the redshift. The black circles with blue interiors correspond to the GRBHs of our sample with SFR and stellar masses derived from the SED fitting. The grey lines represent the main sequence relation from Schreiber et al. (2015), the dashed line is four times the main sequence at $z = 1.5$ representative of starbursting galaxies (most of our our GRBHs are at $z \sim 1.5$).

explain the observed difference in some cases. In all cases the fits return a worse χ^2 with a continuous SFH compared to delayed or delayed + burst SFH. We conclude that the discrepancy on the stellar mass estimation is mainly explained by the introduction of a strong and recent burst.

Figure 12 represents the main sequence of all GRBHs having a stellar mass estimation in Perley et al. (2016) and a SFR_{H_α} in Krühler et al. (2015). The main sequence of star-forming galaxies for $z = 0.5$, 1.5 and 3, covering the GRBH redshifts, are represented using the relation from Schreiber et al. (2015). For the four GRBHs (061121, 080605, 080805, 120119A) with a delayed + burst SFH, our lower stellar mass estimates shift the galaxies to the starbursts domain we define as four times the main sequence. These objects are dusty starbursting hosts and we do not expect such a strong effect for all GRB host galaxies, as illustrated by GRBH 100814A. Comparing our results with Krühler et al. (2011), we find that our SFR estimations are consistent within errorbars for the 4 galaxies we have in common. We derive higher stellar mass for GRBH 080605 and GRBH 080607. They were limited to optical/NIR data up to the *Ks* band, which explained the difference with our stellar mass estimation as we have a better NIR coverage. The old stellar population contributes significantly to the total stellar mass and dominates the NIR stellar emission, so the use of IRAC1 (and IRAC2 for GRBH 080607) detections allows a more reliable stellar mass estimation.

Given the importance of the stellar mass estimation in the evidence of a mild metallicity threshold (Vergani et al. 2015, 2017; Japelj et al. 2016) necessary to form long GRB (LGRB), it would be of interest to revisit GRBH stellar masses estimation on a larger sample. LGRB hosts also offer the opportunity to identify and study distant low mass ($\sim 10^8$–$10^{10}\,M_\odot$) starbursting galaxies generally absent or badly represented in blind surveys.

5. Dust attenuation in GRBHs

In this section, we first characterise the attenuation curves we derived for the seven GRBHs of the Golden sample. Then we study the characteristics of the dust attenuation as a function of GRBH properties (the stellar mass, SFR, sSFR, and A_V^{stars}). We compare the attenuation curves derived from the SED fitting with the extinction curves along the GRB l.o.s. and finally compare these results to radiative transfer simulations to constrain dust-stars geometry in the ISM of these GRBHs.

5.1. Measure of the attenuation curve slopes

The dust attenuation is described using Eq. (6) where the colour excess, $E(B-V)_s$, and the attenuation slope, δ, are

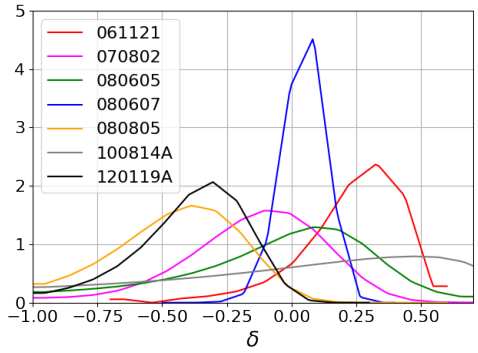

Fig. 13. Probability density functions of the attenuation slope for the GRBHs.

free parameters. The probability density functions obtained with CIGALE for the attenuation slope of each GRBH are shown in Fig. 13. They are well defined with the exception of GRBH 100814A whose PDF is too flat due to the low amount of dust within the host galaxy characterised by a colour excess of $E(B-V)_g = 0.08^{+0.26}_{-0.08}$ mag for the emission lines (Krühler et al. 2015) and $E(B-V)_s = 0.048^{+0.04}_{-0.04}$ mag for the stellar continuum. Therefore we will not consider this galaxy in the following.

There are a great variety of slopes with GRBH 070802, GRBH 080605 and GRBH 080607 similar to the Calzetti attenuation law defined by $\delta = 0$. The attenuation curve of GRBH 061121 is flatter than C00. GRBH 080805 and GRBH 120119A have an attenuation curve slope as steep as the mean SMC extinction curve, corresponding to $\delta \sim -0.5$.

5.2. Variation of the slope with GRB host properties

Figure 14 represents the variation of the attenuation curve slope, δ, with some physical properties of the GRBH. We only have seven GRBHs in the sample so the conclusions are statistically limited. In the first panel representing the evolution of δ with A_V^{stars}, although no obvious trend is seen with a visual inspection of the plot, the orthogonal distance regression shows a trend with highly attenuated galaxies having flatter attenuation curves. This trend has already been observed for galaxies at $z = 1.5-3$ (Salmon et al. 2016) and for galaxies at $0.5 < z < 2$ (Kriek & Conroy 2013). Radiative transfer simulations (i.e. Witt & Gordon 2000; Chevallard et al. 2013) also predict a steeper dust attenuation curves at small attenuation optical depths, and shallow attenuation curve at larger optical depths. In the second panel, representing the variation of δ with the stellar mass, a clear trend is seen with lower (higher) stellar masses correlating with steeper (shallower) attenuation curves. This is also in agreement with the work of Salmon et al. (2016) where the more massive galaxies in their spectroscopic redshift sample tend to prefer "starbust" (i.e. shallow) dust attenuation curves and less massive galaxies the SMC92 (i.e. steep) dust attenuation curves.

The third panel represents the variation of δ with the SFR and a clear trend is seen: GRBH with low (high) SFR have steeper (shallower) attenuation curves.

The bottom panel represents the evolution of δ with the sSFR and again although no trend can be seen with a visual inspection, the orthogonal distance regression shows that steep (shallow) attenuation curves are found in the more (less) active GRBHs. However the large uncertainties make this trend very uncertain. This result contradicts the results in Kriek & Conroy (2013) which show that high H_α equivalent widths (i.e. high sSFRs) correlate with flat attenuation curves.

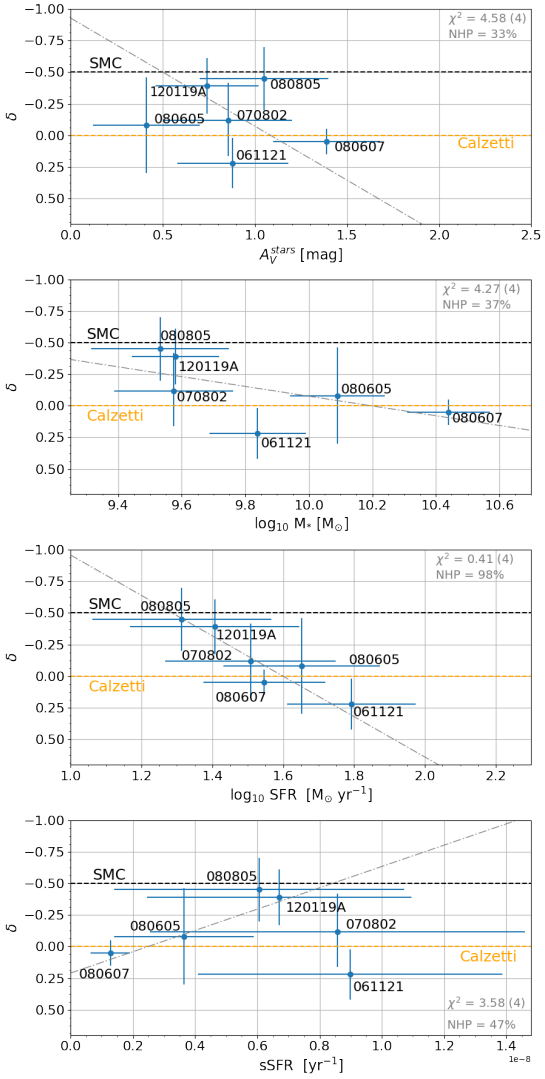

Fig. 14. *Top*: attenuation curve slope as a function of the SED continuum amount of attenuation. *Middle top*: attenuation curve slope versus the stellar mass. *Middle bottom*: attenuation curve slope versus the SFR. *Bottom*: attenuation curve slope versus the specific SFR. The blue points correspond to the quantities derived with CIGALE. The black dashed line represents the slope of the mean SMC extinction curve and the yellow dashed line the slope of the Calzetti law. The grey dash-dotted line illustrates the best fit using an orthogonal distance regression (using SciPy's scipy.odr). The χ^2, number of degrees of freedom and Null Hypothesis Probability (NHP) of these fits are indicated.

5.3. Global dust attenuation and dust extinction along GRB l.o.s.

Top panel of Fig. 15 represents the evolution of the amount of dust extinction along the GRB l.o.s. as a function of the amount of dust attenuation averaged over the whole GRBH. We see that they are correlated and GRB l.o.s. are dustier than the average attenuation of the host galaxy. The orthogonal distance regression returns the relation $A_V^{stars} = (0.71 \pm 0.11) \times A_V^{grb}$ for our sample. The LGRB progenitors are expected to be a result of the collapse of young massive stars and thus they should suffer more attenuation than the more evolved stellar popula-

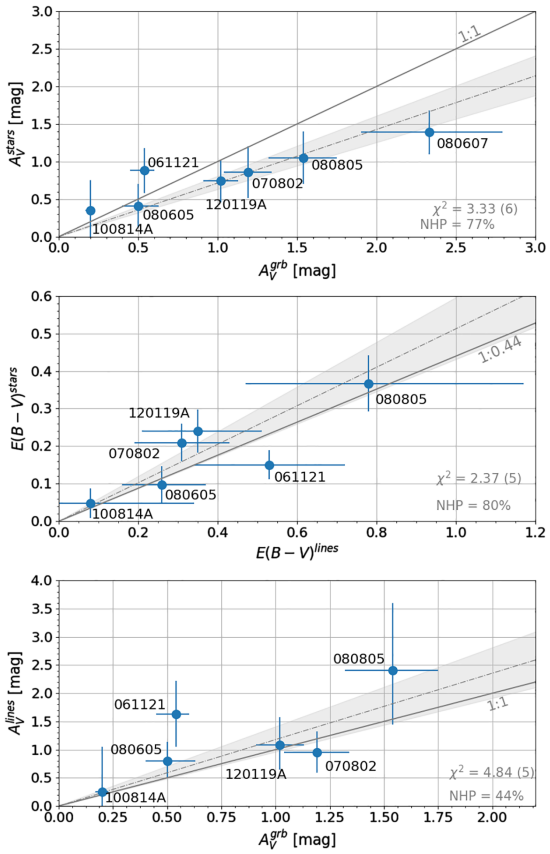

Fig. 15. *Top*: amount of global attenuation in the GRBH in the V band as a function of the amount of extinction in the V band along the GRB l.o.s. *Middle*: colour excess for the stellar continuum as a function of the colour excess for the Balmer lines. The grey line represents the C00 relation. *Bottom*: amount of attenuation of the Balmer lines in the V band as a function as the amount of extinction in the V band along the GRB l.o.s. For all panels the grey dash-dotted line represents the best fit using an orthogonal distance regression (using SciPy's scipy.odr) and the grey shaded area its 1σ uncertainty. The χ^2, number of degrees of freedom and Null Hypothesis Probability (NHP) of these fist are indicated.

tion which had enough time to migrate outside their birth clouds (e.g. C00, Charlot & Fall 2000; Granato et al. 2000). On a larger sample of 23 GRBHs selected with the criteria of having an obscured GRB l.o.s. ($A_V^{grb} > 1$ mag), Perley et al. (2013) find a similar trend: $A_V^{stars} \lesssim A_V^{grb}$. However for $A_V^{grb} < 1$ mag, corresponding to less massive galaxies they find the opposite trend although dispersion is large. The middle panel of Fig. 15 represents the evolution of the colour excess for the stellar continuum as a function of the colour excess for the Balmer lines. For our sample, we have $E(B-V)_s = (0.51 \pm 0.08) \times E(B-V)_g$, which is in agreement with C00. The bottom panel of Fig. 15 represents the amount of attenuation for nebular lines in the V band as a function of the amount of extinction along the GRB l.o.s. The orthogonal distance regression returns: $A_V^{lines} = (1.18 \pm 0.22) \times A_V^{grb}$ which is consistent with the 1:1 relation within 1σ uncertainty, meaning that the GRB and HII regions suffer a similar attenuation.

5.4. Comparison of extinction and attenuation curves

The attenuation curves derived by the SED fitting are compared to the extinction curves along GRB l.o.s. on Fig. 16. There is a great variety of cases that can be sorted into three categories. Category A, in which the attenuation curve is shallower than the extinction curve (061121 and 080605), category B, in which both attenuation and extinction curves are similar (080607, 070802, 120119A), and category C, in which the attenuation curve is steeper than the extinction curve (080805). The attenuation curves of 061121, 080605, and 080607 are consistent with the Calzetti law, those of 070802, 080805, and 120119A are not. We note than the better constrained attenuation curves are those with radio (GRBH 061121) and sub-millimeter (GRBH 080607) detections.

5.4.1. General shape

Category A corresponds to the case with a flat attenuation curve and a steeper extinction curve. A far-UV rise in the extinction curve indicates the presence of small silicate grains and the UV bump the presence of PAHs or small carbonaceous grains. A shallow attenuation curve is usually obtained for high optical depth (Witt & Gordon 2000; Seon & Draine 2016), highly inclined galaxies (Pierini et al. 2004; Inoue 2005), a high density environment (Inoue 2005) or a clumpy ISM (Witt & Gordon 2000; Seon & Draine 2016).

Category B corresponds to similar attenuation and extinction curves. At low optical depth an ISM in which dust and stars are uniformly mixed or stars surrounded by dust (shell geometry) with homogeneous and clumpy local dust distribution can reproduce an attenuation curve with a similar slope as the extinction curve, even as steep as the SMC extinction curve (Witt & Gordon 2000). At higher optical depth only the shell geometry with an homogeneous dust distribution is able to produce such a steep attenuation curve from SMC dust type (Witt & Gordon 2000).

The case of GRB/GRBH 080607 is interesting because it has the highest redshift in our sample and the extinction curve is unusually flat. This may be due either to variations of dust properties and/or geometry in the ISM. The geometrical effect is supported by the detection of a molecular cloud in the afterglow spectrum at >100 pc from the GRB, probably arising in a neighboring star-forming region (Prochaska et al. 2009). Another possible explanation of the flat extinction curve is due to the dust composition: in the earliest evolutionary stage of dust evolution the dust content is dominated by large grains originated from stellar sources which results in a flat extinction curve ($\lesssim$1 Gyr). Later on, the abundance of small grains increases through shattering and accretion processes which results in the progressive apparition of a 2175 Å bump and a steeper extinction curve (Asano et al. 2013, 2014). This explanation can be supported by the redshift of GRBH 08607 of $z = 3.04$ which corresponds to an age of the Universe of about 2.1 Gyr adopting the ΛCDM cosmology of Planck Collaboration XIII (2016). The rather high value of $R_V \sim 4$ measured from the extinction curve is also indicative of a large grain size distribution though the uncertainty is quite large (Prochaska et al. 2009; Zafar et al. 2011). The forthcoming SVOM mission might potentially bring more data to constrain the dust evolution processes at high redshift.

Category C corresponds to an attenuation curve steeper than the extinction curve. A steep attenuation curve can be the result of a low optical depth (Witt & Gordon 2000; Seon & Draine 2016) for example in a face-on galaxy. It may also result from an age-dependent attenuation where the young stellar population is embedded in dense clouds and more attenuated than the old stellar population which had time to migrate to the more diffuse ISM (e.g. Inoue 2005).

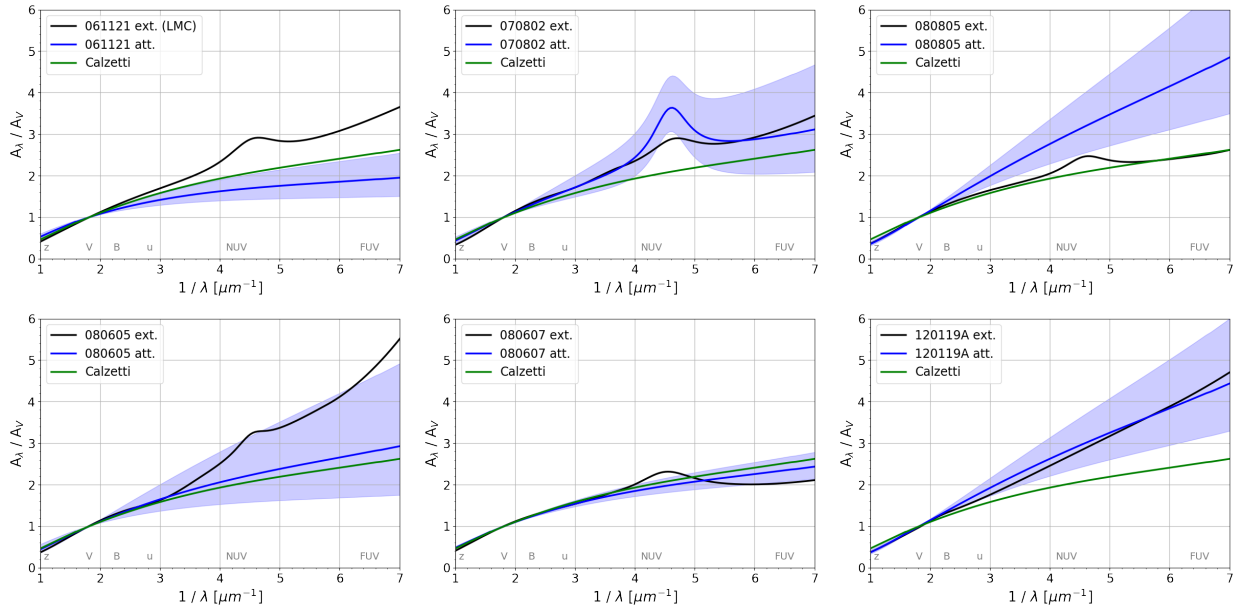

Fig. 16. *Top*: GRBH 061121, GRBH 070802 and GRBH 080805, *bottom*: GRBH 080605, GRBH 080607 and GRBH 120119. The solid black line is the extinction curve normalised to A_V^{grb}, the blue one is the attenuation curve normalised to A_V^{stars} and the green one is the normalised Calzetti law. The blue shaded area represents the 1σ uncertainty on the attenuation curve.

Table 4. Summary of the comparison with radiative transfer model of Seon & Draine (2016).

	Dust model	ISM structure
061121	WD-LMC	Dusty + Very clumpy
070802	WD-LMC	Dusty + Very clumpy
080605	WD-LMC	Dusty + Very clumpy
080607	WD-MW	Shell + Clumpy
080805	WD-MW	Dusty + Homogeneous or Shell + Clumpy
120119A	WG-SMC	Dusty + Homogeneous or Shell + Clumpy

5.4.2. Presence of the UV bump in the attenuation curves

For many years, there has been a debate whether a Calzetti-like attenuation curve can ever arise if the underlying extinction curve exhibits a UV bump. While the works of Gordon et al. (1997), Witt & Gordon (2000) and Pierini et al. (2004) suggested that a Calzetti-like attenuation law implies a bump-free extinction curve, for example, a SMC-like law, Silva et al. (1998) and Granato et al. (2000) could reproduce a Calzetti-like attenuation law with an underlying MW extinction curve. In our sample of GRB extinction curves, five out of six exhibit a UV bump with four spectroscopically confirmed detections. The presence or lack of a UV bump in the attenuation curves should provide valuable information.

The UV bump is best constrained using spectroscopic measurements of galaxies (e.g. Noll et al. 2007) but intermediate filter bands also allow to constrain the bump amplitude (e.g. Buat et al. 2011; Kriek & Conroy 2013). However, this is very difficult using broad filter bands only as it relies only on one filter band overlapping the UV bump with a passband width higher than the bump width. In our sample, GRBHs 061121, 070802, 080605, 080805 and 120119A have a filter band which overlaps the UV bump. The rest-frame spectral coverage of each GRBH observation can be seen in Appendix C. For GRBH 070802, we already reported a bump amplitude of $E_b = 5.3 \pm 2.6$ in Sect. 4.2.2. For the other GRBHs, we already ran CIGALE with the same configuration as described in Sect. 4.1 with a varying UV bump amplitude ($E_b > 0$) and did not find clear evidence of its presence. The PDFs of the UV bump amplitude exhibit a simple power law shape with the highest probability associated to an amplitude of zero and a decreasing probability as the amplitude increases. Given the rather weak UV bump amplitudes measured in the extinction curves, we run CIGALE again letting the UV bump amplitude vary from −2 to 2 this time, similarly as in Buat et al. (2012), in order to obtain better defined PDFs for a more reliable Bayesian estimation of the UV bump amplitude if PDFs are centred around zero. The results are reported in Table 5, all UV bump amplitudes are compatible with zero within 1σ uncertainty. The estimation of the other parameters remain unchanged. We conclude that we do not find evidence of a UV bump with the possible exception of GRBH 070802, but we can not exclude the presence of a weak UV bump in the attenuation curves. Further observations using spectroscopy or intermediate filter bands are required in order to have a better constraint.

5.5. Comparison with radiative transfer simulations

To investigate the ISM geometry, we compared the derived attenuation curves with CIGALE with the results of the recent radiative transfer code developed by Seon & Draine (2016). This model offers the possibility to choose between three

Table 5. Constraints on the UV bump amplitude when allowed to vary between −2 and 2 in the CIGALE run.

GRBH	Filter band overlapping UV bump	$E_{\rm b,ext.} = c_3/\gamma^2$	$E_{\rm b,att.}$
070802	Yes	1.49 ± 0.30	5.3 ± 2.6
080605	Yes	1.19 ± 0.39	-0.26 ± 1.12
080607	No	2.05 ± 0.48	–
080805	Yes	1.33 ± 0.70	-0.16 ± 1.14
120119A	Yes	None	0.69 ± 0.97
061121[a]	Yes	No spectro.	0.03 ± 0.96

Notes. [(a)] GRB 061121 is the only afterglow for which the extinction curve is derived with photometric data only.

theoretical dust models adopted from Weingartner & Draine (2001) and Draine (2003) for the MW, LMC, and SMC-bar, and two empirical models for the MW and SMC from Witt & Gordon (2000). The former dust models are noted WD-MW, WD-LMC and WD-SMC and the later WG-LMC and WG-SMC.

We selected the dust model according to the GRB extinction curves (cf. Table 4). Following Schady et al. (2012) GRB 061121 is best fitted with a LMC-like extinction curve[3]. The extinction curve of GRB 070802 is very similar to the mean LMC2 super shell extinction curve (Gordon et al. 2003) so we choose a LMC dust model. The far-UV rise of the extinction curve of GRB 080605 is similar to an SMC extinction curve, however due to the spectroscopically confirmed detection of a UV bump, we chose an LMC dust model. For GRB 080607 and GRB 080805 due to the flat FUV part and the presence of a UV bump, we select a MW dust model. For GRB 120119A, we choose an SMC-like dust model according to Zafar et al. (2018). For SMC and MW like extinction curves both theoretical and empirical dust models are tested and we kept the one reproducing the best the attenuation curve derived with CIGALE.

The attenuation curves computed with the radiative transfer model of Seon & Draine (2016) are defined with three parameters: $\tau_{\rm V}$, $R_{\rm s}/R_{\rm d}$ and $M_{\rm s}$. $\tau_{\rm V}$ is the optical depth in V band and take discrete values between 0.1 and 20. $R_{\rm s}/R_{\rm d}$ corresponds to the ratio of the distribution radius of stars and dust respectively, it takes discrete values between 0 and 1. $R_{\rm s}/R_{\rm d} = 0$ corresponds to a compact OB association surrounded by a cloud and $R_{\rm s}/R_{\rm d} = 1$ corresponds to the uniform distribution of photon sources over the spherical dusty medium (similar to the "DUSTY" configuration of Witt & Gordon 2000). To qualitatively assess our results we followed a formalism similar to the one of Witt & Gordon (2000) by referring to a Dusty ISM for $R_{\rm s}/R_{\rm d} \geq 0.8$ when stars are approximately uniformly distributed with dust and to a Shell ISM for $R_{\rm s}/R_{\rm d} \leq 0.5$ with the stars surrounded by a dust cloud. $M_{\rm s}$ is the Mach number governing the variance of the ISM density field , in other words, quantifying the clumpiness of the ISM. It takes discrete values between 0 and 20. $M_{\rm s} = 0$ corresponds to a homogeneous ISM and $M_{\rm s} = 20$ to a very clumpy ISM. In the following, we will refer to a homogeneous ISM for $M_{\rm s} \leq 3$, to a Clumpy ISM for $4 \leq M_{\rm s} \leq 15$ and to a Very Clumpy ISM for $M_{\rm s} \geq 15$.

We compared the attenuation curves derived with CIGALE to the attenuation curves computed with the radiative transfer model for the different values of $\tau_{\rm V}$, $R_{\rm s}/R_{\rm d}$, $M_{\rm s}$. For each attenuation curve derived with CIGALE, a χ^2 grid is then built using

$$\chi^2(\tau_{\rm V}, \frac{R_{\rm s}}{R_{\rm d}}, M_{\rm s}) = \sum_{i=1}^{N_{\rm data}} \left(\frac{A^{\rm RT}_{\lambda,i} - A^{\rm SED}_{\lambda,i}}{\sigma^{\rm SED}_i} \right)^2 \quad (8)$$

with $A^{\rm RT}_{\lambda,i}$ the amount of attenuation from the radiative transfer model of Seon & Draine (2016), $A^{\rm SED}_{\lambda,i}$ and $\sigma^{\rm SED}_i$ the amount of attenuation and its 1σ uncertainty derived with CIGALE. These quantities are evaluated at the $N_{\rm data}$ wavelengths used by Seon & Draine (2016) and covering the GRB hosts observations.

From the χ^2 grid, we compute the PDF of each parameter by marginalising the PDF over the two other parameters. The PDFs are shown in Fig. 17 and the results are summarised in Table 4. The cases of GRBH 061121, 070802, 080605 are similar with a low optical depth and high values for $R_{\rm s}/R_{\rm d}$ and $M_{\rm s}$ indicating that a Dusty and Very clumpy ISM best reproduces the attenuation curves derived with CIGALE. Simulations with $R_{\rm s}/R_{\rm d} > 1$ are not provided in the publicly available simulations of Seon & Draine (2016)[4]. It would be interesting to perform radiation transfer simulations with values of $R_{\rm s}/R_{\rm d}$ higher than 1 as in the work of Witt & Gordon (2000) where the *CLOUDY* configuration has $R_{\rm s}/R_{\rm d} \sim 1.45$. For GRBH 080607, the $R_{\rm s}/R_{\rm d}$ PDF peaks at ∼0.5 and the $M_{\rm s}$ PDF disfavours a homogeneous ISM comparing to a Clumpy or even Very clumpy ISM. For GRBH 080805 and 120119A, both having steep attenuation curves, a bimodal solution is found with either a Dusty-homogeneous ISM or a Shell-Clumpy ISM. The attenuation curves computed with the radiative transfer model best fitting the attenuation curves derived with CIGALE are represented in Fig. C.1. All attenuation curves computed with the radiative transfer model with a LMC or MW dust grain type that best fit the CIGALE attenuation curves exhibit a UV bump but the uncertainty associated to the CIGALE attenuation curves does not allow to constrain them.

6. Conclusion

We have selected 30 GRBs with a rest-frame coverage from UV to optical and find that the type of GRB extinction curves and the amount of extinction along the GRB l.o.s. correlate with the host galaxies properties with the more extinguished GRBs preferentially found in the more massive hosts. The UV bump is also preferentially found in the most extinguished GRB l.o.s. It follows that without a rapid follow-up there is an observational bias towards SMC-like extinction curves for GRBs. This correlation presumably indicates that the GRB afterglow probes along its l.o.s. not only the dust in the vicinity of the burst but also the dust located at large distances to be representative enough of the host galaxy.

From these 30 GRBs we have selected seven host galaxies whose SEDs have photometric measurements of the UV rest-frame emission and a UV-to-NIR spectrum reasonably well sampled (with at least six bands). The results of our SED fitting show that a recent burst of star formation is required for five out of seven GRBHs to recover the SFR measured from H_α flux. This leads to a lower estimate of the stellar masses than the ones derived in Perley et al. (2016) using a mass-to-light relation with the IRAC 3.6 μm luminosities. Consequently these GRBHs are shifted to the starburst domain, defined as four times the star-forming main sequence. For these relatively dusty GRBHs, we

[3] We note that Covino et al. (2013) derived an SMC extinction curve for GRB 061121. We have tested both WG-SMC and WD-SMC dust model and obtained similar results.

[4] https://seoncafe.github.io/MoCafe.html

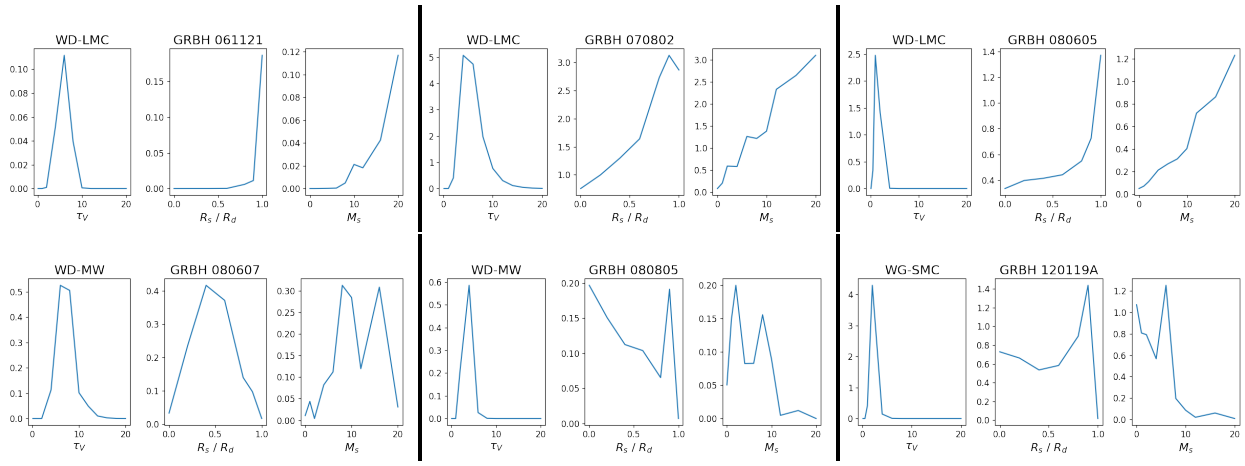

Fig. 17. Probability density functions of τ_V, R_s/R_d and M_s for each GRBH with the chosen dust model.

find that GRB and HII regions suffer a similar attenuation. Our estimates of the amount of attenuation for the whole galaxy, derived from the SED fitting, correlate with the amount of extinction along the GRB l.o.s., with the galaxy attenuation amounting to about 70% of the GRB l.o.s. extinction. The ratio of colour excess between the stellar continuum and the Balmer lines is consistent with the one of C00.

The attenuation curves derived from the SED fitting show a great variety of cases: the attenuation curves have flatter, similar or steeper slopes than the extinction curves. Half of the sample is consistent with the C00 law and there is evidence of a UV bump in only one attenuation curve. We find that steeper (shallower) attenuation curve slopes are found preferentially in the less (more) massive galaxies and with higher (lower) SFR and A_V^{stars}. These trends encourage us to further study these possible correlations on a larger sample of GRBHs.

Comparing our results with the radiative transfer simulations in Seon & Draine (2016), we find a variety of dust-stars geometries. For half of the sample, a uniform distribution of stars and dust with a very clumpy local dust distribution reproduces the derived attenuation curves the best. In one case, the ISM structure is best represented with stars surrounded by a dust cloud with a clumpy local dust distribution. For the two steepest attenuation curves, two configurations are found almost as likely, either a uniform distribution of stars and dust with a homogeneous local dust distribution or stars surrounded by a dust cloud with a clumpy local dust distribution.

This method is promising and a dedicated radiative transfer simulation on each of these objects would allow to understand more precisely the dust-stars distribution in these GRBHs.

Acknowledgements. DC acknowledges H. Hirashita, A.K. Inoue, T.T. Takeuchi and D. Donevski for helpful and stimulating discussions. DC acknowledges support by the Centre National d'Etudes Spatiales and support by the Région Provence-Alpes-Côte d'Azur for the funding of his PhD. JJ acknowledges support from NOVA and NWO-FAPESP grant for advanced instrumentation in astronomy. This work was supported by the Programme National de Cosmologie et Galaxies (PNCG). SDV, SBo, RS, JP, acknowledges the support of the French National Research Agency (ANR) under contract ANR-16-CE31-0003 BEaPro (PI: SDV).

References

Asano, R. S., Takeuchi, T. T., Hirashita, H., & Nozawa, T. 2013, MNRAS, 432, 637
Asano, R. S., Takeuchi, T. T., Hirashita, H., & Nozawa, T. 2014, MNRAS, 440, 134
Battisti, A. J., Calzetti, D., & Chary, R.-R. 2016, ApJ, 818, 13
Battisti, A. J., Calzetti, D., & Chary, R.-R. 2017, ApJ, 840, 109
Bianchi, L., Clayton, G. C., Bohlin, R. C., Hutchings, J. B., & Massey, P. 1996, ApJ, 471, 203
Blanchard, P. K., Berger, E., & Fong, W.-f. 2016, ApJ, 817, 144
Boquien, M., Buat, V., & Perret, V. 2014, A&A, 571, A72
Bruzual, G., & Charlot, S. 2003, MNRAS, 344, 1000
Buat, V., Giovannoli, E., Burgarella, D., et al. 2010, MNRAS, 409, L1
Buat, V., Giovannoli, E., Heinis, S., et al. 2011, A&A, 533, A93
Buat, V., Noll, S., Burgarella, D., et al. 2012, A&A, 545, A141
Calzetti, D., Kinney, A. L., & Storchi-Bergmann, T. 1994, ApJ, 429, 582
Calzetti, D., Armus, L., Bohlin, R. C., et al. 2000, ApJ, 533, 682
Chabrier, G. 2003, PASP, 115, 763
Charlot, S., & Fall, S. M. 2000, ApJ, 539, 718
Chen, H.-W., Perley, D. A., Wilson, C. D., et al. 2010, ApJ, 723, L218
Chevallard, J., Charlot, S., Wandelt, B., & Wild, V. 2013, MNRAS, 432, 2061
Clayton, G. C., & Martin, P. G. 1985, ApJ, 288, 558
Clayton, G. C., Gordon, K. D., Bianchi, L. C., et al. 2015, ApJ, 815, 14
Covino, S., Melandri, A., Salvaterra, R., et al. 2013, MNRAS, 432, 1231
Dale, D. A., & Helou, G. 2002, ApJ, 576, 159
Dale, D. A., Helou, G., Magdis, G. E., et al. 2014, ApJ, 784, 83
De Looze, I., Fritz, J., Baes, M., et al. 2014, A&A, 571, A69
De Pasquale, M., Kuin, N. P. M., Oates, S., et al. 2015, MNRAS, 449, 1024
Draine, B. T. 2003, ARA&A, 41, 241
Elíasdóttir, Á., Fynbo, J. P. U., Hjorth, J., et al. 2009, ApJ, 697, 1725
Fitzpatrick, E. L. 1985, ApJ, 299, 219
Fitzpatrick, E. L., & Massa, D. 1990, ApJS, 72, 163
Fitzpatrick, E. L., & Massa, D. 2007, ApJ, 663, 320
Fruchter, A., Krolik, J. H., & Rhoads, J. E. 2001, ApJ, 563, 597
Fynbo, J. P. U., Jakobsson, P., Prochaska, J. X., et al. 2009, ApJS, 185, 526
Gordon, K. D., & Clayton, G. C. 1998, ApJ, 500, 816
Gordon, K. D., Calzetti, D., & Witt, A. N. 1997, ApJ, 487, 625
Gordon, K. D., Clayton, G. C., Misselt, K. A., Landolt, A. U., & Wolff, M. J. 2003, ApJ, 594, 279
Granato, G. L., Lacey, C. G., Silva, L., et al. 2000, ApJ, 542, 710
Granot, J., & Sari, R. 2002, ApJ, 568, 820
Greiner, J., Krühler, T., Klose, S., et al. 2011, A&A, 526, A30
Heinis, S., Buat, V., Béthermin, M., et al. 2014, MNRAS, 437, 1268
Hopkins, P. F., Strauss, M. A., Hall, P. B., et al. 2004, AJ, 128, 1112
Hunt, L. K., Palazzi, E., Michałowski, M. J., et al. 2014, A&A, 565, A112
Inoue, A. K. 2005, MNRAS, 359, 171
Japelj, J., Covino, S., Gomboc, A., et al. 2015, A&A, 579, A74
Japelj, J., Vergani, S. D., Salvaterra, R., et al. 2016, A&A, 590, A129
Kennicutt, Jr., R. C. 1998, ARA&A, 36, 189
Kriek, M., & Conroy, C. 2013, ApJ, 775, L16
Krügel, E. 2009, A&A, 493, 385
Krühler, T., Greiner, J., Schady, P., et al. 2011, A&A, 534, A108
Krühler, T., Fynbo, J. P. U., Geier, S., et al. 2012, A&A, 546, A8
Krühler, T., Malesani, D., Fynbo, J. P. U., et al. 2015, A&A, 581, A125
Lee, S.-K., Ferguson, H. C., Somerville, R. S., Wiklind, T., & Giavalisco, M. 2010, ApJ, 725, 1644
Maiolino, R., Nagao, T., Grazian, A., et al. 2008, A&A, 488, 463
Maraston, C., Pforr, J., Renzini, A., et al. 2010, MNRAS, 407, 830
Melandri, A., Sbarufatti, B., D'Avanzo, P., et al. 2012, MNRAS, 421, 1265
Misselt, K. A., Clayton, G. C., & Gordon, K. D. 1999, ApJ, 515, 128
Morgan, A. N., Perley, D. A., Cenko, S. B., et al. 2014, MNRAS, 440, 1810

Nardini, M., Elliott, J., Filgas, R., et al. 2014, A&A, 562, A29
Noll, S., Pierini, D., Pannella, M., & Savaglio, S. 2007, A&A, 472, 455
Noll, S., Burgarella, D., Giovannoli, E., et al. 2009a, A&A, 507, 1793
Noll, S., Pierini, D., Cimatti, A., et al. 2009b, A&A, 499, 69
Panuzzo, P., Granato, G. L., Buat, V., et al. 2007, MNRAS, 375, 640
Pei, Y. C. 1992, ApJ, 395, 130
Perley, D. A., Levan, A. J., Tanvir, N. R., et al. 2013, ApJ, 778, 128
Perley, D. A., Perley, R. A., Hjorth, J., et al. 2015, ApJ, 801, 102
Perley, D. A., Tanvir, N. R., Hjorth, J., et al. 2016, ApJ, 817, 8
Perna, R., Lazzati, D., & Fiore, F. 2003, ApJ, 585, 775
Pforr, J., Maraston, C., & Tonini, C. 2012, MNRAS, 422, 3285
Pierini, D., Gordon, K. D., Witt, A. N., & Madsen, G. J. 2004, ApJ, 617, 1022
Planck Collaboration XIII. 2016, A&A, 594, A13
Prevot, M. L., Lequeux, J., Prevot, L., Maurice, E., & Rocca-Volmerange, B. 1984, A&A, 132, 389
Prochaska, J. X., Sheffer, Y., Perley, D. A., et al. 2009, ApJ, 691, L27
Reddy, N. A., Kriek, M., Shapley, A. E., et al. 2015, ApJ, 806, 259
Reddy, N. A., Steidel, C. C., Pettini, M., & Bogosavljević, M. 2016, ApJ, 828, 107
Richards, G. T., Hall, P. B., Vanden Berk, D. E., et al. 2003, AJ, 126, 1131
Salmon, B., Papovich, C., Long, J., et al. 2016, ApJ, 827, 20
Sari, R., Piran, T., & Narayan, R. 1998, ApJ, 497, L17
Savaglio, S., Glazebrook, K., & Le Borgne, D. 2009, ApJ, 691, 182
Schady, P., Dwelly, T., Page, M. J., et al. 2012, A&A, 537, A15
Schlafly, E. F., & Finkbeiner, D. P. 2011, ApJ, 737, 103
Schreiber, C., Pannella, M., Elbaz, D., et al. 2015, A&A, 575, A74
Scicluna, P., & Siebenmorgen, R. 2015, A&A, 584, A108
Seon, K.-I., & Draine, B. T. 2016, ApJ, 833, 201
Silva, L., Granato, G. L., Bressan, A., & Danese, L. 1998, ApJ, 509, 103
Tuffs, R. J., Popescu, C. C., Völk, H. J., Kylafis, N. D., & Dopita, M. A. 2004, A&A, 419, 821
Vergani, S. D., Salvaterra, R., Japelj, J., et al. 2015, A&A, 581, A102
Vergani, S. D., Palmerio, J., Salvaterra, R., et al. 2017, A&A, 599, A120
Viaene, S., Baes, M., Tamm, A., et al. 2017, A&A, 599, A64
Vijh, U. P., Witt, A. N., & Gordon, K. D. 2003, ApJ, 587, 533
Wang, W.-H., Chen, H.-W., & Huang, K.-Y. 2012, ApJ, 761, L32
Waxman, E., & Draine, B. T. 2000, ApJ, 537, 796
Wei, J., Cordier, B., Antier, S., et al. 2016, ArXiv e-prints [arXiv: 1610.06892]
Weingartner, J. C., & Draine, B. T. 2001, ApJ, 548, 296
Wild, V., Charlot, S., Brinchmann, J., et al. 2011, MNRAS, 417, 1760
Witt, A. N., & Gordon, K. D. 2000, ApJ, 528, 799
Witt, A. N., Bohlin, R. C., & Stecher, T. P. 1984, ApJ, 279, 698
Zafar, T., Watson, D., Fynbo, J. P. U., et al. 2011, A&A, 532, A143
Zafar, T., Watson, D., Elíasdóttir, Á., et al. 2012, ApJ, 753, 82
Zafar, T., Møller, P., Watson, D., et al. 2015, A&A, 584, A100
Zafar, T., Watson, D., Møller, P., et al. 2018, MNRAS, 479, 1542
Zahid, H. J., Yates, R. M., Kewley, L. J., & Kudritzki, R. P. 2013, ApJ, 763, 92

Appendix A: GRB samples

Table A.1. GRB for which the extinction curves are derived by fitting with the FM formula in Zafar et al. (2011, 2012).

GRB	z	$T_{\rm SED}$ h	$A_{\rm V}^{\rm Gal}$ mag	Ext. curve	pow/bknp	$A_{\rm V}^{\rm grb}$ mag	$\log_{10} M_{\odot}$	$A_{\rm V}^{\rm lines}$ mag	SFR$_{\rm H_\alpha}$ $M_{\odot}$ yr^{-1}	Z 12 + log(O/H)	References
050401	2.8983	14.7	0.172	SMC-like	bknp	$0.65^{+0.04}_{-0.04}$	9.61				(1), (4)
060729	0.5428	13.2	0.142	SMC-like	pow	$0.07^{+0.02}_{-0.02}$	8.31	$2.19^{+1.32}_{-1.45}$	$0.96^{+2.21}_{-0.69}$		(1), (4), (5)
070125	1.5471	31.5	0.139	SMC-like	bknp	$0.30^{+0.04}_{-0.04}$					(1)
070802	**2.4541**	**2.00**	**0.071**	**LMC-like**	**pow**	$\mathbf{1.19^{+0.15}_{-0.15}}$		$\mathbf{0.95^{+0.37}_{-0.37}}$	$\mathbf{24^{+11}_{-8}}$		(1), (5)
071020	2.1462	5.12	0.160	SMC-like	bknp	$0.43^{+0.04}_{-0.04}$	<9.43				(1), (4)
080605	**1.6403**	**1.74**	**0.360**	**Steep + bump**	**pow**	$\mathbf{0.50^{+0.13}_{-0.10}}$	**10.53**	$\mathbf{0.80^{+0.34}_{-0.31}}$	$\mathbf{47^{+17}_{-12}}$	$\mathbf{8.54^{+0.09}_{-0.09}}$	(2), (4), (5)
080607	**3.0368**	**0.08**	**0.185**	**Flat + bump**	**pow**	$\mathbf{2.33^{+0.46}_{-0.43}}$		**10.45**			(1), (4)
080805	**1.5042**	**1.00**	**0.114**	**Flat + bump**	**pow**	$\mathbf{1.54^{+0.21}_{-0.22}}$	**9.86**	$\mathbf{2.40^{+1.20}_{-0.95}}$	$\mathbf{45^{+79}_{-26.8}}$	$\mathbf{8.49^{+0.13}_{-0.14}}$	(2), (4), (5)
080928	1.6919	15.5	0.179	SMC-like	pow	$0.29^{+0.03}_{-0.03}$	<9.29				(1), (4)
120119A	**1.728**	**1.77**	**0.295**	**SMC**	**pow**	$\mathbf{1.02^{+0.11}_{-0.11}}$	**9.91**	$\mathbf{1.08^{+0.49}_{-0.43}}$	$\mathbf{43^{+24}_{-14}}$	$\mathbf{8.6^{+0.14}_{-0.14}}$	(3), (4), (5)

Notes. The GRBs in bold are the ones in our Golden sample. Columns list (1) the redshift, (2) time at which the SED is extracted, (3) the Galactic extinction, (4) type of extinction curve, (5) whether the GRB afterglow SED is best fitted with a power law or broken power law, (6) the amount of extinction in the V band along the GRB l.o.s. in the host galaxy, (7) stellar mass of the GRB host galaxy from Perley et al. (2016), (8) amount of extinction in the host galaxy derived from the Balmer decrement, (9) the SFR derived from H_α luminosity, (10) the metallicity, (11) references where these quantities are found.

References. (1) Zafar et al. (2011); (2) Zafar et al. (2012); (3) Zafar et al. (2018); (4) Perley et al. (2016); (5) Krühler et al. (2015).

Table A.2. GRB extinction curves derived by scaling the LMC, SMC and MW extinction curves of Pei (1992).

GRB	z	$T_{\rm SED}$ h	$A_{\rm V}^{\rm Gal}$ mag	Ext. curve	pow/bknp	$A_{\rm V}^{\rm grb}$ mag	$\log_{10} M_{\odot}$	$A_{\rm V}^{\rm lines}$ mag	$\rm SFR_{H_\alpha}$ $M_{\odot}\,{\rm yr}^{-1}$	Z $12+\log({\rm O/H})$	References
050820A	2.615	2.78	0.14	LMC	bknp	$0.19^{+0.03}_{-0.03}$	9.38				(3), (1)
060418	1.49	1.39	0.69	SMC	bknp	$0.13^{+0.01}_{-0.02}$					(3)
060607A	3.082	2.22	0.09	SMC	pow	$0.08^{+0.04}_{-0.04}$	<9.45				(3), (1)
060904B	0.703	1.39	0.53	LMC	pow	$0.15^{+0.04}_{-0.04}$					(3)
061121	**1.314**	**1.67**	**0.14**	**LMC**	**bknp**	$\mathbf{0.54^{+0.06}_{-0.09}}$	**10.31**	$1.66^{+0.60}_{-0.60}$	44.2^{+19}_{-10}	$8.5^{+0.09}_{-0.06}$	(3), (1), (4)
071112C	0.823	0.36	0.36	SMC	pow	$0.20^{+0.05}_{-0.04}$	8.89	<0.2		$7.90^{+0.5}_{-0.35}$	(3), (1), (5)
080210	2.641	1.39	0.26	LMC	bknp	$0.25^{+0.03}_{-0.03}$	<9.50				(3), (1)
080319C	1.95	0.14	0.08	SMC	pow	$0.71^{+0.08}_{-0.07}$					(3)
080710	0.845	2.78	0.23	SMC	pow	$0.03^{+0.01}_{-0.01}$	<8.95				(3), (1)
080804	2.204	0.42	0.05	LMC	bknp	$0.10^{+0.01}_{-0.01}$	9.28	$1.17^{+1.57}_{-1.08}$	$15.2^{+41.2}_{-8.7}$		(3), (1), (2)
081121	2.512	2.77	0.16	SMC	bknp	$0.07^{+0.01}_{-0.01}$	9.24				(3), (1)
081222	2.77	0.19	0.06	MW	bknp	$0.04^{+0.02}_{-0.01}$	9.61				(3), (1)
090102	1.546	0.28	0.15	MW	bknp	$0.40^{+0.03}_{-0.03}$					(3)
090424	0.544	0.28	0.08	MW	bknp	$1.14^{+0.09}_{-0.09}$	9.62	$1.42^{+0.54}_{-0.51}$	$2.88^{+1.81}_{-1.81}$	$8.88^{+0.12}_{-0.20}$	(3), (1), (5)
090618	0.54	0.55	0.27	SMC	bknp	$0.15^{+0.01}_{-0.01}$	9.04				(3), (1)
091018	0.971	8.33	0.09	SMC	bknp	$0.10^{+0.01}_{-0.01}$	9.62	$0.18^{+1.72}_{-0.18}$	$1.29^{+3.46}_{-0.32}$	$8.78^{+0.18}_{-0.19}$	(3), (1), (2)
091029	2.752	0.28	0.05	LMC	bknp	$0.06^{+0.03}_{-0.03}$	<9.81				(3), (1)
100814A	**1.44**	**98.4**	**0.054**	**SMC**	**bknp**	$\mathbf{0.20^{+0.03}_{-0.03}}$	**9.52**	$\mathbf{0.25^{+0.80}_{-0.25}}$	$\mathbf{3.2^{+2.9}_{-0.7}}$		(6), (1), (2)
100901A	1.408	66.0	0.270	SMC	bknp	$0.29^{+0.03}_{-0.03}$					(6)
120815A	2.358	2.06	0.320	SMC	bknp	$0.32^{+0.02}_{-0.02}$		$0.18^{+1.05}_{-0.18}$	$2.3^{+2.7}_{-1}$		(6), (1), (2)

Notes. GRBs of the upper part of the table are taken from Schady et al. (2012), GRBs in the lower part are taken from Japelj et al. (2015). The GRBs in bold are the ones in our Golden sample. Columns list (1) the redshift, (2) time at which the SED is extracted, (3) the Galactic extinction, (4) type of extinction curve, (5) whether the GRB afterglow SED is best fitted with a power law or broken power law, (6) the amount of extinction in the V band along the GRB l.o.s. in the host galaxy, (7) stellar mass of the GRB host galaxy from Perley et al. (2016), (8) amount of extinction in the host galaxy derived from the Balmer decrement, (9) the SFR tracer, (10) the SFR derived from $\rm H_\alpha$ luminosity, (11) the metallicity, (12) references where these quantities are found.
References. (1) Perley et al. (2016); (2) Krühler et al. (2015); (3) Schady et al. (2012); (4) Vergani et al. (2017); (5) Japelj et al. (2016); (6) Japelj et al. (2015).

Appendix B: SED data for the golden sample

B.1. GRBH 061121

Multi-wavelength data of the host galaxy are available from Perley et al. (2015). It was one of the four galaxies detected in radio from their VLA survey at 3 GHz. The galaxy was also observed in the optical (*uBgiz* with the Keck-I/LRIS, *R* with the VLT/FORS2) and near-IR (*J* with the P200/WIRC, *K* with the VLT/ISAAC and 3.6 μm with *Spitzer*/IRAC).

B.2. GRBH 070802

The galaxy was observed by Elíasdóttir et al. (2009) with the VLT and detected in the *R* band of the VLT/FORS2 and *K* band of the VLT/ISAAC. Krühler et al. (2011) reported detections with the *i* band of the NTT/EFOSC and *J* band of the VLT/HAWK-I. Further detections in the NIR are reported by Perley et al. (2013) with the HST/WFC3 in F105W and F160W and with *Spitzer*/IRAC. We decided to keep only the IRAC2 measurement as the IRAC1 measurement is affected by a bright star (Perley et al. 2013).

B.3. GRBH 080605

The host galaxy is observed by Krühler et al. (2011) with GROND and detected in the *griz* bands. The HST observations (WFC3/F160W) and LIRIS observation (*J*, *Ks*) are reported by Krühler et al. (2012) and IRAC1 magnitude by Perley et al. (2016).

B.4. GRBH 080607

We used the photometric data published in Perley et al. (2013) from the observations first reported by Chen et al. (2010): the *gVIK* data from the Keck-I observations (LRIS and NIRC), a deep *r*-band measurement from the *Magellan*/IMACS, and near-IR measurements with HST/WFC3 (F160W) and *Spitzer*/IRAC (IRAC1 and IRAC2). ALMA flux at 345 GHz is reported by Wang et al. (2012).

B.5. GRBH 080805

Krühler et al. (2011) reported photometric observations of the host with the NTT/EFOSC (*VRi* bands) and the VLT/HAWK-I (*JK* bands). The HST observations (WFC3/F160W) are reported by Blanchard et al. (2016) and IRAC1 magnitude by Perley et al. (2016). We discarded the *i* measurement whose error is twice larger than in the *V, R* bands.

B.6. GRBH 100814A

The photometry for the host galaxy is taken from Nardini et al. (2014): we consider the last available *griz* GROND observations where the host dominates the afterglow, 63 days after the burst for *iz* and 145 days after the burst for *gr*. De Pasquale et al. (2015) reported a *J* detection with the Calar Alto 3.5 m telescope three years after the burst. We do not consider UVOT data as they are available for only six days after the burst and likely to be contaminated by the GRB afterglow. The *Spitzer*/IRAC observations were carried out and reported by Perley et al. (2016) and the target was detected in the IRAC1 channel.

B.7. GRBH 120119A

Some of the Morgan et al. (2014) observations were conducted at a late epoch after the burst. The host galaxy was clearly detected and its emission measured with the Keck/LRIS in the *B*, *R*, and RG850 bands 0.85 year after the burst, and with the HST/WFC3 in the F125W and F160W bands 0.77 year after the burst. The *Spitzer*/IRAC observations were carried out and reported by Perley et al. (2016) and the target was detected in the IRAC1 channel.

Appendix C: Best fits with radiative transfer simulations

In this appendix, we compare the attenuation curves computed with radiative transfer simulations of Seon & Draine (2016) best fitting attenuation curves derived with CIGALE in Sect. 4.1 using the method explained in Sect. 5.5. Attenuation curves are compared only at wavelengths used in the radiative transfer simulations and covered by the broad-band filter observations. Only the best fit is reported in Fig. C.1 with the corresponding values of τ_V, R_s/R_d and M_s. In this Figure we also report the rest-frame spectral coverage of each host galaxy observation[5].

[5] We note that fitting GRBH 061121 with a WG-SMC dust grain model results in a better fit without UV bump but it does not change qualitatively the description of the ISM structure as the best values for parameters are: $\tau_V = 6.0$, $R_s/R_d = 1.0$ and $M_s = 16$.

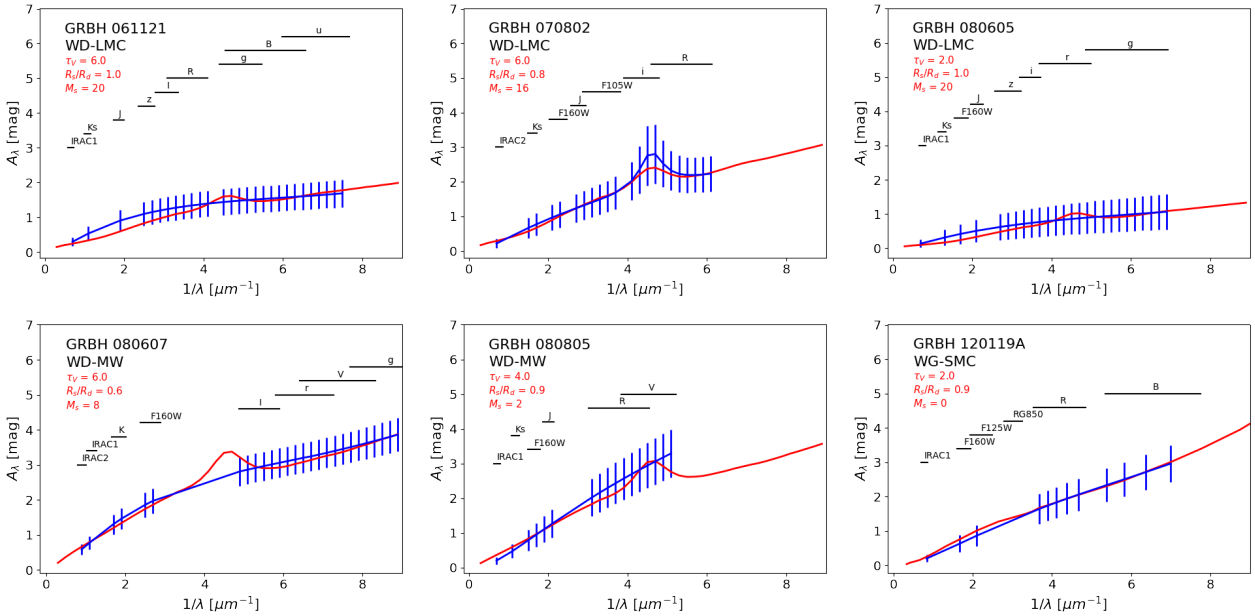

Fig. C.1. Best fits of the attenuation curve derived with CIGALE with the ones from radiative transfer simulations of Seon & Draine (2016). The blue errors bars correspond to the attenuation curve and associated uncertainty derived with CIGALE estimated at wavelengths used in the radiative transfer simulations and covered by observations. The red line corresponds to the attenuation curve from radiative transfer simulations which best fits the CIGALE attenuation curve. The black lines represent the spectral coverage of the host galaxy observations.

Dust properties of a large GRBH sample

In the paper presented in Section IV.3 we showed that we were able to measure the main characteristics of the attenuation curves of GRBHs and found some correlations between the slope of the attenuation curve and the SFR and stellar mass of the galaxies. As the sample was small and statistically not representative enough we decided to study a larger sample of GRBHs focusing on their dust properties and star formation activities, without imposing the restrictive criteria of having rest-frame UV detection for the GRB extinction curve. We will also use the results of the Section IV.2.3.3 to localise the GRBHs in the parameter space of the SD16 RT model in order to infer some information about the dust type, local dust distribution and dust-star geometry in the ISM of these GRBHs, especially through the $E(B-V)-\delta$ diagram.

1. Selection of dusty GRBHs

One of the main objective of this section is to search for correlations between the slope of the attenuation curve and some physical parameters of the GRBHs. As we have seen in Section 3 the shape of the attenuation curve is not well constrained when the amount of dust in the V band is small, such as for GRBH 100814A with A_V^{grb}=$0.20^{+0.03}_{-0.03}$ mag [Japelj et al., 2016]. Using the correlation we found between the amount of extinction along the GRB line of sight, A_V^{grb} and the overall attenuation in the GRBH, A_V^{stars} in our sample of dusty GRBs / GRBHs, we impose a criteria of having at least A_V^{grb}>0.2 mag. In order to measure accurately the physical parameters we further require to have at least 5 photometric measurements of the GRBH from the UV to NIR in the host rest-frame with at least one detection at a wavelength below 2000 Å as the effect of dust are more important in the UV.
To summarise, we selected the GRBH according to the following 4 criteria :
- The GRBH must have a spectroscopic redshift
- The amount of extinction in V band measured along the GRB l.o.s must be at least 0.2 mag.
- The GRBH must have been detected in at least 5 bands from UV to NIR
- One of these detections must be below 2000 Å

The evaluation of A_V^{grb} is sensitive to the available data (photometry and/or spectroscopy) and the method used to fit these data, when different estimation of A_V^{grb} not compatible with each other exist in the literature, we decided to include the GRB in our sample if one of the estimate is higher than 0.2 mag.
The sample is composed of 23 GRBHs presented in Table V.1, which is the largest sample of "dusty" GRBHs covering rest-frame UV to radio data. The photometry and emission lines fluxes were compiled from different works and are reported in Tables D.1 and D.2 of Appendix D. 19 out of of the 23 GRBHs have available Balmer emission lines flux measurements. In the previous chapter the emission lines diagnostics were indirectly used to check whether our SED fitting results were in agreement with them. For this analysis, we decide to include them directly in the SED fitting procedure, as described in the next section.

2. SED fitting

2.1. Including emission lines in the SED fitting procedure

Table V.1– Sample of GRBHs fulfilling our selection criteria. Columns list (1) the galaxy identification, (2) the redshift, (3) the amount of extinction in the V band derived along the GRB line of sigth, (4) photometric bands with a detection of the host in the UV/Visible/NIR, (5) bands with a detection of the host in the MIR/FIR/mm/Radio, and (5) the emission lines fluxes we considered in our analysis, (6) metallicity.

Ident.	z	A_V^{grb}	UV/VIS/NIR detections	MIR/FIR/mm/Radio detections	Emission lines	Z
GRBH		mag				12 + log(O/H)
050915A	2.5275[a]	∼1.4[b]	g,V,R,I,K, IRAC 3.6μm, IRAC 4.5μm		H_β	
051022A	0.8061[a]	>9.34[b]	U,B,V,F606W, r, i, I, z, J F160W, K, IRAC 3.6μm, IRAC 4.5μm	VLA 5.23 GHz	H_α, H_β	$8.49^{+0.09}_{-0.09}$ [a]
060306	1.5597[a]	>8.5[e]	B, g, R, I, z, K, IRAC 3.6μm, IRAC 4.5μm		H_α	$9.12^{+0.18}_{-0.42}$ [h]
060319	1.172[b]	>1.8[b]	u, g, R, z, K, IRAC 3.6μm, IRAC 4.5μm			
060814	1.9223[a]	>1.1[e]	V, R, I, F125W, F160W, K, IRAC 3.6μm, IRAC 4.5μm	VLA 3 GHz	H_α, H_β	$8.38^{+0.14}_{-0.28}$ [h]
060912A	0.9362[a]	$0.46^{+0.23}_{-0.22}$ [f]	U, B, V, R, I, F160W, K, IRAC 3.6μm		H_α, H_β	$8.61^{+0.11}_{-0.12}$ [a]
061121	1.3145[c]	$0.54^{+0.06}_{-0.09}$ [f]	u, B, g, R, i, z, J, K, IRAC 3.6μm	VLA 3 GHz	H_α, H_β	$8.5^{+0.06}_{-0.09}$ [h]
070306	1.4965[a]	$5.5^{+1.2}_{-1.0}$ [g]	u, g', r', R, r', I, z', F125W, F160W, Ks,	PACS 100μm, PACS 160μm,	H_α, H_β	$8.54^{+0.09}_{-0.09}$ [a]
			IRAC 3.6μm, IRAC 4.5μm	VLA 3GHz		
070521	2.0865[a]	>2.3[e]	B, V, I, z, J, F160W, K, IRAC 3.6μm, IRAC 4.5μm	VLA 5.23 GHz	H_α	
070802	2.4538[a]	$1.19^{+0.15}_{-0.15}$ [h]	R,i, F105W, J, F160W, K, IRAC 4.5μm		H_α, H_β	
071021	2.4515[a]	∼1.5[b]	B, g, V, I, z, F105W, J, F160W, K, IRAC 3.6μm, IRAC 4.5μm		H_α, H_β	
080207	2.0856[a]	>2.32[b]	g, R, I, z', F110W, F160W, Ks, IRAC 3.6μm, IRAC 4.5μm,	PACS 100μm, PACS 160μm,	H_α, H_β	$8.74^{+0.15}_{-0.15}$ [a]
			IRAC 5.8μm, IRAC 8.0μm	VLA 5.23 GHz	H_α, H_β	
080325	1.78[b]	>2.67[b]	B, Rc, i', z', F125W, F160W, Ks, IRAC 3.6μm, IRAC 4.5μm	PACS 100μm, PACS 160μm		
080605	1.6408[a]	$0.50^{+0.13}_{-0.10}$ [i]	g', r', i', z', J, F160W, Ks, IRAC 3.6μm		H_α, H_β	$8.54^{+0.09}_{-0.09}$ [a]
080607	3.038[b]	$2.33^{+0.46}_{-0.43}$ [h]	g, V, r, I, F160W, K, IRAC 3.6μm, IRAC 4.5μm	ALMA 345 GHz		
080805	1.5052[a]	$1.54^{+0.21}_{-0.22}$ [i]	V, R, J, F160W, K, IRAC 3.6μm		H_α, H_β	$8.49^{+0.13}_{-0.14}$ [a]
081109	0.9785[a]	$3.4^{+0.4}_{-0.3}$ [g]	uvm2, uvw1, U, g', V, r', i', I, z', Y, J, F160W, K, IRAC1, 2		H_α, H_β	$8.75^{+0.09}_{-0.09}$ [a]
081221	2.2590[a]	>1.4[e]	B, g, V, r', I, z, F105W, F160W, K, IRAC 3.6μm, IRAC 4.5μm		H_α	
090407	1.4478[a]	>1.57[b]	B, g, R, I, z, F160W, K, IRAC 3.6μm, IRAC 4.5μm		H_α, H_β	$8.85^{+0.13}_{-0.13}$ [a]
090417B	0.345[d]	>2.66[b]	uvw2, uvm2, uvw1, u, b, g', r', R, i', z', J, F160W, Ks,	PACS 100μm, PACS 160μm		
			IRAC 3.6μm, IRAC 4.5μm			
090926B	1.2427[a]	$1.4^{+1.1}_{-0.6}$ [g]	U, g', r', i', z', J, H, K, IRAC 3.6μm		H_α, H_β	$8.34^{+0.15}_{-0.17}$ [a]
100621A	0.5426[a]	$3.8^{+0.2}_{-0.2}$ [g]	uvw2, uvm2, uvw1, u, U, g', r', i', z', Y, J, F160W, K,		H_α, H_β	$8.52^{+0.10}_{-0.10}$ [a]
			IRAC 3.6μm, IRAC 4.5μm			
120119A	1.7291[a]	$1.02^{+0.11}_{-0.11}$ [j]	B, g', R, I, z', F125W, F160W, K, IRAC 3.6μm		H_α, H_β	$8.6^{+0.14}_{-0.14}$ [a]

[a] Krühler et al., 2015 [b] D. A. Perley et al., 2013 [c] Hjorth et al., 2012 [d] Holland et al., 2010 [e] Covino et al., 2013 [f] Schady et al., 2012 [g] Krühler et al., 2011
[h] Zafar et al., 2011 [i] Zafar et al., 2012 [j] Zafar et al., 2018b [h] Vergani et al., 2017

2.1.1. Motivation

Very massive stars emit a significant fraction of their photons in the Lyman continuum, shortward of 91.2nm, and these energetic photons will ionise the surrounding gas and re-emits the energy in the form of emission lines and a continuum from the UV to the radio domain. Emission lines are thus providing us information about the recent star formation, especially through the hydrogen recombination lines. The contribution of the nebular emission to broadband fluxes is usually negligible for quiescent star-forming galaxies but it can be important for starbursting dwarf galaxies, very young star-forming regions and also for some high-z galaxies [Anders et Fritze-v. Alvensleben, 2003 ; Boquien et al., 2010 ; Stark et al., 2013 ; de Barros et al., 2014]. GRB host galaxies are usually quite active in star formation, as showed in Section IV.3 where 5 out of the 7 GRBHs we studied required a burst of recent star formation, and so the contribution of the nebular emission to the broadband SED can be important and needs to be taken into account when studying GRBH SEDs. Emission lines were already included in our previous work, but here we use the emission lines fluxes as an input of the SED fitting procedure and include them in the χ^2 computation. We start by briefly describing how the nebular emission is computed in CIGALE and then we describe how we compute the emission line flux.

2.1.2. Modelling nebular emission in CIGALE [Boquien *et al., 2018*]

Before explaining how we computed the emission lines fluxes, we briefly describe in this section how the emission lines are modelled in CIGALE. The modelling of the nebular emission is based on the nebular templates of Inoue, 2011 generated with CLOUDY [Ferland et al., 1998 ; Ferland et al., 2013] which predicts the intensities of 124 lines relative to H_β from HeII at 30.38nm to NII at 205.4μm for a given ionisation parameter, U, and metallicity, Z, which is assumed to be the same as the stellar one. The electron density is fixed to 100 cm^{-3}. The abundances are based on the Orion nebula and the helium and nitrogen abundances are scaled by metallicity following the prescription in Nagao et al., 2011.
In practice, the nebular emission spectrum is computed for the lines and continuum separately. First the normalised emission lines luminosity spectrum is computed by selecting a template for the given U and Z. Each line is modelled with a Gaussian shape whose line width is defined by the user. Then this spectrum is scaled with the the ionising photon luminosity computed for the adopted composite stellar population assuming that all Lyman continuum photons ionise the surrounding gas. If some of these photons escape the galaxy or are absorbed by dust the emission line spectrum is reduced by factor following the prescription of Inoue, 2011. In our analysis, we assume that all all Lyman continuum photons are ionising the surrounding gas and the ionisation parameter is set to -2.
The normalised nebular continuum spectrum is computed according to Inoue, 2010 with the same parameters as for the lines, then it is scaled to the Lyman continuum photon luminosity in a similar manner as for the lines. Only the hydrogen continuum is considered as helium and other metals continua are negligible.

2.1.3. Computing emission line fluxes in CIGALE

For our analysis, all the emission lines fluxes measurement are taken from Krühler et al., 2015, with the exception of GRBH 061221 taken from Vergani et al., 2017 where they followed the same prescription as in Krühler et al., 2015 to measure the fluxes. This ensures a consistency between the measurements. Consequently we decided to implement a new module in CIGALE to compute the emission lines fluxes in a similar manner as Krühler et al., 2015. As described in Krühler et al., 2015 : "*fluxes of emission lines were measured by fitting a superposition of Gaussian functions to the data, with the*

continuum set in small (± 40 Å) regions around the wavelength of interest free of emission-, telluric-, and sky-lines". Their fluxes are corrected for Galactic foreground reddening and for slit-loss based on broadband photometry. They are not corrected for host-intrinsic extinction. The Balmer lines fluxes are not corrected for the underlying Balmer stellar absorption as the signal to noise ratio of the emission lines and stellar continuum is not high enough to resolve and fit the absorption component separately. From the analysis of 1350 galaxies at z∼0.8, Zahid et al., 2011 found that the Balmer absorption correction for H_β has an equivalent width (EW) of ~ 0.5 Å for galaxies of $10^9 M_\odot$ and ~ 1 Å for galaxies of $10^{10} M_\odot$. In Krühler et al., 2015, they estimate the uncertainty associated to this correction to be on average $\lesssim 5\%$ for H_β which is below the average statistical uncertainty on the line flux measurement. This correction is negligible for H_α as the emission line EW is large enough (> 20Å in the rest-frame). The correction will be more important for H_δ and H_γ emission lines.

The intensities of the hydrogen recombination lines are sensitive to the initial mass function (IMF), dust extinction and adopted stellar population synthesis (SPS) model. Among the Balmer lines, we only considered H_α and H_β and not H_δ and H_γ in our analysis as the low signal to noise ratio of the spectrum did not allow to correct for the underlying Balmer stellar absorption in Krühler et al., 2015. Emission lines other than hydrogen recombination lines, such as OII, OIII, NeIII and NII are not considered as they are sensitive to more parameters such as the ionisation parameter, the metallicity leading to degeneracies, i.e. the same flux can be computed for different combination of these parameters [Steidel et al., 2014].

We modified the public version v0.12 of CIGALE to reproduce the method described in Krühler et al., 2015 to compute the emission line flux. This modified version of CIGALE computes emission lines fluxes in a 3 steps procedure :

- Definition of the wavelength range of an emission line (λ^{EL}_{min}, λ^{EL}_{max}) satisfying $L_{nebular} > L_{cont} \cdot factor$, with L_{lines} the nebular emission luminosity, L_{cont} the stellar continuum luminosity and $factor$ arbitrarily set to 10^{-3}.
- Computation of the continuum as the average value of two 40 Å regions blueward and redward of λ^{EL}_{min} and λ^{EL}_{max} respectively (illustrated by the black and red lines in Figure V.1).
- Computation of the emission line flux as the area under the green line and above the black line of the Figure V.1.
- The computed emission line flux is not corrected for the host extinction.

This procedure is performed for each template of the SED fitting process.

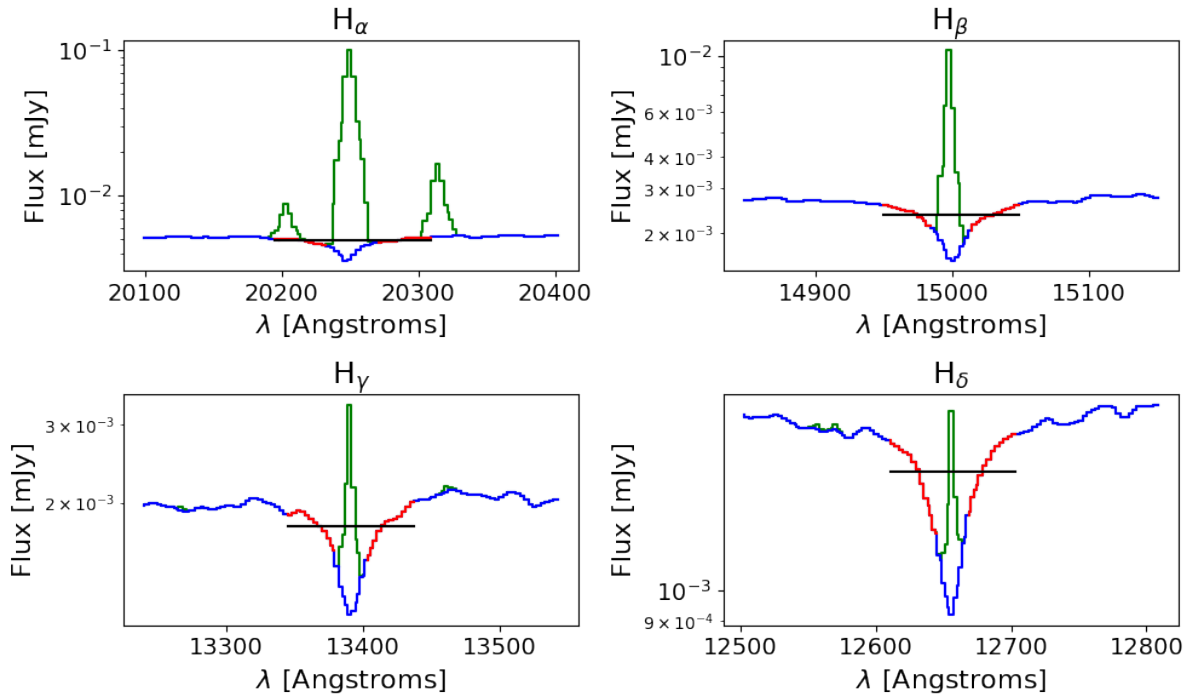

Figure V.1– Balmer emission lines fluxes computed with CIGALE for the best fit of GRBH 080207. The green and blue lines correspond to the nebular emission and stellar continuum respectively. The red lines correspond to 40Å regions where the continuum is estimated. The black line is the mean value of the 2 40Å regions. The final flux computed with CIGALE corresponds to the area between the green and black lines.

In order to integrate the emission lines fluxes comparison to the fitting procedure, the χ^2 is computed in CIGALE as :

$$\begin{aligned} \chi^2_{tot} &= \chi^2_{Broadbands} + \chi^2_{EL} \\ \chi^2_{tot} &= \sum_{i=1}^{N_{Broadbands}} \left(\frac{F^{mod}_{\lambda,i} - F^{obs}_{\lambda,i}}{\sigma^{obs}_i} \right)^2 + \sum_{j=1}^{N_{EL}} \left(\frac{F^{mod}_{\lambda,j} - F^{obs}_{\lambda,j}}{\sigma^{obs}_j} \right)^2 \end{aligned} \tag{V.1}$$

where $F^{obs}_{\lambda,i}$ and $F^{obs}_{\lambda,j}$ are the fluxes measured from the photometric broadbands and for the emission lines respectively. $F^{mod}_{\lambda,i}$ and $F^{mod}_{\lambda,j}$ correspond to the fluxes computed with CIGALE for the photometric broadbands and emission lines respectively. The broadbands and emission lines fluxes are expressed in mJy and 10^{-17} erg.cm^{-2}.s^{-1} respectively, so that they have about the same order of magnitude in order not to give too much weight to one of the two χ^2.

2.2. Choice of parameters

The main parameters and range of input values are reported in Table V.2. As in our previous work, we have adopted a delayed star formation rate (SFR $\propto$ t/τ_0^2 · e$^{-t/\tau_0}$), on top of which a young burst of constant star formation with a free age and amplitude is added (see left panel of Figure V.2). This scenario aims at reproducing both the general star formation history of distant galaxies (i.e. Lee et al. 2010 ; Maraston et al. 2010 ; Pforr et al. 2012) and a possible recent burst of star formation. The SFH

including young and old stellar populations is defined as :

$$SFR(t) \propto \begin{cases} \frac{t}{\tau_0^2} \cdot e^{-t/\tau_0} & \text{if } t < t_0 - t_1 \\ \frac{t}{\tau_0^2} \cdot e^{-t/\tau_0} + k \cdot e^{-(t-t_0+t_1)/\tau_1} & \text{if } t \geq t_0 - t_1 \end{cases} \tag{V.2}$$

with t_0 the age of the main stellar population and t_1 the beginning of the recent episode of star formation, τ_0 and τ_1 the peak of stellar formation for the main population and the burst respectively. The amplitude of the burst episode, k, is linked to the fraction of mass, f_{burst}, created during the burst as :

$$k = \frac{f_{burst}}{1 - f_{burst}} \cdot \frac{\sum_{t=0}^{t_0} \frac{t}{\tau_0^2} \cdot e^{-t/\tau_0}}{\sum_{t=t_0-t_1}^{t_0} e^{-(t-t_0+t_1)/\tau_1}} \tag{V.3}$$

The age of the main stellar population is free to vary from 1 Gyr up to 8 Gyrs. The peak of the star formation is free to vary from 1 to 10 Gyrs which allows to model various shape from nearly constant SFH (high τ) to a rising or declining exponential SFH (see Figure V.2).

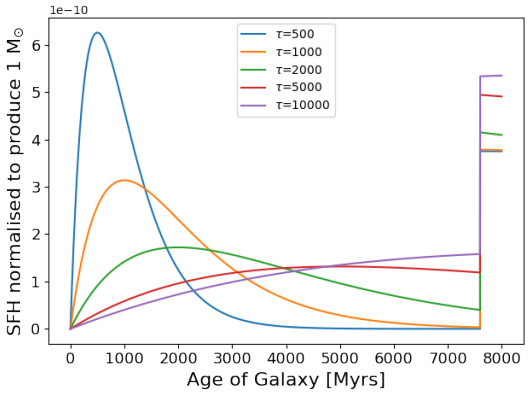

Figure V.2– Delayed SFH + recent burst of star formation, normalised to produce 1 solar mass. Delayed SFH with a recent burst defined with an age of 400 Myrs and τ_b=10^6 Myrs.

Balmer lines and UV continuum are probing the recent star formation, with a typical age lower than 100 Myrs [Boquien et al., 2014], the age of the burst (i.e. the young stellar population) is allowed to vary from 1 Myr to 100 Myr. The fraction of stellar mass in the recent burst is allowed to vary from 0 to 50% of the main stellar population with a smaller sampling between 0 and 10%.

The initial mass function of Chabrier, 2003 is adopted with the stellar synthesis models of Bruzual et Charlot, 2003. The metalliciy is not well constrained by broadband photometry, and so we decided to fixed the metallicity to be the closest value to the measurements (see Table V.1). The measurements were made using the method in Maiolino et al., 2008 which expressed the metallicity using the oxygen abundance, 12+log(O/H), with the solar value being 12+log(O/H)=8.69 [Asplund et al., 2009]. In CIGALE the metallicity is defined with the mass fraction and the available values for the stellar synthesis models of Bruzual et Charlot, 2003 are Z=0.0001, 0.0004, 0.004, 0.008, 0.02 (solar value) and 0.05. Given the measurements span the range $8.34 < 12+\log(O/H) < 9.12$, we choose the metal mass fraction to be either 0.008, 0.02 or 0.05. In CIGALE, the metallicity is assumed to be the same for the stellar sources and the gas.

The dust attenuation is modelled differently for the nebular emission and the stellar continuum. For

the stellar continuum, we use the SBL18 recipe defined in Section IV.2.1.2, which offers the possibility of varying the steepness of of the original starburst law [Calzetti et al., 2000] and adding a bump centered at 2175Å. The nebular emission (and therefore the Balmer lines) is attenuated assuming a simple screen model, adopting a Milky Way extinction curve using the formalism of Cardelli et al., 1989 with R_V=3.1 and a color excess $E(B-V)_{lines}$. The nebular and stellar emission attenuation models are linked through the ratio $E(B-V)_{stars}/E(B-V)_{lines}$ with $E(B-V)_{stars}$ the color excess applied to the stellar continuum.

The input parameters to model the dust attenuation are the color excess of the nebular emission $E(B-V)_{lines}$, the ratio $E(B-V)_{stars}/E(B-V)_{lines}$, and the slope, δ, of the attenuation curve applied to the stellar continuum. The values adopted for the input parameters are summarised in Table V.2. $E(B-V)_{lines}$ is varying from 0.01 to 2.0 mag. The ratio was found to be 0.44 for local starburst in Calzetti, 2001 but recent works found more similar values between the ionised gas and the stellar continuum for high-z galaxies [Kashino et al., 2013; Puglisi et al., 2016]. Consequently, we let this ratio vary between 0.2 and 1. The slope, δ, is free to vary between -1 and 0.5 covering the range of values found in Section IV.2.3.3. As seen in Buat et al., 2018; Corre et al., 2018 it is extremely challenging to detect a UV bump with wide broadband photometry only, so for this analysis, no bump was added with the exception of GRBH 070802 [Corre et al., 2018]. In the following the attenuation of the continuum obtained from the SED fitting will be denoted A_V^{stars}.

The stellar emission absorbed by dust is re-emitted in the IR, using IR templates from Dale et al., 2014 which are parametrised with a single parameter α_{IR} corresponding to the exponent of the distribution of heating intensity over dust mass. A single template ($\alpha_{IR} = 2$) is used except for galaxies detected in the MIR or FIR for which different α_{IR} between 1 and 3 are tested to cover the range of values found from quiescent to active star-forming galaxies (Dale et Helou 2002). Using [NII]/H_α and [OIII]/H_β ratios to separate star-forming galaxies and AGNs in the Baldwin-Phillips-Terlevich (BPT) classification diagram [Baldwin et al., 1981; Kewley et al., 2001], Krühler et al., 2015 did not find any GRBH in the AGNs region. Consequently, IR templates are used without AGN contribution.

In the radio domain, where some of the GRBHs have been detected, the emission is due to both thermal processes and non–thermal processes. The former ones are related to the ionisation of the gas by massive stars and the latter ones to the acceleration of charged particle through a magnetic field, i.e. a synchrotron emission. The thermal emission in the radio domain is already modelled by the nebular continuum emission. The synchrotron emission is modelled using the correlation between the radio flux at 1.4GHz and the total IR luminosity, q_{TIR}, and a power-law spectral slope α normalised at 1.4GHz. q_{TIR} is defined as :

$$q_{TIR} \equiv log_{10}\left(\frac{L_{TIR}}{3.75 \cdot 10^{12} Hz}\right) - log_{10}\left(\frac{L_{1.4GHz}}{W.Hz^{-1}}\right) \tag{V.4}$$

with L_{TIR} the total IR (8-1000 μm) luminosity and $L_{1.4GHz}$ the luminosity at 1.4 GHz. Knowing the total IR luminosity, q_{TIR} is used to compute the flux at 1.4GHz which gives the normalisation of the power-slope law for the non-thermal flux as :

$$F_{non-thermal} \propto \left(\frac{\nu_{1.4GHz}}{\nu}\right)^{\alpha} \cdot \frac{L_{TIR}}{10^{q_{TIR}}} \tag{V.5}$$

This simple recipe is assuming that the spectrum is dominated by non-thermal emission at 1.4GHz [Condon, 1992; Yun et al., 2001; Bell, 2003]. When no or few other data are available in the FIR domain, it can also help to constrain the IR emission. At most, GRBHs are detected in one band in the

Table V.2– Input parameters for SED fitting with CIGALE

Parameter	Symbol	Range
Dust attenuation		
Color excess for nebular emission[1]	$E(B-V)_{\rm lines}$	0.01,0.05, 0.1 to 2.0 with steps of 0.1 mag
Ratio of color excess	$\frac{E(B-V)_{stars}}{E(B-V)_{lines}}$	0.2, 0.4, 0.6, 0.8, 1.0
Attenuation curve for stellar continuum[2]	δ	[-1 :+0.5] per bin of 0.1
Delayed star formation history + recent burst		
Age of the main stellar population	t_0	1000, 2000, 3500, 5000, 8000 Myr
Peak of the star formation (delayed SFH)	τ	1000, 2000, 3000, 5000, 7000, 10000 Myr
Age of the burst	$t_{\rm b}$	1, 3, 5, 10, 15, 20, 30, 40, 50, 75, 100 Myr
Stellar mass fraction due to the burst	$f_{\rm b}$	0, 0.01, 0.03, 0.05, 0.075, 0.1, 0.15, 0.20
		0.25, 0.3, 0.35, 0.4, 0.45, 0.50
Dust emission in the IR		
powerlaw slope $dU/dM_d \propto U^{\alpha}$ [4]	α_{IR}	1.0, 1.5, 2.0, 2.5, 3.0
Non-thermal radio emission		
TIR/radio luminosities ratio	q_{TIR}	1.5, 2.0, 2.5, 3.0
Metallicity[3]	Z	0.008, 0.02

[1] $E(B-V)_{\rm lines}$ is the color excess between the B and V bands applied on the nebular emission lines.
[2] Defined in Eq.IV.3
[3] The metallicity is set to one of the 2 values (Z=0.02 being the solar metallicity)
[4] M_d corresponds to the dust mass heated by the the radiation field intensity U. α_{IR} is fixed to 2 when no IR detection is available.

radio domain, so we fixed α to 0.7 and q_{TIR} to 2.5 which are typical values for star-forming galaxies [Delhaize et al., 2017]. When there is one detection in the FIR and radio, q_{TIR} is allowed to vary between 1.5 and 3 to [Delhaize et al., 2017]. Starbursting galaxies are expecting to be IR-excess sources, meaning high q_{TIR} ∼3 [Galvin et al., 2018].

2.3. Results

The main results are reported in Table V.3. For each GRBH, CIGALE was run for the 2 metallicities, Z=0.008 and 0.02, and we kept the one returning the best χ^2. For GRBHs 060306 and 090407 with high metallicity measurement, CIGALE was also run with Z=0.05. If the mass fraction, f_{burst}, created during the burst is compatible with 0 we ran CIGALE again, this time with a delayed SFH without any recent burst of stellar formation and kept the results as the reference.

From Figure V.3 we see that most GRBHs have SFR [1] and $E(B-V)_{lines}$ in good agreement with the SFR_{α} and $E(B-V)_{Balmer}$ derived from Balmer emission lines when available. They are only marginally consistent for GRBH 100621A and not consistent for 051022A and 071021. For GRBH 051021 the power-law slope of the dust attenuation is not constrained (see Appendix D.3) and for GRBH 071021 the SFR is one order of magnitude higher than the $FR_{H_{\alpha}}$. They will not be included in the following qualitative analysis.

As seen in Table V.3, 4 out of the 23 GRBHs have a burst fraction clearly not compatible with 0, meaning that a recent burst of star formation is clearly required to reproduce the observed SED of these GRBHs. For 5 other GRBHs, the burst fraction is also not compatible with 0 but not by much. For For

Table V.3– Summary of SED fitting results. Columns list (1) the galaxy identification, (2) SFR averaged over the past 10Myrs, (3) SFR derived from H_α luminosity measurement, (4) stellar mass, (5) amount of attenuation in the V band, (6) slope of the attenuation curve, (7) color exces for the nebular emission, (8) Balmer decrement, (9) ratio of color excess, (10) metallicity returning the best fit, (11) fraction of total stellar mass created in the burst.

GRBH	SFR	SFR_{H_α}	$M_\star$	A_V	δ	$E(B-V)_{lines}$	$E(B-V)_{Balmer}$	$\frac{E(B-V)_{cont}}{E(B-V)_{lines}}$	Z	f_{burst}
	$M_\odot$ yr^{-1}	$M_\odot$ yr^{-1}	$10^9 M_\odot$	mag	slope	mag	mag			%
(1)	(2)	(3)	(4)	(5)	(6)	(7)	(8)	(9)	(10)	(11)
050915A	277.96 ± 251.03	$196.00^{+1563.00}_{-174.00}$	28.95 ± 11.92	1.69 ± 0.66	-0.08 ± 0.19	0.85 ± 0.30	$0.84^{+0.61}_{-0.60}$	0.47 ± 0.11	0.02	0.16 ± 0.15
051022A	36.68 ± 7.91	$60.00^{+12.00}_{-10.00}$	9.70 ± 3.44	0.64 ± 0.11	-0.85 ± 0.13	0.38 ± 0.08	$0.56^{+0.05}_{-0.04}$	0.72 ± 0.13	0.02	0.15 ± 0.14
060306	25.89 ± 8.40	$17.60^{+83.60}_{-11.00}$	19.40 ± 4.49	0.90 ± 0.26	-0.31 ± 0.19	0.51 ± 0.32	$0.44^{+0.69}_{-0.40}$	0.68 ± 0.24	0.05	-
060319	14.40 ± 7.38	-	15.03 ± 3.31	1.38 ± 0.39	0.24 ± 0.15	0.50 ± 0.20	-	0.55 ± 0.23	0.008	-
060814	66.71 ± 21.53	$54.00^{+89.00}_{-19.00}$	33.77 ± 8.31	1.00 ± 0.33	0.31 ± 0.23	0.30 ± 0.12	$0.17^{+0.39}_{-0.17}$	0.55 ± 0.19	0.008	-
060912A	6.33 ± 1.81	$5.10^{+2.60}_{-1.60}$	6.55 ± 1.24	0.32 ± 0.15	-0.51 ± 0.31	0.16 ± 0.09	$0.16^{+0.10}_{-0.09}$	0.76 ± 0.20	0.02	-
061121	51.65 ± 13.14	$44.20^{+19.00}_{-10.00}$	6.93 ± 2.37	1.02 ± 0.23	0.05 ± 0.19	0.46 ± 0.10	$0.57^{+0.22}_{-0.22}$	0.42 ± 0.09	0.008	0.26 ± 0.16
070306	119.81 ± 28.17	$101.00^{+24.00}_{-18.00}$	17.62 ± 5.59	1.58 ± 0.18	0.32 ± 0.16	0.53 ± 0.09	$0.43^{+0.08}_{-0.07}$	0.44 ± 0.08	0.008	0.15 ± 0.14
070521	49.93 ± 14.58	$26.00^{+34.00}_{-17.00}$	23.99 ± 5.50	1.41 ± 0.31	-0.34 ± 0.17	0.80 ± 0.39	-	0.67 ± 0.25	0.02	-
070802	23.81 ± 12.16	$24.00^{+11.00}_{-8.00}$	4.22 ± 1.80	0.79 ± 0.30	-0.14 ± 0.35	0.32 ± 0.15	$0.31^{+0.12}_{-0.12}$	0.62 ± 0.21	0.008	0.16 ± 0.15
071021	187.20 ± 51.74	$32.00^{+20.00}_{-12.00}$	107.60 ± 27.76	2.24 ± 0.25	0.15 ± 0.06	0.76 ± 0.11	$0.19^{+0.16}_{-0.17}$	0.61 ± 0.07	0.02	-
080207	120.73 ± 11.19	$77.00^{+86.00}_{-38.00}$	47.95 ± 6.20	1.86 ± 0.12	-0.33 ± 0.08	0.97 ± 0.11	$0.66^{+0.28}_{-0.25}$	0.62 ± 0.07	0.02	-
080325	66.09 ± 24.30	-	55.85 ± 9.22	1.96 ± 0.25	-0.00 ± 0.08	0.76 ± 0.23	-	0.66 ± 0.19	0.008	-
080605	46.19 ± 19.81	$47.00^{+17.00}_{-12.00}$	11.06 ± 4.20	0.45 ± 0.28	-0.05 ± 0.39	0.20 ± 0.14	$0.26^{+0.11}_{-0.10}$	0.55 ± 0.22	0.02	0.15 ± 0.14
080607	40.72 ± 11.20	-	30.09 ± 9.30	1.59 ± 0.26	0.08 ± 0.10	1.04 ± 0.58	-	0.47 ± 0.29	0.02	-
080805	27.57 ± 15.93	$45.00^{+79.00}_{-26.00}$	3.34 ± 1.67	1.25 ± 0.36	-0.47 ± 0.27	0.56 ± 0.19	$0.78^{+0.39}_{-0.31}$	0.75 ± 0.18	0.02	0.20 ± 0.16
081109	11.79 ± 4.17	$11.80^{+4.10}_{-2.90}$	17.86 ± 3.49	0.47 ± 0.21	-0.14 ± 0.26	0.30 ± 0.11	$0.36^{+0.11}_{-0.10}$	0.39 ± 0.10	0.02	-
081221	75.12 ± 20.27	$35.00^{+106.00}_{-22.00}$	33.13 ± 7.06	1.48 ± 0.27	0.02 ± 0.10	0.75 ± 0.16	$0.31^{+0.55}_{-0.31}$	0.46 ± 0.12	0.02	-
090407	14.06 ± 4.87	$13.80^{+18.80}_{-6.70}$	10.54 ± 2.79	1.18 ± 0.26	-0.50 ± 0.17	0.68 ± 0.13	$0.69^{+0.34}_{-0.26}$	0.63 ± 0.08	0.02	-
090417B	0.87 ± 0.27	-	4.29 ± 0.84	0.53 ± 0.14	-0.43 ± 0.19	0.41 ± 0.25	-	0.58 ± 0.29	0.008	-
090926B	12.86 ± 4.73	$26.00^{+19.00}_{-11.00}$	13.00 ± 2.96	0.37 ± 0.19	-0.57 ± 0.29	0.44 ± 0.20	$0.63^{+0.20}_{-0.18}$	0.24 ± 0.10	0.008	-
100621A	11.80 ± 2.20	$8.70^{+0.80}_{-0.80}$	1.18 ± 0.52	0.34 ± 0.11	-0.39 ± 0.22	0.14 ± 0.06	$0.05^{+0.03}_{-0.03}$	0.83 ± 0.20	0.02	0.29 ± 0.14
120119A	43.05 ± 16.57	$43.00^{+24.00}_{-14.00}$	3.30 ± 1.31	1.07 ± 0.28	-0.29 ± 0.19	0.38 ± 0.13	$0.35^{+0.16}_{-0.14}$	0.81 ± 0.18	0.008	0.27 ± 0.16

GRBH 060306 the oxygen abundance measured in KRÜHLER et al., 2015 is very high and we found that a metallicity of Z=0.05 returns a better fit compared to Z=0.02.

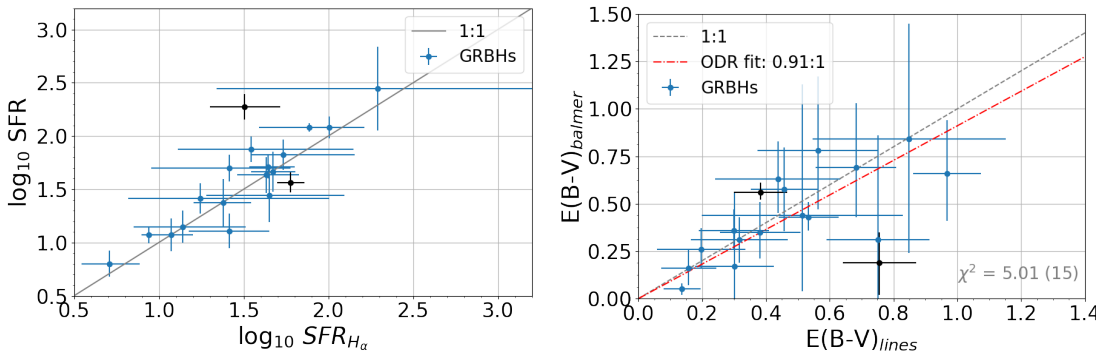

Figure V.3– *Left* : SFR as a function of the SFR_{H_α}. *Right* : $E(B-V)_{lines}$ as a function of $E(B-V)_{Balmer}$

An example of best fit SED can be seen in Figure V.4. The best fit SED of all the GRBHs can be seen in Appendix D.2. The probability distribution function of the power-law slope, δ, for the dust attenuation modelling of stellar continuum can be seen in Appendix D.3.

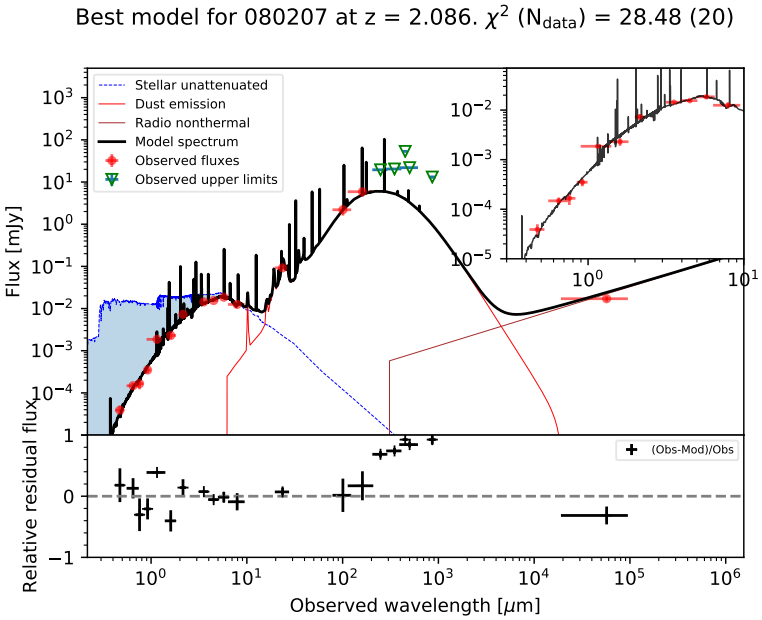

Figure V.4– Best-fitted SED for GRBH 080207. Red points are the observed fluxes with their uncertainties. The black line represents the best fitted spectrum composed of attenuated stellar emission, dust emission, non-thermal radio emission and nebular lines. The dashed blue line represents the unattenuated stellar emission and the blue shaded area indicates the amount dust attenuation. The green triangle correspond to upper limit in flux. The lower panel shows the relative residual.

2.3.1. Localisation of the GRBHs on the Main Sequence

In Figure V.5, we report the excess of SFR of our GRBHs comparing to the Main Sequence using the relation in SCHREIBER et al., 2015 for given stellar masses. If we consider starburst galaxies those with a SFR excess higher than 4, then only 6 GRBHs satisfy this criteria : 051022A, 061121, 070306, 080805, 100621A, 120119A. As seen in the next section, GRBH 100621A is quite sensitive to the adopted SFH and further checks are required for this galaxy. We note that our SFR is only marginally consistent with

[1]. SFR refers to the SFR averaged over the past 10 Myrs in CIGALE.

the SFR_{H_α} due to a higher H_α flux estimation, this could decrease the SFR excess we find here. In the literature, Krühler et al., 2011 found similar SFR estimation and slightly stellar mass than ours, leading to an SFR excess of $\sim$ 23, Vergani et al., 2015 found a similar stellar mass and higher SFR estimates than ours leading to a SFR excess of $\sim$39.

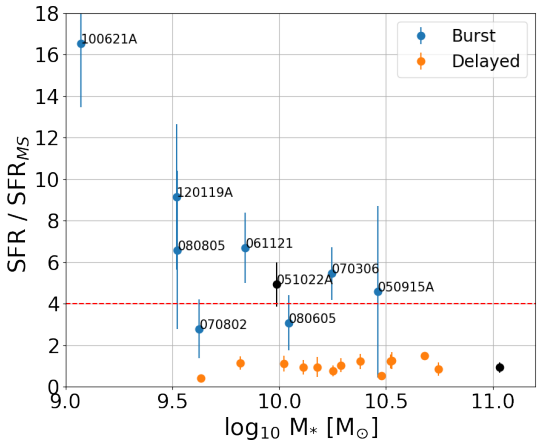

Figure V.5– Excess of SFR comparing to the Main Sequence as a function of the stellar mass. The Main Sequence is computed following the prescription in Schreiber et al., 2015. The blue points correspond to the GRBHs best fitted with a delayed+burst SFH. The orange points correspond to the GRBHs best fitted with a delayed SFH. Black points correspond to GRBH 051022A and 071021. The red dashed line correspond to an excess of 4. We define starburst galaxies those having a SFR excess higher than 4.

2.3.2. GRBHs attenuation and SD16 RT model

We have seen in Section IV.2.3 that a given combination of dust attenuation parameter values, especially $E(B-V)_{continuum}$ and δ, can give information on the type of dust and the global structure of the ISM of the galaxy. In Figures V.6 to V.8 we report the $E(B-V)_{continuum}$-δ values of our SED fitting to the parameter space of the RT model of Seon et Draine, 2016 for the WG-SMC, WD-LMC and WD-MW dust models respectively. We did not consider the WD-SMC and WG-MW dust models as our attenuation recipe does not fit accurately enough the shape of the attenuation curves for these types of dust.

2.3.2.a. Type of dust

First regarding the type of dust, we note that all the GRBHs, represented by the red errorbars, can be reproduced by WG-SMC and WD-MW dust models with the exception of one GRBH (060814) at the bottom left with a flat attenuation curve (δ=0.31) associated with low $E(B-V)_{continuum}$ $\sim$0.15 mag. The WD-LMC dust model can not reproduce the GRBHs located in the bottom left part of the Figure V.8 corresponding to flat attenuation curves ($\delta \gtrsim 0$) with low color excess ($E(B-V)_{continuum} \lesssim 0.25$). However, for the WD-LMC there are more values of M_s and R_s/R_d than the WG-SMC and WD-MW dust models able to produce steeper attenuation curves ($\delta \lesssim$ -0.4) associated to rather high color excess ($E(B-V)_{continuum} \gtrsim 0.4$).
We conclude that both WD-MW and WG-SMC dust models can explain the data, and that the WD-LMC failed to reproduce flat attenuation curve with low color excess.

2.3.2.b. Dust-star geometry and local dust distribution.

Now regarding the geometries, there is a great variety of configurations and not one single geometry which could explain all the GRBHs. From the bottom panels of Figure V.6, we see that steep (flat) attenuation curves are associated to low (high) optical depth, this is true for all dust models.

From the top panel of Figure V.6, we see that GRBHs with steep attenuation curves with $\delta \lesssim$ -0.25 are only reproduced by dark blue points, meaning that only an homogeneous dust distribution can reproduced them. GRBHs having very flat attenuation curves with $\delta \gtrsim$0.25, are only reproduced by yellow-green points corresponding to a clumpy ISM. For GRBHs having -0.25$\gtrsim \delta \lesssim$0.25, both clumpy and homogeneous ISM are found. The same conclusion can be drawn for the WD-MW dust model but not for the WD-LMC one.

From the middle panel of Figure V.6, we see that GRBHs with the flattest attenuation curves ($\delta \gtrsim$0.25), are only reproduced by yellow points corresponding to R_s/R_d=1 meaning that no dust layer is surrounding the stellar sources. The other GRBHs can not be reproduced by yellow points corresponding to R_s/R_d=1, meaning that a layer of dust is surrounding the stellar sources. The same conclusion can be drawn for the WD-MW dust model but not for the WD-LMC one.

We conclude that for the WD-MW and WG-SMC dust models, GRBHs with steep attenuation curves ($\delta \lesssim$ -0.25) are best reproduced by an homogeneous local dust distribution, dust layer surrounding the stellar sources and a low optical depth. GRBHs with flat attenuation curves ($\delta \gtrsim$ 0.25) are best reproduced by a clumpy local dust distribution, R_s/R_d=1 and a high optical depth. Such general trends are not seen for the WD-LMC dust model, and each GRBH needs to be studied individually. If the extinction curve along the GRB line of sight was measured and covering rest-frame UV to optical/NIR, the presence or absence of a UV bump and the steepness of the FUV rise could allow to rule out some of the dust models and therefore to draw stronger conclusions on the geometrical can be drawn, as in Corre et al., 2018.

Our conclusions on the type of dust and the geometry of the ISM for the GRBHs are based on the SD16 RT model which assumed a spherical geometry. It will be interesting to perform the same analysis with a RT model using a different geometry.

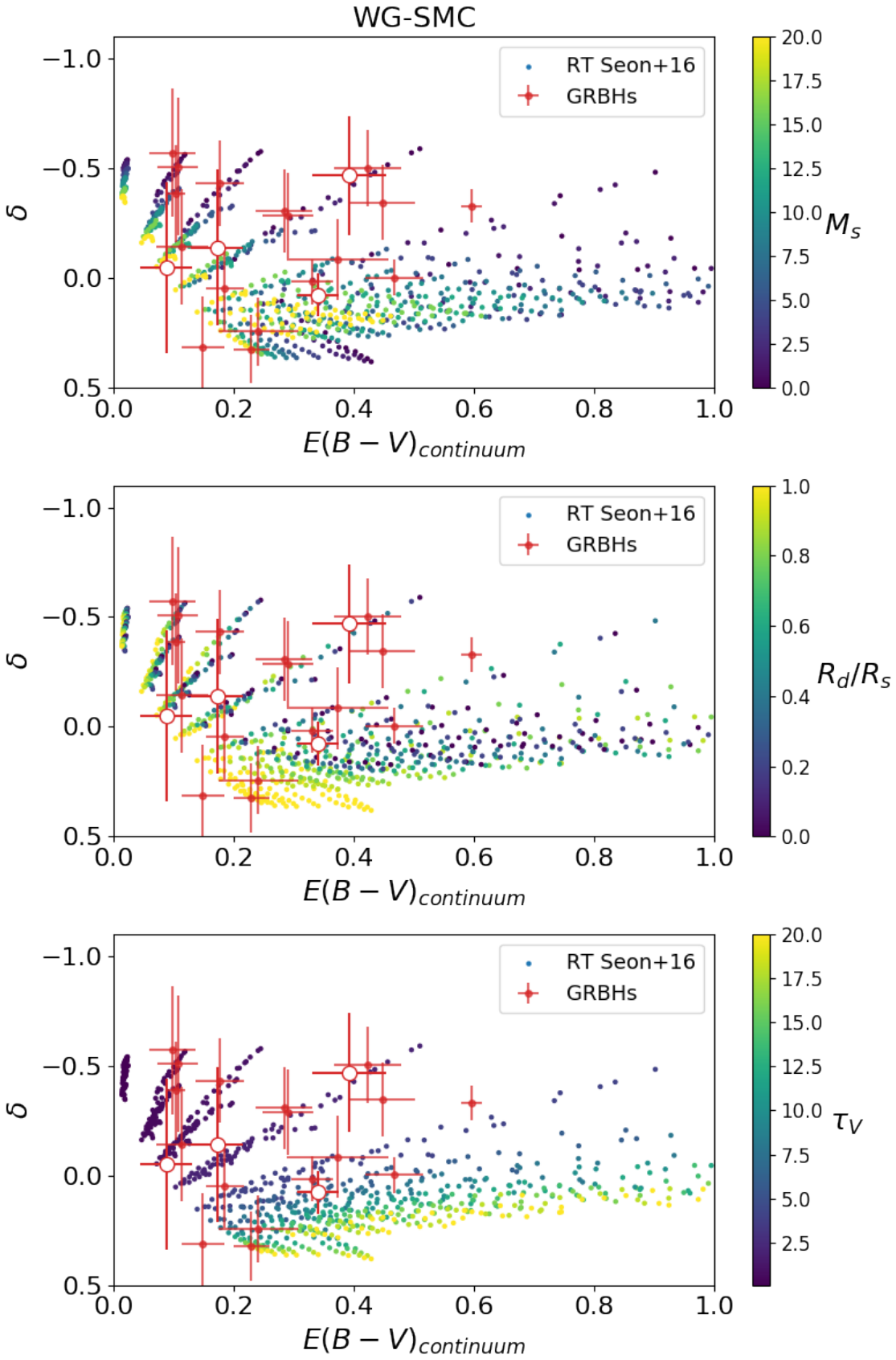

Figure V.6– δ-$E(B-V)_{continuum}$ relation for the WG-SMC dust model. From top to bottom, the color encodes the clumpiness of the ISM with low (high) M_s corresponding to an homogeneous (clumpy) local dust distribution, the R_s/R_d and the optical depth (τ_V). The points correspond to the best fit values of the SD16 attenuation curves. The red error bars correspond to the mean values and their uncertainties found with our SED fitting. The empy red points correspond to GRBHs with a spectroscopically confirmed UV bump in their GRB extinction curve.

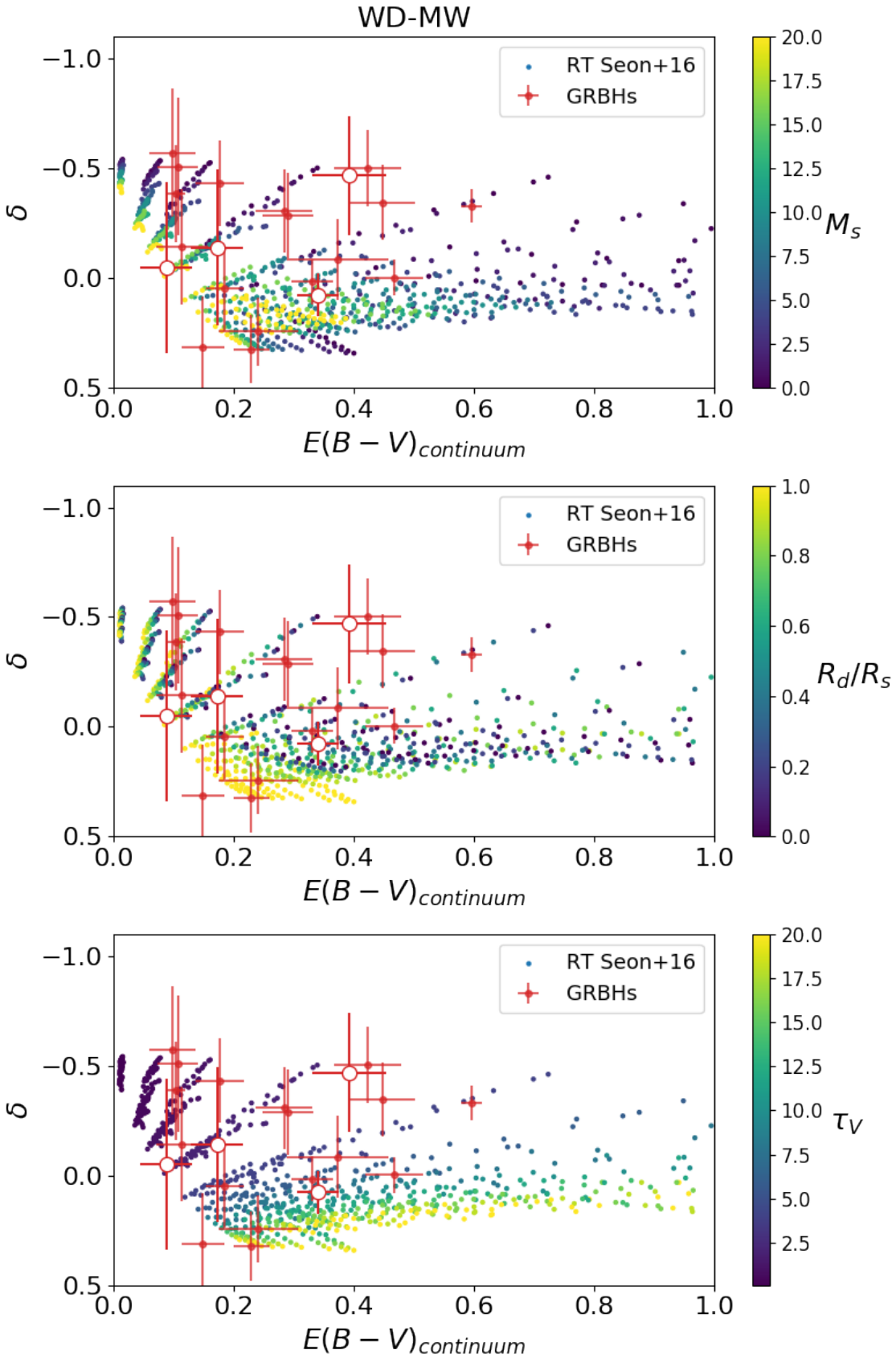

Figure V.7– Same as Figure V.6 but for the WD-MW dust model.

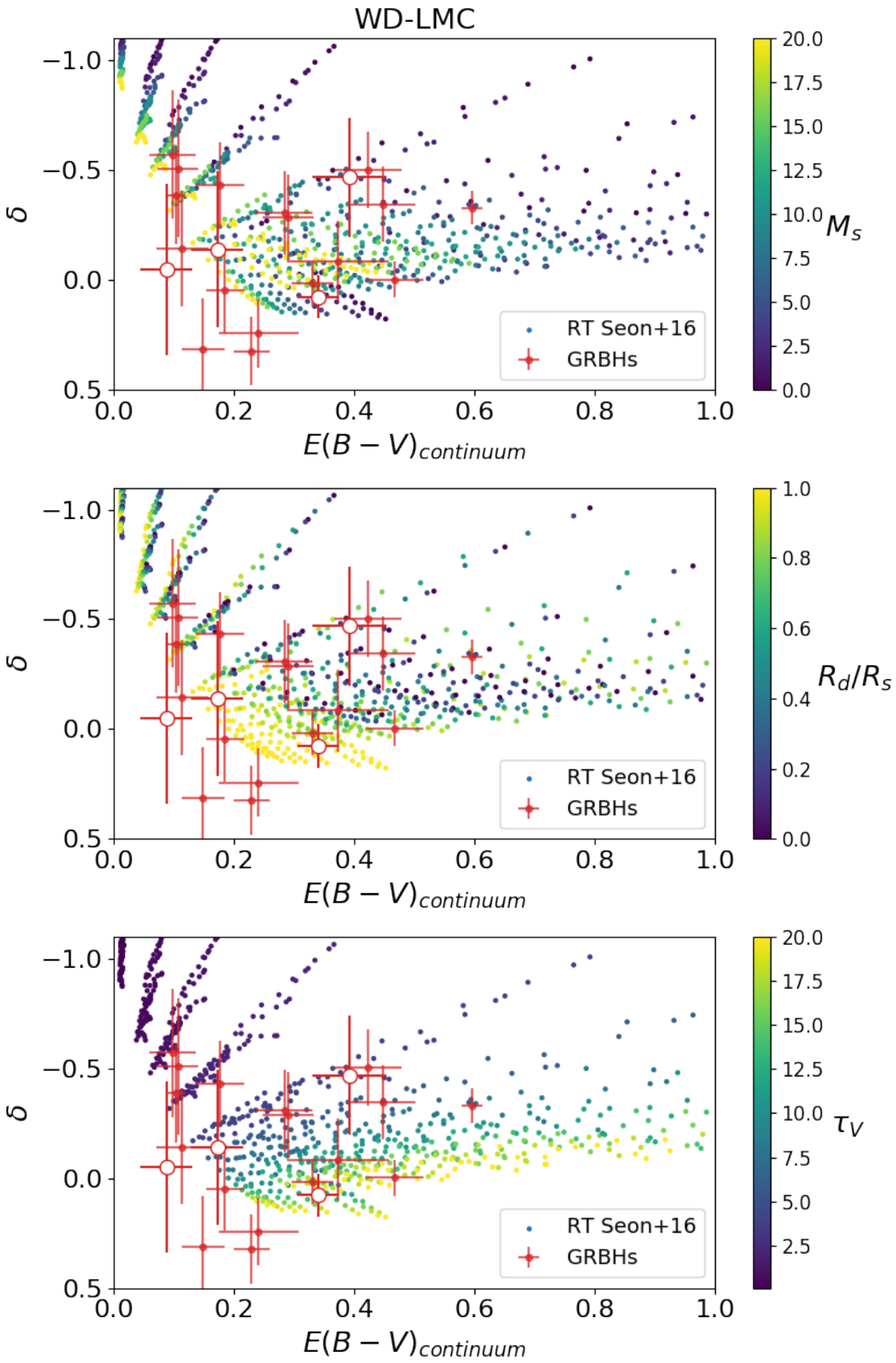

Figure V.8– Same as Figure V.6 but for the WD-LMC dust model.

2.3.3. Correlations of dust parameters with GRBH physical parameters

Now we search for relations between dust properties and physical parameters of the galaxies in order to understand the influence of the environment on the shape of the attenuation curves.

2.3.3.a. Attenuation curve slope vs A_V^{stars}.

From the RT simulations we have seen in Section IV.2.3 that the parameter influencing the most the shape of the attenuation curve is the optical depth. Consequently, we began to search for a correlation between δ and A_V^{stars}. As we can see in Figure V.9, attenuation becomes flatter (steeper) as A_V increases (decreases). The general trend is similar, although with a large dispersion, with the mean relations of Chevallard et al., 2013; Salim et al., 2018 obtained respectively using different RT simulations and from observations of local galaxies, but our averaged trend is above their relations. In order to understand the origin of this difference, we have first checked that the combination of (δ, A_V) values found for our GRBHs are allowed by the SD16 RT model. The relation of Chevallard et al., 2013 is derived as the mean relation of a compilation of RT models [Silva et al., 1998; Tuffs et al., 2004; Pierini et al., 2004; Jonsson et al., 2010] which have different MW dust grain properties but none of them have properties similar to the WD-LMC of Weingartner et Draine, 2001 ones. As seen in Figure IV.21, the averaged δ-A_V relation for the WD-MW and WG-SMC are in a good agreement with the relation of Chevallard et al., 2013, however the WD-LMC dust model gives an averaged trend above the relation of Chevallard et al., 2013. The difference might then be at least partly explained by different dust types in the GRBHs.

The relation of Salim et al., 2018 is obtained on a sample of 230 000 galaxies, and for A_V=1.15 and 1.4 mag the steepest attenuation curves in their sample are δ ∼-0.2 and 0. This is still too flat in comparison to our GRBH attenuation curves. In their analysis they fixed the ratio $E(B-V)_{stars}/E(B-V)_{lines}$ to 0.44 and they applied different attenuation to the young and old stellar populations. These differences make a direct comparison with our analysis difficult and uncertain.

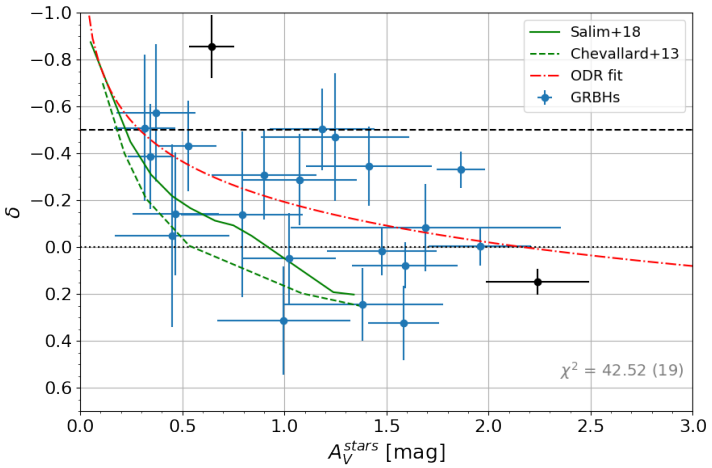

Figure V.9– Slope of the attenuation curve as a function of A_V^{stars}. The blue points are the GRBHs. The dashed dotted red line correspond to an orthogonal distance regression (ODR) fit : δ=(0.57 ± 0.18) $\times log_{10}(A_V)$ -(0.19 ±0.04). The green line is the mean relation found on a sample of ∼ 230000 local galaxies in Salim et al., 2018. The dashed green line represents the average relation found in Chevallard et al., 2013 using different RT simulations. Black points correspond to GRBH 051022A and 071021 and are not included in the ODR fit

2.3.3.b. Attenuation curve slope vs SFR, $M_\odot$ and sSFR.

We now check whether the shape of the attenuation curve varies with the stellar mass, SFR, sSFR and the line broadening, σ, taken from KRÜHLER et al., 2015. σ correlates rather well with the velocity dispersion [RICHARD et al., 2011], which is an indicator of the stellar mass independent of our SED fitting. In Figure V.10, we see that δ correlates with the SFR and stellar mass with more (less) massive and star forming galaxies have flatter (steeper) attenuation curves. As seen in the top right panel, δ correlates well σ, confirming the correlation with the stellar mass. Even if a correlation is found between δ and the SFR and $M_\odot$, no correlation is found with the sSFR. As seen in Figure V.11 we find a correlation between A_V and the stellar mass. As the stellar mass is also correlated to the SFR through the main sequence, it might indicate that A_V is the main driver of the relations between δ and the SFR and $M_\odot$. In Figure V.10, a light gradient in A_V is seen along the δ-axis for the δ-$M_\odot$ diagram. this is less clear in the δ-SFR diagram. In order to conclude whether the main driver of the δ-$M_\odot$ and δ-SFR relations is A_V we would need to study a larger sample of galaxies. For instance, on a more statistically significant sample of 230 000 local galaxies, SALIM et al., 2018 found a clear gradient in δ along the A_V axis for the A_V-log$M_\odot$ relation (their Figure 4), clearly indicating that the correlation δ-$M_\odot$ is driven by A_V and not by physical origins.

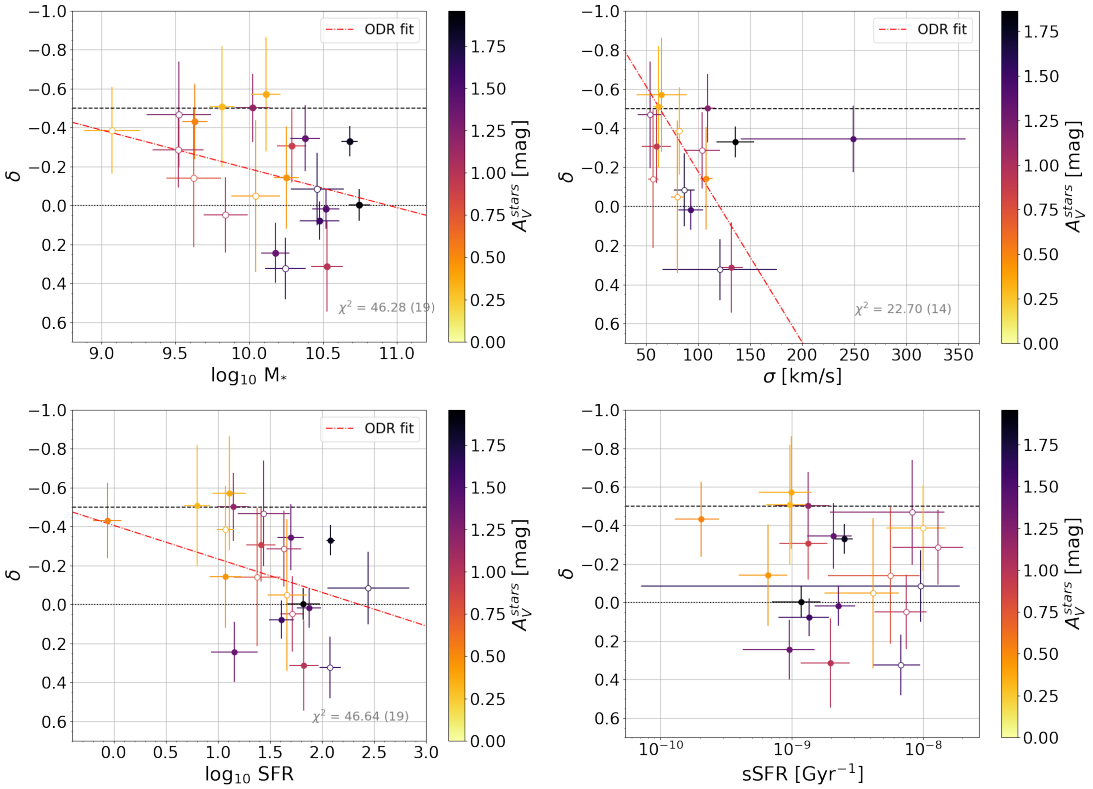

Figure V.10– Slope of the attenuation curve as a function of the stellar mass, line broadening, SFR and sSFR. The line broadening are taken from KRÜHLER et al., 2015. The color encodes A_V^{stars}. The empty and filled circles represent GRBHs best fitted with a delayed+burst and delayed SFH respectively. The ODR fit is represented with the dashed dotted red line.

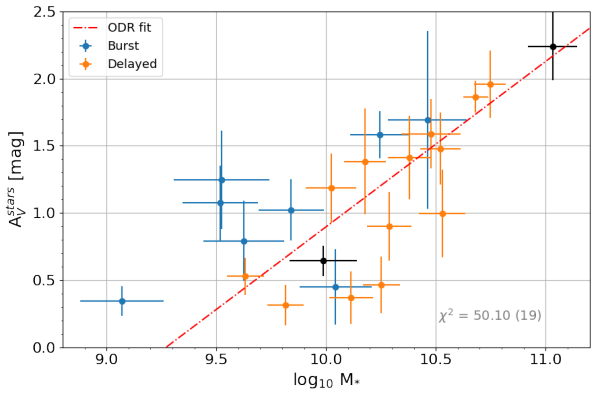

Figure V.11– Amount of attenuation in the V band as a function of the stellar mass. The blue points correspond to the GRBHs best fitted with a delayed+burst SFH. The orange points correspond to the GRBHs best fitted with a delayed SFH. The dashed dotted red line correspond to the ODR fit : A_V^{stars}=0.85 $\times log_{10} M_\odot$ - 7.51. Black points correspond to GRBH 051022A and 071021 and are not included in the ODR fit.

2.3.4. Comparison of the different tracers of dust attenuation

In Figure V.12 we compare the different tracers of the amount of attenuation for the nebular, stellar component and along the GRB line of sight. First we see in the top right panel that A_V^{lines}, computed as $3.1 \times E(B-V)_{lines}$ is very similar to A_V^{Balmer} derived from the Balmer decrement in Krühler et al., 2015. From the top left panel we see a trend between A_V^{Balmer} and A_V^{stars} but the dispersion is large and uncertainties associated to A_V^{Balmer} are too large to draw strong conclusions. The bottom left panel of Figure V.12 illustrates the average ratio $E(B-V)_{continuum}/E(B-V)_{lines}$ for our sample estimated to be 0.56±0.04 with the ODR fit, which is slightly higher than the 0.44 found in Calzetti et al., 1994; Calzetti et al., 2000. Finally in the bottom right panel, we compare the amount of attenuation in the V band averaged over the galaxy with the amount of extinction in the V band along the GRB line of sight. Though the estimation of A_V^{grb} has been performed using different techniques we see that $A_V^{stars} \lesssim A_V^{grb}$ apart from 2 GRBHs.There are cases with A_V^{stars} much smaller than A_V^{grb} indicating that the GRB is likely to be deeply embedded in dust. Due to the introduction of the emission lines, the amount of attenuation is better constrained and the the relation A_V^{stars}=0.71 $\cdot$ A_V^{grb} found in Corre et al., 2018 is revised to A_V^{stars}=0.87 $\cdot$ A_V^{grb} as some A_V^{stars} estimates are a bit higher, but it is clear that this relation is not universal.

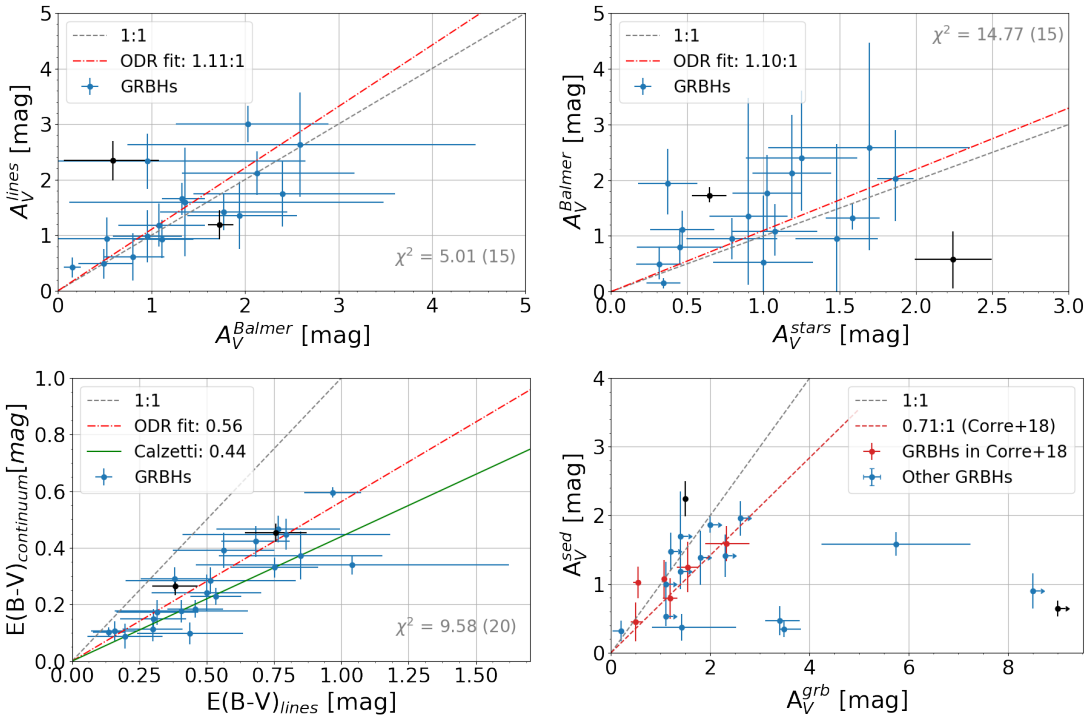

Figure V.12– *Top left :* A_V^{lines} as a function of A_V^{Balmer}. *Top right :* A_V^{Balmer} as a function of A_V^{stars}. *Bottom left :* $E(B-V)_{continuum}$ as a function of $E(B-V)_{lines}$. *Bottom right :* A_V^{stars} as a function of A_V^{grb}. Blue points represents the GRBHs. The dashed dotted red line correspond to the ODR fit. Black points correspond to GRBH 051022A and 071021 and are not included in the ODR fit. Red points in the bottom right panel correspond to GRBHs studied in Corre et al., 2018.

2.4. Robustness of the SED fitting

2.4.1. Influence of SFH

To check whether the choice of the adopted SFH has an influence on the evaluation of the parameters, we report the results of the SED fitting with and without a recent burst of star formation in the Figure V.13. We see that the SFH with a recent burst of star formation history leads to slightly lower stellar mass and higher SFR and A_V as expected. However, the estimation of the slope of the attenuation curve, δ, remains similar for most of the GRBHs except for 070306 and 100621A. For the former one, the attenuation curve remains very flat in both cases so it does not change the qualitative assessment, while for the latter one the shape of the attenuation curve is found extremely flat with the delayed SFH and steep with the delayed+burst SFH. We conclude that apart from GRBH 100621A our results related to the shape of the attenuation curves are not qualitatively influenced by the SFH.

An other point to stress from this Figure is that our stellar mass estimates are generally lower than those derived for the SHOALS survey in D. A. Perley et al., 2016b.

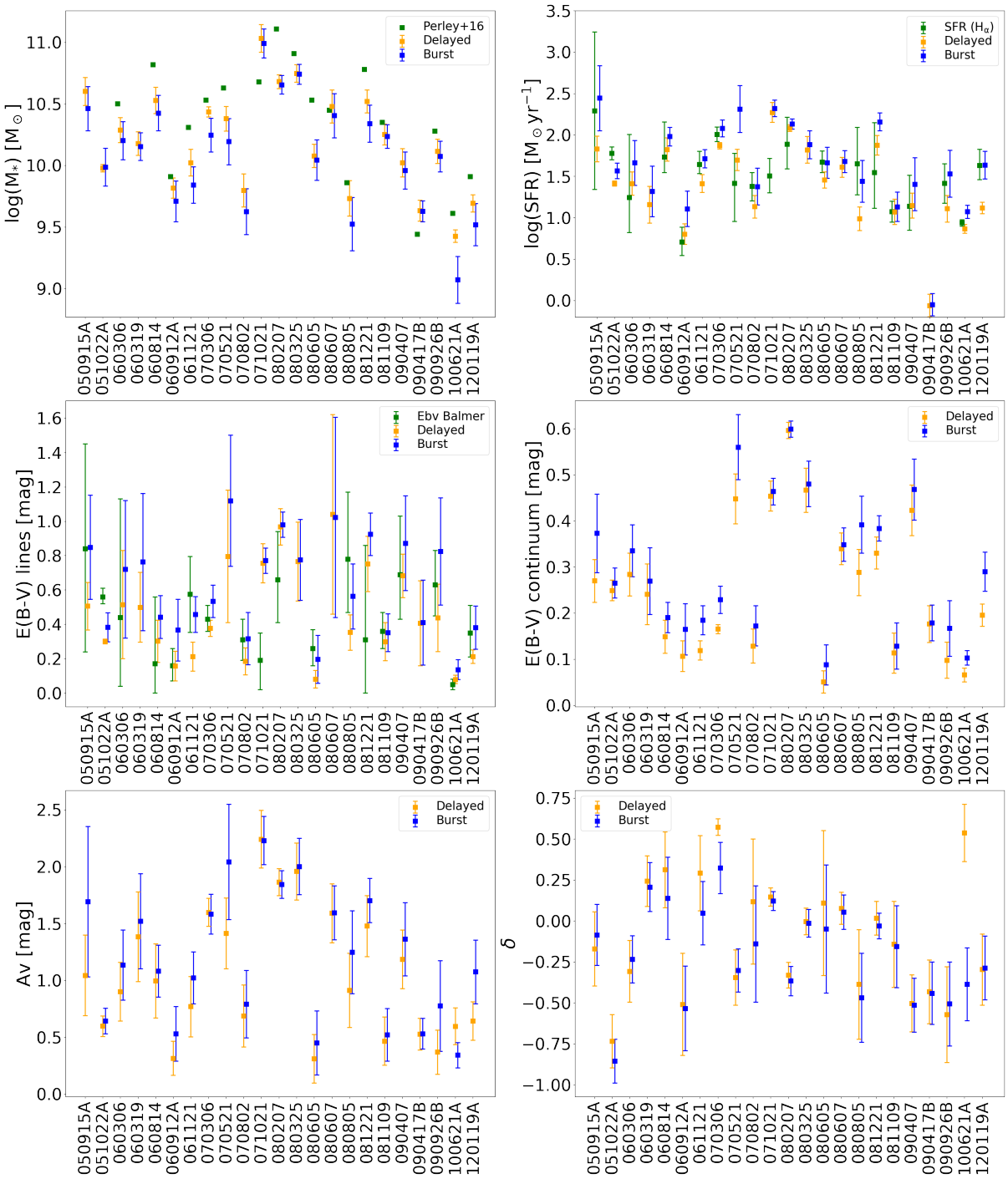

Figure V.13– Comparison of the estimation of parameters for each GRBH depending on the adopted SFH : delayed or delayed+burst. The stellar masses estimated are compared to those derived using the IRAC1 luminosities in D. A. Perley et al., 2016b. The SFRs and $E(B-V)_{lines}$ are compared to SFR_{H_α} and $E(B-V)_{Balmer}$ from H_α in Krühler et al., 2015 ; Vergani et al., 2017.

2.4.2. Influence of emission lines

We also checked whether the introduction of the H_α and H_β emission lines influence the results significantly. From Figure V.14 we see that the introduction of emission lines allows to better constrain emission lines fluxes but the fluxes were already well estimated without. As a consequence the amount of attenuation applied to the nebular emission ($E(B-V)_{lines}$) is better constrained as well as the ratio $E(B-V)_{continuum}/E(B-V)_{lines}$. Apart from few cases, there is little influence on the attenuation of

the stellar emission (A_V^{stars} and $E(B-V)_{continuum}$), and almost no influence on the slope of the attenuation curve. There is also little influence on the stellar mass (not shown in the figure) and on the SFR. We conclude that our results related to the shape of the attenuation curves are not influenced by the introduction of the emission lines but that $E(B-V)_{lines}$ and the ratio $E(B-V)_{continuum}/E(B-V)_{lines}$ are much better constrained with the introduction of the emission lines in the fitting procedure.

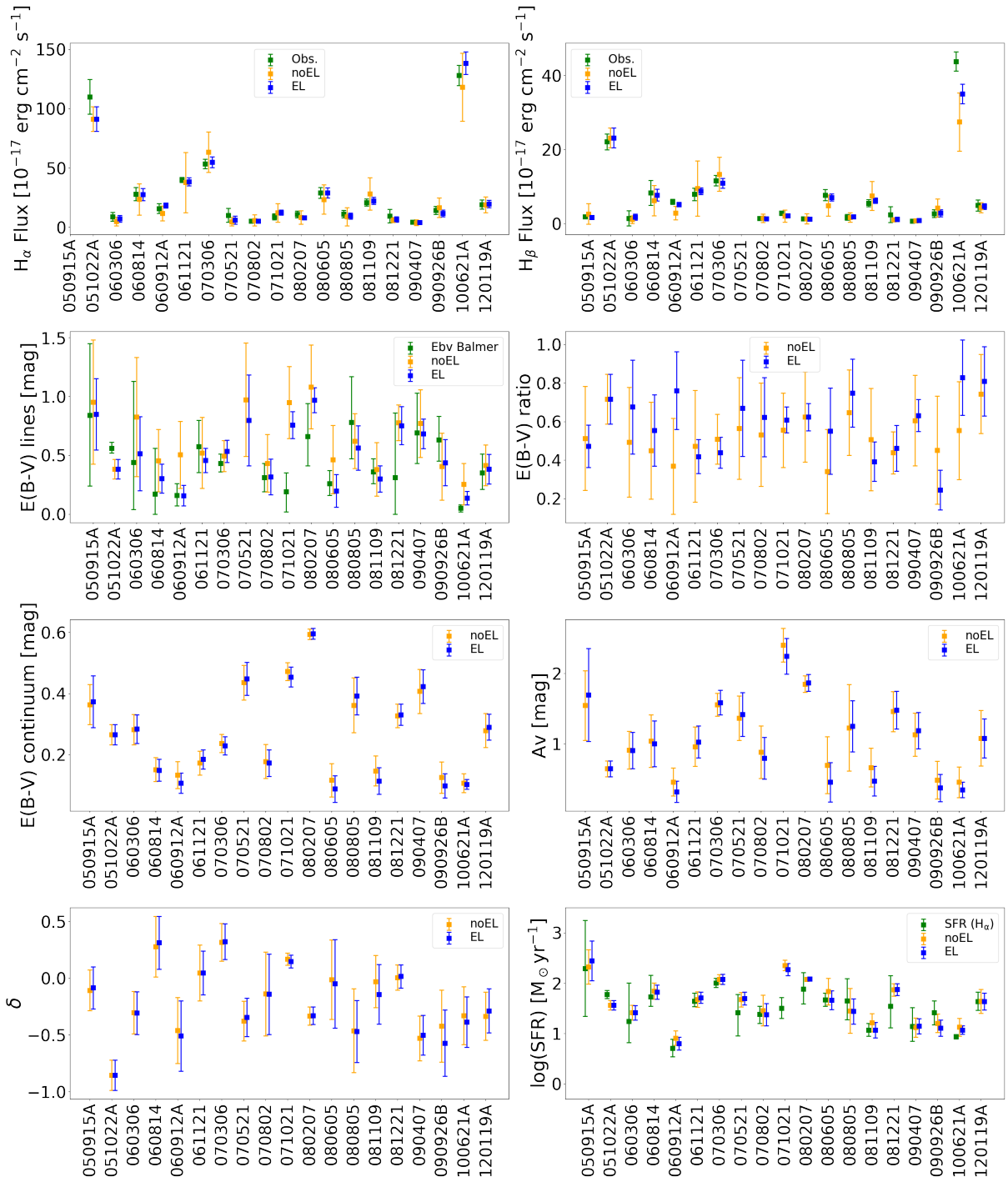

Figure V.14– Comparison of the estimation of parameters for each GRBH with and without introducing the emission lines in the fitting procedure. The SFRs and $E(B-V)_{lines}$ are compared to SFR_{H_α} and $E(B-V)_{Balmer}$ from H_α in Krühler et al., 2015; Vergani et al., 2017. H_α and H_β fluxes are compared to those measured in Krühler et al., 2015; Vergani et al., 2017.

3. Conclusions

We have built the largest sample of dusty GRBHs combining rest-frame UV to radio data as well as Balmer emission lines. We performed a SED fitting using CIGALE code. We used the SBL18 recipe to model the shape of the attenuation curve of these GRBHs as it offers the flexibility to reproduce various shape of attenuation curves as seen in Chapter IV. The introduction of Balmer lines allows a better constrain on the attenuation applied to nebular emission and also to the stellar emission although with much less influence. The power law slope of the attenuation curve is well constrained for most of the GRBHs allowing to study what are the physical parameters of the galaxy influencing its shape. We find a large variety of cases ranging from attenuation curves flatter than the C00 law to as steep as the SMC extinction curve even with a large amount of attenuation. It confirms the non-universality of the attenuation curve as already found in many works [Buat et al., 2011; Buat et al., 2012; Buat et al., 2018; Wild et al., 2011; Kriek et Conroy, 2013; Reddy et al., 2015; Reddy et al., 2016; Salmon et al., 2016; Battisti et al., 2016; Battisti et al., 2017; Salim et al., 2018].

Comparing the values from our SED fitting to those fitted on the SD16 RT model with the same SBL18 recipe, we found that both WD-MW and WG-SMC dust models are able to reproduce the GRBHs data. The WD-LMC dust model is found likely to produce the steepest GRBH attenuation curves associated to large A_V but is unable to reproduce flat attenuation curves with low amount of attenuation. As a rough summary we can say that, based on the SD16 RT model and the WD-MW and WG-SMC dust models, GRBHs with steep attenuation curves are likely to have a rather homogeneous local dust distribution associated to $R_s/R_d \lesssim 0.8$ meaning that the stellar sources are surrounded by a dust layer of various thickness. On the contrary, GRBHs with flat attenuation curves are likely to have a more clumped ISM associated to $R_s/R_d \sim 1$ meaning that the stellar sources are distributed up to the dust distribution radius, i.e. they are not surrounded by a layer of dust.

When comparing the variation of the slope of the attenuation curves with physical parameters of the GRBHs, we found that the amount of attenuation of the stellar emission, the stellar mass and SFR correlate with the slope of the attenuation curve with higher A_V^{stars}, stellar mass and SFR associated to steeper attenuation curves. We find a correlation between A_V^{stars} and stellar mass which might indicate that A_V is the main driver of the correlations with δ.However, we did not find an evidence as clear as in Salim et al., 2018 but the sample sizes are quite different. As seen in Chapter IV we saw that the most influential parameter of the RT model for the shape of the attenuation curves was the optical depth and it would be logical to find A_V as the main driver of the correlation between δ and the stellar mass and SFR. We do not find any correlation with the sSFR as reported by Salim et al., 2018.

When comparing the different tracers of dust attenuation we saw that A_V^{lines} correlates with A_V^{Balmer}, A_V^{stars} is also found to correlate with A_V^{Balmer} although with a higher dispersion. We found an average value of 0.56 ± 0.04 for the ratio of the color excess applied to the stellar component to the one applied to the stellar component. In average we find that $A_V^{stars} \lesssim A_V^{grb}$, but for some cases A_V^{grb} is much smaller what we interpret as GRBs deeply embedded in a molecular cloud.

From the 9 GRBHs best fitted with a recent burst of star formation, 6 of them can be considered as starburst galaxies.

Perspectives and conclusions

1. Perspectives

1.1. COLIBRI

The effort in modelling the scientific performances of COLIBRI showed that it will be able to detect high-redshift and dusty GRBs. We showed that even if COLIBRI will be equipped with only 3 detectors, an adapted observation strategy where the filters change after each observation allows to obtain a relative accuracy of $\sim 10\%$ on the photometric redshift estimation but also allows to estimate the optical spectral slope of the intrinsic emission of the GRB, the visual extinction along the line of sight of the GRB in the host galaxy and to test different extinction laws among the mean MW, LMC and SMC extinction curves. These estimations obtained in the first minutes after the GRB trigger will be extremely useful to trigger larger facilities equipped with a spectrograph, such as the NOT or the VLT, to provide valuable information of the ISM of the GRB host galaxies.
The ETC will be integrated to COLIBRI's website to help observers to plan their observations. The image simulator will be used to provide images to feed the reduction pipeline. The photometric redshift code will be used for the quick analysis automatically performed by COLIBRI for each observation.

From a technical point of view, all the codes developed throughout this thesis are open sources and available at https ://github.com/dcorre. An effort will be made to improve the documentation.

1.2. Improving modelling of dust attenuation

1.2.1. Modified starburst law with correction for IR slope

As we have seen in Section IV.2.3, the modified starbust law proposed by Noll et al., 2009 ; Salim et al., 2018 is able to reproduce most of the RT attenuation curves in the UV-optical domain but not in the NIR where the attenuation is usually underestimated. This can introduce a systematic bias in the stellar mass estimation as the flux in NIR is predominantly emitted by the old stellar population, responsible for the majority of the stellar mass. Previous works, such as Lo Faro et al., 2017 showed that the attenuation curve computed with the formulation of Noll et al., 2009 provides a less grey attenuation curve in the NIR comparing to the attenuation curves computed using radiative transfer models or the Charlot et Fall, 2000 model. This lower attenuation in the NIR leads to lower stellar mass estimates from SED fitting, with a median factor of 1.4 up to a factor 10 [Lo Faro et al., 2017].
In order to correct for this effect we introduced a correction for the slope in the NIR domain. The idea is to keep the N09 and SBL18 formalism in the optical-UV domain so that the results could still be compared to the literature while improving the fit in the NIR domain. To do so we start from the original equation of Calzetti et al., 2000 (Eq. IV.2), and for wavelengths below 550 nm the formalism is the same as Noll et al., 2009 ; Salim et al., 2018 whereas we modify the slope by adding a new parameter, ϵ, at wavelengths above 550 nm :

$$k_{\rm CalzIR}(\lambda) = [2.659 \times (-1.857 + 1.040/\lambda) + R_{\rm V}] \times \left(\frac{\lambda}{\lambda_V}\right)^{\delta+\epsilon}$$

$(0.63\mu{\rm m} \leq \lambda \leq 2.20\mu{\rm m})$

$$= \left[2.659 \times (-2.156 + 1.509/\lambda - 0.198/\lambda^2 + 0.011/\lambda^3) + R_V\right] \times \left(\frac{\lambda}{\lambda_V}\right)^{\delta+\epsilon}$$

$(0.55\mu{\rm m} < \lambda < 0.63\mu{\rm m})$

$$= \left[2.659 \times (-2.156 + 1.509/\lambda - 0.198/\lambda^2 + 0.011/\lambda^3) + R_V\right] \times \left(\frac{\lambda}{\lambda_V}\right)^{\delta} + D_{\lambda_0,\gamma,E_{\rm b}}(\lambda)$$

$(0.12\mu{\rm m} \leq \lambda \leq 0.55\mu{\rm m})$

(VI.1)

with $R_{\rm V} = A_{\rm V}/E(B-V)_{star} = 4.05 \pm 0.80$. An illustration of the influence of ϵ on the shape of the normalised attenuation curve is seen on Figure VI.1. We note that for flat attenuation curves ($\delta \geqslant 0$), $\epsilon > 0.7$ leads to a very strong modification of the attenuation curve shape. The modification is smoother in the case of δ = -0.5.

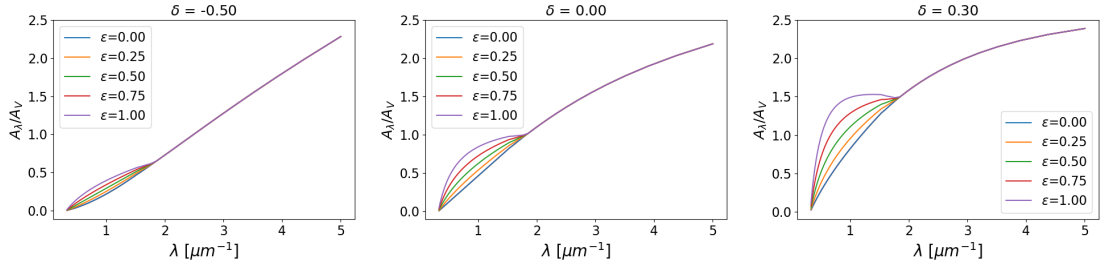

Figure VI.1– Illustration of the influence of ϵ on the shape of the normalised attenuation curve for δ = -0.5, 0.0 and 0.3 from left to right.

1.2.2. Double power law attenuation

We also investigated whether a more simple double power-law recipe is able to reproduce the attenuation curves from the SD16 RT model. It is defined with a spectral break located at 550nm as :

$$\begin{aligned} A_\lambda &= A_V \times \left(\frac{\lambda}{\lambda_V}\right)^{\alpha_1} + D_{\lambda_0,\gamma,E_{\rm b}}(\lambda) \qquad , (\lambda \leq 550nm) \\ A_\lambda &= A_V \times \left(\frac{\lambda}{\lambda_V}\right)^{\alpha_2} \qquad\qquad\qquad\qquad , (\lambda > 550nm) \end{aligned} \tag{VI.2}$$

where α_1, α_2 are the slopes of the attenuation curve and A_V is the normalizing coefficient at 550nm. The recipe will de denoted DBPL in the following.

1.2.3. Comparison with attenuation curves from RT

Following the same method as in Section IV.2.3, we compare the ability of this new recipe to fit the SD16 RT attenuation curves to the original N09 recipe. The new parameter, ϵ, introduced in VI.1 is letting free to vary between 0 and 2. We also plot the results for the double power-law.
From Figure VI.2, we see that the SBL18 recipe with the ϵ correction (red points) is better reproducing the NIR shape, while the optical/UV part remains unchanged, of the RT attenuation curves than the

SBL18 recipe (blue points), except one point corresponding to 2.2 μm, i.e. the K band. This is explained by the original formulation of Calzetti et al., 2000 which implies that the attenuation is 0 at ~ 3 μm and generally causes a steep decrease of attenuation. In order to solve the under estimation of attenuation in the K band, one solution will be to update the values of the coefficients of the polynomial for wavelength above 0.63 μm in Equation VI.1 using the RT attenuation curves of SD16.
As seen in the left panel of Figure VI.3 the new parameter, ϵ introduced to correct the power law slope in NIR is correlated with the power law slope, δ. This correlation could be used to avoid to introduce a new parameter in the fitting procedure while decreasing the systematic bias of underestimating the stellar masses when using the N09 or SBL18 recipes.

The DBPL recipe is better reproducing the NIR attenuation for most of the dust model while reproducing the other wavelength with a similar accuracy as the SBL18+NIR correction recipe and even better accuracy for the WG-SMC dust model.
We tested the influence of the choice of the attenuation curve on the estimation of the physical properties of the galaxies for only one GRBH so far, GRBH 080207 which has FIR detections allowing a good constraint of the amount of dust. The stellar mass is 20% larger when using the SBL18 + NIR correction instead of the SBL18 recipe, and others parameters remain unchanged. The stellar increases by $\sim 33\%$ when using the DBPL instead of the SBL18, and the SFR decreases from 120 to 103 instead $M_{\odot}.yr^{-1}$, the others parameters are unchanged. The shape of the best-fit attenuation curves are very similar as seen in the right panel of Figure VI.3.

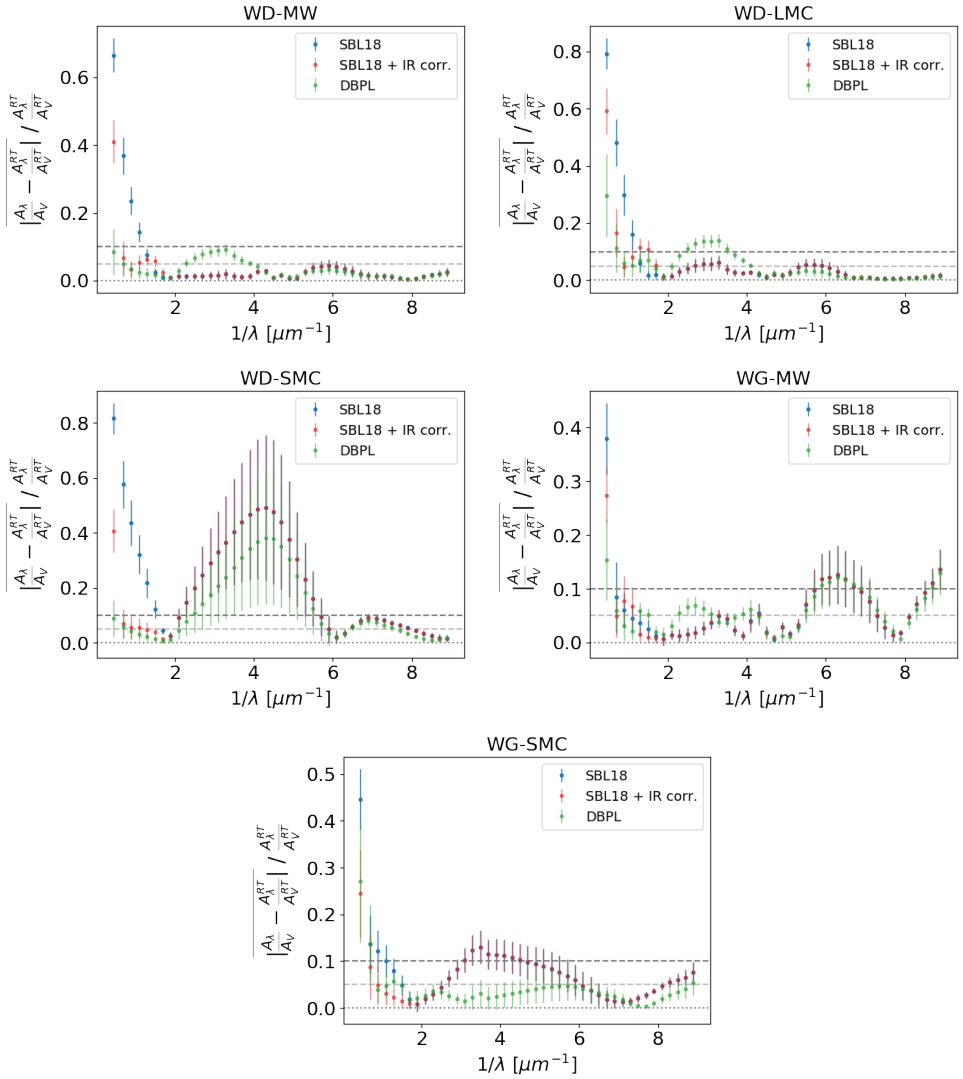

Figure VI.2– Averaged absolute relative difference of the best fit of RT attenuation curves adopting the WD dust models with different attenuation recipes : SBL18 (blue points), SBL18 + NIR correction (red points), DBPL (green points) for different dust types : WD-MW (top left), WD-LMC (top right), WD-SMC (middle left), WG-SMC (middle right) and WG-MW (bottom).

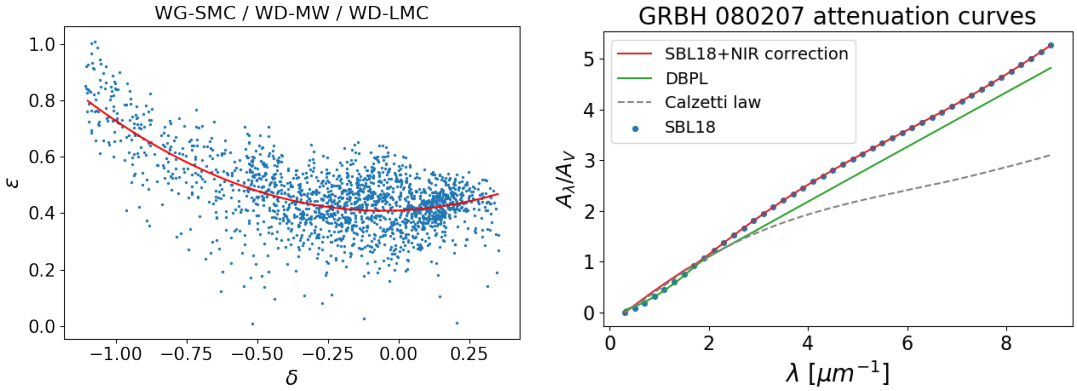

Figure VI.3– *Left :* ϵ as a function of the power law slope, δ, The blue points correspond to the best fit values for the WG-SMC, WD-MW and WD-LMC dust models. The red line is the best fit using : $\epsilon = 0.41 + 0.041 \cdot \delta + 0.358 \cdot \delta^2$. *Right :* Attenuation curves derived from the SED fitting of GRBH 080207 for different recipes : SBL18, SBL18 + NIR correction and DBPL. The original starburst law of C00 is also represented.

As a perspective, it will be very informative to continue to test the ability of other attenuation recipes, such as the age dependent attenuation recipe of Charlot et Fall, 2000, to reproduce the attenuation curves of RT radiative transfer models which will in return also provide a physical meaning to the best fit values of these recipes, as we did in this thesis for the SBL18 recipe. As a long-term perspective, for the GRBHs with data spanning the rest-frame UV to far-IR/sub-mm, the use of radiative transfer simulations using stellar and nebular emission from a stellar synthesis model, such as in the recent work of Law et al., 2018, will allow to study more consistently the dust properties and geometrical distribution of stars and dust in these distant galaxies.

1.3. GRBH attenuation curves

In this thesis we have showed that the attenuation curves of distant star forming galaxies can be reliably derived when they are detected in at least 5 photometric bands spanning the rest-frame UV to NIR. However, the firm detection of the UV bump in the attenuation curve require spectroscopic observation of the host galaxy. This is of particular interest regarding the debate which started in the late 1990s - early 2000s and is still on-going, whether a Calzetti-like attenuation curve can ever arise if the underlying extinction curve exhibits a UV bump. One caveat is that the GRB probes a single sightline whereas the GRB host galaxy is an average over the galaxy, so spatial variations will be an issue. Consequently a large sample is needed.
If the extinction curve along the GRB l.o.s can be systematically measured with a spectrograph, the combination of the extinction curve with the attenuation curve will represent a unique opportunity to constrain the dust properties in distant star-forming galaxies.

2. Conclusion

In this thesis an Exposure Time Calculator and an image simulator has been developed for COLIBRI, an optical/NIR follow-up telescope of the forthcoming SVOM mission. The simulations have showed that COLIBRI thanks to its sensitivity and rapid response time is very well adapted to the detection of high redshift GRBs and dusty GRBs. A Bayesian photometric redshift code dedicated to GRBs has also been developed and validated with observed GRB afterglows. Based on two different mock samples of GRB light curves, the photometric redshift accuracy delivered COLIBRI has been estimated to be $\sim$ 10% for $3.5 < z < 8$ and $\sim$ 14% for z > 8. All these codes are open-source and available for the community.

The dusty GRBs that will be detected by COLIBRI are preferentially located in dusty massive galaxies, and the second part of the thesis was dedicated to the study of dust properties in these galaxies. We first showed that the dust attenuation recipe commonly used to derive the attenuation curves of galaxies is flexible enough to reproduce the variety of shapes observed in radiative transfer simulations for different type of dusts and dust/stars geometries, although there is a tendency of underestimating the attenuation in the NIR. This study also permitted to give a physical representation of the parameters used in the attenuation recipe in terms of geometrical distribution of dust and stars in the ISM. On a sample of 30 GRB extinction curves selected to have rest-frame UV/optical coverage, we found that extinction curves exhibiting a UV bump are preferentially found in the dustiest line of sights and the more massive galaxies and that a rapid follow-up, typically in less than 3 hours, is required to detect them. After a few hours after the trigger, only SMC-like extinction curves with low to moderate dust content are found, indicating an observational bias against the dusty extinction curves with a UV bump. From these 30 GRBs we derived the attenuation curve for the 7 host galaxies having a well sampled SED from the rest-frame UV to NIR. A great diversity of shapes is found and the attenuation curve is even steeper than the extinction curve in one case. Comparing our results with radiative transfer simulations allowed us to derive some information about the dust/star geometry in these galaxies. Further observations of the host galaxies with spectroscopy or narrow-bands filter would allow to state on the presence of the UV bump in the attenuation curves.

From a larger sample of 23 GRB host galaxies at $0.54 < z < 3.04$, we derived their attenuation curves and found various shapes confirming the non-universality of the attenuation curve. We found that the slope of the attenuation curve correlates with physical properties of the galaxy with flatter UV slopes associated to higher A_V^{stars}, stellar mass and SFR. We find some indication that the amount of attenuation, A_V^{stars}, might be the main driver of the correlation between the UV slope of the attenuation curve and the stellar mass and SFR. Based on the SD16 radiative transfer model, GRB host galaxies with steep attenuation curves are likely to have a rather homogeneous local dust distribution and stellar sources surrounded by a dust layer of various thickness. On the contrary, GRBHs with flat attenuation curves are likely to have a more clumped ISM and stellar sources not surrounded by a layer of dust. As an aside result of the SED fitting, we found in general lower stellar mass estimates than in the Swift Gamma-Ray Burst Host Galaxy Legacy Survey (SHOALS). From the 23 GRBHs, 17 are following the main sequence of star forming galaxies and 6 are considered starburst galaxies.

Bibliographie

[1] Abbott, B. P. et al. "*Gravitational Waves and Gamma-Rays from a Binary Neutron Star Merger : GW170817 and GRB 170817A*". In : ApJL, **848** L13 (oct. 2017), L13. DOI : 10.3847/2041-8213/aa920c. arXiv : 1710.05834 [astro-ph.HE]. URL : http://adsabs.harvard.edu/abs/2017ApJ...848L..13A (cf. p. 30).

[2] Abbott, B. P. et al. "*Prospects for observing and localizing gravitational-wave transients with Advanced LIGO, Advanced Virgo and KAGRA*". In : Living Reviews in Relativity, **21** 3 (avr. 2018), 3. DOI : 10.1007/s41114-018-0012-9. arXiv : 1304.0670 [gr-qc]. URL : http://adsabs.harvard.edu/abs/2018LRR....21....3A (cf. p. 39).

[3] Adrián-Martínez, S. et al. "*Letter of intent for KM3NeT 2.0*". In : Journal of Physics G Nuclear Physics, **43**:8, 084001 (août 2016), 084001. DOI : 10.1088/0954-3899/43/8/084001. arXiv : 1601.07459 [astro-ph.IM]. URL : http://adsabs.harvard.edu/abs/2016JPhG...43h4001A (cf. p. 39).

[4] Álvarez-Márquez, J. et al. "*Dust properties of Lyman-break galaxies at z ˜ 3*". In : A&A, **587** A122 (mar. 2016), A122. DOI : 10.1051/0004-6361/201527190. arXiv : 1512.04120. URL : http://adsabs.harvard.edu/abs/2016A&A...587A.122A (cf. p. 37).

[5] Anders, P. et Fritze-v. Alvensleben, U. "*Spectral and photometric evolution of young stellar populations : The impact of gaseous emission at various metallicities*". In : A&A, **401** (avr. 2003), 1063–1070. DOI : 10.1051/0004-6361:20030151. eprint : astro-ph/0302146. URL : http://adsabs.harvard.edu/abs/2003A&A...401.1063A (cf. p. 122).

[6] Aoki, K., Tanaka, I., Nakata, F., Ohta, K., Yuma, S. et Kawai, N. "*GRB 090417B : Subaru NIR observations.*" In : GRB Coordinates Network, **9145** (2009). URL : http://adsabs.harvard.edu/abs/2009GCN..9145....1A (cf. p. 205).

[7] Arabsalmani, M. et al. "*Mass and metallicity scaling relations of high-redshift star-forming galaxies selected by GRBs*". In : MNRAS, **473** (jan. 2018), 3312–3324. DOI : 10.1093/mnras/stx2451. arXiv : 1709.06574. URL : http://adsabs.harvard.edu/abs/2018MNRAS.473.3312A (cf. p. 32, 33, 99).

[8] Asplund, M., Grevesse, N., Sauval, A. J. et Scott, P. "*The Chemical Composition of the Sun*". In : Annual Review of Astronomy and Astrophysics, **47** (sept. 2009), 481–522. DOI : 10.1146/annurev.astro.46.060407.145222. arXiv : 0909.0948 [astro-ph.SR]. URL : https://ui.adsabs.harvard.edu/#abs/2009ARA&A..47..481A (cf. p. 125).

[9] Baldwin, J. A., Phillips, M. M. et Terlevich, R. "*Classification parameters for the emission-line spectra of extragalactic objects*". In : PASP, **93** (fév. 1981), 5–19. DOI : 10.1086/130766. URL : http://adsabs.harvard.edu/abs/1981PASP...93....5B (cf. p. 126).

[10] Battisti, A. J., Calzetti, D. et Chary, R.-R. "*Characterizing Dust Attenuation in Local Star-forming Galaxies : UV and Optical Reddening*". In : ApJ, **818** 13 (fév. 2016), 13. DOI : 10.3847/0004-637X/818/1/13. arXiv : 1601.00208. URL : http://adsabs.harvard.edu/abs/2016ApJ...818...13B (cf. p. 6, 83, 141).

[11] Battisti, A. J., Calzetti, D. et Chary, R.-R. "*Characterizing Dust Attenuation in Local Star-forming Galaxies : Near-infrared Reddening and Normalization*". In : ApJ, **840** 109 (mai 2017), 109. doi : 10.3847/1538-4357/aa6fb2. arXiv : 1704.07426. url : http://cdsads.u-strasbg.fr/abs/2017ApJ...840..109B (cf. p. 6, 83, 141).

[12] Bell, E. F. "*Estimating Star Formation Rates from Infrared and Radio Luminosities : The Origin of the Radio-Infrared Correlation*". In : ApJ, **586** (avr. 2003), 794–813. doi : 10.1086/367829. eprint : astro-ph/0212121. url : http://adsabs.harvard.edu/abs/2003ApJ...586..794B (cf. p. 126).

[13] Berger, E. "*The Host Galaxies of Short-Duration Gamma-Ray Bursts : Luminosities, Metallicities, and Star-Formation Rates*". In : ApJ, **690** (jan. 2009), 231–237. doi : 10.1088/0004-637X/690/1/231. arXiv : 0805.0306. url : http://adsabs.harvard.edu/abs/2009ApJ...690..231B (cf. p. 29).

[14] Berger, E., Cowie, L. L., Kulkarni, S. R., Frail, D. A., Aussel, H. et Barger, A. J. "*A Submillimeter and Radio Survey of Gamma-Ray Burst Host Galaxies : A Glimpse into the Future of Star Formation Studies*". In : ApJ, **588** (mai 2003), 99–112. doi : 10.1086/373991. eprint : astro-ph/0210645. url : http://adsabs.harvard.edu/abs/2003ApJ...588...99B (cf. p. 30).

[15] Berger, E. et al. "*A New Population of High-Redshift Short-Duration Gamma-Ray Bursts*". In : ApJ, **664** (août 2007), 1000–1010. doi : 10.1086/518762. eprint : astro-ph/0611128. url : http://adsabs.harvard.edu/abs/2007ApJ...664.1000B (cf. p. 29).

[16] Bessell, M. S. "*UBVRI photometry. II - The Cousins VRI system, its temperature and absolute flux calibration, and relevance for two-dimensional photometry*". In : PASP, **91** (oct. 1979), 589–607. doi : 10.1086/130542. url : http://adsabs.harvard.edu/abs/1979PASP...91..589B (cf. p. 60).

[17] Bianchi, L., Clayton, G. C., Bohlin, R. C., Hutchings, J. B. et Massey, P. "*Ultraviolet Extinction by Interstellar Dust in External Galaxies : M31*". In : ApJ, **471** (nov. 1996), 203. doi : 10.1086/177963. url : http://adsabs.harvard.edu/abs/1996ApJ...471..203B (cf. p. 35).

[18] Blanchard, P. K., Berger, E. et Fong, W.-f. "*The Offset and Host Light Distributions of Long Gamma-Ray Bursts : A New View From HST Observations of Swift Bursts*". In : ApJ, **817** 144 (fév. 2016), 144. doi : 10.3847/0004-637X/817/2/144. arXiv : 1509.07866 [astro-ph.HE]. url : http://adsabs.harvard.edu/abs/2016ApJ...817..144B (cf. p. 198, 200, 202, 203, 205, 206).

[19] Blandford, R. D. et McKee, C. F. "*Fluid dynamics of relativistic blast waves*". In : Physics of Fluids, **19** (août 1976), 1130–1138. doi : 10.1063/1.861619. url : http://adsabs.harvard.edu/abs/1976PhFl...19.1130B (cf. p. 43).

[20] Blandford, R. D. et Znajek, R. L. "*Electromagnetic extraction of energy from Kerr black holes*". In : MNRAS, **179** (mai 1977), 433–456. doi : 10.1093/mnras/179.3.433. url : http://adsabs.harvard.edu/abs/1977MNRAS.179..433B (cf. p. 28).

[21] Bless, R. C. et Savage, B. D. "*Observations of Interstellar Extinction in the Ultraviolet with the OAO Satellite*". In : *Ultraviolet Stellar Spectra and Related Ground-Based Observations*. Sous la dir. de R. Muller, L. Houziaux et H. E. Butler. **36** IAU Symposium. 1970, 28. url : http://adsabs.harvard.edu/abs/1970IAUS...36...28B (cf. p. 34).

[22] Bloom, J. S. et Prochaska, J. X. "*Constraints on the Diverse Progenitors of GRBs from the Large-Scale Environments*". In : *Gamma-Ray Bursts in the Swift Era*. Sous la dir. de S. S. Holt, N. Gehrels et J. A. Nousek. **836** American Institute of Physics Conference Series. Mai 2006, 473–482. doi : 10.1063/1.2207943. eprint : astro-ph/0602058. url : http://adsabs.harvard.edu/abs/2006AIPC..836..473B (cf. p. 29).

[23] Boer, M. et al. "*The Gamma-Ray Burst Hunt at La Silla the TAROT-S Very Fast Moving Telescope*". In : The Messenger, **113** (sept. 2003), 45–48. URL : http://cdsads.u-strasbg.fr/abs/2003Msngr.113...45B (cf. p. 30).

[24] Boissier, S., Salvaterra, R., Le Floc'h, E., Basa, S., Buat, V., Prantzos, N., Vergani, S. D. et Savaglio, S. "*A method for quantifying the gamma-ray burst bias. Application in the redshift range of 0-1.1*". In : A&A, **557** A34 (sept. 2013), A34. DOI : 10.1051/0004-6361/201321666. arXiv : 1307.0950 [astro-ph.CO]. URL : https://ui.adsabs.harvard.edu/#abs/2013A&A...557A..34B (cf. p. 32).

[25] Bolmer, J., Greiner, J., Krühler, T., Schady, P., Ledoux, C., Tanvir, N. R. et Levan, A. J. "*Dust reddening and extinction curves toward gamma-ray bursts at $z > 4$*". In : A&A, **609** A62 (jan. 2018), A62. DOI : 10.1051/0004-6361/201731255. arXiv : 1709.06867. URL : http://adsabs.harvard.edu/abs/2018A&A...609A..62B (cf. p. 36).

[26] Boquien, M., Buat, V. et Perret, V. "*Impact of star formation history on the measurement of star formation rates*". In : A&A, **571** A72 (nov. 2014), A72. DOI : 10.1051/0004-6361/201424441. arXiv : 1409.5792. URL : http://adsabs.harvard.edu/abs/2014A&A...571A..72B (cf. p. 125).

[27] Boquien, M., Burgarella, D., Roehlly, Y., Buat, V., Ciesla, L., Corre, D., Inoue, A. K. et Salas, H. "*CIGALE : a python Code Investigating GALaxy Emission*". In : A&A, (2018) (cf. p. 122).

[28] Boquien, M., Duc, P.-A., Galliano, F., Braine, J., Lisenfeld, U., Charmandaris, V. et Appleton, P. N. "*Star Formation in Collision Debris : Insights from the Modeling of Their Spectral Energy Distribution*". In : AJ, **140** (déc. 2010), 2124–2144. DOI : 10.1088/0004-6256/140/6/2124. arXiv : 1010.2201. URL : http://adsabs.harvard.edu/abs/2010AJ....140.2124B (cf. p. 122).

[29] Bruzual, G. et Charlot, S. "*Stellar population synthesis at the resolution of 2003*". In : MNRAS, **344** (oct. 2003), 1000–1028. DOI : 10.1046/j.1365-8711.2003.06897.x. eprint : astro-ph/0309134. URL : http://adsabs.harvard.edu/abs/2003MNRAS.344.1000B (cf. p. 125).

[30] Buat, V., Boquien, M., Malek, K., Corre, D., salas, H., Roehlly, Y., Shirley, R. et Efstathiou, A. "*Dust attenuation and Halpha emission in a sample of galaxies observed with Herschel at $0.6 < z < 1.6$*". In : A&A, (sept. 2018). arXiv : 1809.00161. URL : http://adsabs.harvard.edu/abs/2018arXiv180900161B (cf. p. 6, 83, 126, 141).

[31] Buat, V. et al. "*GOODS-Herschel : evidence of a UV extinction bump in galaxies at $z > 1$*". In : A&A, **533** A93 (sept. 2011), A93. DOI : 10.1051/0004-6361/201117264. arXiv : 1107.1049. URL : http://adsabs.harvard.edu/abs/2011A&A...533A..93B (cf. p. 6, 83, 141).

[32] Buat, V. et al. "*GOODS-Herschel : dust attenuation properties of UV selected high redshift galaxies*". In : A&A, **545** A141 (sept. 2012), A141. DOI : 10.1051/0004-6361/201219405. arXiv : 1207.3528. URL : http://adsabs.harvard.edu/abs/2012A&A...545A.141B (cf. p. 6, 83, 141).

[33] Butler, N., Bloom, J., Filippenko, A., Li, W., Foley, R., Alatalo, K., Kocevski, D., Perley, D. et Pooley, D. "*Rapidly Detecting Extincted Bursts with KAIT and PAIRITEL*". In : *Gamma-Ray Bursts in the Swift Era*. Sous la dir. de S. S. Holt, N. Gehrels et J. A. Nousek. **836** American Institute of Physics Conference Series. Mai 2006, 277–280. DOI : 10.1063/1.2207901. URL : http://adsabs.harvard.edu/abs/2006AIPC..836..277B (cf. p. 30).

[34] Butler, N. et al. "*First Light with RATIR : An Automated 6-band Optical/NIR Imaging Camera*". In : *Ground-based and Airborne Instrumentation for Astronomy IV*. **8446** Proceedings of the SPIE conference. Sept. 2012, 844610. doi : 10.1117/12.926471. url : http://adsabs.harvard.edu/abs/2012SPIE.8446E..10B (cf. p. 30).

[35] Calzetti, D. "*The effects of dust on the spectral energy distribution of star-forming galaxies*". In : New Astron. Rev., **45** (oct. 2001), 601–607. doi : 10.1016/S1387-6473(01)00144-0. eprint : astro-ph/0008403. url : http://adsabs.harvard.edu/abs/2001NewAR..45..601C (cf. p. 126).

[36] Calzetti, D., Armus, L., Bohlin, R. C., Kinney, A. L., Koornneef, J. et Storchi-Bergmann, T. "*The Dust Content and Opacity of Actively Star-forming Galaxies*". In : ApJ, **533** (avr. 2000), 682–695. doi : 10.1086/308692. eprint : astro-ph/9911459. url : http://adsabs.harvard.edu/abs/2000ApJ...533..682C (cf. p. 6, 73–75, 126, 137, 142, 144).

[37] Calzetti, D., Kinney, A. L. et Storchi-Bergmann, T. "*Dust extinction of the stellar continua in starburst galaxies : The ultraviolet and optical extinction law*". In : ApJ, **429** (juil. 1994), 582–601. doi : 10.1086/174346. url : http://adsabs.harvard.edu/abs/1994ApJ...429..582C (cf. p. 6, 74, 137).

[38] Calzetti, D., Kinney, A. L. et Storchi-Bergmann, T. "*Dust Obscuration in Starburst Galaxies from Near-Infrared Spectroscopy*". In : ApJ, **458** (fév. 1996), 132. doi : 10.1086/176797. url : http://adsabs.harvard.edu/abs/1996ApJ...458..132C (cf. p. 78).

[39] Campisi, M. A., Tapparello, C., Salvaterra, R., Mannucci, F. et Colpi, M. "*Metallicity properties of the simulated host galaxies of long gamma-ray bursts and the fundamental metallicity relation*". In : MNRAS, **417** (oct. 2011), 1013–1021. doi : 10.1111/j.1365-2966.2011.19326.x. arXiv : 1105.1378. url : http://adsabs.harvard.edu/abs/2011MNRAS.417.1013C (cf. p. 33).

[40] Cardelli, J. A., Clayton, G. C. et Mathis, J. S. "*The relationship between infrared, optical, and ultraviolet extinction*". In : ApJ, **345** (oct. 1989), 245–256. doi : 10.1086/167900. url : http://adsabs.harvard.edu/abs/1989ApJ...345..245C (cf. p. 35, 79, 126).

[41] Castro-Tirado, A. J. et al. "*The dark nature of <ASTROBJ>GRB 051022</ASTROBJ> and its host galaxy*". In : A&A, **475** (nov. 2007), 101–107. doi : 10.1051/0004-6361:20066748. arXiv : 0708.3043. url : http://adsabs.harvard.edu/abs/2007A&A...475..101C (cf. p. 198).

[42] Chabrier, G. "*Galactic Stellar and Substellar Initial Mass Function*". In : PASP, **115** (juil. 2003), 763–795. doi : 10.1086/376392. eprint : astro-ph/0304382. url : http://adsabs.harvard.edu/abs/2003PASP..115..763C (cf. p. 73, 125).

[43] Charlot, S. et Fall, S. M. "*A Simple Model for the Absorption of Starlight by Dust in Galaxies*". In : ApJ, **539** (août 2000), 718–731. doi : 10.1086/309250. eprint : astro-ph/0003128. url : http://adsabs.harvard.edu/abs/2000ApJ...539..718C (cf. p. 72, 142, 146).

[44] Chevallard, J., Charlot, S., Wandelt, B. et Wild, V. "*Insights into the content and spatial distribution of dust from the integrated spectral properties of galaxies*". In : MNRAS, **432** (juil. 2013), 2061–2091. doi : 10.1093/mnras/stt523. arXiv : 1303.6631. url : http://adsabs.harvard.edu/abs/2013MNRAS.432.2061C (cf. p. 7, 83, 93, 95, 135).

[45] Chincarini, G. et al. "*The First Survey of X-Ray Flares from Gamma-Ray Bursts Observed by Swift : Temporal Properties and Morphology*". In : ApJ, **671** (déc. 2007), 1903–1920. doi : 10.1086/521591. arXiv : astro-ph/0702371 [astro-ph]. url : https://ui.adsabs.harvard.edu/#abs/2007ApJ...671.1903C (cf. p. 27).

[46] Christensen, L., Hjorth, J. et Gorosabel, J. "*UV star-formation rates of GRB host galaxies*". In : A&A, **425** (oct. 2004), 913–926. doi : 10.1051/0004-6361:20040361. arXiv : astro-ph/0407066 [astro-ph]. url : https://ui.adsabs.harvard.edu/#abs/2004A&A...425..913C (cf. p. 30).

[47] Clayton, G. C., Gordon, K. D., Bianchi, L. C., Massa, D. L., Fitzpatrick, E. L., Bohlin, R. C. et Wolff, M. J. "*New Ultraviolet Extinction Curves for Interstellar Dust in M31*". In : ApJ, **815** 14 (déc. 2015), 14. doi : 10.1088/0004-637X/815/1/14. arXiv : 1510.06983. url : http://adsabs.harvard.edu/abs/2015ApJ...815...14C (cf. p. 35).

[48] Clayton, G. C. et Martin, P. G. "*Interstellar dust in the Large Magellanic Cloud*". In : ApJ, **288** (jan. 1985), 558–568. doi : 10.1086/162821. url : http://adsabs.harvard.edu/abs/1985ApJ...288..558C (cf. p. 35).

[49] Cline, T. L., Desai, U. D., Klebesadel, R. W. et Strong, I. B. "*Energy Spectra of Cosmic Gamma-Ray Bursts*". In : ApJ, **185** (oct. 1973), L1. doi : 10.1086/181309. url : https://ui.adsabs.harvard.edu/#abs/1973ApJ...185L...1C (cf. p. 24).

[50] Condon, J. J. "*Radio emission from normal galaxies*". In : ARA&A, **30** (1992), 575–611. doi : 10.1146/annurev.aa.30.090192.003043. url : http://adsabs.harvard.edu/abs/1992ARA&A..30..575C (cf. p. 126).

[51] Cordier, B., Desclaux, F., Foliard, J. et Schanne, S. "*SVOM pointing strategy : how to optimize the redshift measurements ?*" In : *American Institute of Physics Conference Series*. Sous la dir. de M. Galassi, D. Palmer et E. Fenimore. **1000** American Institute of Physics Conference Series. Mai 2008, 585–588. doi : 10.1063/1.2943538. arXiv : 0807.0739. url : http://adsabs.harvard.edu/abs/2008AIPC.1000..585C (cf. p. 38).

[52] Corre, D., Buat, V., Basa, S., Boissier, S., Japelj, J., Palmerio, J., Salvaterra, R., Vergani, S. D. et Zafar, T. "*Investigation of dust attenuation and star formation activity in galaxies hosting GRBs*". In : A&A, (juil. 2018). arXiv : 1807.00635. url : http://adsabs.harvard.edu/abs/2018arXiv180700635C (cf. p. 126, 131, 137, 138).

[53] Costa, E. et al. "*Discovery of an X-ray afterglow associated with the γ-ray burst of 28 February 1997*". In : Nature, **387** (juin 1997), 783–785. doi : 10.1038/42885. eprint : astro-ph/9706065. url : http://adsabs.harvard.edu/abs/1997Natur.387..783C (cf. p. 25).

[54] Covino, S. et al. "*Dust extinctions for an unbiased sample of gamma-ray burst afterglows*". In : MNRAS, **432** (juin 2013), 1231–1244. doi : 10.1093/mnras/stt540. arXiv : 1303.4743 [astro-ph.HE]. url : http://adsabs.harvard.edu/abs/2013MNRAS.432.1231C (cf. p. 31, 34, 36, 61, 121).

[55] Cucchiara, A., Fumagalli, M., Rafelski, M., Kocevski, D., Prochaska, J. X., Cooke, R. J. et Becker, G. D. "*Unveiling the Secrets of Metallicity and Massive Star Formation Using DLAs along Gamma-Ray Bursts*". In : ApJ, **804** 51 (mai 2015), 51. doi : 10.1088/0004-637X/804/1/51. arXiv : 1408.3578. url : http://adsabs.harvard.edu/abs/2015ApJ...804...51C (cf. p. 34).

[56] Cucchiara, A. et al. "*A Photometric Redshift of $z \sim 9.4$ for GRB 090429B*". In : ApJ, **736** 7 (juil. 2011), 7. doi : 10.1088/0004-637X/736/1/7. arXiv : 1105.4915. url : http://adsabs.harvard.edu/abs/2011ApJ...736....7C (cf. p. 30).

[57] Dale, D. A. et Helou, G. "*The Infrared Spectral Energy Distribution of Normal Star-forming Galaxies : Calibration at Far-Infrared and Submillimeter Wavelengths*". In : ApJ, **576** (sept. 2002), 159–168. doi : 10.1086/341632. eprint : astro-ph/0205085 (cf. p. 126).

[58] Dale, D. A., Helou, G., Magdis, G. E., Armus, L., Díaz-Santos, T. et Shi, Y. "*A Two-parameter Model for the Infrared/Submillimeter/Radio Spectral Energy Distributions of Galaxies and Active Galactic Nuclei*". In : ApJ, **784** 83 (mar. 2014), 83. DOI : 10.1088/0004-637X/784/1/83. arXiv : 1402.1495 (cf. p. 73, 126).

[59] de Barros, S., Schaerer, D. et Stark, D. P. "*Properties of z ˜ 3-6 Lyman break galaxies. II. Impact of nebular emission at high redshift*". In : A&A, **563** A81 (mar. 2014), A81. DOI : 10.1051/0004-6361/201220026. arXiv : 1207.3663. URL : http://adsabs.harvard.edu/abs/2014A&A...563A..81D (cf. p. 122).

[60] Delhaize, J. et al. "*The VLA-COSMOS 3 GHz Large Project : The infrared-radio correlation of star-forming galaxies and AGN to $z \lesssim 6$*". In : A&A, **602** A4 (juin 2017), A4. DOI : 10.1051/0004-6361/201629430. arXiv : 1703.09723. URL : http://adsabs.harvard.edu/abs/2017A&A...602A...4D (cf. p. 127).

[61] Draine, B. T. "*Interstellar Dust Grains*". In : ARA&A, **41** (2003), 241–289. DOI : 10.1146/annurev.astro.41.011802.094840. eprint : astro-ph/0304489. URL : http://adsabs.harvard.edu/abs/2003ARA&A..41..241D (cf. p. 35, 81, 84, 97).

[62] Eichler, D., Livio, M., Piran, T. et Schramm, D. N. "*Nucleosynthesis, neutrino bursts and gamma-rays from coalescing neutron stars*". In : Nature, **340** (juil. 1989), 126–128. DOI : 10.1038/340126a0. URL : http://adsabs.harvard.edu/abs/1989Natur.340..126E (cf. p. 29).

[63] Elíasdóttir, Á. et al. "*Dust Extinction in High-z Galaxies with Gamma-Ray Burst Afterglow Spectroscopy : The 2175 Å Feature at $z = 2.45$*". In : ApJ, **697** (juin 2009), 1725–1740. DOI : 10.1088/0004-637X/697/2/1725. arXiv : 0810.2897. URL : http://adsabs.harvard.edu/abs/2009ApJ...697.1725E (cf. p. 36, 201).

[64] Elliott, J. et al. "*The low-extinction afterglow in the solar-metallicity host galaxy of γ-ray burst 110918A*". In : A&A, **556** A23 (août 2013), A23. DOI : 10.1051/0004-6361/201220968. arXiv : 1306.0892 [astro-ph.HE]. URL : http://adsabs.harvard.edu/abs/2013A&A...556A..23E (cf. p. 31).

[65] Fenimore, E. E. et al. "*The intrinsic luminosity of γ-ray bursts and their host galaxies*". In : Nature, **366** (nov. 1993), 40–42. DOI : 10.1038/366040a0. URL : http://adsabs.harvard.edu/abs/1993Natur.366...40F (cf. p. 29).

[66] Ferland, G. J., Korista, K. T., Verner, D. A., Ferguson, J. W., Kingdon, J. B. et Verner, E. M. "*CLOUDY 90 : Numerical Simulation of Plasmas and Their Spectra*". In : PASP, **110** (juil. 1998), 761–778. DOI : 10.1086/316190. URL : http://adsabs.harvard.edu/abs/1998PASP..110..761F (cf. p. 122).

[67] Ferland, G. J., Porter, R. L., van Hoof, P. A., Williams, R. J., Abel, N. P., Lykins, M. L., Shaw, G., Henney, W. J. et Stancil, P. C. "*The 2013 Release of Cloudy*". In : Revista Mexicana de Astronomía y Astrofísica, **49** (avr. 2013), 137–163. arXiv : 1302.4485 [astro-ph.GA]. URL : http://adsabs.harvard.edu/abs/2013RMxAA..49..137F (cf. p. 122).

[68] Fishman, G. J. et al. "*The First BATSE Gamma-Ray Burst Catalog*". In : The Astrophysical Journal Supplement Series, **92** (mai 1994), 229. DOI : 10.1086/191968. URL : https://ui.adsabs.harvard.edu/#abs/1994ApJS...92..229F (cf. p. 24, 25).

[69] Fitzpatrick, E. L. "*Interstellar extinction variations in the Large Magellanic Cloud*". In : ApJ, **299** (déc. 1985), 219–235. DOI : 10.1086/163694. URL : http://adsabs.harvard.edu/abs/1985ApJ...299..219F (cf. p. 35).

[70] Fitzpatrick, E. L. "*Correcting for the Effects of Interstellar Extinction*". In : The Publications of the Astronomical Society of the Pacific, **111** (jan. 1999), 63–75. DOI : 10.1086/316293. eprint : astro-ph/9809387. URL : http://adsabs.harvard.edu/abs/1999PASP..111...63F (cf. p. 35).

[71] Fitzpatrick, E. L. et Massa, D. "*An analysis of the shapes of ultraviolet extinction curves. III - an atlas of ultraviolet extinction curves*". In : ApJs, **72** (jan. 1990), 163–189. DOI : 10.1086/191413. URL : http://adsabs.harvard.edu/abs/1990ApJS...72..163F (cf. p. 35, 45).

[72] Fitzpatrick, E. L. et Massa, D. "*An Analysis of the Shapes of Ultraviolet Extinction Curves. IV. Extinction without Standards*". In : AJ, **130** (sept. 2005), 1127–1140. DOI : 10.1086/431900. eprint : astro-ph/0506416. URL : http://adsabs.harvard.edu/abs/2005AJ....130.1127F (cf. p. 34).

[73] Fitzpatrick, E. L. et Massa, D. "*An Analysis of the Shapes of Interstellar Extinction Curves. V. The IR-through-UV Curve Morphology*". In : ApJ, **663** (juil. 2007), 320–341. DOI : 10.1086/518158. arXiv : 0705.0154. URL : http://adsabs.harvard.edu/abs/2007ApJ...663..320F (cf. p. 35, 45, 85).

[74] Fong, W. et Berger, E. "*The Locations of Short Gamma-Ray Bursts as Evidence for Compact Object Binary Progenitors*". In : ApJ, **776** 18 (oct. 2013), 18. DOI : 10.1088/0004-637X/776/1/18. arXiv : 1307.0819 [astro-ph.HE]. URL : http://adsabs.harvard.edu/abs/2013ApJ...776...18F (cf. p. 29).

[75] Foreman-Mackey, D., Hogg, D. W., Lang, D. et Goodman, J. "*emcee : The MCMC Hammer*". In : PASP, **125** (mar. 2013), 306–312. DOI : 10.1086/670067. arXiv : 1202.3665 [astro-ph.IM]. URL : http://adsabs.harvard.edu/abs/2013PASP..125..306F (cf. p. 53, 56, 84).

[76] Fox, A. J., Ledoux, C., Vreeswijk, P. M., Smette, A. et Jaunsen, A. O. "*High-ion absorption in seven GRB host galaxies at z = 2-4. Evidence for both circumburst plasma and outflowing interstellar gas*". In : A&A, **491** (nov. 2008), 189–207. DOI : 10.1051/0004-6361:200810286. arXiv : 0809.3247. URL : http://adsabs.harvard.edu/abs/2008A&A...491..189F (cf. p. 34).

[77] Fox, D. B. et al. "*The afterglow of GRB 050709 and the nature of the short-hard γ-ray bursts*". In : Nature, **437** (oct. 2005), 845–850. DOI : 10.1038/nature04189. eprint : astro-ph/0510110. URL : http://adsabs.harvard.edu/abs/2005Natur.437..845F (cf. p. 29).

[78] Fruchter, A. S. et al. "*Long γ-ray bursts and core-collapse supernovae have different environments*". In : Nature, **441** (mai 2006), 463–468. DOI : 10.1038/nature04787. eprint : astro-ph/0603537. URL : http://adsabs.harvard.edu/abs/2006Natur.441..463F (cf. p. 30).

[79] Fruchter, A. S. et al. "*Hubble Space Telescope and Palomar Imaging of GRB 990123 : Implications for the Nature of Gamma-Ray Bursts and Their Hosts*". In : ApJ, **519** (juil. 1999), L13–L16. DOI : 10.1086/312094. arXiv : astro-ph/9902236 [astro-ph]. URL : https://ui.adsabs.harvard.edu/#abs/1999ApJ...519L..13F (cf. p. 30).

[80] Fryer, C. L., Hungerford, A. L. et Young, P. A. "*Light-Curve Calculations of Supernovae from Fallback Gamma-Ray Bursts*". In : ApJL, **662** (juin 2007), L55–L58. DOI : 10.1086/519523. arXiv : 0705.0716. URL : http://adsabs.harvard.edu/abs/2007ApJ...662L..55F (cf. p. 28).

[81] Fryer, C. L., Woosley, S. E. et Hartmann, D. H. "*Formation Rates of Black Hole Accretion Disk Gamma-Ray Bursts*". In : ApJ, **526** (nov. 1999), 152–177. DOI : 10.1086/307992. eprint : astro-ph/9904122. URL : http://adsabs.harvard.edu/abs/1999ApJ...526..152F (cf. p. 28).

[82] Fynbo, J. P. et al. "*On the Lyalpha emission from gamma-ray burst host galaxies : Evidence for low metallicities*". In : A&A, **406** (juil. 2003), L63–L66. doi : 10.1051/0004-6361:20030931. arXiv : astro-ph/0306403 [astro-ph]. url : https://ui.adsabs.harvard.edu/#abs/2003A&A...406L..63F (cf. p. 30).

[83] Fynbo, J. P. et al. "*Low-resolution Spectroscopy of Gamma-ray Burst Optical Afterglows : Biases in the Swift Sample and Characterization of the Absorbers*". In : The Astrophysical Journal Supplement Series, **185** (déc. 2009), 526–573. doi : 10.1088/0067-0049/185/2/526. arXiv : 0907.3449 [astro-ph.CO]. url : https://ui.adsabs.harvard.edu/#abs/2009ApJS..185..526F (cf. p. 31).

[84] Fynbo, J. U. et al. "*Detection of the optical afterglow of GRB 000630 : Implications for dark bursts*". In : A&A, **369** (avr. 2001), 373–379. doi : 10.1051/0004-6361:20010112. arXiv : astro-ph/0101425 [astro-ph]. url : https://ui.adsabs.harvard.edu/#abs/2001A&A...369..373F (cf. p. 31).

[85] Fynbo, J. P. U., Prochaska, J. X., Sommer-Larsen, J., Dessauges-Zavadsky, M. et Møller, P. "*Reconciling the Metallicity Distributions of Gamma-Ray Burst, Damped Lyα, and Lyman Break Galaxies at $z \approx 3$*". In : ApJ, **683** (août 2008), 321–328. doi : 10.1086/589555. arXiv : 0801.3273 [astro-ph]. url : https://ui.adsabs.harvard.edu/#abs/2008ApJ...683..321F (cf. p. 32).

[86] Galama, T. J. et al. "*On the possible association of SN 1998bw and GRB 980425*". In : Astronomy and Astrophysics Supplement Series, **138** (sept. 1999), 465–466. doi : 10.1051/aas:1999311. url : http://adsabs.harvard.edu/abs/1999A&AS..138..465G (cf. p. 28).

[87] Galvin, T. J. et al. "*The spectral energy distribution of powerful starburst galaxies - I. Modelling the radio continuum*". In : MNRAS, **474** (fév. 2018), 779–799. doi : 10.1093/mnras/stx2613. arXiv : 1710.01967. url : http://adsabs.harvard.edu/abs/2018MNRAS.474..779G (cf. p. 127).

[88] Gehrels, N. "*The Swift Gamma-Ray Burst Mission*". In : *Gamma-Ray Bursts : 30 Years of Discovery*. Sous la dir. d'E. Fenimore et M. Galassi. **727** American Institute of Physics Conference Series. Sept. 2004, 637–641. doi : 10.1063/1.1810924. eprint : astro-ph/0405233. url : http://adsabs.harvard.edu/abs/2004AIPC..727..637G (cf. p. 27, 37).

[89] Gehrels, N., Piro, L. et Leonard, P. "*The brightest explosions in the Universe*". In : Scientific American Reports, **17** (2007), 34–41. doi : doi:10.1038/scientificamerican0407-34sp (cf. p. 27).

[90] Goodman, J. et Weare, J. "*Ensemble Samplers with affine invariance*". In : Comm. App. Math. Comp. Sci., **5** (2010), 65–80. doi : 10.2140/camcos.2010.5.65. url : http://msp.org/camcos/2010/5-1/p04.xhtml (cf. p. 53, 56).

[91] Gordon, K. D. et Clayton, G. C. "*Starburst-like Dust Extinction in the Small Magellanic Cloud*". In : ApJ, **500** (juin 1998), 816–824. doi : 10.1086/305774. eprint : astro-ph/9802003. url : http://adsabs.harvard.edu/abs/1998ApJ...500..816G (cf. p. 35, 79).

[92] Gordon, K. D., Clayton, G. C., Misselt, K. A., Landolt, A. U. et Wolff, M. J. "*A Quantitative Comparison of the Small Magellanic Cloud, Large Magellanic Cloud, and Milky Way Ultraviolet to Near-Infrared Extinction Curves*". In : ApJ, **594** (sept. 2003), 279–293. doi : 10.1086/376774. eprint : astro-ph/0305257. url : http://adsabs.harvard.edu/abs/2003ApJ...594..279G (cf. p. 35).

[93] Gordon, K. D. et al. "*The Panchromatic Hubble Andromeda Treasury. XV. The BEAST : Bayesian Extinction and Stellar Tool*". In : ApJ, **826** 104 (août 2016), 104. doi : 10.3847/0004-637X/826/2/104. arXiv : 1606.06182. url : http://adsabs.harvard.edu/abs/2016ApJ...826..104G (cf. p. 34).

[94] Gorosabel, J. et al. "*The GRB 030329 host : a blue low metallicity subluminous galaxy with intense star formation*". In : A&A, **444** (déc. 2005), 711–721. DOI : 10.1051/0004-6361:20052768. arXiv : astro-ph/0507488 [astro-ph]. URL : https://ui.adsabs.harvard.edu/#abs/2005A&A...444..711G (cf. p. 30).

[95] Graham, J. F. et Fruchter, A. S. "*The Metal Aversion of Long-duration Gamma-Ray Bursts*". In : ApJ, **774** 119 (sept. 2013), 119. DOI : 10.1088/0004-637X/774/2/119. arXiv : 1211.7068 [astro-ph.HE]. URL : http://adsabs.harvard.edu/abs/2013ApJ...774..119G (cf. p. 31, 32).

[96] Granot, J. et Sari, R. "*The Shape of Spectral Breaks in Gamma-Ray Burst Afterglows*". In : ApJ, **568** (avr. 2002), 820–829. DOI : 10.1086/338966. eprint : astro-ph/0108027. URL : http://adsabs.harvard.edu/abs/2002ApJ...568..820G (cf. p. 43, 44, 60, 62, 63, 97).

[97] Granot, J., Piran, T. et Sari, R. "*The Synchrotron Spectrum of Fast Cooling Electrons Revisited*". In : ApJ, **534** (mai 2000), L163–L166. DOI : 10.1086/312661. arXiv : astro-ph/0001160 [astro-ph]. URL : https://ui.adsabs.harvard.edu/#abs/2000ApJ...534L.163G (cf. p. 43).

[98] Greiner, J. *GCN CIRCULAR 9215, GRB 090423 : GROND detection and preliminary photo-z*. Rapp. tech. 2009. URL : %5Curl%7Bhttp://gcn.gsfc.nasa.gov/gcn/gcn3/9215.gcn3%7D (cf. p. 172).

[99] Greiner, J. "*GRB 080913 at redshift 6.7*". In : Astrophys. J., **693** (2009), 1610–1620. DOI : 10.1088/0004-637X/693/2/1610. arXiv : 0810.2314 [astro-ph]. URL : https://inspirehep.net/record/799328 (cf. p. 172).

[100] Greiner, J. *GRB database of Jochen Greiner*. Rapp. tech. database. URL : http://www.mpe.mpg.de/~jcg/grbgen.html (cf. p. 56, 59, 172, 173).

[101] Greiner, J. et al. "*A very luminous magnetar-powered supernova associated with an ultra-long γ-ray burst*". In : Nature, **523** (juil. 2015), 189–192. DOI : 10.1038/nature14579. URL : https://ui.adsabs.harvard.edu/#abs/2015Natur.523..189G (cf. p. 29).

[102] Greiner, J. et al. "*GROND, a 7-Channel Imager*". In : Publications of the Astronomical Society of the Pacific, **120** (avr. 2008), 405. DOI : 10.1086/587032. arXiv : 0801.4801. URL : http://adsabs.harvard.edu/abs/2008PASP..120..405G (cf. p. 30).

[103] Greiner, J. et al. "*The nature of "dark" gamma-ray bursts*". In : A&A, **526** A30 (fév. 2011), A30. DOI : 10.1051/0004-6361/201015458. arXiv : 1011.0618 [astro-ph.HE]. URL : https://ui.adsabs.harvard.edu/#abs/2011A&A...526A..30G (cf. p. 30, 31, 34, 36).

[104] Groot, P. J. et al. "*GRB 970228*". In : IAU Circ., **6584** (mar. 1997). URL : http://adsabs.harvard.edu/abs/1997IAUC.6584....1G (cf. p. 25).

[105] Hagen, L. M., Siegel, M. H., Hoversten, E. A., Gronwall, C., Immler, S. et Hagen, A. "*Swift Ultraviolet Survey of the Magellanic Clouds (SUMaC) - I. Shape of the ultraviolet dust extinction law and recent star formation history of the Small Magellanic Cloud*". In : MNRAS, **466** (avr. 2017), 4540–4557. DOI : 10.1093/mnras/stw2954. arXiv : 1611.00064. URL : http://adsabs.harvard.edu/abs/2017MNRAS.466.4540H (cf. p. 95).

[106] Haislip, J. B. "*A photometric redshift of z = 6.39 +/- 0.12 for GRB 050904*". In : Nature, **440** (mar. 2006), 181–183. DOI : 10.1038/nature04552. eprint : astro-ph/0509660. URL : http://adsabs.harvard.edu/abs/2006Natur.440..181H (cf. p. 174).

[107] Hashimoto, T. et al. "*"Dark" GRB 080325 in a Dusty Massive Galaxy at z 2*". In : ApJ, **719** (août 2010), 378–384. doi : 10.1088/0004-637X/719/1/378. arXiv : 1003.3717. url : http://adsabs.harvard.edu/abs/2010ApJ...719..378H (cf. p. 202).

[108] Hirschi, R., Meynet, G. et Maeder, A. "*Stellar evolution with rotation. XIII. Predicted GRB rates at various Z*". In : A&A, **443** (nov. 2005), 581–591. doi : 10.1051/0004-6361:20053329. arXiv : astro-ph/0507343 [astro-ph]. url : https://ui.adsabs.harvard.edu/#abs/2005A&A...443..581H (cf. p. 28).

[109] Hjorth, J. "*The supernova-gamma-ray burst-jet connection*". In : Philosophical Transactions of the Royal Society of London Series A, **371** (avr. 2013), 20120275–20120275. doi : 10.1098/rsta.2012.0275. arXiv : 1304.7736 [astro-ph.HE]. url : http://adsabs.harvard.edu/abs/2013RSPTA.37120275H (cf. p. 29).

[110] Hjorth, J. et al. "*A very energetic supernova associated with the γ-ray burst of 29 March 2003*". In : Nature, **423** (juin 2003), 847–850. doi : 10.1038/nature01750. arXiv : astro-ph/0306347 [astro-ph]. url : https://ui.adsabs.harvard.edu/#abs/2003Natur.423..847H (cf. p. 28).

[111] Hjorth, J. et al. "*The Optically Unbiased Gamma-Ray Burst Host (TOUGH) Survey. I. Survey Design and Catalogs*". In : ApJ, **756** 187 (sept. 2012), 187. doi : 10.1088/0004-637X/756/2/187. arXiv : 1205.3162 [astro-ph.CO]. url : http://adsabs.harvard.edu/abs/2012ApJ...756..187H (cf. p. 31, 121, 198–200, 202).

[112] Holland, S. T. et al. "*GRB 090417B and its Host Galaxy : A Step Toward an Understanding of Optically Dark Gamma-ray Bursts*". In : ApJ, **717** (juil. 2010), 223–234. doi : 10.1088/0004-637X/717/1/223. arXiv : 1005.1675 [astro-ph.CO]. url : http://adsabs.harvard.edu/abs/2010ApJ...717..223H (cf. p. 121, 205).

[113] Hopkins, P. F. et al. "*Dust Reddening in Sloan Digital Sky Survey Quasars*". In : AJ, **128** (sept. 2004), 1112–1123. doi : 10.1086/423291. eprint : astro-ph/0406293. url : http://adsabs.harvard.edu/abs/2004AJ....128.1112H (cf. p. 97).

[114] Hunt, L. K. et al. "*New light on gamma-ray burst host galaxies with Herschel*". In : A&A, **565** A112 (mai 2014), A112. doi : 10.1051/0004-6361/201323340. arXiv : 1402.4006. url : http://adsabs.harvard.edu/abs/2014A&A...565A.112H (cf. p. 32, 198, 200–203, 205).

[115] Hunt, L., Palazzi, E., Rossi, A., Savaglio, S., Cresci, G., Klose, S., Michałowski, M. et Pian, E. "*The Extremely Red Host Galaxy of GRB 080207*". In : ApJ, **736** L36 (août 2011), L36. doi : 10.1088/2041-8205/736/2/L36. arXiv : 1106.3988. url : http://adsabs.harvard.edu/abs/2011ApJ...736L..36H (cf. p. 202).

[116] Inoue, A. K. "*Lyman 'bump' galaxies - I. Spectral energy distribution of galaxies with an escape of nebular Lyman continuum*". In : MNRAS, **401** (jan. 2010), 1325–1333. doi : 10.1111/j.1365-2966.2009.15730.x. arXiv : 0908.3925. url : http://adsabs.harvard.edu/abs/2010MNRAS.401.1325I (cf. p. 122).

[117] Inoue, A. K. "*Rest-frame ultraviolet-to-optical spectral characteristics of extremely metal-poor and metal-free galaxies*". In : MNRAS, **415** (août 2011), 2920–2931. doi : 10.1111/j.1365-2966.2011.18906.x. arXiv : 1102.5150. url : http://adsabs.harvard.edu/abs/2011MNRAS.415.2920I (cf. p. 122).

[118] Jakobsson, P., Hjorth, J., Fynbo, J. P., Watson, D., Pedersen, K., Björnsson, G. et Gorosabel, J. "*Swift Identification of Dark Gamma-Ray Bursts*". In : The Astrophysical Journal, **617** (déc. 2004), L21–L24. DOI : 10.1086/427089. arXiv : astro-ph/0411036 [astro-ph]. URL : https://ui.adsabs.harvard.edu/#abs/2004ApJ...617L..21J (cf. p. 31).

[119] Japelj, J. et al. "*Are long gamma-ray bursts biased tracers of star formation ? Clues from the host galaxies of the Swift/BAT6 complete sample of bright LGRBs. II. Star formation rates and metallicities at $z < 1$*". In : A&A, **590** A129 (mai 2016), A129. DOI : 10.1051/0004-6361/201628314. arXiv : 1604.01034 [astro-ph.HE]. URL : http://adsabs.harvard.edu/abs/2016A&A...590A.129J (cf. p. 6, 31, 32, 34, 36, 120).

[120] Jaunsen, A. O. et al. "*GRB 070306 : A Highly Extinguished Afterglow*". In : ApJ, **681** 453-461 (juil. 2008), 453–461. DOI : 10.1086/588602. arXiv : 0803.4017. URL : http://adsabs.harvard.edu/abs/2008ApJ...681..453J (cf. p. 200).

[121] Jonsson, P., Groves, B. A. et Cox, T. J. "*High-resolution panchromatic spectral models of galaxies including photoionization and dust*". In : MNRAS, **403** (mar. 2010), 17–44. DOI : 10.1111/j.1365-2966.2009.16087.x. URL : http://adsabs.harvard.edu/abs/2010MNRAS.403...17J (cf. p. 135).

[122] Kann, D. A. "*The Afterglows of Swift-era Gamma-ray Bursts. I. Comparing pre-Swift and Swift-era Long/Soft (Type II) GRB Optical Afterglows*". In : ApJ, **720** (sept. 2010), 1513–1558. DOI : 10.1088/0004-637X/720/2/1513. arXiv : 0712.2186. URL : http://adsabs.harvard.edu/abs/2010ApJ...720.1513K (cf. p. 43, 60–62).

[123] Kann, D. A., Klose, S. et Zeh, A. "*Signatures of Extragalactic Dust in Pre-Swift GRB Afterglows*". In : ApJ, **641** (avr. 2006), 993–1009. DOI : 10.1086/500652. eprint : astro-ph/0512575. URL : http://adsabs.harvard.edu/abs/2006ApJ...641..993K (cf. p. 61).

[124] Kashino, D. et al. "*The FMOS-COSMOS Survey of Star-forming Galaxies at $z \tilde{} 1.6$. I. Hα-based Star Formation Rates and Dust Extinction*". In : ApJ, **777** L8 (nov. 2013), L8. DOI : 10.1088/2041-8205/777/1/L8. arXiv : 1309.4774. URL : http://adsabs.harvard.edu/abs/2013ApJ...777L...8K (cf. p. 126).

[125] Kennicutt Jr., R. C. "*Star Formation in Galaxies Along the Hubble Sequence*". In : ARA&A, **36** (1998), 189–232. DOI : 10.1146/annurev.astro.36.1.189. eprint : astro-ph/9807187. URL : http://adsabs.harvard.edu/abs/1998ARA&A..36..189K (cf. p. 99).

[126] Kewley, L. J., Dopita, M. A., Sutherland, R. S., Heisler, C. A. et Trevena, J. "*Theoretical Modeling of Starburst Galaxies*". In : ApJ, **556** (juil. 2001), 121–140. DOI : 10.1086/321545. eprint : astro-ph/0106324. URL : http://adsabs.harvard.edu/abs/2001ApJ...556..121K (cf. p. 126).

[127] Kim, S.-H., Martin, P. G. et Hendry, P. D. "*The size distribution of interstellar dust particles as determined from extinction*". In : ApJ, **422** (fév. 1994), 164–175. DOI : 10.1086/173714. URL : http://adsabs.harvard.edu/abs/1994ApJ...422..164K (cf. p. 79).

[128] Kistler, M. D., Yüksel, H., Beacom, J. F., Hopkins, A. M. et Wyithe, J. S. B. "*The Star Formation Rate in the Reionization Era as Indicated by Gamma- Ray Bursts*". In : ApJ, **705** (nov. 2009), L104–L108. DOI : 10.1088/0004-637X/705/2/L104. arXiv : 0906.0590 [astro-ph.CO]. URL : https://ui.adsabs.harvard.edu/#abs/2009ApJ...705L.104K (cf. p. 33).

[129] Klebesadel, R. W., Strong, I. B. et Olson, R. A. "*Observations of Gamma-Ray Bursts of Cosmic Origin*". In : ApJ, **182** (juin 1973), L85. DOI : 10.1086/181225. URL : http://adsabs.harvard.edu/abs/1973ApJ...182L..85K (cf. p. 24).

[130] Kouveliotou, C., Meegan, C. A., Fishman, G. J., Bhat, N. P., Briggs, M. S., Koshut, T. M., Paciesas, W. S. et Pendleton, G. N. "*Identification of two classes of gamma-ray bursts*". In : ApJ, **413** (août 1993), L101–L104. DOI : 10.1086/186969. URL : http://adsabs.harvard.edu/abs/1993ApJ...413L.101K (cf. p. 25).

[131] Kriek, M. et Conroy, C. "*The Dust Attenuation Law in Distant Galaxies : Evidence for Variation with Spectral Type*". In : ApJ, **775** L16 (sept. 2013), L16. DOI : 10.1088/2041-8205/775/1/L16. arXiv : 1308.1099. URL : http://adsabs.harvard.edu/abs/2013ApJ...775L..16K (cf. p. 6, 7, 83, 92, 141).

[132] Krühler, T. et al. "*The 2175 Å Dust Feature in a Gamma-Ray Burst Afterglow at Redshift 2.45*". In : ApJ, **685** (sept. 2008), 376–383. DOI : 10.1086/590240. arXiv : 0805.2824. URL : http://adsabs.harvard.edu/abs/2008ApJ...685..376K (cf. p. 30).

[133] Krühler, T. et al. "*The SEDs and host galaxies of the dustiest GRB afterglows*". In : A&A, **534** A108 (oct. 2011), A108. DOI : 10.1051/0004-6361/201117428. arXiv : 1108.0674 [astro-ph.CO]. URL : http://adsabs.harvard.edu/abs/2011A&A...534A.108K (cf. p. 30, 98, 121, 130, 200, 201, 203–206).

[134] Krühler, T. et al. "*The metal-enriched host of an energetic γ-ray burst at $z \quad 1.6$*". In : A&A, **546** A8 (oct. 2012), A8. DOI : 10.1051/0004-6361/201118670. arXiv : 1203.1919 [astro-ph.CO]. URL : http://adsabs.harvard.edu/abs/2012A&A...546A...8K (cf. p. 31, 203).

[135] Krühler, T. et al. "*GRB hosts through cosmic time. VLT/X-Shooter emission-line spectroscopy of 96 γ-ray-burst-selected galaxies at $0.1 < z < 3.6$*". In : A&A, **581** A125 (sept. 2015), A125. DOI : 10.1051/0004-6361/201425561. arXiv : 1505.06743. URL : http://adsabs.harvard.edu/abs/2015A&A...581A.125K (cf. p. 31–33, 121–123, 126, 129, 136, 137, 139, 140, 207).

[136] Kulkarni, S. R., Frail, D. A., Wieringa, M. H., Ekers, R. D., Sadler, E. M., Wark, R. M., Higdon, J. L., Phinney, E. S. et Bloom, J. S. "*Radio emission from the unusual supernova 1998bw and its association with the γ-ray burst of 25 April 1998*". In : Nature, **395** (oct. 1998), 663–669. DOI : 10.1038/27139. URL : https://ui.adsabs.harvard.edu/#abs/1998Natur.395..663K (cf. p. 28).

[137] Laskar, T. et al. "*GRB 120521C at z 6 and the Properties of High-redshift GRBs*". In : Astrophys. J., **781** (2014), 1. DOI : 10.1088/0004-637X/781/1/1. arXiv : 1307.6586 [astro-ph.HE] (cf. p. 53).

[138] Law, K.-H., Gordon, K. D. et Misselt, K. A. "*DirtyGrid I : 3D Dust Radiative Transfer Modeling of Spectral Energy Distributions of Dusty Stellar Populations*". In : The Astrophysical Journal Supplement Series, **236** 32 (juin 2018), 32. DOI : 10.3847/1538-4365/aabf41. URL : http://adsabs.harvard.edu/abs/2018ApJS..236...32L (cf. p. 146).

[139] Lawless, J. F. "*Statistical Models and Methods for Lifetime Data*". In : sous la dir. de Wiley. John Wiley et Sons, Inc., 2002. Chap. Observation Schemes, Censoring, and Likelihood, 49–78. URL : http://dx.doi.org/10.1002/9781118033005.ch2 (cf. p. 53).

[140] Le Floc'h, E., Charmandaris, V., Forrest, W. J., Mirabel, I. F., Armus, L. et Devost, D. "*Probing Cosmic Star Formation Using Long Gamma-Ray Bursts : New Constraints from the Spitzer Space Telescope*". In : ApJ, **642** (mai 2006), 636–652. DOI : 10.1086/501118. eprint : astro-ph/0601251. URL : http://adsabs.harvard.edu/abs/2006ApJ...642..636L (cf. p. 30).

[141] Le Floc'h, E. et al. "*Are the hosts of gamma-ray bursts sub-luminous and blue galaxies ?*" In : A&A, **400** (mar. 2003), 499–510. DOI : 10.1051/0004-6361:20030001. arXiv : astro-ph/0301149 [astro-ph]. URL : https://ui.adsabs.harvard.edu/#abs/2003A&A...400..499L (cf. p. 30, 32).

[142] Lee, S.-K., Ferguson, H. C., Somerville, R. S., Wiklind, T. et Giavalisco, M. "*The Estimation of Star Formation Rates and Stellar Population Ages of High-redshift Galaxies from Broad-band Photometry*". In : ApJ, **725** (déc. 2010), 1644–1651. DOI : 10.1088/0004-637X/725/2/1644. arXiv : 1010.1966. URL : http://adsabs.harvard.edu/abs/2010ApJ...725.1644L (cf. p. 124).

[143] Leitherer, C., Li, I.-H., Calzetti, D. et Heckman, T. M. "*Global Far-Ultraviolet (912-1800 Å) Properties of Star-forming Galaxies*". In : ApJS, **140** (juin 2002), 303–329. DOI : 10.1086/342486 (cf. p. 84).

[144] Levesque, E. M., Kewley, L. J., Graham, J. F. et Fruchter, A. S. "*A High-metallicity Host Environment for the Long-duration GRB 020819*". In : ApJL, **712** (mar. 2010), L26–L30. DOI : 10.1088/2041-8205/712/1/L26. arXiv : 1001.0970 [astro-ph.HE]. URL : http://adsabs.harvard.edu/abs/2010ApJ...712L..26L (cf. p. 31).

[145] Littlejohns, O. M. "*A detailed study of the optical attenuation of gamma-ray bursts in the Swift era*". In : MNRAS, **449** (mai 2015), 2919–2936. DOI : 10.1093/MNRAS/stv479. arXiv : 1412.6530 [astro-ph.HE]. URL : http://adsabs.harvard.edu/abs/2015MNRAS.449.2919L (cf. p. 173).

[146] Lo Faro, B., Buat, V., Roehlly, Y., Alvarez-Marquez, J., Burgarella, D., Silva, L. et Efstathiou, A. "*Characterizing the UV-to-NIR shape of the dust attenuation curve of IR luminous galaxies up to $z \sim 2$*". In : MNRAS, **472** (déc. 2017), 1372–1391. DOI : 10.1093/mnras/stx1901. arXiv : 1707.09805. URL : http://adsabs.harvard.edu/abs/2017MNRAS.472.1372L (cf. p. 142).

[147] MacFadyen, A. I. et Woosley, S. E. "*Collapsars : Gamma-Ray Bursts and Explosions in "Failed Supernovae"*". In : ApJ, **524** (oct. 1999), 262–289. DOI : 10.1086/307790. eprint : astro-ph/9810274. URL : http://adsabs.harvard.edu/abs/1999ApJ...524..262M (cf. p. 28).

[148] Madau, P. "*Radiative transfer in a clumpy universe : The colors of high-redshift galaxies*". In : ApJ, **441** (mar. 1995), 18–27. DOI : 10.1086/175332. URL : http://adsabs.harvard.edu/abs/1995ApJ...441...18M (cf. p. 46).

[149] Maiolino, R. et al. "*AMAZE. I. The evolution of the mass-metallicity relation at $z > 3$*". In : A&A, **488** (sept. 2008), 463–479. DOI : 10.1051/0004-6361:200809678. arXiv : 0806.2410 [astro-ph]. URL : https://ui.adsabs.harvard.edu/#abs/2008A&A...488..463M (cf. p. 33, 125).

[150] Mannucci, F., Cresci, G., Maiolino, R., Marconi, A. et Gnerucci, A. "*A fundamental relation between mass, star formation rate and metallicity in local and high-redshift galaxies*". In : MNRAS, **408** (nov. 2010), 2115–2127. DOI : 10.1111/j.1365-2966.2010.17291.x. arXiv : 1005.0006. URL : http://adsabs.harvard.edu/abs/2010MNRAS.408.2115M (cf. p. 33).

[151] Mannucci, F., Salvaterra, R. et Campisi, M. A. "*The metallicity of the long GRB hosts and the fundamental metallicity relation of low-mass galaxies*". In : MNRAS, **414** (juin 2011), 1263–1268. DOI : 10.1111/j.1365-2966.2011.18459.x. arXiv : 1011.4506 [astro-ph.CO]. URL : https://ui.adsabs.harvard.edu/#abs/2011MNRAS.414.1263M (cf. p. 33).

[152] Maraston, C., Pforr, J., Renzini, A., Daddi, E., Dickinson, M., Cimatti, A. et Tonini, C. "*Star formation rates and masses of z ˜ 2 galaxies from multicolour photometry*". In : MNRAS, **407** (sept. 2010), 830–845. DOI : 10.1111/j.1365-2966.2010.16973.x. arXiv : 1004.4546. URL : http://adsabs.harvard.edu/abs/2010MNRAS.407..830M (cf. p. 124).

[153] Mazets, E. P. et al. "*Catalog of cosmic gamma-ray bursts from the KONUS experiment data. I.*" In : Astrophysics and Space Science, **80** (nov. 1981), 3–83. DOI : 10.1007/BF00649140. URL : http://adsabs.harvard.edu/abs/1981Ap&SS..80....3M (cf. p. 24).

[154] Meegan, C. A. et al. "*The 4B BATSE gamma-ray burst catalog*". In : *Gamma-Ray Bursts, 4th Hunstville Symposium*. Sous la dir. de C. A. Meegan, R. D. Preece et T. M. Koshut. **428** American Institute of Physics Conference Series. Mai 1998, 3–9. doi : 10.1063/1.55355. url : http://adsabs.harvard.edu/abs/1998AIPC..428....3M (cf. p. 25).

[155] Meiksin, A. "*Colour corrections for high redshift objects due to intergalactic attenuation*". In : Mon. Not. Roy. Astron. Soc., **365** (2006), 807–812. doi : 10.1111/J.1365-2966.2005.09756.X. arXiv : astro-ph/0512435 [astro-ph] (cf. p. 46, 50).

[156] Melandri, A. et al. "*The dark bursts population in a complete sample of bright Swift long gamma-ray bursts*". In : MNRAS, **421** (avr. 2012), 1265–1272. doi : 10.1111/j.1365-2966.2011.20398.x. arXiv : 1112.4480 [astro-ph.HE]. url : http://adsabs.harvard.edu/abs/2012MNRAS.421.1265M (cf. p. 31).

[157] Mészáros, P. "*Gamma-ray bursts*". In : Reports on Progress in Physics, **69** (août 2006), 2259–2321. doi : 10.1088/0034-4885/69/8/R01. eprint : astro-ph/0605208. url : http://adsabs.harvard.edu/abs/2006RPPh...69.2259M (cf. p. 26, 27).

[158] Metzger, B. D. et al. "*Electromagnetic counterparts of compact object mergers powered by the radioactive decay of r-process nuclei*". In : MNRAS, **406** (août 2010), 2650–2662. doi : 10.1111/j.1365-2966.2010.16864.x. arXiv : 1001.5029 [astro-ph.HE]. url : http://adsabs.harvard.edu/abs/2010MNRAS.406.2650M (cf. p. 30).

[159] Metzger, M. R., Djorgovski, S. G., Kulkarni, S. R., Steidel, C. C., Adelberger, K. L., Frail, D. A., Costa, E. et Frontera, F. "*Spectral constraints on the redshift of the optical counterpart to the γ-ray burst of 8 May 1997*". In : Nature, **387** (juin 1997), 878–880. doi : 10.1038/43132. url : http://adsabs.harvard.edu/abs/1997Natur.387..878M (cf. p. 25).

[160] Michałowski, M. J. et al. "*The Optically Unbiased GRB Host (TOUGH) Survey. VI. Radio Observations at $z < 1$ and Consistency with Typical Star-forming Galaxies*". In : ApJ, **755** 85 (août 2012), 85. doi : 10.1088/0004-637X/755/2/85. arXiv : 1205.4239 [astro-ph.CO]. url : http://adsabs.harvard.edu/abs/2012ApJ...755...85M (cf. p. 32).

[161] Misselt, K. A., Clayton, G. C. et Gordon, K. D. "*A Reanalysis of the Ultraviolet Extinction from Interstellar Dust in the Large Magellanic Cloud*". In : ApJ, **515** (avr. 1999), 128–139. doi : 10.1086/307010. eprint : astro-ph/9811036. url : http://adsabs.harvard.edu/abs/1999ApJ...515..128M (cf. p. 35).

[162] Morgan, A. N. et al. "*Evidence for dust destruction from the early-time colour change of GRB 120119A*". In : MNRAS, **440** (mai 2014), 1810–1823. doi : 10.1093/mnras/stu344. arXiv : 1305.1928 [astro-ph.HE]. url : http://adsabs.harvard.edu/abs/2014MNRAS.440.1810M (cf. p. 206).

[163] Nagao, T., Maiolino, R., Marconi, A. et Matsuhara, H. "*Metallicity diagnostics with infrared fine-structure lines*". In : A&A, **526** A149 (fév. 2011), A149. doi : 10.1051/0004-6361/201015471. arXiv : 1012.2471. url : http://adsabs.harvard.edu/abs/2011A&A...526A.149N (cf. p. 122).

[164] Narayan, R., Paczynski, B. et Piran, T. "*Gamma-ray bursts as the death throes of massive binary stars*". In : ApJ, **395** (août 1992), L83–L86. doi : 10.1086/186493. eprint : astro-ph/9204001. url : http://adsabs.harvard.edu/abs/1992ApJ...395L..83N (cf. p. 28, 29).

[165] Noll, S., Burgarella, D., Giovannoli, E., Buat, V., Marcillac, D. et Muñoz-Mateos, J. C. "*Analysis of galaxy spectral energy distributions from far-UV to far-IR with CIGALE : studying a SINGS test sample*". In : A&A, **507** (déc. 2009), 1793–1813. DOI : 10.1051/0004-6361/200912497. arXiv : 0909.5439. URL : http://adsabs.harvard.edu/abs/2009A&A...507.1793N (cf. p. 7, 9, 73–75, 92, 98, 142).

[166] Nousek, J. A. et al. "*Evidence for a Canonical Gamma-Ray Burst Afterglow Light Curve in the Swift XRT Data*". In : ApJ, **642** (mai 2006), 389–400. DOI : 10.1086/500724. arXiv : astro-ph/0508332 [astro-ph]. URL : https://ui.adsabs.harvard.edu/#abs/2006ApJ...642..389N (cf. p. 27).

[167] Paczynski, B. "*Gamma-ray bursters at cosmological distances*". In : ApJL, **308** (sept. 1986), L43–L46. DOI : 10.1086/184740. URL : http://adsabs.harvard.edu/abs/1986ApJ...308L..43P (cf. p. 26, 29).

[168] Palmerio, J. et al. "*Are LGRBs biased tracers of star formation ? Clues from the host galaxies of the Swift/BAT6 complete sample of bright LGRBs*". In : submitted to A&A, (soumis) (cf. p. 32, 33).

[169] Pannella, M. et al. "*GOODS-Herschel : Star Formation, Dust Attenuation, and the FIR-radio Correlation on the Main Sequence of Star-forming Galaxies up to $z \simeq 4$*". In : ApJ, **807** 141 (juil. 2015), 141. DOI : 10.1088/0004-637X/807/2/141. arXiv : 1407.5072. URL : http://adsabs.harvard.edu/abs/2015ApJ...807..141P (cf. p. 37).

[170] Pei, Y. C. "*Interstellar dust from the Milky Way to the Magellanic Clouds*". In : ApJ, **395** (août 1992), 130–139. DOI : 10.1086/171637. URL : http://adsabs.harvard.edu/abs/1992ApJ...395..130P (cf. p. 35, 45–47, 75, 98).

[171] Perley, D. A. et Perley, R. A. "*Radio Constraints on Heavily Obscured Star Formation within Dark Gamma-Ray Burst Host Galaxies*". In : ApJ, **778** 172 (déc. 2013), 172. DOI : 10.1088/0004-637X/778/2/172. arXiv : 1305.2941. URL : http://adsabs.harvard.edu/abs/2013ApJ...778..172P (cf. p. 198, 199, 201–205).

[172] Perley, D. A. et al. "*The Host Galaxies of Swift Dark Gamma-ray Bursts : Observational Constraints on Highly Obscured and Very High Redshift GRBs*". In : The Astronomical Journal, **138** (déc. 2009), 1690–1708. DOI : 10.1088/0004-6256/138/6/1690. arXiv : 0905.0001 [astro-ph.HE]. URL : http://adsabs.harvard.edu/abs/2009AJ....138.1690P (cf. p. 30).

[173] Perley, D. A. et al. "*A Population of Massive, Luminous Galaxies Hosting Heavily Dust-obscured Gamma-Ray Bursts : Implications for the Use of GRBs as Tracers of Cosmic Star Formation*". In : ApJ, **778** 128 (déc. 2013), 128. DOI : 10.1088/0004-637X/778/2/128. arXiv : 1301.5903. URL : http://adsabs.harvard.edu/abs/2013ApJ...778..128P (cf. p. 31, 32, 121, 198–205).

[174] Perley, D. A. et al. "*Connecting GRBs and ULIRGs : A Sensitive, Unbiased Survey for Radio Emission from Gamma-Ray Burst Host Galaxies at $0 < z < 2.5$*". In : ApJ, **801** 102 (mar. 2015), 102. DOI : 10.1088/0004-637X/801/2/102. arXiv : 1407.4456 [astro-ph.HE]. URL : http://adsabs.harvard.edu/abs/2015ApJ...801..102P (cf. p. 199, 200).

[175] Perley, D. A. et al. "*The Swift Gamma-Ray Burst Host Galaxy Legacy Survey. I. Sample Selection and Redshift Distribution*". In : ApJ, **817** 7 (jan. 2016), 7. DOI : 10.3847/0004-637X/817/1/7. arXiv : 1504.02482. URL : http://adsabs.harvard.edu/abs/2016ApJ...817....7P (cf. p. 31).

[176] Perley, D. A. et al. "*The Swift GRB Host Galaxy Legacy Survey. II. Rest-frame Near-IR Luminosity Distribution and Evidence for a Near-solar Metallicity Threshold*". In : ApJ, **817** 8 (jan. 2016), 8. doi : 10.3847/0004-637X/817/1/8. arXiv : 1504.02479. url : http://adsabs.harvard.edu/abs/2016ApJ...817....8P (cf. p. 8, 31, 33, 99, 138, 139, 200, 203, 206).

[177] Pforr, J., Maraston, C. et Tonini, C. "*Recovering galaxy stellar population properties from broad-band spectral energy distribution fitting*". In : MNRAS, **422** (juin 2012), 3285–3326. doi : 10.1111/j.1365-2966.2012.20848.x. arXiv : 1203.3548. url : http://adsabs.harvard.edu/abs/2012MNRAS.422.3285P (cf. p. 124).

[178] Phinney, E. S. "*The Rate of Neutron Star Binary Mergers in the Universe : Minimal Predictions for Gravity Wave Detectors*". In : ApJ, **380** (oct. 1991), L17. doi : 10.1086/186163. url : https://ui.adsabs.harvard.edu/#abs/1991ApJ...380L..17P (cf. p. 29).

[179] Pierini, D., Gordon, K. D., Witt, A. N. et Madsen, G. J. "*Dust Attenuation in Late-Type Galaxies. I. Effects on Bulge and Disk Components*". In : ApJ, **617** (déc. 2004), 1022–1046. doi : 10.1086/425651. eprint : astro-ph/0409183. url : http://adsabs.harvard.edu/abs/2004ApJ...617.1022P (cf. p. 74, 83, 135).

[180] Piran, T. "*Gamma-ray bursts and the fireball model*". In : Physics Reports, **314** (juin 1999), 575–667. doi : 10.1016/S0370-1573(98)00127-6. eprint : astro-ph/9810256. url : http://adsabs.harvard.edu/abs/1999PhR...314..575P (cf. p. 26).

[181] Planck Collaboration et Ade, P. A. "*Planck 2015 results. XIII. Cosmological parameters*". In : ArXiv e-prints, (fév. 2015). arXiv : 1502.01589. url : http://adsabs.harvard.edu/abs/2015arXiv150201589P (cf. p. 61).

[182] Prevot, M. L., Lequeux, J., Prevot, L., Maurice, E. et Rocca-Volmerange, B. "*The typical interstellar extinction in the Small Magellanic Cloud*". In : A&A, **132** (mar. 1984), 389–392. url : http://adsabs.harvard.edu/abs/1984A&A...132..389P (cf. p. 35).

[183] Prochaska, J. X. et al. "*The Galaxy Hosts and Large-Scale Environments of Short-Hard Gamma-Ray Bursts*". In : ApJ, **642** (mai 2006), 989–994. doi : 10.1086/501160. eprint : astro-ph/0510022. url : http://adsabs.harvard.edu/abs/2006ApJ...642..989P (cf. p. 29).

[184] Prochaska, J. X., Bloom, J. S., Chen, H.-W., Hurley, K. C., Melbourne, J., Dressler, A., Graham, J. R., Osip, D. J. et Vacca, W. D. "*The Host Galaxy of GRB 031203 : Implications of Its Low Metallicity, Low Redshift, and Starburst Nature*". In : ApJ, **611** (août 2004), 200–207. doi : 10.1086/421988. arXiv : astro-ph/0402085 [astro-ph]. url : https://ui.adsabs.harvard.edu/#abs/2004ApJ...611..200P (cf. p. 30).

[185] Puglisi, A. et al. "*Dust attenuation in $z \sim 1$ galaxies from Herschel and 3D-HST Hα measurements*". In : A&A, **586** A83 (fév. 2016), A83. doi : 10.1051/0004-6361/201526782. arXiv : 1507.00005. url : http://adsabs.harvard.edu/abs/2016A&A...586A..83P (cf. p. 126).

[186] Rau, A. et al. "*A Very Metal-poor Damped Lyman-α System Revealed Through the Most Energetic GRB 090926A*". In : ApJ, **720** (sept. 2010), 862–871. doi : 10.1088/0004-637X/720/1/862. arXiv : 1004.3261 [astro-ph.CO]. url : http://adsabs.harvard.edu/abs/2010ApJ...720..862R (cf. p. 34).

[187] Reddy, N. A., Steidel, C. C., Pettini, M. et Bogosavljević, M. "*Spectroscopic Measurements of the Far-Ultraviolet Dust Attenuation Curve at $z \sim 3$*". In : ApJ, **828** 107 (sept. 2016), 107. doi : 10.3847/0004-637X/828/2/107. arXiv : 1606.00434. url : http://adsabs.harvard.edu/abs/2016ApJ...828..107R (cf. p. 6, 83, 141).

[188] Reddy, N. A. et al. "*The MOSDEF Survey : Measurements of Balmer Decrements and the Dust Attenuation Curve at Redshifts $z \sim 1.4$-2.6*". In : ApJ, **806** 259 (juin 2015), 259. DOI : 10.1088/0004-637X/806/2/259. arXiv : 1504.02782. URL : http://adsabs.harvard.edu/abs/2015ApJ...806..259R (cf. p. 6, 83, 141).

[189] Rees, M. J. et Meszaros, P. "*Relativistic fireballs - Energy conversion and time-scales*". In : MNRAS, **258** (sept. 1992), 41P–43P. DOI : 10.1093/mnras/258.1.41P. URL : http://adsabs.harvard.edu/abs/1992MNRAS.258P..41R (cf. p. 26, 27).

[190] Rees, M. J. et Meszaros, P. "*Unsteady outflow models for cosmological gamma-ray bursts*". In : ApJL, **430** (août 1994), L93–L96. DOI : 10.1086/187446. eprint : astro-ph/9404038. URL : http://adsabs.harvard.edu/abs/1994ApJ...430L..93R (cf. p. 26).

[191] Richard, J., Jones, T., Ellis, R., Stark, D. P., Livermore, R. et Swinbank, M. "*The emission line properties of gravitationally lensed $1.5 < z < 5$ galaxies*". In : MNRAS, **413** (mai 2011), 643–658. DOI : 10.1111/j.1365-2966.2010.18161.x. arXiv : 1011.6413. URL : http://adsabs.harvard.edu/abs/2011MNRAS.413..643R (cf. p. 136).

[192] Richards, G. T. et al. "*Red and Reddened Quasars in the Sloan Digital Sky Survey*". In : AJ, **126** (sept. 2003), 1131–1147. DOI : 10.1086/377014. eprint : astro-ph/0305305. URL : http://adsabs.harvard.edu/abs/2003AJ....126.1131R (cf. p. 97).

[193] Rossi, A. et al. "*A deep search for the host galaxies of gamma-ray bursts with no detected optical afterglow*". In : A&A, **545** A77 (sept. 2012), A77. DOI : 10.1051/0004-6361/201117201. arXiv : 1202.1434 [astro-ph.CO]. URL : https://ui.adsabs.harvard.edu/#abs/2012A&A...545A..77R (cf. p. 31).

[194] Rosswog, S., Liebendörfer, M., Thielemann, F. .-.-K., Davies, M. B., Benz, W. et Piran, T. "*Mass ejection in neutron star mergers*". In : A&A, **341** (jan. 1999), 499–526. arXiv : astro-ph/9811367 [astro-ph]. URL : https://ui.adsabs.harvard.edu/#abs/1999A&A...341..499R (cf. p. 30).

[195] Rowlinson, A. et al. "*Discovery of the afterglow and host galaxy of the low-redshift short GRB 080905A*". In : MNRAS, **408** (oct. 2010), 383–391. DOI : 10.1111/j.1365-2966.2010.17115.x. arXiv : 1006.0487 [astro-ph.HE]. URL : http://adsabs.harvard.edu/abs/2010MNRAS.408..383R (cf. p. 29).

[196] Salim, S., Boquien, M. et Lee, J. C. "*Dust Attenuation Curves in the Local Universe : Demographics and New Laws for Star-forming Galaxies and High-redshift Analogs*". In : ApJ, **859** 11 (mai 2018), 11. DOI : 10.3847/1538-4357/aabf3c. arXiv : 1804.05850. URL : http://adsabs.harvard.edu/abs/2018ApJ...859...11S (cf. p. 7, 9, 76, 83, 84, 93, 95, 135, 136, 141, 142).

[197] Salmon, B. et al. "*Breaking the Curve with CANDELS : A Bayesian Approach to Reveal the Non-Universality of the Dust-Attenuation Law at High Redshift*". In : ApJ, **827** 20 (août 2016), 20. DOI : 10.3847/0004-637X/827/1/20. arXiv : 1512.05396. URL : http://adsabs.harvard.edu/abs/2016ApJ...827...20S (cf. p. 6, 7, 83, 93–95, 141).

[198] Salvaterra, R. et al. "*GRB090423 at a redshift of $z \sim 8.1$*". In : Nature, **461** (oct. 2009), 1258–1260. DOI : 10.1038/nature08445. arXiv : 0906.1578. URL : http://adsabs.harvard.edu/abs/2009Natur.461.1258S (cf. p. 30, 31).

[199] Sari, R., Piran, T. et Narayan, R. "*Spectra and Light Curves of Gamma-Ray Burst Afterglows*". In : ApJ, **497** (avr. 1998), L17–L20. DOI : 10.1086/311269. eprint : astro-ph/9712005. URL : http://adsabs.harvard.edu/abs/1998ApJ...497L..17S (cf. p. 43, 97).

[200] Savaglio, S., Glazebrook, K. et Le Borgne, D. "*The Galaxy Population Hosting Gamma-Ray Bursts*". In : ApJ, **691** (jan. 2009), 182–211. DOI : 10.1088/0004-637X/691/1/182. arXiv : 0803.2718. URL : http://adsabs.harvard.edu/abs/2009ApJ...691..182S (cf. p. 30).

[201] Savaglio, S. et al. "*Supersolar metal abundances in two galaxies at $z \sim 3.57$ revealed by the GRB 090323 afterglow spectrum*". In : MNRAS, **420** (fév. 2012), 627–636. DOI : 10.1111/j.1365-2966.2011.20074.x. arXiv : 1110.4642 [astro-ph.CO]. URL : https://ui.adsabs.harvard.edu/#abs/2012MNRAS.420..627S (cf. p. 31).

[202] Schady, P. "*Gamma-ray bursts and their use as cosmic probes*". In : Royal Society Open Science, **4** 170304 (juil. 2017), 170304. DOI : 10.1098/rsos.170304. arXiv : 1707.05214. URL : http://adsabs.harvard.edu/abs/2017RSOS....470304S (cf. p. 34, 36).

[203] Schady, P., Savaglio, S., Krühler, T., Greiner, J. et Rau, A. "*The missing gas problem in GRB host galaxies : evidence for a highly ionised component*". In : A&A, **525** A113 (jan. 2011), A113. DOI : 10.1051/0004-6361/201015608. arXiv : 1010.2034. URL : http://adsabs.harvard.edu/abs/2011A&A...525A.113S (cf. p. 34).

[204] Schady, P. et al. "*The dust extinction curves of gamma-ray burst host galaxies*". In : A&A, **537** A15 (jan. 2012), A15. DOI : 10.1051/0004-6361/201117414. arXiv : 1110.3218. URL : http://adsabs.harvard.edu/abs/2012A&A...537A..15S (cf. p. 6, 34, 36, 121).

[205] Schady, P. et al. "*Super-solar metallicity at the position of the ultra-long GRB 130925A*". In : A&A, **579** A126 (juil. 2015), A126. DOI : 10.1051/0004-6361/201526060. URL : https://ui.adsabs.harvard.edu/#abs/2015A&A...579A.126S (cf. p. 31).

[206] Schlafly, E. F. et Finkbeiner, D. P. "*Measuring Reddening with Sloan Digital Sky Survey Stellar Spectra and Recalibrating SFD*". In : ApJ, **737** 103 (août 2011), 103. DOI : 10.1088/0004-637X/737/2/103. arXiv : 1012.4804 [astro-ph.GA]. URL : http://adsabs.harvard.edu/abs/2011ApJ...737..103S (cf. p. 198).

[207] Schlegel, D. J., Finkbeiner, D. P. et Davis, M. "*Maps of Dust Infrared Emission for Use in Estimation of Reddening and Cosmic Microwave Background Radiation Foregrounds*". In : ApJ, **500** (juin 1998), 525–553. DOI : 10.1086/305772. eprint : astro-ph/9710327. URL : http://adsabs.harvard.edu/abs/1998ApJ...500..525S (cf. p. 56).

[208] Schreiber, C. et al. "*The Herschel view of the dominant mode of galaxy growth from $z = 4$ to the present day*". In : A&A, **575** A74 (mar. 2015), A74. DOI : 10.1051/0004-6361/201425017. arXiv : 1409.5433. URL : http://adsabs.harvard.edu/abs/2015A&A...575A..74S (cf. p. 31, 129, 130).

[209] Schulze, S. et al. "*The Optically Unbiased GRB Host (TOUGH) Survey. VII. The Host Galaxy Luminosity Function : Probing the Relationship between GRBs and Star Formation to Redshift ~ 6*". In : ApJ, **808** 73 (juil. 2015), 73. DOI : 10.1088/0004-637X/808/1/73. arXiv : 1503.04246. URL : http://adsabs.harvard.edu/abs/2015ApJ...808...73S (cf. p. 32).

[210] Seon, K.-I. et Draine, B. T. "*Radiative Transfer Model of Dust Attenuation Curves in Clumpy, Galactic Environments*". In : ApJ, **833** 201 (déc. 2016), 201. DOI : 10.3847/1538-4357/833/2/201. arXiv : 1606.02030. URL : http://adsabs.harvard.edu/abs/2016ApJ...833..201S (cf. p. 7, 9, 10, 73, 74, 77, 78, 80, 92, 93, 130).

[211] Silva, L., Granato, G. L., Bressan, A. et Danese, L. "*Modeling the Effects of Dust on Galactic Spectral Energy Distributions from the Ultraviolet to the Millimeter Band*". In : ApJ, **509** (déc. 1998), 103–117. DOI : 10.1086/306476. URL : http://adsabs.harvard.edu/abs/1998ApJ...509..103S (cf. p. 74, 135).

[212] Sollerman, J., Östlin, G., Fynbo, J. P., Hjorth, J., Fruchter, A. et Pedersen, K. "*On the nature of nearby GRB/SN host galaxies*". In : New Astronomy, **11** (nov. 2005), 103–115. doi : 10.1016/j.newast.2005.06.004. arXiv : astro-ph/0506686 [astro-ph]. url : https://ui.adsabs.harvard.edu/#abs/2005NewA...11..103S (cf. p. 30).

[213] Stanek, K. Z. et al. "*Spectroscopic Discovery of the Supernova 2003dh Associated with GRB 030329*". In : ApJ, **591** (juil. 2003), L17–L20. doi : 10.1086/376976. eprint : astro-ph/0304173. url : http://adsabs.harvard.edu/abs/2003ApJ...591L..17S (cf. p. 28, 29).

[214] Stark, D. P., Schenker, M. A., Ellis, R., Robertson, B., McLure, R. et Dunlop, J. "*Keck Spectroscopy of 3 < z < 7 Faint Lyman Break Galaxies : The Importance of Nebular Emission in Understanding the Specific Star Formation Rate and Stellar Mass Density*". In : ApJ, **763** 129 (fév. 2013), 129. doi : 10.1088/0004-637X/763/2/129. arXiv : 1208.3529. url : http://adsabs.harvard.edu/abs/2013ApJ...763..129S (cf. p. 122).

[215] Steidel, C. C. et al. "*Strong Nebular Line Ratios in the Spectra of z ˜ 2-3 Star Forming Galaxies : First Results from KBSS-MOSFIRE*". In : ApJ, **795** 165 (nov. 2014), 165. doi : 10.1088/0004-637X/795/2/165. arXiv : 1405.5473. url : http://adsabs.harvard.edu/abs/2014ApJ...795..165S (cf. p. 123).

[216] Svensson, K. M. et al. "*The dark GRB 080207 in an extremely red host and the implications for gamma-ray bursts in highly obscured environments*". In : MNRAS, **421** (mar. 2012), 25–35. doi : 10.1111/j.1365-2966.2011.19811.x. arXiv : 1109.3167. url : http://adsabs.harvard.edu/abs/2012MNRAS.421...25S (cf. p. 202).

[217] Tanvir, N. R., Levan, A. J., Fruchter, A. S., Hjorth, J., Hounsell, R. A., Wiersema, K. et Tunnicliffe, R. L. "*A 'kilonova' associated with the short-duration γ-ray burst GRB 130603B*". In : Nature, **500** (août 2013), 547–549. doi : 10.1038/nature12505. arXiv : 1306.4971 [astro-ph.HE]. url : http://adsabs.harvard.edu/abs/2013Natur.500..547T (cf. p. 30).

[218] Tanvir, N. R. et al. "*The submillimetre properties of gamma-ray burst host galaxies*". In : MNRAS, **352** (août 2004), 1073–1080. doi : 10.1111/j.1365-2966.2004.08001.x. eprint : astro-ph/0406233. url : http://adsabs.harvard.edu/abs/2004MNRAS.352.1073T (cf. p. 30).

[219] Tanvir, N. R. et al. "*A γ-ray burst at a redshift of z˜8.2*". In : Nature, **461** (oct. 2009), 1254–1257. doi : 10.1038/nature08459. arXiv : 0906.1577 [astro-ph.CO]. url : http://adsabs.harvard.edu/abs/2009Natur.461.1254T (cf. p. 30, 31).

[220] Tanvir, N. R. et al. "*The Properties of GRB 120923A at a Spectroscopic Redshift of z≈7.8*". In : ApJ, **865** 107 (oct. 2018), 107. doi : 10.3847/1538-4357/aadba9. arXiv : 1703.09052 [astro-ph.HE]. url : http://adsabs.harvard.edu/abs/2018ApJ...865..107T (cf. p. 30).

[221] Thöne, C. C. et al. "*Photometry and spectroscopy of GRB 060526 : a detailed study of the afterglow and host galaxy of a z = 3.2 gamma-ray burst*". In : A&A, **523** A70 (nov. 2010), A70. doi : 10.1051/0004-6361/200810340. arXiv : 0806.1182. url : http://adsabs.harvard.edu/abs/2010A&A...523A..70T (cf. p. 34).

[222] Thöne, C. C. et al. "*GRB 100219A with X-shooter - abundances in a galaxy at z =4.7*". In : MNRAS, **428** (fév. 2013), 3590–3606. doi : 10.1093/mnras/sts303. arXiv : 1206.2337 [astro-ph.HE]. url : http://adsabs.harvard.edu/abs/2013MNRAS.428.3590T (cf. p. 34).

[223] Trenti, M., Perna, R. et Jimenez, R. "*The Luminosity and Stellar Mass Functions of GRB Host Galaxies : Insight Into the Metallicity Bias*". In : ApJ, **802** 103 (avr. 2015), 103. doi : 10.1088/0004-637X/802/2/103. arXiv : 1406.1503 [astro-ph.GA]. url : https://ui.adsabs.harvard.edu/#abs/2015ApJ...802..103T (cf. p. 32).

[224] Trenti, M., Perna, R., Levesque, E. M., Shull, J. M. et Stocke, J. T. "*Gamma-Ray Burst Host Galaxy Surveys at Redshift $z \gtrsim 4$: Probes of Star Formation Rate and Cosmic Reionization*". In : ApJ, **749** L38 (avr. 2012), L38. doi : 10.1088/2041-8205/749/2/L38. arXiv : 1202.0010 [astro-ph.CO]. url : https://ui.adsabs.harvard.edu/#abs/2012ApJ...749L..38T (cf. p. 33).

[225] Tuffs, R. J., Popescu, C. C., Völk, H. J., Kylafis, N. D. et Dopita, M. A. "*Modelling the spectral energy distribution of galaxies. III. Attenuation of stellar light in spiral galaxies*". In : A&A, **419** (juin 2004), 821–835. doi : 10.1051/0004-6361:20035689. eprint : astro-ph/0401630. url : http://adsabs.harvard.edu/abs/2004A&A...419..821T (cf. p. 74, 83, 135).

[226] Tunnicliffe, R. L. et al. "*On the nature of the 'hostless' short GRBs*". In : MNRAS, **437** (jan. 2014), 1495–1510. doi : 10.1093/mnras/stt1975. arXiv : 1402.0766 [astro-ph.HE]. url : http://adsabs.harvard.edu/abs/2014MNRAS.437.1495T (cf. p. 29).

[227] Turpin, D. "*Study of the high-energy transient objects in the Universe in the era of the multi-messenger observations*". PhD Thesis. Universite Toulouse 3 Paul Sabatier (UT3 Paul Sabatier), déc. 2016. url : https://tel.archives-ouvertes.fr/tel-01560820 (cf. p. 43, 63).

[228] Valencic, L. A., Clayton, G. C. et Gordon, K. D. "*Ultraviolet Extinction Properties in the Milky Way*". In : ApJ, **616** (déc. 2004), 912–924. doi : 10.1086/424922. eprint : astro-ph/0408409. url : http://adsabs.harvard.edu/abs/2004ApJ...616..912V (cf. p. 34).

[229] van den Heuvel, E. P. et Lorimer, D. R. "*On the galactic and cosmic merger rate of double neutron stars.*" In : MNRAS, **283** (nov. 1996), L37–L40. doi : 10.1093/mnras/283.2.L37. url : https://ui.adsabs.harvard.edu/#abs/1996MNRAS.283L..37V (cf. p. 29).

[230] van der Horst, A. J., Kouveliotou, C., Gehrels, N., Rol, E., Wijers, R. A. J., Cannizzo, J. K., Racusin, J. et Burrows, D. N. "*Optical Classification of Gamma-Ray Bursts in the Swift Era*". In : ApJ, **699** (juil. 2009), 1087–1091. doi : 10.1088/0004-637X/699/2/1087. arXiv : 0905.0524 [astro-ph.HE]. url : http://adsabs.harvard.edu/abs/2009ApJ...699.1087V (cf. p. 31).

[231] van Dyk, S. D., Hamuy, M. et Filippenko, A. V. "*Supernovae and Massive Star Formation Regions*". In : Astronomical Journal, **111** (mai 1996), 2017. doi : 10.1086/117937. url : http://adsabs.harvard.edu/abs/1996AJ....111.2017V (cf. p. 28).

[232] van Paradijs, J. et al. "*Transient optical emission from the error box of the γ-ray burst of 28 February 1997*". In : Nature, **386** (avr. 1997), 686–689. doi : 10.1038/386686a0. url : http://adsabs.harvard.edu/abs/1997Natur.386..686V (cf. p. 25).

[233] Vedrenne, G. et Atteia, J.-L. "*Gamma-Ray Bursts : The brightest explosions in the Universe*". 2009. url : http://adsabs.harvard.edu/abs/2009grbb.book.....V (cf. p. 26).

[234] Vergani, S. D. et al. "*Are long gamma-ray bursts biased tracers of star formation ? Clues from the host galaxies of the Swift/BAT6 complete sample of LGRBs . I. Stellar mass at $z < 1$*". In : A&A, **581** A102 (sept. 2015), A102. doi : 10.1051/0004-6361/201425013. arXiv : 1409.7064 [astro-ph.HE]. url : http://adsabs.harvard.edu/abs/2015A&A...581A.102V (cf. p. 32, 130, 199, 200, 206).

[235] Vergani, S. D. et al. "*The chemical enrichment of long gamma-ray bursts nurseries up to $z = 2$*". In : A&A, **599** A120 (mar. 2017), A120. DOI : 10.1051/0004-6361/201629759. arXiv : 1701.02312 [astro-ph.HE]. URL : http://adsabs.harvard.edu/abs/2017A&A...599A.120V (cf. p. 31–33, 121, 122, 139, 140, 207).

[236] Vernet, J. et al. "*X-shooter, the new wide band intermediate resolution spectrograph at the ESO Very Large Telescope*". In : A&A, **536** A105 (déc. 2011), A105. DOI : 10.1051/0004-6361/201117752. arXiv : 1110.1944 [astro-ph.IM]. URL : https://ui.adsabs.harvard.edu/#abs/2011A&A...536A.105V (cf. p. 32).

[237] Viaene, S. et al. "*The Herschel Exploitation of Local Galaxy Andromeda (HELGA). VII. A SKIRT radiative transfer model and insights on dust heating*". In : A&A, **599** A64 (mar. 2017), A64. DOI : 10.1051/0004-6361/201629251. arXiv : 1609.08643. URL : http://adsabs.harvard.edu/abs/2017A&A...599A..64V (cf. p. 97).

[238] Wang, W.-H., Chen, H.-W. et Huang, K.-Y. "*ALMA Submillimeter Continuum Imaging of the Host Galaxies of GRB 021004 and GRB 080607*". In : ApJ, **761** L32 (déc. 2012), L32. DOI : 10.1088/2041-8205/761/2/L32. arXiv : 1211.2807. URL : http://adsabs.harvard.edu/abs/2012ApJ...761L..32W (cf. p. 203).

[239] Wang, X.-G. "*How Bad or Good Are the External Forward Shock Afterglow Models of Gamma-Ray Bursts ?*" In : ApJs, **219** 9 (juil. 2015), 9. DOI : 10.1088/0067-0049/219/1/9. arXiv : 1503.03193 [astro-ph.HE]. URL : http://adsabs.harvard.edu/abs/2015ApJS..219....9W (cf. p. 61, 62).

[240] Wei, J. et al. "*The Deep and Transient Universe in the SVOM Era : New Challenges and Opportunities - Scientific prospects of the SVOM mission*". In : ArXiv e-prints, (oct. 2016). arXiv : 1610.06892 [astro-ph.IM]. URL : http://adsabs.harvard.edu/abs/2016arXiv161006892W (cf. p. 38, 39, 41).

[241] Weingartner, J. C. et Draine, B. T. "*Dust Grain-Size Distributions and Extinction in the Milky Way, Large Magellanic Cloud, and Small Magellanic Cloud*". In : ApJ, **548** (fév. 2001), 296–309. DOI : 10.1086/318651. eprint : astro-ph/0008146. URL : http://adsabs.harvard.edu/abs/2001ApJ...548..296W (cf. p. 35, 81, 82, 84, 135).

[242] Wild, V., Charlot, S., Brinchmann, J., Heckman, T., Vince, O., Pacifici, C. et Chevallard, J. "*Empirical determination of the shape of dust attenuation curves in star-forming galaxies*". In : MNRAS, **417** (nov. 2011), 1760–1786. DOI : 10.1111/j.1365-2966.2011.19367.x. arXiv : 1106.1646. URL : http://adsabs.harvard.edu/abs/2011MNRAS.417.1760W (cf. p. 6, 83, 141).

[243] Witt, A. N., Bohlin, R. C. et Stecher, T. P. "*The variation of galactic interstellar extinction in the ultraviolet*". In : ApJ, **279** (avr. 1984), 698–704. DOI : 10.1086/161934. URL : http://adsabs.harvard.edu/abs/1984ApJ...279..698W (cf. p. 35).

[244] Witt, A. N. et Gordon, K. D. "*Multiple Scattering in Clumpy Media. I. Escape of Stellar Radiation from a Clumpy Scattering Environment*". In : ApJ, **463** (juin 1996), 681. DOI : 10.1086/177282. URL : http://adsabs.harvard.edu/abs/1996ApJ...463..681W (cf. p. 78).

[245] Witt, A. N. et Gordon, K. D. "*Multiple Scattering in Clumpy Media. II. Galactic Environments*". In : ApJ, **528** (jan. 2000), 799–816. DOI : 10.1086/308197. eprint : astro-ph/9907342. URL : http://adsabs.harvard.edu/abs/2000ApJ...528..799W (cf. p. 7, 37, 73, 74, 77, 78, 82, 93, 94).

[246] Witt, A. N., Thronson Jr., H. A. et Capuano Jr., J. M. "*Dust and the transfer of stellar radiation within galaxies*". In : ApJ, **393** (juil. 1992), 611–630. doi : 10.1086/171530. url : http://adsabs.harvard.edu/abs/1992ApJ...393..611W (cf. p. 78).

[247] Woosley, S. E. "*Gamma-ray bursts from stellar mass accretion disks around black holes*". In : ApJ, **405** (mar. 1993), 273–277. doi : 10.1086/172359. url : http://adsabs.harvard.edu/abs/1993ApJ...405..273W (cf. p. 28).

[248] Woosley, S. E. et Bloom, J. S. "*The Supernova Gamma-Ray Burst Connection*". In : Annual Review of Astronomy and Astrophysics, **44** (sept. 2006), 507–556. doi : 10.1146/annurev.astro.43.072103.150558. eprint : astro-ph/0609142. url : http://adsabs.harvard.edu/abs/2006ARA&A..44..507W (cf. p. 28).

[249] Xiang, F. Y., Li, A. et Zhong, J. X. "*Diffuse Interstellar Bands and the Ultraviolet Extinction Curves : The Missing Link Revisited*". In : ApJ, **835** 107 (jan. 2017), 107. doi : 10.3847/1538-4357/835/1/107. arXiv : 1610.06857. url : http://adsabs.harvard.edu/abs/2017ApJ...835..107X (cf. p. 35).

[250] Xu, D. et al. "*Discovery of the Broad-lined Type Ic SN 2013cq Associated with the Very Energetic GRB 130427A*". In : ApJ, **776** 98 (oct. 2013), 98. doi : 10.1088/0004-637X/776/2/98. arXiv : 1305.6832 [astro-ph.HE]. url : http://adsabs.harvard.edu/abs/2013ApJ...776...98X (cf. p. 29).

[251] Yoon, S. .-.-C. et Langer, N. "*Evolution of rapidly rotating metal-poor massive stars towards gamma-ray bursts*". In : A&A, **443** (nov. 2005), 643–648. doi : 10.1051/0004-6361:20054030. arXiv : astro-ph/0508242 [astro-ph]. url : https://ui.adsabs.harvard.edu/#abs/2005A&A...443..643Y (cf. p. 28).

[252] Yüksel, H., Kistler, M. D., Beacom, J. F. et Hopkins, A. M. "*Revealing the High-Redshift Star Formation Rate with Gamma-Ray Bursts*". In : ApJL, **683** (août 2008), L5. doi : 10.1086/591449. arXiv : 0804.4008. url : http://adsabs.harvard.edu/abs/2008ApJ...683L...5Y (cf. p. 33).

[253] Yun, M. S., Reddy, N. A. et Condon, J. J. "*Radio Properties of Infrared-selected Galaxies in the IRAS 2 Jy Sample*". In : ApJ, **554** (juin 2001), 803–822. doi : 10.1086/323145. eprint : astro-ph/0102154. url : http://adsabs.harvard.edu/abs/2001ApJ...554..803Y (cf. p. 126).

[254] Zafar, T., Møller, P., Watson, D., Fynbo, J. P., Krogager, J.-K., Zafar, N., Saturni, F. G., Geier, S. et Venemans, B. P. "*Extinction curve template for intrinsically reddened quasars*". In : A&A, **584** A100 (déc. 2015), A100. doi : 10.1051/0004-6361/201526570. arXiv : 1510.01708. url : http://adsabs.harvard.edu/abs/2015A&A...584A.100Z (cf. p. 97).

[255] Zafar, T., Watson, D., Fynbo, J. P., Malesani, D., Jakobsson, P. et de Ugarte Postigo, A. "*The extinction curves of star-forming regions from z = 0.1 to 6.7 using GRB afterglow spectroscopy*". In : A&A, **532** A143 (août 2011), A143. doi : 10.1051/0004-6361/201116663. arXiv : 1102.1469. url : http://adsabs.harvard.edu/abs/2011A&A...532A.143Z (cf. p. 6, 34, 36, 50, 121).

[256] Zafar, T. et al. "*The Properties of the 2175 Å Extinction Feature Discovered in GRB Afterglows*". In : ApJ, **753** 82 (juil. 2012), 82. doi : 10.1088/0004-637X/753/1/82. arXiv : 1205.0387 [astro-ph.CO]. url : http://adsabs.harvard.edu/abs/2012ApJ...753...82Z (cf. p. 6, 36, 121).

[257] Zafar, T. et al. "*The 2175 Å Extinction Feature in the Optical Afterglow Spectrum of GRB 180325A at z = 2.25*". In : ApJ, **860** L21 (juin 2018), L21. doi : 10.3847/2041-8213/aaca3f. arXiv : 1806.00293. url : http://adsabs.harvard.edu/abs/2018ApJ...860L..21Z (cf. p. 99).

[258] Zafar, T. et al. "*VLT/X-shooter GRBs : Individual extinction curves of star-forming regions*". In : MNRAS, **479** (sept. 2018), 1542–1554. DOI : 10.1093/mnras/sty1380. arXiv : 1805.07016. URL : http://adsabs.harvard.edu/abs/2018MNRAS.479.1542Z (cf. p. 6, 34, 36, 121).

[259] Zafar, T. et al. "*X-shooting GRBs at high redshift : probing dust production history**". In : MNRAS, **480** (oct. 2018), 108–118. DOI : 10.1093/mnras/sty1876. arXiv : 1807.03597. URL : http://adsabs.harvard.edu/abs/2018MNRAS.480..108Z (cf. p. 36, 61).

[260] Zahid, H. J., Kewley, L. J. et Bresolin, F. "*The Mass-Metallicity and Luminosity-Metallicity Relations from DEEP2 at z ~ 0.8*". In : ApJ, **730** 137 (avr. 2011), 137. DOI : 10.1088/0004-637X/730/2/137. arXiv : 1006.4877. URL : http://adsabs.harvard.edu/abs/2011ApJ...730..137Z (cf. p. 123).

[261] Zeh, A., Klose, S. et Hartmann, D. H. "*A Systematic Analysis of Supernova Light in Gamma-Ray Burst Afterglows*". In : ApJ, **609** (juil. 2004), 952–961. DOI : 10.1086/421100. arXiv : astro-ph/0311610 [astro-ph]. URL : https://ui.adsabs.harvard.edu/#abs/2004ApJ...609..952Z (cf. p. 29).

[262] Zerbi, F. M. et al. "*The REM telescope : a robotic multiwavelength facility*". In : *Ground-based Instrumentation for Astronomy*. Sous la dir. d'A. F. Moorwood et M. Iye. **5492** Proceedings of the SPIE conference. Sept. 2004, 1590–1601. DOI : 10.1117/12.551145. URL : http://adsabs.harvard.edu/abs/2004SPIE.5492.1590Z (cf. p. 30).

[263] Zhang, B., Fan, Y. Z., Dyks, J., Kobayashi, S., Mészáros, P., Burrows, D. N., Nousek, J. A. et Gehrels, N. "*Physical Processes Shaping Gamma-Ray Burst X-Ray Afterglow Light Curves : Theoretical Implications from the Swift X-Ray Telescope Observations*". In : ApJ, **642** (mai 2006), 354–370. DOI : 10.1086/500723. arXiv : astro-ph/0508321 [astro-ph]. URL : https://ui.adsabs.harvard.edu/#abs/2006ApJ...642..354Z (cf. p. 27).

[264] Zhang, W., Woosley, S. E. et Heger, A. "*The Propagation and Eruption of Relativistic Jets from the Stellar Progenitors of Gamma-Ray Bursts*". In : ApJ, **608** (juin 2004), 365–377. DOI : 10.1086/386300. eprint : astro-ph/0308389. URL : http://adsabs.harvard.edu/abs/2004ApJ...608..365Z (cf. p. 28).

ANNEXES

A. Validation of the photometric redshift code on real GRB data

A.1. GRB data

Table A.1– GROND photometric measurements. Magnitudes expressed in AB system and not corrected for the Galactic foreground reddening.

GRB	g	r	i	z	J	H	Ks	ref.
080913	> 23.3	> 23.6	> 23.0	21.71 ± 0.11	19.96 ± 0.03	19.64 ± 0.05	19.17 ± 0.11	J. Greiner, 2009b
090423	> 25.0	> 25.1	> 24.2	> 24.0	21.6 ± 0.1	21.2 ± 0.1	20.9 ± 0.1	J. Greiner, 2009a
090516	23.6 ± 0.1	21.44 ± 0.1	20.38 ± 0.1	19.95 ± 0.1	19.6 ± 0.1	19.2 ± 0.1	19.1 ± 0.1	J. Greiner, database
130408A	21.0 ± 0.1	19.7 ± 0.1	19.1 ± 0.1	18.8 ± 0.1	18.0 ± 0.1	17.8 ± 0.1	> 17.0	J. Greiner, database
131117A	20.9 ± 0.1	19.6 ± 0.1	19.1 ± 0.1	19.0 ± 0.1	19.0 ± 0.1	18.9 ± 0.1	18.7 ± 0.3	J. Greiner, database
140515A	> 24.1	> 24.5	> 24.2	22.1 ± 0.1	20.9 ± 0.2	20.9 ± 0.2	> 19.1	J. Greiner, database
140614A	> 21.6	20.6 ± 0.2	19.5 ± 0.1	19.2 ± 0.1	19.0 ± 0.2	18.5 ± 0.2	> 17.6	J. Greiner, database
141109A	20.7 ± 0.1	19.7 ± 0.1	19.4 ± 0.1	19.2 ± 0.1	19 ± 0.1	18.8 ± 0.1	18.5 ± 0.1	J. Greiner, database
150910A	21.5 ± 0.2	21.2 ± 0.2	21.0 ± 0.2	20.8 ± 0.2	> 19.8	> 19.3	> 18.1	J. Greiner, database
151027B	> 22.4	20.8 ± 0.08	20.1 ± 0.07	20.1 ± 0.07	20.1 ± 0.4	19.1 ± 0.3	> 18.3	J. Greiner, database
160203A	18.9 ± 0.1	18.0 ± 0.1	17.7 ± 0.1	17.6 ± 0.1	17.0 ± 0.1	16.7 ± 0.1	-	J. Greiner, database

Table A.2– RATIR photometric measurements. Magnitudes expressed in AB system and not corrected for the Galactic foreground reddening.

GRB	r	i	z	Y	J	H	ref.
130215A	17.47 ± 0.06	17.22 ± 0.05	16.94 ± 0.06	16.8 ± 0.14	16.72 ± 0.06	-	Littlejohns, 2015
130606A	> 23.02	21.13 ± 0.06	18.79 ± 0.03	18.4 ± 0.03	18.32 ± 0.03	17.92 ± 0.03	J. Greiner, database
130907AA	20.01 ± 0.03	19.31 ± 0.02	18.82 ± 0.05	18.45 ± 0.06	18.16 ± 0.06	17.62 ± 0.06	Littlejohns, 2015
130925A	20.92 ± 0.17	21.31 ± 0.18	20.67 ± 0.11	20.80 ± 0.17	20.02 ± 0.09	19.74 ± 0.11	Littlejohns, 2015
140419A	16.22 ± 0.01	15.81 ± 0.01	15.66 ± 0.01	15.46 ± 0.02	15.31 ± 0.01	15.26 ± 0.02	J. Greiner, database
140518A	20.52 ± 0.32	19.0 ± 0.08	18.6 ± 0.06	18.2 ± 0.05	18.12 ± 0.04	17.8 ± 0.03	Littlejohns, 2015
160625B	18.28 ± 0.01	18.08 ± 0.01	17.95 ± 0.01	17.78 ± 0.01	17.77 ± 0.02	17.65 ± 0.02	J. Greiner, database

Table A.3– Other photometric measurements. Magnitudes expressed in AB system and not corrected for the Galactic foreground reddening.

GRB	laica V	cafos R	fors2 I	fors2 z	isaac J	isaac H	isaac Ks	ref.
050904	> 24.6	> 23.9	24.45 ± 0.2	21.8 ± 0.2	20.7 ± 0.06	20.37 ± 0.07	20 ± 0.07	Haislip, 2006

GRB	fors2 B	fors2 R	gmos i	gmos z	fors2 z	niri J	niri H	niri K	ref.

A.2. Best-fitted SED

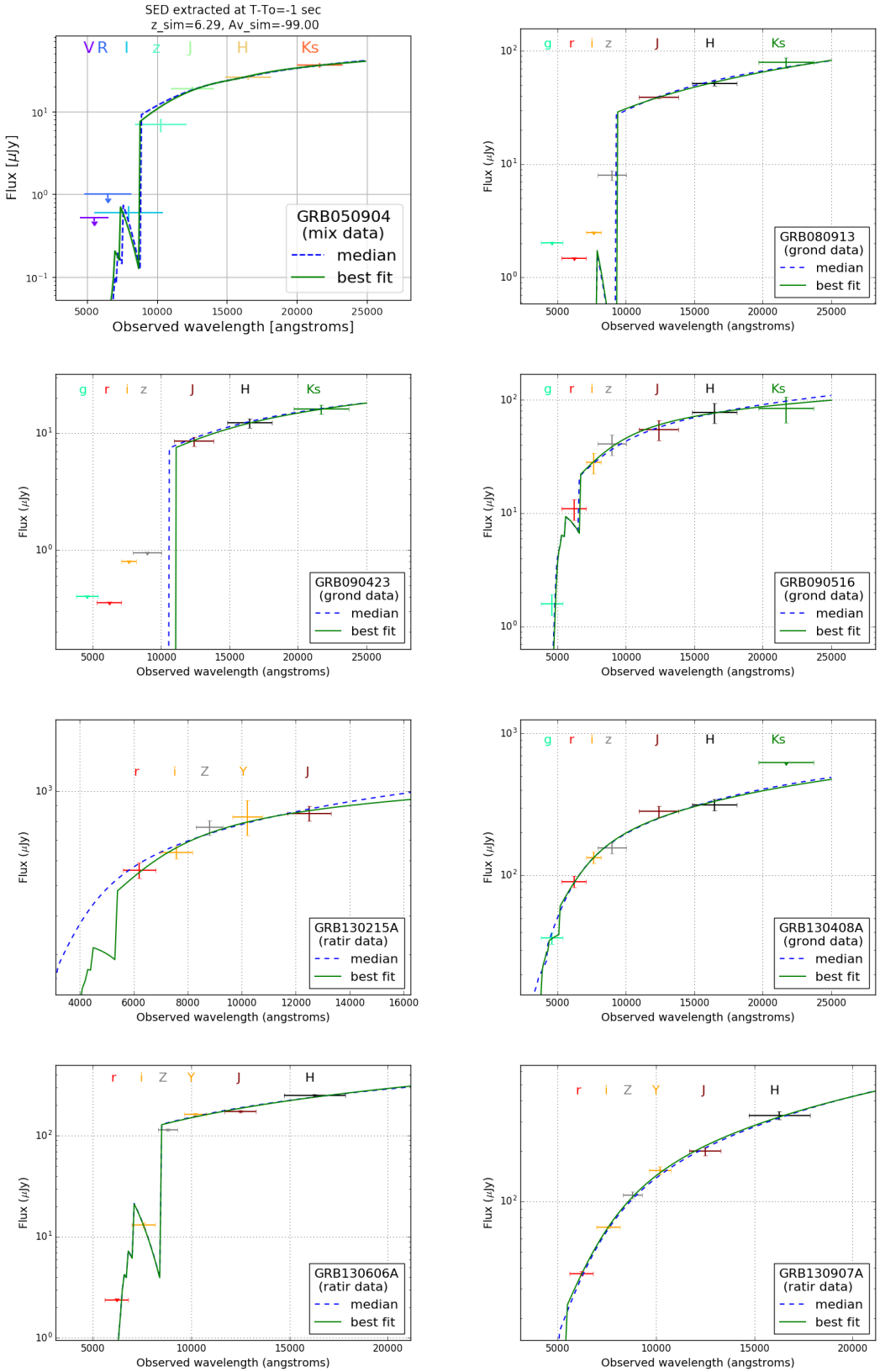

Figure A.4– Best fitted SED template. The colored points represent the measurements, the blue dashed line the fit using the median values of z, A_V,β,$norm$ a posteriori distributions. The green line represents the best fit.

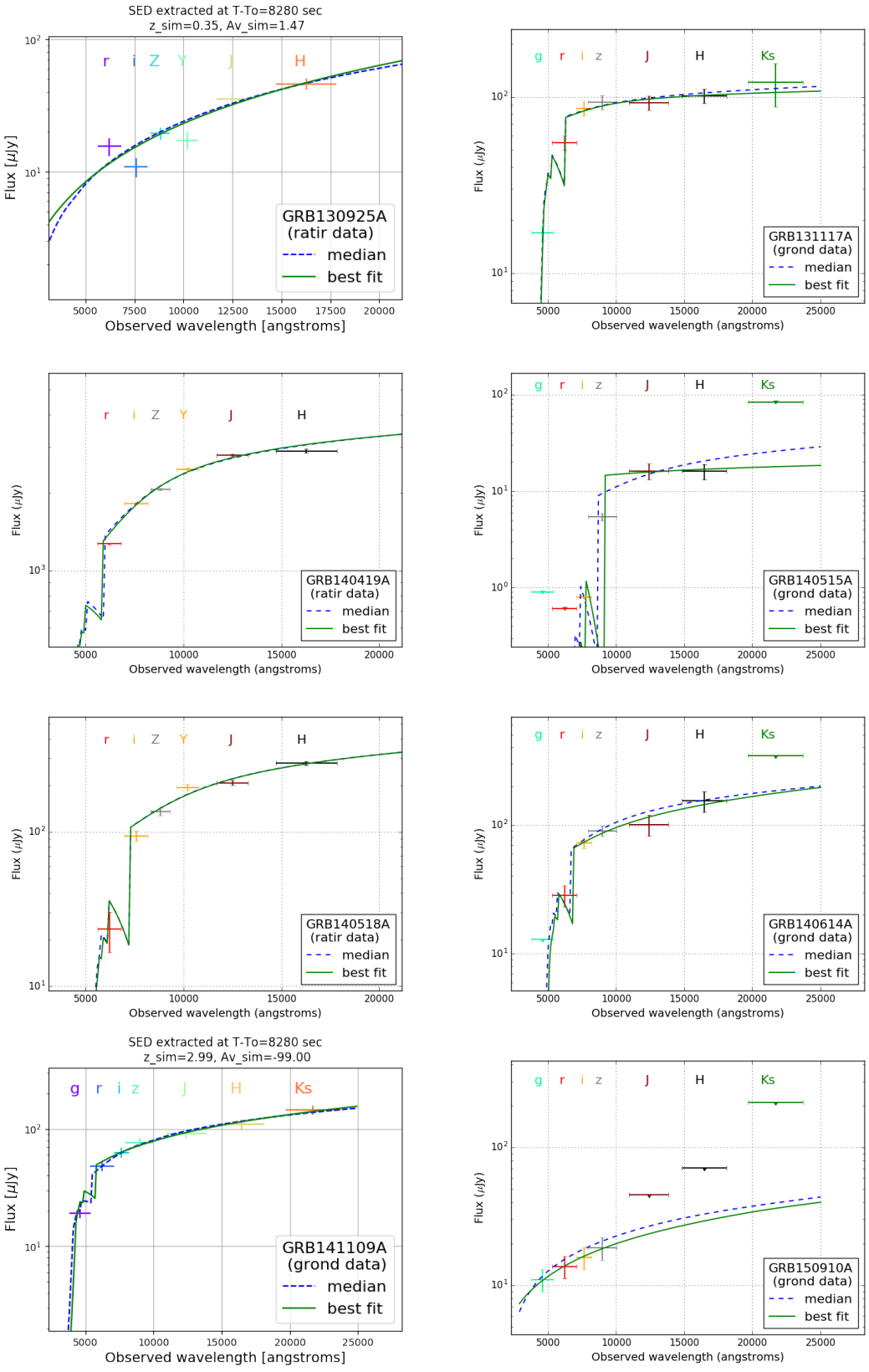

Figure A.5– Best fitted SED template. The colored points represent the measurements, the blue dashed line the fit using the median values of z, A_V,β,$norm$ a posteriori distributions. The green line represents the best fit.

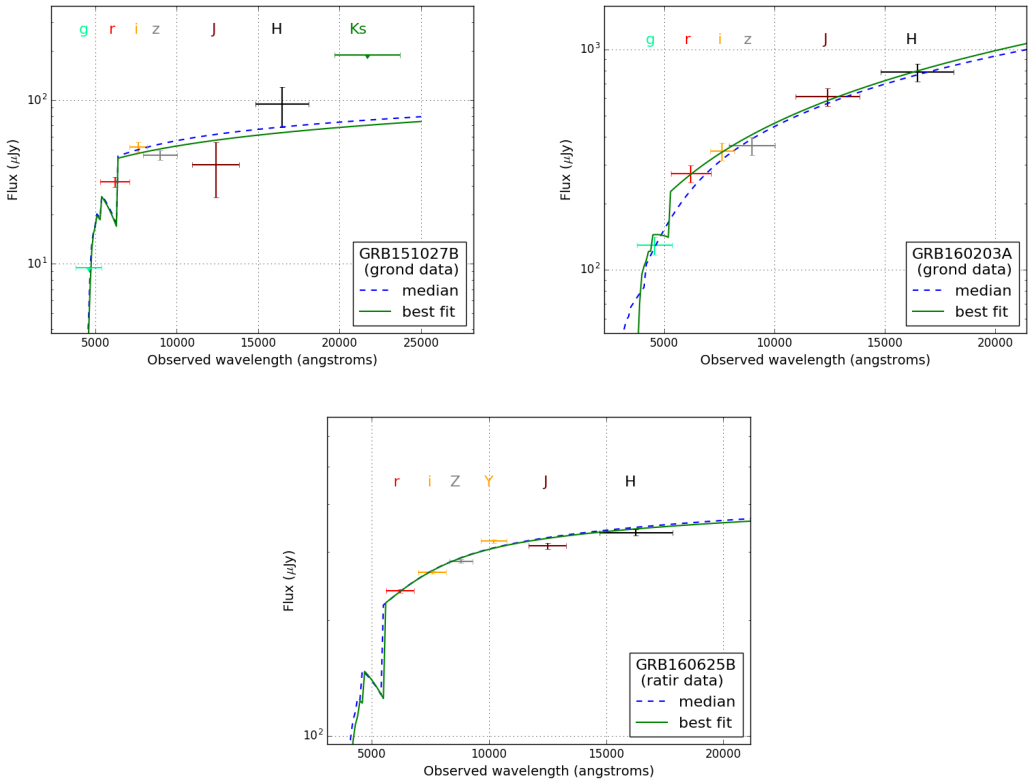

Figure A.6– Best fitted SED template. The colored points represent the measurements, the blue dashed line the fit using the median values of z, A_V,β,$norm$ a posteriori distributions. The green line represents the best fit.

B. SPIE proceeding : End-to-end simulations for COLIBRI, ground follow-up telescope for the SVOM mission.

End-to-end simulations for COLIBRI, ground follow-up telescope for the SVOM mission.

D. Corre, S. Basa, A. Klotz, A. M. Watson, M. Ageron, et al.

D. Corre, S. Basa, A. Klotz, A. M. Watson, M. Ageron, P. Ambert, F. Ángeles, J. L. Atteia, P. E. Blanc, O. Boulade, J. Boy, E. Cadena, B. Cordier, S. Cuevas Cardona, F. Dolon, D. Dornic, D. Dubreuil, A. S. Farah, L. Figueroa, J. Floriot, J. Fuentes-Fernández, P. Gallais, E. Jiménez-Bailón, R. Langarica Lebre, J. F. Le Borgne, W. H. Lee, A. Le Van Suu, M. Marcos, R. Mathon, C. Meessen, J. L. Ochoa, E. Pallier, J. Platzer, F. Quirós, S. Ronayette, D. Turpin, H. Valentin, S. D. Vergani, "End-to-end simulations for COLIBRI, ground follow-up telescope for the SVOM mission.," Proc. SPIE 10705, Modeling, Systems Engineering, and Project Management for Astronomy VIII, 107051R (10 July 2018); doi: 10.1117/12.2313127

Event: SPIE Astronomical Telescopes + Instrumentation, 2018, Austin, Texas, United States

End-to-end simulations for COLIBRI, ground follow-up telescope for the SVOM mission.

Corre D.[1], Basa S.[1], Klotz A.[2], Watson A.M.[3], Ageron M.[4], Ambert P.[2], Ángeles F.[3], Atteia J.L.[2], Blanc P.E.[5], Boulade O.[6], Boy J.[2], Cadena E.[7], Cordier B.[6], Cuevas Cardona S.[3], Dolon F.[5], Dornic D.[4], Dubreuil D.[6], Farah A.S.[3], Figueroa L.[7], Floriot J.[1], Fuentes-Fernández J.[3], Gallais P.[6], Jiménez-Bailón E.[7], Langarica Lebre R.[3], Le Borgne J.F.[2], Lee W.H.[3], Le Van Suu A.[5], Marcos M.[1], Mathon R.[2], Meesen C.[4], Ochoa J.L.[7], Pallier E.[2], Platzer J.[2], Quirós F.[7], Ronayette S.[6], Turpin D.[8], Valentin H.[2], and Vergani S.D.[9]

[1]Aix Marseille Université, CNRS, LAM, Laboratoire d'Astrophysique de Marseille, Marseille, France
[2]IRAP, Université de Toulouse, CNRS, UPS, CNES, Toulouse, France
[3]Instituto de Astronomía, Universidad Nacional Autónoma de México, Apartado Postal 70-264, 04510 México, CDMX, Mexico
[4]Aix Marseille Université, CNRS/IN2P3, CPPM, Marseille, France
[5]Aix Marseille Université, CNRS/INSU, OSU PYTHEAS - Observatoire de Haute Provence, France
[6]CEA Saclay - DRF/Irfu/Departement d'Astrophysique, 91191 Gif-sur-Yvette, France
[7]Instituto de Astronomía, Universidad Nacional Autónoma de México, Apartado Postal 106, 22860 Ensenada, Baja California, México
[8]National Astronomical Observatories/Chinese Academy of Science 20A Datun Road, Beijing, 100012, China
[9]GEPI, Observatoire de Paris, PSL Research University, CNRS, Univ. Paris Diderot, Sorbonne Paris Cité, Place Jules Janssen, F-92195 Meudon, France

ABSTRACT

We present an overview of the development of the end-to-end simulations programs developed for COLIBRI (Catching OpticaL and Infrared BRIght), a 1.3m robotic follow-up telescope of the forthcoming SVOM (Space Variable Object Monitor) mission dedicated to the detection and study of gamma-ray bursts (GRBs). The overview contains a description of the Exposure Time Calculator, Image Simulator and photometric redshift code developed in order to assess the performance of COLIBRI. They are open source Python packages and were developed to be easily adaptable to any optical/ Near-Infrared imaging telescopes. We present the scientific performances of COLIBRI, which allows detecting about 95% of the current GRB dataset. Based on a sample of 500 simulated GRBs, a new Bayesian photometric redshift code predicts a relative photometric redshift accuracy of about 5% from redshift 3 to 7.

Keywords: SVOM, Gamma-Ray Burst, COLIBRI, photometric redshift, Exposure Time Calculator, Image simulator, optical/NIR telescope, end-to-end simulations

Corre D.: E-mail: david.corre@lam.fr
Basa S.: E-mail: stephane.basa@lam.fr

Modeling, Systems Engineering, and Project Management for Astronomy VIII
edited by George Z. Angeli, Philippe Dierickx, Proc. of SPIE Vol. 10705
107051R · © 2018 SPIE · CCC code: 0277-786X/18/$18

1. INTRODUCTION

Simulations are an essential part of the development process of any telescope. During the mission proposal and definition phases, they allow scientists to assess scientific performance of the mission by computing limiting magnitudes, images or spectra for instance. During later stages of the mission development, science simulations help to compare different instrument designs as they allow to assess how these designs affect the performance of the telescope. In this contribution we present the status of the end-to-end simulations of COLIBRI, future ground follow-up telescope of the SVOM mission. COLIBRI is a collaboration between France and Mexico, it will be installed at the Observatorio Astronómico Nacional in Mexico in 2020 which offers very good observing conditions (median seeing of 0.8 arcsec and about 85% of clear nights). The aim of end-to-end simulations is to model the scientific performance of this robotic optical/NIR telescope. One of the scientific requirement of COLIBRI is to provide a photometric redshift during the first minutes of observations of the GRBs by the SVOM mission, so this end-to-end simulation also aims at estimating the accuracy of the photometric redshift estimation.
In the following we start by listing the scientific requirements for COLIBRI in Section 2. In Section 3, we briefly describe the optical design of the telescope before describing the modelling of the telescope response and finally report the performances of COLIBRI in terms of limiting magnitudes. The Section 4 is dedicated to the study of the accuracy of the photometric redshift estimation. In Sections 4.1 to 4.3, we review the specific needs for this study: generating multi-wavelength GRB light curves, defining an observation strategy and a photometric redshift code. In Section 4.4 we present the results of the estimated photometric redshift accuracy based on a mock sample of 500 GRBs.

2. SCIENTIFIC REQUIREMENTS

Gamma-Ray Bursts detection takes place in space because gamma rays are stopped by Earth's atmosphere. This task is devoted to the ECLAIRs telescope, in the X-/γ-ray energy range with a very large field of view, whose detection rate is estimated to be about 80 per year, with approximately 20% of very distant events with redshift greater than 6. An estimate of the event's position in the sky is then transmitted in a few tens of seconds to ground telescope for follow-up observations, transiting through the VHF alert network. COLIBRI is part of a set of 1-m class telescopes included in the SVOM system. Their functions are summarized as follows:
- to provide a localizations and multi-wavelength GRB observations less than 5 minutes after the VHF alert transmission. This is complementary to the slower on-board procedure, based on the chain: ECLAIRs => MXT (Microchannel X-ray telescope) => VT (Visible Telescope), which requires a platform repositioning and data transfer to the ground. It is also crucial for GRBs that cannot be observed quickly due to spacecraft constrains (estimated to about 20% of SVOM GRBs).
- to provide an identification of low signal to noise triggers provided by ECLAIRs, for which the platform slew is not requested. These triggers due to, for example, GRBs highly extinguished or located at very high redshift have potentially a very strong scientific impact.
- to localize and observe dark GRBs, i.e. events detected in gamma, x-ray domains, but not in the visible domain.
- to provide an indication of the GRB redshift if possible 5 minutes after the beginning of observations in order to trigger further observations with the SVOM satellite and the ground largest facilities. A fast localization is essential for a spectroscopic follow-up with the largest facilities.

It follows that the field of view must be larger than the size of GRB error boxes provided by ECLAIRs, typically 20'. In order to be able to observe the vast majority of the GRBs observed so far, the sensitivity must be able to observe targets with limiting magnitudes up to R = 19 and J = 18 for an exposure of 30s and R = 22 and J = 20 (AB system) for an exposure of 300s with SNR (Signal-to-Noise Ratio) > 10. This requirement imposes a diameter of about 1 meter for the telescope. Starting observations in the first minute after the trigger, will permit studying the prompt emission, the transition between the prompt and the afterglow emissions, the detection and characterization of the reverse shock with a temporal resolution of few to several seconds. The SVOM alert network has already an intrinsic delay: about 50% of the alerts will arrive 30 seconds after the trigger. Due to this intrinsic delay and to be able to observe the first minute, observations must start maximum 30 seconds after the arrival of the alert. One should keep in mind that GRB afterglows decay very quickly, typically like $t^{-\alpha}$

with $\alpha \sim 1$. Because of this intrinsic property, a longer exposure time cannot compensate for a late arrival as the gain in sensitivity is compensated by the reduction of the GRB brightness. The main scientific requirements are summarised in Table 1.

Table 1: Summary of main scientific requirements

Observatory availability (without considering weather conditions)	90%
Field of View	26' in visible, 21.7' in NIR
Delay for pointing	$\lesssim$ 30 seconds
Precision of localisation	$<$ 0.5"
Spectral coverage	400-1700 nm
Limiting magnitude (300s, AB mag)	R=22, J=20
Real-time data processing (localisation and redshift estimation)	$<$ 5 minutes

3. TELESCOPE DESIGN AND MODELLING

This section aims at describing the modelling of the telescope response. In Section 3.1, the telescope optical design is briefly described. In Section 3.2, we describe the Exposure Time Calculator (ETC) and Image Simulator (IS) developed for assessing the performances of COLIBRI. In Section 3.3, we present the limiting magnitudes and compared the COLIBRI sensitivity with a dataset of observed GRB light curves.

3.1 Optical design summary

COLIBRI has a primary mirror diameter of 1.3 meter and a secondary mirror diameter of 0.58 meter. The telescope will have 2 or 3 (goal) simultaneous channels: 1 or 2 in the visible and 1 in the NIR domain. In the following we will only consider the goal optical design with 3 channels. The visible channels are equipped with DDRAGO-B and DDRAGO-R and the NIR channel with CAGIRE instruments. An overview of the telescope design is seen in Figure 1. The main characteristics of the telescope instruments are summarised in Table 2.

Table 2: Main characteristics of COLIBRI instruments.

	DDRAGO (B and R)	CAGIRE
Sensor	e2v	SOFRADIR
Wavelength coverage	400-1000 nm	1000-1700 nm
Number of pixels	4096x4096	2048x2048
Pixel size	15 μm	15 μm
Well capacity	350000 e^-	80000 e^-
Readout noise	8 e^-	20 e^-
Operating temperature	170 K	100 K
Associated Dark current	$<$0.001 $e^-/pix/s$	$\sim$0.003 $e^-/pix/s$
Sky resolution	0.38 $arcsec/pix$	0.63 $arcsec/pix$
Field of View	26 $arcmin$	21.7 $arcmin$

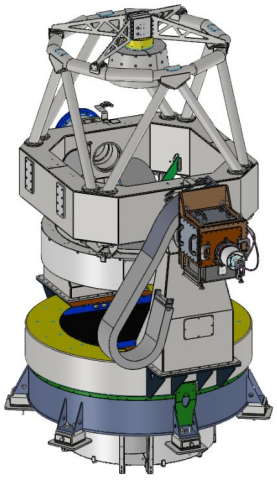

Figure 1: The COLIBRI telescope and DDRAGO interim instrument.

3.2 Modelling

3.2.1 Exposure Time Calculator

The use of Exposure Time Calculators (ETC) is a common practice in astronomy. Many observatories propose an ETC to observers to plan their observing proposals as it allows them to estimate the exposure time required to reach the desired SNR for a given target or to estimate the SNR for a given target and exposure time. In the context of concept and design studies of new telescopes, an ETC is used to assess the scientific performances of a given optical design in order to check whether it meets the scientific requirements and to compare performances of different optical designs.
Usually, ETCs are specific to one instrument, however with the search for optical counterpart of cosmic events, astronomy is entering an era of complex follow-up strategy involving several facilities. Consequently, we have developed an ETC that can be used for different optical/NIR telescopes in order to be able to simulate an observation strategy involving several facilities. The characteristics of the telescope and the instrument are an input of the ETC in a hjson format. It takes into account the observation site characteristics (atmospheric transmission, seeing and sky background), the telescope characteristics (aperture, focal length, wavelength dependent transmission of each optical element, etc) and detector characteristics (quantum efficiency, dark current, readout noise, gain). The ETC allows to compare the scientific performance of designs with different number and kind of optical elements, coatings and detector characteristics. The ETC estimates the number of electrons produced by the different physical processes at stake (source signal, dark current, sky background, etc). An illustration of the output the ETC is seen on Figure 2. This ETC is an open source Python package[*].

3.2.2 Image Simulator

An image simulator (IS) allows to compute realistic raw images in order to feed and test the detection/reduction pipeline. Stars and galaxies are simulated by convolving either point sources or galaxy model with the Point Spread Function (PSF). PSFs are either generated with Zemax for the adopted optical design or standard PSF profiles (Airy, Moffat, Gaussian). Realistic field views can be simulated by querying different astronomical catalogs such as Pan-STARRS, 2MASS, NOMAD-1. Different features such as pixel dependent gain, vignetting, cosmic rays can be taken into account by loading maps in fits format. The ability to reproduce observed images is an essential step in the validation of the image simulator. An example can be seen on Figure 3, where we reproduce with our IS a real image of GRB170202a taken by Zadko Australia telescope. This image simulator is an open source Python package[†].

3.3 Performances

The limiting magnitudes in the different bands for a total exposure time of 30 seconds, 5 minutes and 1 hour are reported in Table 3.
The sensitivity of COLIBRI is compared to a dataset of observed GRB light curves in Figure 4. More than ∼95% of the GRBs dataset would have been detected by COLIBRI. However ∼23% of the SVOM alerts will be immediately observable. Even if COLIBRI starts observing 12 hours after the trigger, despite this long delay and decrease in the GRB brightness, COLIBRI has still sufficient sensitivity to allow the detection of ∼80% of the GRBs dataset in the NIR domain thanks to its 5σ limiting magnitude of 20.51 for a total exposure of 5min (10x30s) in the J band.

[*] https://pyETC.readthedocs.io
[†] https://ImSimpy.readthedocs.io

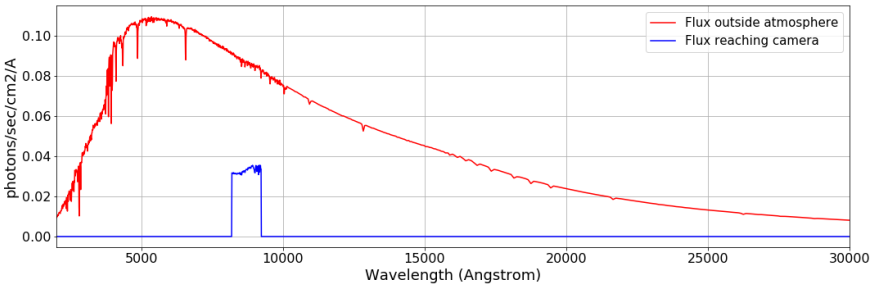

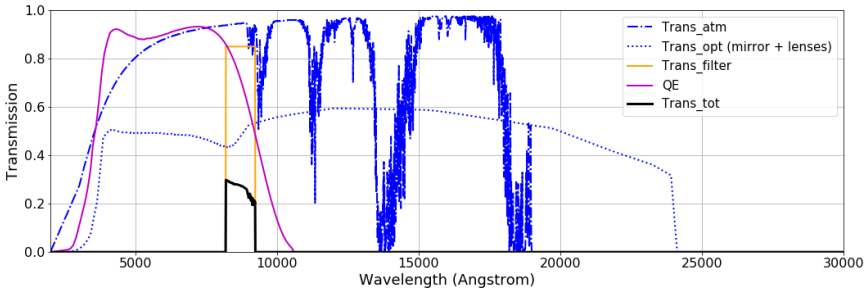


```
--------- Integrated over 7 pixels------------------

Photo-electrons created: brightest pix |  total of 7 pixels, 1 exposure(s) of 5.00 sec in z band
        by:
        - Object:          181236.95   |    907998.80   (electrons)
        - Sky:                 73.21   |       512.44   (electrons)
        - Readout:              8.00   |        56.00   (electrons)
        - Dark current:         0.01   |         0.04   (electrons)
        - Digitization:         0.43   |         3.03   (electrons)

SNR: -central pixel: 425.56
     -integrated over 7 pixels: 952.39
```

Figure 2: Example of ETC's outputs for the spectrum of HIP86443 for an exposure of 5 seconds in z band. *Top*: HIP86443 spectrum and COLIBRI's throughput. *Bottom*: extract of the results summarising the electrons generated and the reached SNR.

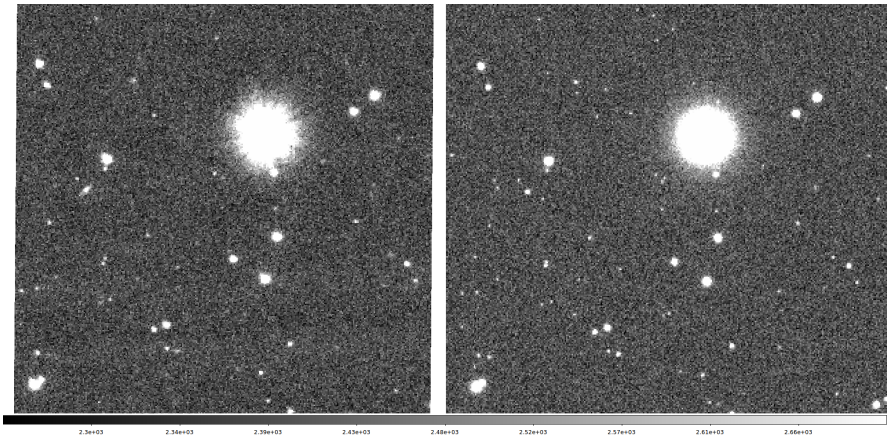

Figure 3: *Left*: Image of GRB170202A taken with Zadko Australia telescope for an exposure of 30 seconds in a clear filter band. Field of view centered at RA, DEC = 152.518, 4.998 degrees (J2000). *Right*: Simulated image with Zadko telescope characteristics and observation site characteristics (sky background, seeing, atmosphere transmission), stars are simulated using the NOMAD-1 catalog.

Table 3: Limiting AB magnitudes for different exposure time and SNR=5 with a seeing at zenith of 0.8", an airmass of 1.5. Dark stands for a sky brightness at the new moon and bright at full moon. The total exposure time of 5 minutes and 1 hour are stacks of 30s individual exposure.

band	30s		10min (20x30s)		1h (120x30s)	
	dark	bright	dark	bright	dark	bright
g	21.76	20.81	23.44	22.46	24.42	23.43
r	21.54	20.94	23.22	22.60	24.20	23.57
i	20.98	20.50	22.65	22.15	23.62	23.13
z	20.21	19.94	21.87	21.59	22.85	22.57
y	19.19	19.15	20.85	20.81	21.83	21.79
J	19.53		21.18		22.15	
H	18.79		20.42		21.39	
gri	22.12	21.36	23.77	23.00	24.75	23.98
zy	20.25	20.06	21.90	21.71	22.88	22.68
B	21.39	20.47	23.07	22.12	24.05	23.10

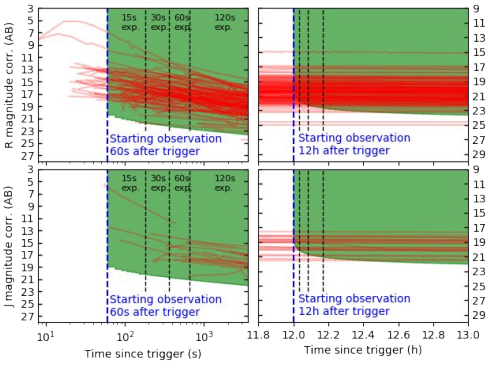

Figure 4: *Top*: GRB light curves observed in the R band. *Bottom*: GRB light curves in the J band. *Left*: Light curves during the first hour after the trigger. *Right*: Light curves between 11.8 and 13 hours after the trigger. Red lines are the observed light curves, the green shaded area represents the sensitivity of COLIBRI. The observations consist in stack of 30s individual exposure with SNR=5, an airmass of 1.5 and 7 days after the new moon. The vertical black dashed lines correspond to 5, 10 and 30 minutes after the beginning of the observations.

3.3.1 Real case: GRB080607

An objective of COLIBRI end-to-end simulations is to use real GRB light curves and to study whether COLIBRI would have detected the GRB at a given time and to simulate the corresponding raw images in the desired bands. COLIBRI with its fast response time, good sensitivity and NIR spectral coverage is designed to detect dusty high redshift GRBs. We present here the case of GRB080607, a high extinguished GRB (A_V=2.33 mag[1]) at redshift 3.03. This kind of GRB are among the most interesting ones to study the dust properties in the host galaxy, but only a few of them have been detected so far. This specific GRB is very interesting because a very early follow-up (less than 30s after the trigger in optical and less than 100s in the NIR) has been performed and thus a very well time sampling multi-wavelength light curve is available.

The multi-wavelength light curve of GRB080607 is seen on Figure 5. Data are taken from a GRB database under construction, which compiled all GRB observations (Turpin, Klotz, Cordier, Gendre (in prep.)). Each band is interpolated using a spline interpolation. We define 4 times at which observations start: 100 seconds, 10 minutes, 30 minutes and 1 hour. At a given time we fit the Spectral Energy Distribution (SED) with a power law, the same extinction law as in [1] and taking into account the transmission of the Inter Galactic Medium (IGM) using the prescriptions of [2]:

$$F_\nu(\lambda, z, A_V, \beta, t_0) \;=\; F_0(t_0) \times (\frac{\lambda}{\lambda_0})^{\beta(t_0)} \times \cdot 10^{-0.4 A_\lambda} \times exp\,[-\tau_{IGM}(z))] \qquad (1)$$

where F_0 and λ_0 are the flux and effective wavelength of the H band at a given time, t_0. β is the spectral slope, A_λ the extinction curve and $\tau_{IGM}(z)$ the transmission of the IGM for a source located at redshift z.

The SED is fitted at several times between the beginning and end of observations: t_0 and $t_0 + t_{exp}$, with t_{exp} the exposure time. This allows to integrate the flux both in time and wavelength in order to simulate what would have seen COLIBRI at a given time for a given exposure time in a given filter band. The results are reported in Figure 6. In the left panel all observations are performed with a single exposure of 30s, corresponding to the first image COLIBRI would have taken if observations start at 100s, 10min, 30min or 1h after the trigger. We see that is clearly detected up to 30 minutes after the trigger, whereas at 1 hour after the trigger it is only weakly

detected in J and H bands. The right panel corresponds to the case where the GRB is detected at 100s after the trigger and later on the exposure time is adjusted: 2 exposures of 30s at 10min, 10 exposures of 30s at 30min and 20 exposures of 30s at 1h after the trigger. The GRB is clearly detected at all times in each band. These simulation results confirm the potential of COLIBRI to detect dusty GRBs even at high redshift.

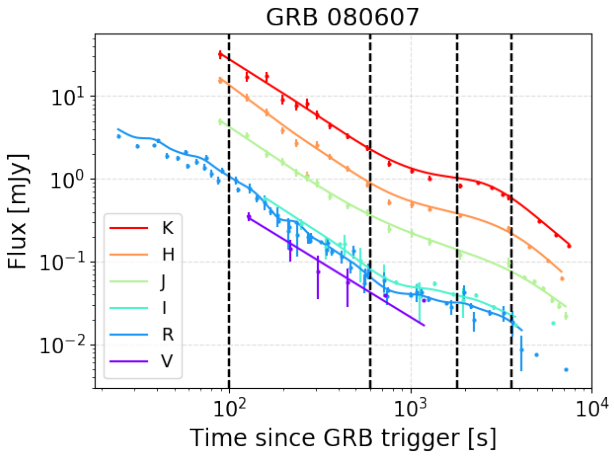

Figure 5: Multi-wavelength light curve of GRB080607. Dots represent real observations and the solid line is a spline interpolation for each filter band. The black dashed line represent the time at which we extract the SED, from left to right: 100 seconds, 10 minutes, 30 minutes and 1 hour.

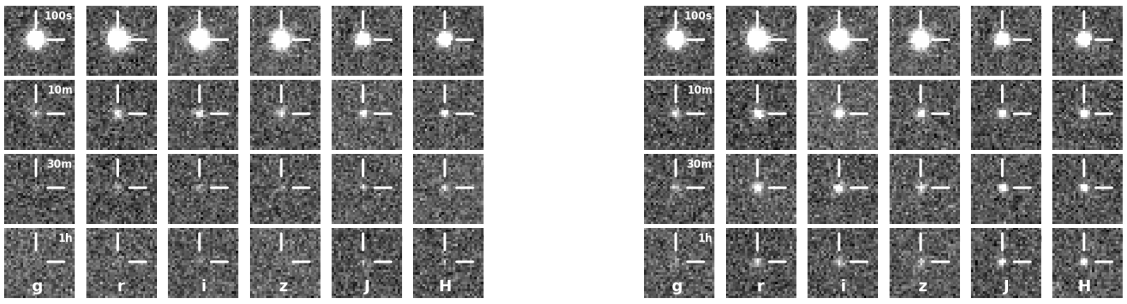

Figure 6: *From top to bottom:* images of GRB080607 seen in each filter band of COLIBRI starting at 100 seconds, 10 minutes, 30 minutes and 1 hour after the GRB trigger. *Left:* each image is a single exposure of 30 seconds. *Right:* Exposure time is adapted to the time at which the observations start: 30s exposure time at 100s, 2x30s at 10min, 10x30s at 30min and 20x30s at 1h.

4. ESTIMATION OF PHOTOMETRIC REDSHIFT ACCURACY

One of the main motivation to perform an end-to-end simulation for COLIBRI is to assess the accuracy on the photometric redshift estimation after 5 minutes of observations with the adopted optical design of the telescope. The SED fitting procedure to obtain photometric redshifts is based on the fit of the overall shape of the spectra and on the detection of the strong spectral properties, here only two prominent signatures can hint information about the redshift: the Lyman break at $912 \times (1+z)$Å and the Lyman-α at $1216 \times (1+z)$Å.

In Sections 4.1 and 4.2 we first describe the steps to simulate the first 5 minutes of a GRB observation with COLIBRI: the GRB light curves modelling and setting an observation strategy. In Section 4.3 we describe the photometric redshift algorithm. In Section 4.4 we present the results.

4.1 GRB afterglow light curves modelling

The first part of the end-to-end simulation is the modelling of multi-wavelength GRB light curves. We first need to compute the intrinsic emission spectrum of the GRB, then to take into account the dust extinction in the host galaxy and the transmission in the IGM.

- **GRB emission spectrum:** GRB afterglows are well described by synchrotron emission from accelerated electrons in relativistic blast wave interacting with an external medium [3, 4]. The observed synchrotron spectrum is composed of series of power-law segments joined at certain break frequencies (see [3, 4]). We have implemented a standard synchrotron model[‡] following the prescriptions of [4, described by the following parameters:
- E_{52}: total energy in the shell (in $10^{52} ergs$)
- p: index of the electron power-law distribution
- ϵ_B: fraction of shock energy converted to the magnetic fields energy.
- ϵ_e: fraction of shock energy used to accelerate the electrons
- n_0: particle density in the ambient medium (cm^{-3})
- Y: Inverse Compton parameter, to take into account the Inverse Compton effects on the cooling of electrons. Set to zero for all GRBs.

For the circumburst environment, we only simulate GRBs with a constant density profile, $\rho = n_0$.
More sophisticated models, such as the introduction of a reverse shock might be used in future developments.

- **Host galaxy dust reddening:** the dust along the line-of-sight of the GRB absorbs and scatters the emitted photons. This process occurs more efficiently at shorter wavelength which "reddens" the light, i.e. blue light is more attenuated than the red light. The wavelengths affected are primarily from the ultra-violet to the NIR. To model the effect of the intrinsic reddening due to dust in the circumburst medium of the host galaxy, different dust extinction laws can be used: the average Milky Way (MW), Small Magellanic Cloud (SMC) or Large Magellanic Cloud (LMC) from [5].

- **IGM transmission:** the Lyman-α forest phenomenon is related to the presence of intergalactic neutral hydrogen along the line of sight between the observer and the source. The Lyman series spectral lines represent the transition of an electron from the ground state ($n = 1$) to an excited one ($n > 1$). We use the method developed in [2] to simulate the effect of the Lyman-α forest.

- **Galactic dust reddening:** to take into account the galactic dust reddening, we use the position (RA,DEC) of the GRB in order to estimate the color excess $E(B-V)$ along this line of sight from the dust maps from [6]. To convert the color excess into an extinction in each band the extinction law of [7] is used.

4.2 Observation strategy

Once the GRB light curves are simulated we need to set an observation strategy describing at what time after the GRB trigger COLIBRI is observing the GRB, in which filter and how long to expose. The main objective of the simulation is to study the first 5 minutes of observations and we have selected 3 times at which the observations start: t_0+60s representing the most favourable case of a GRB observable as soon as the alert is received, t_0+12h representing the extreme case of a GRB exploding at dawn and t_0+24h to study the evolution of photometric redshift with time.
A good photometric redshift estimation required a good spectral coverage to localise the wavelength at which Lyman-α or Lyman break occur. At the beginning of the observations, very large filters are used to optimise the detection of the GRB, *gri* and *zy* for the visible channels and J band in the NIR channel. As soon as the GRB

[‡] https://pyGRBaglow.readthedocs.io

is detected in one band, the filters are successively changing between g, r and i in the DDRAGO-B channel, between z and y in the DDRAGO-R channel and between J and H for the NIR channel in order to have a good spectral coverage. Each observation has an exposure time of 30s.

4.3 Photometric redshift algorithm

The photometric redshift code is based on a Monte Carlo Markov Chain analysis using the python package *emcee*[8] which provides an affine-invariant Ensemble sampler and a Parallel-Tempering (PT) Ensemble sampler allowing a Bayesian estimate of the posterior density function of the free parameters. From these posteriors we can estimate the uncertainties and correlations between the parameters. The PT Ensemble sampler allows a better sampling of the parameter space in case of multiple regions of high likelihood, for instance in the case where there is a high probability for a GRB to be either at high redshift or highly extinguished.
The likelihood function needs to account for both detections and non-detections, this is given by (e.g [9, 10]):

$$L = \prod p(e_i)^{\delta_i} F(e_i)^{1-\delta_i} \tag{2}$$

where $e_i = m_{obs,i} - m_{model,i}$ is the residuals, with $m_{obs,i}$ and $m_{model,i}$ the observed and computed magnitudes in a given filter i. δ_i is a 0/1 variable indicating whether an observation is a detection (1) or an upper limit (0), $p(e_i)$ is the probability density function (PDF) of the residuals and $F(e_i)$ the survival function also known as the complementary cumulative distribution function of the residuals. By definition $F(x)$ represents the probability of exceeding x, so here $F(e_i)$ represents the probability that $m_{model,i}$ exceeds $m_{obs,i}$.
For a Gaussian model error the PDF is given by:

$$p(e_i) = \frac{1}{\sqrt{2\pi\sigma_i}} \cdot e^{-e_i^2/2\sigma_i^2} \tag{3}$$

where σ_i are the measurement uncertainties.
The survival function is defined as: $F(e_i) = 1 - 0.5\left(1 + erf\left(\frac{e_i}{\sqrt{2}\sigma_i}\right)\right)$ where $erf(x)$ is the error function.
The AB magnitude is computed by integrating the flux over the passband:

$$m_{model,i} = -2.5 \cdot log_{10}\left(\frac{\int F_\nu(\lambda, z, A_V, \beta) \cdot T_\lambda^i \cdot \lambda^{-1}\,\mathrm{d}\lambda}{\int T_\lambda^i \cdot \lambda^{-1}\,\mathrm{d}\lambda}\right) + 23.9 \tag{4}$$

where $F_\nu(\lambda, z, A_V, \beta)$ is a power law template spectrum as defined in Equation 1. A broken-power law template can also be used. T_λ^i is the system throughput curve using filter i.
The photometric redshift code is an open source Python package[§].
In order to test and validate the code, we have selected GRBs having a spectroscopic measurement of the redshift and spamming a wide range of redshifts. The estimation of the photometric redshift and its 1σ uncertainty can be seen in Figure 8 in Appendix A. The agreement with the spectroscopic is very good above $z > 3$. For $z < 3$, Lyman-α does not enter the optical filter band and as we do not have UV observations it results in larger uncertainties.

4.4 Results

We create a mock sample of 500 GRB afterglows spamming the redshift range from 0 to 10. The parameters of the synchrotron model of [4] are drawn from distributions based on GRB observations [11]. The distribution of all parameters can be seen in Appendix B. An example of the end-to-end simulation for 1 GRB afterglow is given in Appendix C.
The accuracy of the photometric redshift estimation is seen in Figure 7 where the estimated photometric redshift, the absolute accuracy $z_{phot} - z_{sim}$ and relative accuracy $(z_{phot} - z_{sim})/(1 + z_{sim})$ are plotted as a function of the input redshift for 5 minutes of observations starting 60s, 12h and 24h after t_0. The redshift range can be split in 3 regions:

[§] http://pyGRBz.readthedocs.io

- z <3 where the Lyman-α does not enter the g band.
- 3< z <7 where there is a good spectral coverage thanks to the use of contiguous filter bands: g, r, i, z, y.
- z >7 where a detection is only possible in the NIR bands (J, H).

As expected, for $z < 3$ COLIBRI will not be able to constrain accurately the redshift but will deliver an upper limit. For the range 3< z <7 COLIBRI will be able to derive photometric redshifts with good accuracy. The bad estimations are due to small SNRs resulting in a detection in only one or few bands. At $z > 7$ with detections only in J and H there is a degeneracy between the spectral slope, β, the redshift and the amount of extinction in the host galaxy. A high SNR is required to break degeneracy between the redshift and reddening. This is illustrated in Figure 7 where at t_0+60s the z_{phot} of GRBs at $z \sim 9.7$ are accurately estimated whereas at t_0+12h and t_0+24h it is not possible anymore to distinguish a high redshift GRB from a highly extinguished GRB because of the SNR decrease.

For this mock sample, we derive the statistics on the number of detections, mean absolute and relative accuracy for the 3 redshift range at the 3 different times in Table 4.

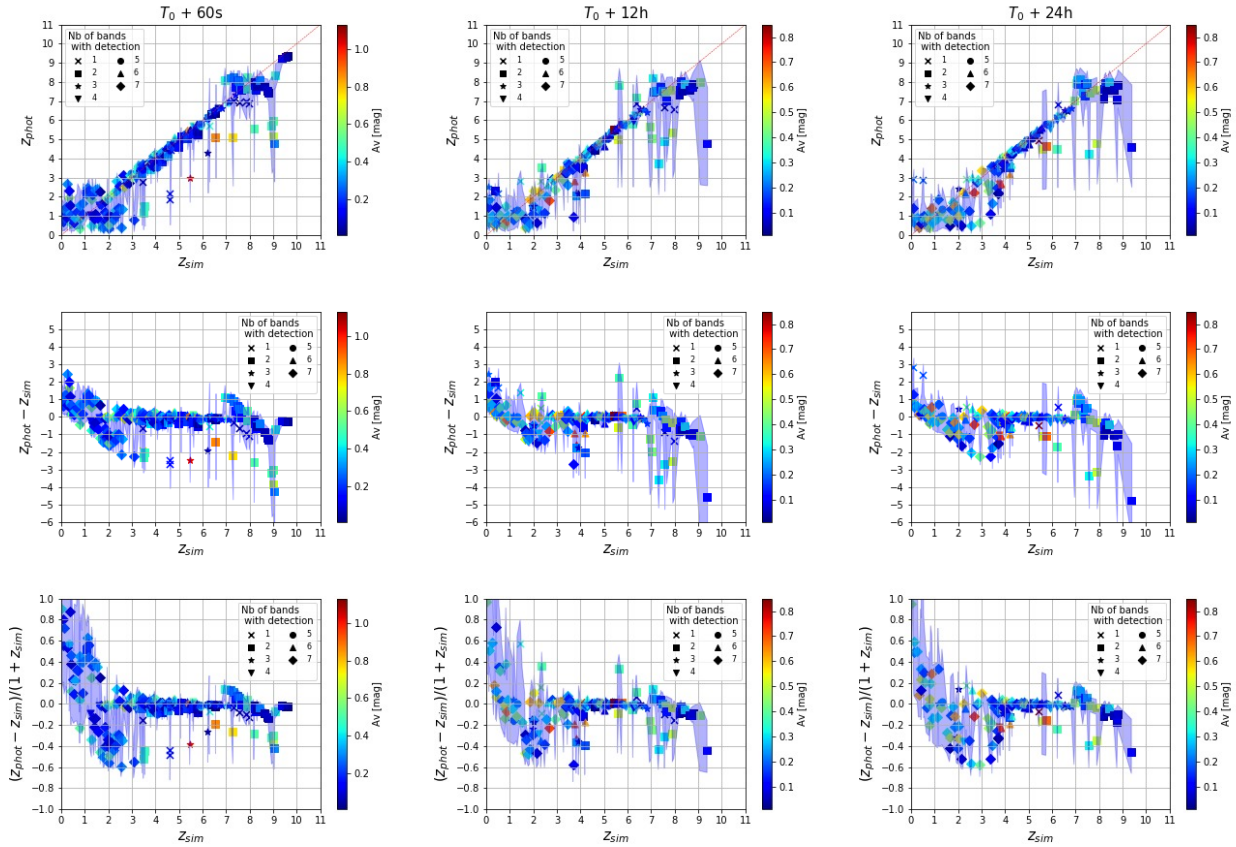

Figure 7: Results of the estimation of z_{phot} for the 500 GRBs observed during 5 minutes starting at t_0+60s, t_0+12h and t_0+24h (from left to right). From top to bottom: z_{phot}, absolute difference $z_{phot} - z_{sim}$ and relative difference $(z_{phot} - z_{sim})/(1 + z_{sim})$ as a function of the input redshift z_{sim}. The colorbar encodes the amount of attenuation in the V band i the host galaxy. The symbols, located at the z_{phot} estimation, represents how many bands have a SNR>3. The blue shaded area represents the 1σ uncertainty associated to the photometric redshift estimation.

Table 4: Statistics summary of the photometric redshift estimation for the mock sample. For the three times and 3 redshift range the number of detected GRBs, mean absolute and relative accuracy are reported.

		nb of detections	$\overline{\lvert z_{phot} - z_{sim} \rvert}$	$\overline{(\lvert z_{phot} - z_{sim} \rvert)/(1 + z_{sim})}$
	z < 3	81 / 107 (75.7%)	0.74	0.37
t_0+60s	3 ≤ z ≤ 7	135 / 253 (53.3%)	0.23	0.041
	z > 7	37 / 140 (26.4%)	0.93	0.10
	z < 3	55 / 107 (51.4%)	0.62	0.33
t_0+12h	3 ≤ z ≤ 7	92 / 253 (36.4%)	0.30	0.056
	z > 7	26 / 140 (18.6%)	1.10	0.12
	z < 3	50 / 107 (46.7%)	0.57	0.26
t_0+24h	3 ≤ z ≤ 7	80 / 253 (31.6%)	0.32	0.062
	z > 7	22 / 140 (15.7%)	1.09	0.12

5. CONCLUSION

The end-to-end simulator for COLIBRI accounts for the observation site characteristics (atmospheric transmission, seeing and sky background), the telescope characteristics (aperture, wavelength dependent transmission of each optical element, default or user defined Point Spread Functions) and detector characteristics (quantum efficiency, dark current, pixel dependent readout noise and gain,etc). It allows simulating realistic field of views by querying different astronomical catalogs (i.e. Pan-STARRS, NOMAD-1, 2MASS). The COLIBRI sensitivity reaches magnitude 21.2 in r band and 19.5 in J band (AB system, 30 s exposure time, SNR=5), which allows detecting about 95% of the observed GRB dataset. Starting observations 12 hours after the trigger, despite the decrease in the GRB brightness, COLIBRI has still sufficient sensitivity to detect about 70% of the GRB dataset in the NIR domain. To satisfy the requirement of delivering a photometric redshift indication, a Bayesian photometric redshift code dedicated to GRB has been developed. The photometric redshift accuracy is estimated on a sample of 500 simulated GRBs. The expected relative accuracy is about 5% in the redshift range of interest: $3 < z < 7$.

The end-to-end simulator will be used to test different observation strategies in order to select the few predefined strategies that will be automatically used in the first 5 minutes of COLIBRI observations.
The next step for the end-to-end simulations will be to include the pipeline responsible for source extractions, which is in current development. This will allow to perform a realistic simulation of a set of observations with COLIBRI: from the simulations of GRB light curves to the production of corresponding images and sources extraction before performing a photometric redshift estimation. This end-to-end simulator will be used for other ground follow-up telescopes of the SVOM mission.

The end-to-end simulator will be in continuously development up to the installation of COLIBRI at OAN in 2020. For instance, it will be updated when the behavior of the detectors will be tested in the laboratory to ensure that the end-to-end simulator is a faithful modelling of COLIBRI.

APPENDIX A. VALIDATION OF THE PHOTOMETRIC REDSHIFT CODE.

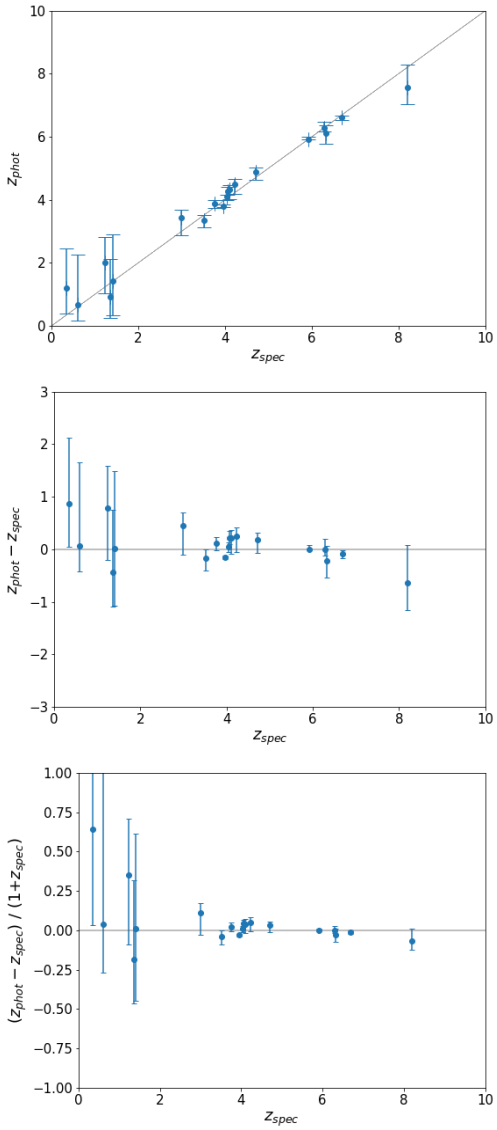

Figure 8: Estimation of the photometric redshift and its 1σ uncertainty as a function of the spectroscopic redshift of observed GRBs. From top to bottom: z_{phot}, absolute accuracy $z_{phot} - z_{spec}$ and relative accuracy $(z_{phot} - z_{spec})/(1 + z_{spec})$ as a function of the spectroscopic redshift z_{spec}

Table 5: Spectroscopic redshift measurements are taken from [12]. The photometric redshift estimation and its 1σ uncertainty are given in the third column.

GRB	z_{spec}	z_{phot}
050904	6.29	$6.29^{+0.20}_{-0.12}$
080913	6.695	$6.61^{+0.08}_{-0.08}$
090423	8.26	$7.56^{+0.71}_{-0.53}$
090516	4.109	$4.32^{+0.15}_{-0.29}$
130215A	0.597	$0.66^{+1.60}_{-0.49}$
130408A	3.757	$3.87^{+0.12}_{-0.13}$
130606A	5.913	$5.92^{+0.08}_{-0.06}$
130907A	1.238	$2.02^{+0.80}_{-0.98}$
130925A	0.347	$1.21^{+1.25}_{-0.82}$
131117A	4.042	$4.10^{+0.07}_{-0.11}$
140419A	3.956	$3.80^{+0.04}_{-0.04}$
140515A	6.32	$6.11^{+0.27}_{-0.32}$
140518A	4.707	$4.89^{+0.14}_{-0.25}$
140614A	4.233	$4.48^{+0.17}_{-0.29}$
141109A	2.993	$3.44^{+0.26}_{-0.55}$
150910A	1.359	$0.92^{+1.19}_{-0.66}$
151027B	4.063	$4.28^{+0.17}_{-0.11}$
160203A	3.52	$3.35^{+0.17}_{-0.24}$
160625B	1.406	$1.43^{+1.46}_{-1.10}$

APPENDIX B. PARAMETERS DISTRIBUTION FOR THE MOCK SAMPLE.

The distribution for the redshit is a Gaussian probability distribution with mean 5.5 and a standard deviation of 4 truncated at 0 and 10 in order to especially probe the redshift range 3 to 9. The distribution for the amount of extinction in the V band is a Gaussian probability distribution with mean 0.1 mag and a standard deviation of 0.3 mag truncated at 0 and 2 mags. The extinction law is randomly drawn between a SMC, LMC and MW with respectively 60%, 20% and 20% probability. The parameters of the synchrotron model of [4] are drawn from distributions based on GRB observations [11]. There is one caveat by randomly drawing a parameter value from a distribution independently from the other distributions, i.e. not taking into account the correlation between parameters. Consequently it might sometimes result in a non realistic set of parameter values. This might explain the GRB afterglows with a rather long rise flux in the light curves in Figure 11. One solution would be to tight some of the parameters during the draw.

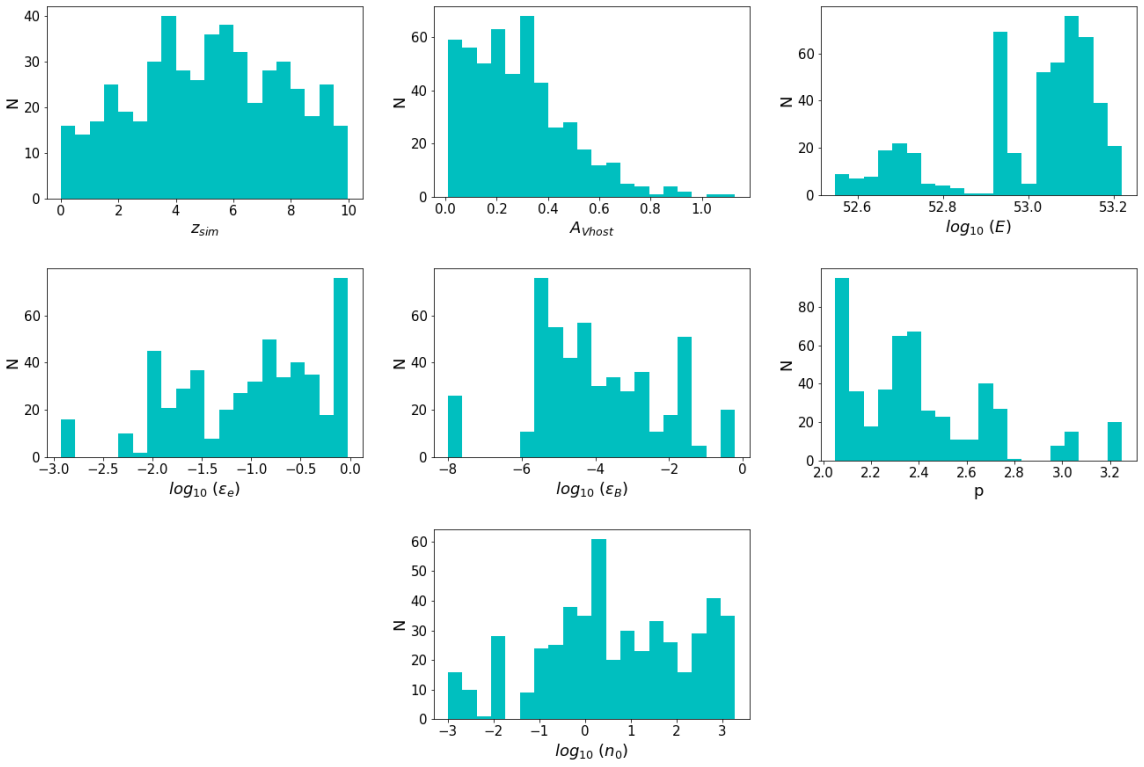

Figure 9: Parameters distributions used to build the mock sample of 500 GRBs. z_{sim} is the redshift, A_{Vhost} the amount of attenuation in the host galaxy in the V band, E is the isotropic kinetic energy of the ejecta (in $ergs$), ϵ_B is the fraction of shock energy converted to the magnetic fields energy, ϵ_e is the fraction of shock energy used to accelerate the electrons, p is the index of the electron power-law distribution, and n_0 is the particle density in the ambient medium (cm^{-3}).

APPENDIX C. EXAMPLE OF AN END-TO-END SIMULATION FOR A SINGLE GRB.

We present here an example of the end-to-end simulation process for a single GRB. From the GRB afterglow light curves the ETC is used to compute the magnitudes and SNR in each band at different time given by the observation strategy (top left panel of Figure 10). The photometric error is defined as $\sigma_{tot} = \sqrt{(1/SNR)^2 + \sigma_{sys}^2)}$ with σ_{sys} the systematic uncertainty, set to 0.04 and 0.06 mag for the visible and NIR channels respectively. The magnitude is then varied using a Gaussian probability distribution with σ_{tot} as the standard deviation. Each band is fitted with a single power law. Then the SED is extracted at the time where the flux in the reddest band is the highest (bottom left panel of Figure 10). This SED is fitted using the photometric redshift code which computes the 1D and 2D Probability Density Functions for each parameters (top right panel of Figure 10). The fitted SED is plotted in bottom right panel of Figure 10.

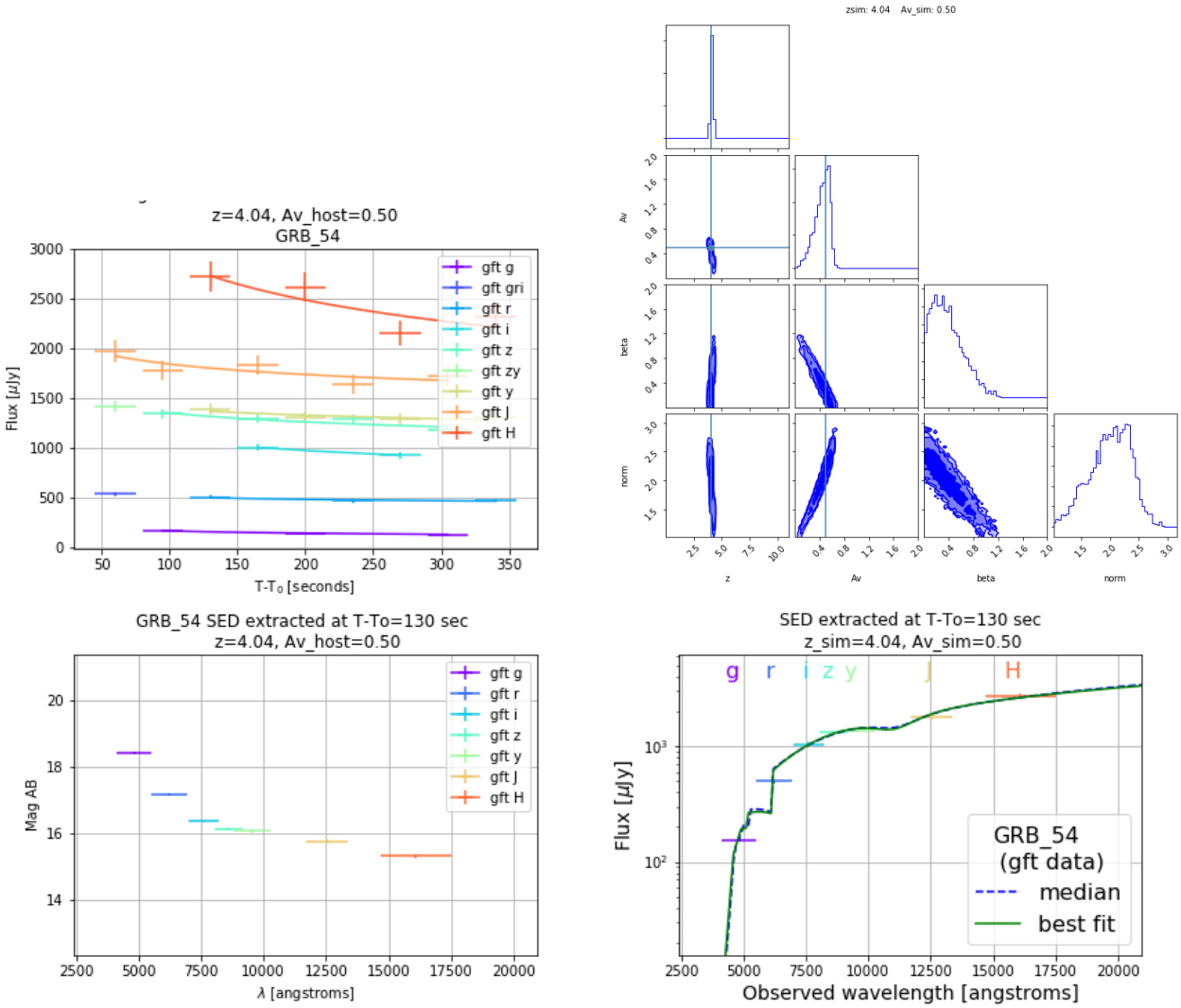

Figure 10: Example of a end-to-end simulation for a single GRB.

APPENDIX D. LIGHT CURVES OF OUR GRB MOCK SAMPLE.

The GRB afterglow light curves of the 500 GRBs in the r and J bands are showed in Figure 11.

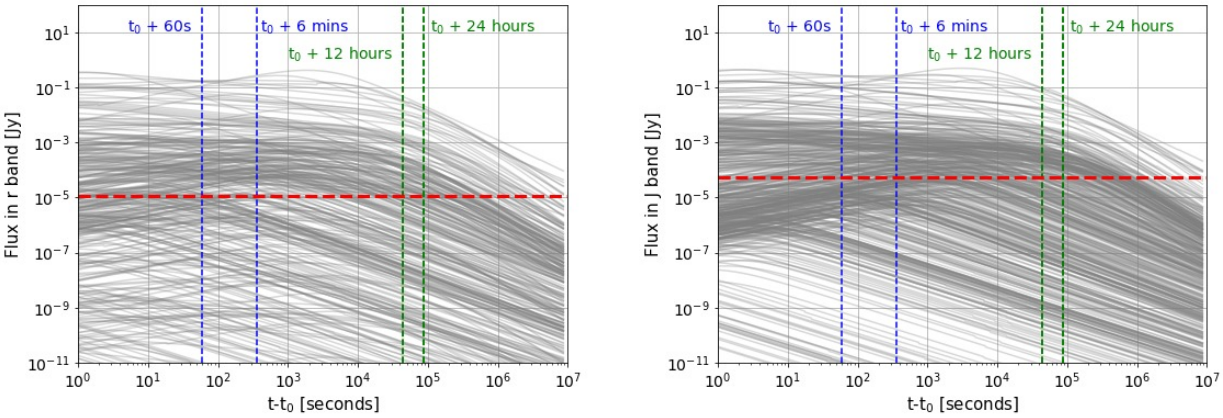

Figure 11: Light curves in r (left) and J (right) bands of the 500 GRBs in our mock sample. The dashed red line represents the 5σ limiting magnitude for an exposure of 30s. For an airmass of 1.5, a seeing at zenith of 0.8" and 7 days after the new moon this corresponds to an AB magnitude of 21.27 and 19.54 in r and J bands respectively. The different time at which the observations are represented by the blue and green dashed lines.

ACKNOWLEDGMENTS

DC acknowledges support by the Centre National d'Etudes Spatiales and support by the Région Provence-Alpes-Côte d'Azur for the funding of his PhD.

REFERENCES

[1] Zafar, T., Watson, D., Fynbo, J. P. U., Malesani, D., Jakobsson, P., and de Ugarte Postigo, A., "The extinction curves of star-forming regions from z = 0.1 to 6.7 using GRB afterglow spectroscopy," *Astronomy and Astrophysics* **532**, A143 (Aug. 2011).

[2] Meiksin, A., "Colour corrections for high redshift objects due to intergalactic attenuation," *Mon. Not. Roy. Astron. Soc.* **365**, 807–812 (2006).

[3] Sari, R., Piran, T., and Narayan, R., "Spectra and Light Curves of Gamma-Ray Burst Afterglows," *Astrophysical Journal, Letters* **497**, L17–L20 (Apr. 1998).

[4] Granot, J. and Sari, R., "The Shape of Spectral Breaks in Gamma-Ray Burst Afterglows," *Astrophysical Journal* **568**, 820–829 (Apr. 2002).

[5] Pei, Y. C., "Interstellar dust from the Milky Way to the Magellanic Clouds," *Astrophysical Journal* **395**, 130–139 (Aug. 1992).

[6] Schlafly, E. F. and Finkbeiner, D. P., "Measuring Reddening with Sloan Digital Sky Survey Stellar Spectra and Recalibrating SFD," *Astrophysical Journal* **737**, 103 (Aug. 2011).

[7] Cardelli, J. A., Clayton, G. C., and Mathis, J. S., "The relationship between infrared, optical, and ultraviolet extinction," *Astrophysical Journal* **345**, 245–256 (Oct. 1989).

[8] Foreman-Mackey, D., Hogg, D. W., Lang, D., and Goodman, J., "emcee: The MCMC Hammer," *Publications of the ASP* **125**, 306 (Mar. 2013).

[9] Lawless, J. F., [*Statistical Models and Methods for Lifetime Data*], ch. Observation Schemes, Censoring, and Likelihood, 49–78, John Wiley and Sons, Inc. (2002).

[10] Laskar, T., Berger, E., Tanvir, N., Zauderer, B. A., Margutti, R., Levan, A., Perley, D., Fong, W.-f., Wiersema, K., Menten, K., and Hrudkova, M., "GRB 120521C at z ˜ 6 and the Properties of High-redshift γ-Ray Bursts," *Astrophysical Journal* **781**, 1 (Jan. 2014).

[11] Turpin, D., *Study of the high-energy transient objects in the Universe in the era of the multimessenger observations*, phd thesis, Universite Toulouse 3 Paul Sabatier (UT3 Paul Sabatier) (Dec. 2016).

[12] Greiner, J., "Gamma-Ray Bursts database." http://www.mpe.mpg.de/~jcg/grbgen.html. (Accessed: 15 Mai 2018).

C. Comparing C00 and SBL18 recipes to RT models : fitting the normalised attenuation curve

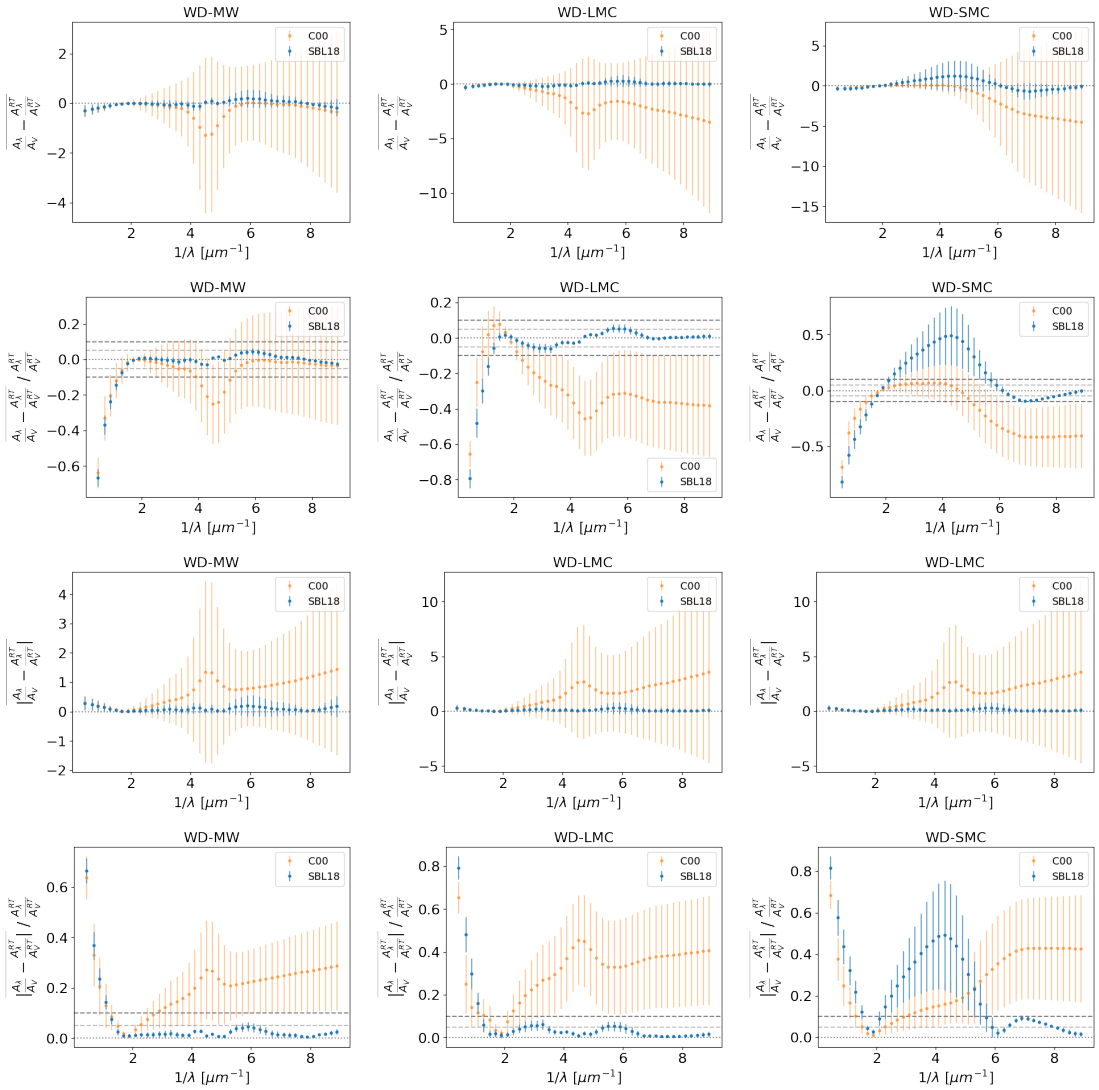

Figure C.1– Absolute and relative difference of the best fit of RT attenuation curves adopting the WD dust models with different attenuation recipes : C00 (orange points), SBL18 (blue points). *From left to right :* WD-MW, WD-LMC and WD-SMC dust types. *From top to bottom :* absolute difference between the intrinsic shape of RT attenuation curve, i.e. A_λ^{RT}/A_V^{RT}, and the intrinsic shape of the best fit for a given recipe, i.e, $A_\lambda^{recipe}/A_V^{recipe}$, relative difference, absolute values of the absolute difference, and the absolute values of the relative difference. The dotted grey line represents no deviation, the light and dark grey dashed lines represent a deviation of 5 and 10 % respectively. A_V^{recipe} was fixed to A_V^{RT} for the fit.

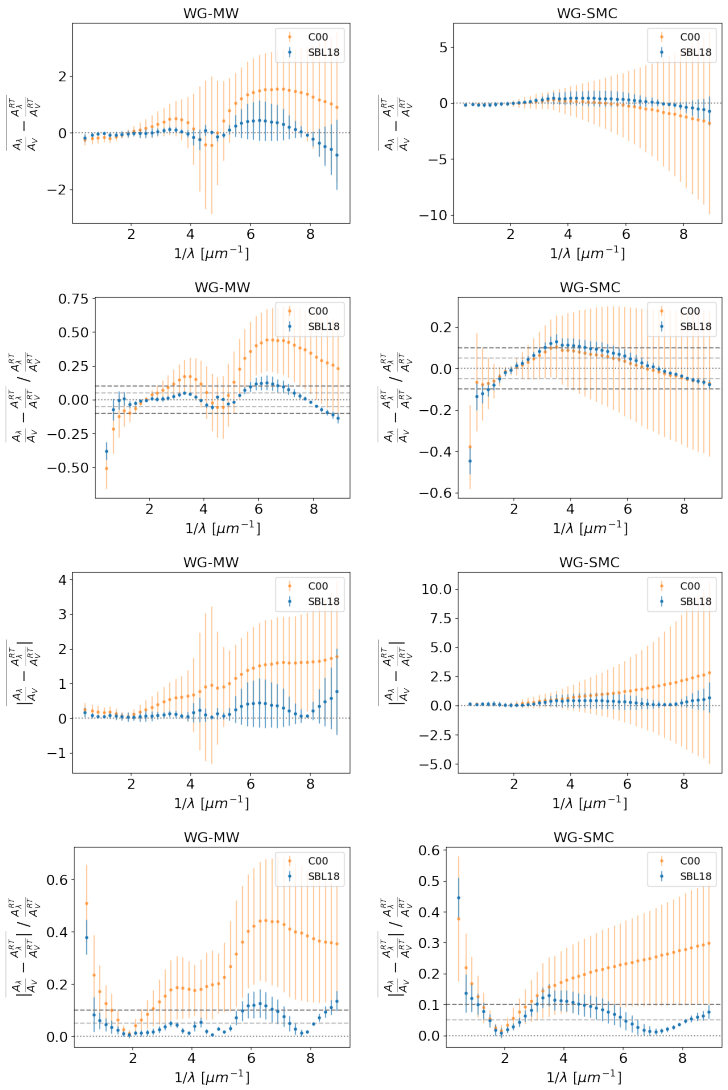

Figure C.2– Same as Figure C.1 but for the WG dust models.

D. GRBHs data and best fit results with CIGALE

D.1. GRBHs photometry and emission lines fluxes

Table D.1– GRB host photometry. Magnitudes are given in the standard calibration system for each filter. Both magnitudes and fluxes are corrected for Galactic extinction using Schlafly et Finkbeiner, 2011

Host	Band	Magnitude	Flux (μJy)	Instrument	Reference
050915A	g	25.12 ± 0.17	0.33 ± 0.05	Keck-I/LRIS	D. A. Perley et al., 2013
	V	24.99 ± 0.11	0.37 ± 0.04	Keck-I/LRIS	D. A. Perley et al., 2013
	R	24.69 ± 0.16	0.48 ± 0.07	VLT/FORS2	Hjorth et al., 2012
	I	24.26 ± 0.09	0.72 ± 0.06	Keck-I/LRIS	D. A. Perley et al., 2013
	K	22.57 ± 0.24	3.41 ± 0.75	VLT/ISAAC	Hjorth et al., 2012
	3.6 μm	21.65 ± 0.10	7.91 ± 0.73	Spizer/IRAC1	D. A. Perley et al., 2013
	4.5 μm	21.64 ± 0.10	8.02 ± 0.74	Spitzer/IRAC2	D. A. Perley et al., 2013
051022A	U	23.41 ± 0.20	1.57 ± 0.29	1.5m OSN	Castro-Tirado et al., 2007
	B	22.52 ± 0.10	3.55 ± 0.33	1.5m OSN	Castro-Tirado et al., 2007
	V	21.91 ± 0.13	6.23 ± 0.75	Danish/DFOSC	D. A. Perley et al., 2013
	F606W	22.02 ± 0.01	5.65 ± 0.03	HST/WFC1	Blanchard et al., 2016
	r	21.80 ± 0.03	6.90 ± 0.19	Gemini-S/GMOS	D. A. Perley et al., 2013
	i	21.35 ± 0.13	10.49 ± 1.26	Gemini-S/GMOS	D. A. Perley et al., 2013
	I	21.12 ± 0.10	12.92 ± 1.19	KeckII/DEIMOS	D. A. Perley et al., 2013
	z	20.96 ± 0.06	14.98 ± 0.83	Gemini-S/GMOS	D. A. Perley et al., 2013
	J	20.62 ± 0.11	20.57 ± 2.08	UKIRT/WFCAM	D. A. Perley et al., 2013
	F160W	20.72 ± 0.10	18.69 ± 1.72	HST/WFC3IR	D. A. Perley et al., 2013
	K	20.12 ± 0.09	32.58 ± 2.70	UKIRT/WFCAM	D. A. Perley et al., 2013
	3.6 μm	20.41 ± 0.04	25.00 ± 1.00	Spizer/IRAC1	L. K. Hunt et al., 2014
	4.5 μm	20.70 ± 0.06	19.00 ± 1.00	Spitzer/IRAC2	L. K. Hunt et al., 2014
	100 μm		6500.00 ± 1000.00	Herschel/PACS	L. K. Hunt et al., 2014
	160 μm		< 21400.00	Herschel/PACS	L. K. Hunt et al., 2014
	250 μm		< 17700.00	Herschel/SPIRE	L. K. Hunt et al., 2014
	350 μm		< 15600.00	Herschel/SPIRE	L. K. Hunt et al., 2014
	500 μm		< 19500.00	Herschel/SPIRE	L. K. Hunt et al., 2014
	5.23 GHz		13.30 ± 3.60	VLA	D. A. Perley et R. A. Perley, 2013

Host	Band	Magnitude	Flux (μJy)	Instrument	Reference
060306	u	25.57 ± 0.20	0.22 ± 0.04	Keck-I/LRIS	D. A. Perley et al., 2013
	B	25.13 ± 0.10	0.32 ± 0.03	Keck-I/LRIS	D. A. Perley et al., 2013
	g	25.07 ± 0.18	0.34 ± 0.06	Keck-I/LRIS	D. A. Perley et al., 2013
	R	24.60 ± 0.20	0.52 ± 0.10	Keck-I/LRIS	D. A. Perley et al., 2013
	I	23.80 ± 0.09	1.10 ± 0.09	Keck-I/LRIS	D. A. Perley et al., 2013
	z	23.72 ± 0.17	1.18 ± 0.19	Keck-I/LRIS	D. A. Perley et al., 2013
	K	21.99 ± 0.10	5.78 ± 0.53	Gemini-N/NIRI	D. A. Perley et al., 2013
	3.6 μm	21.13 ± 0.07	12.79 ± 0.82	Spizer/IRAC1	D. A. Perley et al., 2013
	4.5 μm	21.13 ± 0.07	12.84 ± 0.83	Spitzer/IRAC2	D. A. Perley et al., 2013
	5.23 GHz		< 31.20	VLA	D. A. Perley et R. A. Perley, 2013
	3 GHz		< 19.20	VLA	D. A. Perley et al., 2015
060319	u	24.59 ± 0.11	0.53 ± 0.05	Keck-I/LRIS	D. A. Perley et al., 2013
	g	24.44 ± 0.09	0.61 ± 0.05	Keck-I/LRIS	D. A. Perley et al., 2013
	R	24.34 ± 0.14	0.67 ± 0.09	Keck-I/LRIS	D. A. Perley et al., 2013
	z	22.90 ± 0.10	2.51 ± 0.23	Keck-I/LRIS	D. A. Perley et al., 2013
	K	22.09 ± 0.14	5.30 ± 0.68	Keck-I/NIRC	D. A. Perley et al., 2013
	3.6 μm	21.36 ± 0.04	10.33 ± 0.38	Spizer/IRAC1	D. A. Perley et al., 2013
	4.5 μm	21.49 ± 0.05	9.20 ± 0.42	Spitzer/IRAC2	D. A. Perley et al., 2013
060814	V	23.04 ± 0.10	2.20 ± 0.20	Keck-I/LRIS	D. A. Perley et al., 2013
	R	22.95 ± 0.11	2.39 ± 0.24	VLT/FORS2	Hjorth et al., 2012
	I	22.76 ± 0.13	2.86 ± 0.34	Keck-I/LRIS	D. A. Perley et al., 2013
	F125W	22.09 ± 0.15	5.28 ± 0.73	HST/WFC3IR	D. A. Perley et al., 2013
	F160W	21.75 ± 0.15	7.24 ± 1.00	HST/WFC3IR	D. A. Perley et al., 2013
	K	21.93 ± 0.10	6.12 ± 0.56	VLT/ISAAC	Hjorth et al., 2012
	3.6 μm	21.37 ± 0.09	10.26 ± 0.85	Spizer/IRAC1	D. A. Perley et al., 2013
	4.5 μm	21.17 ± 0.07	12.38 ± 0.80	Spitzer/IRAC2	D. A. Perley et al., 2013
	3 GHz		11.34 ± 3.12	VLA	D. A. Perley et al., 2015
060912A	U	23.77 ± 0.14	1.13 ± 0.15	TNG/DOLORES	Vergani et al., 2015
	B	23.26 ± 0.11	1.80 ± 0.18	TNG/DOLORES	Vergani et al., 2015
	V	23.35 ± 0.14	1.66 ± 0.21	TNG/DOLORES	Vergani et al., 2015
	R	22.76 ± 0.04	2.87 ± 0.11	VLT/FORS2	Hjorth et al., 2012

Host	Band	Magnitude	Flux (μJy)	Instrument	Reference
	I	22.80 ± 0.13	2.75 ± 0.33	TNG/DOLORES	Vergani et al., 2015
	J	> 21.90	< 6.31	TNG/DOLORES	Vergani et al., 2015
	F160W	21.55 ± 0.01	8.73 ± 0.10	HST/WFC3	Blanchard et al., 2016
	K	21.73 ± 0.09	7.39 ± 0.61	VLT/ISAAC	Hjorth et al., 2012
	3.6 μm	21.55 ± 0.03	8.70 ± 0.24	Spizer/IRAC1	D. A. Perley et al., 2016b
	3 GHz		< 10.10	VLA	D. A. Perley et al., 2015
061121	u	22.84 ± 0.10	2.64 ± 0.24	Keck-I/LRIS	D. A. Perley et al., 2015
	B	23.06 ± 0.05	2.17 ± 0.10	Keck-I/LRIS	D. A. Perley et al., 2015
	g	22.80 ± 0.04	2.74 ± 0.10	Keck-I/LRIS	D. A. Perley et al., 2015
	R	22.84 ± 0.03	2.65 ± 0.07	VLT/FORS2	Hjorth et al., 2012
	i	22.59 ± 0.10	3.35 ± 0.31	Keck-I/LRIS	D. A. Perley et al., 2015
	z	22.30 ± 0.08	4.38 ± 0.32	Keck-I/LRIS	D. A. Perley et al., 2015
	J	22.16 ± 0.28	4.98 ± 1.29	P200/WIRC	D. A. Perley et al., 2015
	K	22.01 ± 0.19	5.70 ± 1.00	VLT/ISAAC	Hjorth et al., 2012
	3.6 μm	21.49 ± 0.10	9.20 ± 0.85	Spizer/IRAC1	D. A. Perley et al., 2015
	3 GHz		17.07 ± 5.47	VLA	D. A. Perley et al., 2015
070306	u	23.06 ± 0.46	2.18 ± 0.92	SDSS	Jaunsen et al., 2008
	g'	22.81 ± 0.09	2.73 ± 0.23	GROND	Krühler et al., 2011
	r'	23.02 ± 0.09	2.25 ± 0.19	GROND	Krühler et al., 2011
	R	23.03 ± 0.08	2.23 ± 0.16	VLT/FORS2	Hjorth et al., 2012
	i'	22.77 ± 0.13	2.84 ± 0.34	GROND	Krühler et al., 2011
	I	22.58 ± 0.19	3.36 ± 0.59	NOT/ALFOSC	Jaunsen et al., 2008
	z'	22.83 ± 0.17	2.69 ± 0.42	GROND	Krühler et al., 2011
	F125W	21.89 ± 0.03	6.36 ± 0.18	HST/WFC3IR	D. A. Perley et al., 2013
	F160W	21.68 ± 0.03	7.75 ± 0.21	HST/WFC3IR	D. A. Perley et al., 2013
	Ks	21.58 ± 0.10	8.50 ± 0.78	VLT/ISAAC	Hjorth et al., 2012
	3.6 μm	21.55 ± 0.11	8.70 ± 0.90	Spizer/IRAC1	L. K. Hunt et al., 2014
	4.5 μm	20.96 ± 0.14	15.00 ± 2.00	Spitzer/IRAC2	L. K. Hunt et al., 2014
	100 μm		4900.00 ± 700.00	Herschel/PACS	L. K. Hunt et al., 2014
	160 μm		10700.00 ± 2000.00	Herschel/PACS	L. K. Hunt et al., 2014
	3 GHz		11.30 ± 2.80	VLA	D. A. Perley et al., 2015

Host	Band	Magnitude	Flux (μJy)	Instrument	Reference
070521	B	27.50 ± 0.35	0.04 ± 0.01	Keck-I/LRIS	D. A. Perley et al., 2013
	V	26.46 ± 0.28	0.09 ± 0.02	Keck-I/LRIS	D. A. Perley et al., 2013
	I	25.31 ± 0.37	0.27 ± 0.09	Keck-I/LRIS	D. A. Perley et al., 2013
	z	24.63 ± 0.28	0.51 ± 0.13	Keck-I/LRIS	D. A. Perley et al., 2013
	J	23.41 ± 0.34	1.57 ± 0.49	Keck-I/MOSFIRE	D. A. Perley et al., 2013
	F160W	23.04 ± 0.10	2.21 ± 0.20	HST/WFC3IR	D. A. Perley et al., 2013
	K	22.75 ± 0.18	2.89 ± 0.48	Gemini-N/NIRI	D. A. Perley et al., 2013
	3.6 μm	21.85 ± 0.13	6.58 ± 0.79	Spizer/IRAC1	D. A. Perley et al., 2013
	4.5 μm	21.50 ± 0.11	9.12 ± 0.92	Spitzer/IRAC2	D. A. Perley et al., 2013
	5.23 GHz		28.00 ± 10.30	VLA	D. A. Perley et R. A. Perley, 2013
070802	R	25.15 ± 0.09	0.32 ± 0.03	VLT/FORS2	Elíasdóttir et al., 2009
	i	25.46 ± 0.30	0.24 ± 0.07	NTT/EFOSC	Krühler et al., 2011
	F105W	24.73 ± 0.09	0.47 ± 0.04	HST/WFC3IR	D. A. Perley et al., 2013
	J	24.48 ± 0.30	0.58 ± 0.16	NTT/EFOSC	Krühler et al., 2011
	F160W	24.04 ± 0.05	0.88 ± 0.04	HST/WFC3IR	D. A. Perley et al., 2013
	K	23.39 ± 0.30	1.60 ± 0.44	VLT/ISAAC	Elíasdóttir et al., 2009
	4.5 μm	23.59 ± 0.24	1.33 ± 0.29	Spitzer/IRAC2	D. A. Perley et al., 2013
071021	B	26.17 ± 0.20	0.12 ± 0.02	Keck-I/LRIS	D. A. Perley et al., 2013
	g	25.63 ± 0.12	0.20 ± 0.02	Keck-I/LRIS	D. A. Perley et al., 2013
	V	25.16 ± 0.17	0.31 ± 0.05	Keck-I/LRIS	D. A. Perley et al., 2013
	I	24.31 ± 0.20	0.69 ± 0.13	Keck-I/LRIS	D. A. Perley et al., 2013
	z	24.72 ± 0.30	0.47 ± 0.13	Keck-I/LRIS	D. A. Perley et al., 2013
	F105W	24.23 ± 0.10	0.74 ± 0.07	HST/WFC3IR	D. A. Perley et al., 2013
	J	22.91 ± 0.43	2.50 ± 1.00	VLT/ISAAC	L. K. Hunt et al., 2014
	F160W	23.20 ± 0.04	1.91 ± 0.07	HST/WFC3IR	D. A. Perley et al., 2013
	K	22.12 ± 0.23	5.16 ± 1.09	Keck-I/NIRC	D. A. Perley et al., 2013
	3.6 μm	21.12 ± 0.06	12.90 ± 0.70	Spizer/IRAC1	L. K. Hunt et al., 2014
	4.5 μm	20.89 ± 0.07	16.00 ± 1.00	Spitzer/IRAC2	L. K. Hunt et al., 2014
	100 μm		< 6000.00	Herschel/PACS	L. K. Hunt et al., 2014
	160 μm		< 19700.00	Herschel/PACS	L. K. Hunt et al., 2014
	250 μm		< 19800.00	Herschel/SPIRE	L. K. Hunt et al., 2014

Host	Band	Magnitude	Flux (μJy)	Instrument	Reference
	350 μm		< 16200.00	Herschel/SPIRE	L. K. Hunt et al., 2014
	500 μm		< 21900.00	Herschel/SPIRE	L. K. Hunt et al., 2014
	5.23 GHz		< 25.40	VLA	D. A. Perley et R. A. Perley, 2013
080207	g	27.42 ± 0.30	0.04 ± 0.01	Keck-I/LRIS	Svensson et al., 2012
	R	25.98 ± 0.18	0.15 ± 0.02	VLT/FORS2	Hjorth et al., 2012
	I	25.85 ± 0.29	0.17 ± 0.04	Keck-I/LRIS	Svensson et al., 2012
	z'	25.04 ± 0.19	0.35 ± 0.06	Gemini/GMOS	L. Hunt et al., 2011
	F110W	23.23 ± 0.02	1.86 ± 0.04	HST/WFC3IR	Blanchard et al., 2016
	F160W	23.00 ± 0.19	2.30 ± 0.40	HST/NICMOS3	L. K. Hunt et al., 2014
	Ks	21.74 ± 0.15	7.30 ± 1.00	VLT/ISAAC	L. Hunt et al., 2011
	3.6 μm	21.00 ± 0.02	14.40 ± 0.31	Spizer/IRAC1	L. Hunt et al., 2011
	4.5 μm	20.92 ± 0.03	15.51 ± 0.44	Spizer/IRAC2	L. Hunt et al., 2011
	5.8 μm	20.73 ± 0.09	18.53 ± 1.58	Spizer/IRAC3	L. Hunt et al., 2011
	8.0 μm	21.16 ± 0.15	12.52 ± 1.76	Spizer/IRAC4	L. Hunt et al., 2011
	24 μm	18.99 ± 0.08	92.43 ± 6.50	Spizer/MIPS1	L. Hunt et al., 2011
	100 μm		2200.00 ± 600.00	Herschel/PACS	L. K. Hunt et al., 2014
	160 μm		5900.00 ± 1400.00	Herschel/PACS	L. K. Hunt et al., 2014
	250 μm		< 19500.00	Herschel/SPIRE	L. K. Hunt et al., 2014
	350 μm		< 20400.00	Herschel/SPIRE	L. K. Hunt et al., 2014
	450 μm		< 53220.00	JCMT/SCUBA2	Svensson et al., 2012
	500 μm		< 21900.00	Herschel/SPIRE	L. K. Hunt et al., 2014
	850 μm		< 13122.00	JCMT/SCUBA2	Svensson et al., 2012
	5.23 GHz		17.10 ± 2.50	VLA	D. A. Perley et R. A. Perley, 2013
080325	B	25.67 ± 0.11	0.20 ± 0.02	Subaru/Suprime	Hashimoto et al., 2010
	Rc	25.47 ± 0.16	0.24 ± 0.03	Subaru/Suprime	Hashimoto et al., 2010
	i'	24.87 ± 0.16	0.41 ± 0.06	Subaru/Suprime	Hashimoto et al., 2010
	z'	24.47 ± 0.07	0.59 ± 0.04	Subaru/Suprime	Hashimoto et al., 2010
	F125W	22.76 ± 0.04	2.87 ± 0.11	HST/WFC3IR	D. A. Perley et al., 2013
	F160W	22.45 ± 0.04	3.81 ± 0.14	HST/WFC3IR	D. A. Perley et al., 2013
	Ks	21.67 ± 0.06	7.81 ± 0.43	Subaru/MOIRCS	Hashimoto et al., 2010
	3.6 μm	20.94 ± 0.06	15.30 ± 0.80	Spizer/IRAC1	L. K. Hunt et al., 2014

Host	Band	Magnitude	Flux (μJy)	Instrument	Reference
	4.5 μm	21.04 ± 0.06	13.90 ± 0.80	Spizer/IRAC2	L. K. Hunt et al., 2014
	100 μm		1400.00 ± 400.00	Herschel/PACS	L. K. Hunt et al., 2014
	160 μm		5000.00 ± 800.00	Herschel/PACS	L. K. Hunt et al., 2014
	250 μm		< 18000.00	Herschel/SPIRE	L. K. Hunt et al., 2014
	350 μm		< 16800.00	Herschel/SPIRE	L. K. Hunt et al., 2014
	500 μm		< 26700.00	Herschel/SPIRE	L. K. Hunt et al., 2014
	5.23 GHz		< 12.40	VLA	D. A. Perley et R. A. Perley, 2013
080605	g'	22.70 ± 0.07	3.02 ± 0.19	GROND	Krühler et al., 2011
	r'	22.52 ± 0.07	3.55 ± 0.23	GROND	Krühler et al., 2011
	i'	22.60 ± 0.08	3.32 ± 0.24	GROND	Krühler et al., 2011
	z'	22.60 ± 0.11	3.32 ± 0.34	GROND	Krühler et al., 2011
	J	22.23 ± 0.30	4.68 ± 1.29	WHT/LIRIS	Krühler et al., 2012
	F160W	21.98 ± 0.04	5.87 ± 0.22	HST/WFC3	Krühler et al., 2012
	Ks	21.81 ± 0.30	6.86 ± 1.90	WHT/LIRIS	Krühler et al., 2012
	3.6 μm	21.59 ± 0.10	8.42 ± 0.78	Spitzer/IRAC1	D. A. Perley et al., 2016b
080607	g	26.68 ± 0.15	0.08 ± 0.01	Keck-I/LRIS	D. A. Perley et al., 2013
	V	26.68 ± 0.20	0.08 ± 0.01	Keck-I/LRIS	D. A. Perley et al., 2013
	r	26.70 ± 0.46	0.08 ± 0.03	Magellan/IMACS	D. A. Perley et al., 2013
	I	26.23 ± 0.21	0.12 ± 0.02	Keck-I/LRIS	D. A. Perley et al., 2013
	F160W	24.69 ± 0.03	0.48 ± 0.01	HST/WFC3	D. A. Perley et al., 2013
	K	24.18 ± 0.43	0.77 ± 0.31	Keck-I/NIRC	D. A. Perley et al., 2013
	3.6 μm	22.90 ± 0.17	2.50 ± 0.39	Spizer/IRAC1	D. A. Perley et al., 2013
	4.5 μm	22.65 ± 0.16	3.16 ± 0.47	Spitzer/IRAC2	D. A. Perley et al., 2013
	345 GHz		313.00 ± 94.00	ALMA	W.-H. Wang et al., 2012
	5.23 GHz		< 17.80	VLA	D. A. Perley et R. A. Perley, 2013
080805	V	25.59 ± 0.20	0.21 ± 0.04	NTT/EFOSC	Krühler et al., 2011
	R	25.41 ± 0.20	0.25 ± 0.05	NTT/EFOSC	Krühler et al., 2011
	J	23.57 ± 0.20	1.35 ± 0.25	VLT/HAWK-I	Krühler et al., 2011
	F160W	23.25 ± 0.02	1.82 ± 0.03	HST/WFC3	Blanchard et al., 2016
	K	23.09 ± 0.20	2.11 ± 0.39	VLT/HAWK-I	Krühler et al., 2011
	3.6 μm	22.69 ± 0.08	3.04 ± 0.22	Spitzer/IRAC1	D. A. Perley et al., 2016b

Host	Band	Magnitude	Flux (μJy)	Instrument	Reference
081109	*uvm2*	23.45 ± 0.30	1.51 ± 0.42	SWIFT/UVOT	Krühler et al., 2011
	uvw1	23.29 ± 0.30	1.75 ± 0.48	SWIFT/UVOT	Krühler et al., 2011
	U	23.15 ± 0.14	2.00 ± 0.26	NTT/EFOSC	Krühler et al., 2011
	g'	23.01 ± 0.07	2.28 ± 0.15	GROND	Krühler et al., 2011
	V	22.80 ± 0.06	2.76 ± 0.15	VLT/FORS2	Krühler et al., 2011
	r'	22.70 ± 0.07	3.03 ± 0.20	GROND	Krühler et al., 2011
	i'	21.98 ± 0.08	5.87 ± 0.43	GROND	Krühler et al., 2011
	I	21.93 ± 0.09	6.13 ± 0.51	VLT/FORS2	Krühler et al., 2011
	z'	21.97 ± 0.09	5.93 ± 0.49	GROND	Krühler et al., 2011
	Y	21.61 ± 0.08	8.23 ± 0.61	VLT/HAWK-I	Krühler et al., 2011
	J	21.36 ± 0.06	10.41 ± 0.58	VLT/HAWK-I	Krühler et al., 2011
	F160W	21.28 ± 0.03	11.16 ± 0.31	HST/WFC3IR	D. A. Perley et al., 2013
	K	21.04 ± 0.08	13.88 ± 1.02	VLT/HAWK-I	Krühler et al., 2011
	3.6 μm	20.71 ± 0.07	18.96 ± 1.22	Spizer/IRAC1	D. A. Perley et al., 2013
	4.5 μm	20.90 ± 0.09	15.84 ± 1.31	Spitzer/IRAC2	D. A. Perley et al., 2013
081221	B	25.45 ± 0.11	0.24 ± 0.02	Keck-I/LRIS	D. A. Perley et al., 2013
	g	25.00 ± 0.17	0.36 ± 0.06	Keck-I/LRIS	D. A. Perley et al., 2013
	V	25.12 ± 0.14	0.32 ± 0.04	Keck-I/LRIS	D. A. Perley et al., 2013
	r'	24.65 ± 0.20	0.50 ± 0.09	GROND	D. A. Perley et al., 2013
	I	24.40 ± 0.30	0.63 ± 0.17	Keck-I/LRIS	D. A. Perley et al., 2013
	z	23.99 ± 0.15	0.92 ± 0.13	Keck-I/LRIS	D. A. Perley et al., 2013
	F105W	23.82 ± 0.07	1.08 ± 0.07	HST/WFC3IR	D. A. Perley et al., 2013
	F160W	23.05 ± 0.04	2.19 ± 0.08	HST/WFC3IR	D. A. Perley et al., 2013
	K	22.54 ± 0.13	3.50 ± 0.42	Gemini-N/NIRI	D. A. Perley et al., 2013
	3.6 μm	21.63 ± 0.10	8.05 ± 0.74	Spizer/IRAC1	D. A. Perley et al., 2013
	4.5 μm	21.48 ± 0.10	9.29 ± 0.86	Spitzer/IRAC2	D. A. Perley et al., 2013
	5.23 GHz		< 17.20	VLA	D. A. Perley et R. A. Perley, 2013
090407	B	27.17 ± 0.33	0.05 ± 0.01	Keck-I/LRIS	D. A. Perley et al., 2013
	g	26.21 ± 0.29	0.12 ± 0.03	Keck-I/LRIS	D. A. Perley et al., 2013
	R	25.82 ± 0.17	0.17 ± 0.03	Keck-I/LRIS	D. A. Perley et al., 2013
	I	24.79 ± 0.23	0.44 ± 0.09	Keck-I/LRIS	D. A. Perley et al., 2013

Host	Band	Magnitude	Flux (μJy)	Instrument	Reference
	z	> 23.76	< 1.14	VLT/FORS2	**Malesani09**
	F160W	22.95 ± 0.02	2.39 ± 0.04	HST/WFC3	Blanchard et al., 2016
	K	22.24 ± 0.12	4.63 ± 0.51	Gemini-N/NIRI	D. A. Perley et al., 2013
	3.6 μm	21.96 ± 0.13	5.99 ± 0.72	Spizer/IRAC1	D. A. Perley et al., 2013
	4.5 μm	21.92 ± 0.15	6.17 ± 0.85	Spitzer/IRAC2	D. A. Perley et al., 2013
	5.23 GHz		< 15.10	VLA	D. A. Perley et R. A. Perley, 2013
090417B	*uvw2*	24.29 ± 0.19	0.70 ± 0.12	SWIFT/UVOT	Holland et al., 2010
	uvm2	24.05 ± 0.29	0.87 ± 0.23	SWIFT/UVOT	Holland et al., 2010
	uvw1	24.54 ± 0.56	0.56 ± 0.29	SWIFT/UVOT	Holland et al., 2010
	u	24.04 ± 0.38	0.88 ± 0.31	SWIFT/UVOT	Holland et al., 2010
	B	23.07 ± 0.13	2.15 ± 0.26	NOT/ALFOSC	Holland et al., 2010
	g'	22.96 ± 0.16	2.38 ± 0.35	SDSS	**http://www.sdss.org/dr13/**
	r'	21.56 ± 0.09	8.60 ± 0.71	SDSS	**http://www.sdss.org/dr13/**
	R	21.49 ± 0.03	9.21 ± 0.25	NOT/ALFOSC	Holland et al., 2010
	i'	21.40 ± 0.11	9.97 ± 1.01	SDSS	**http://www.sdss.org/dr13/**
	z'	20.74 ± 0.24	18.37 ± 4.06	SDSS	**http://www.sdss.org/dr13/**
	J	20.89 ± 0.50	16.06 ± 7.40	Subaru/MOIRCS	Aoki et al., 2009
	F160W	20.69 ± 0.01	19.20 ± 0.18	HST/WFC3IR	D. A. Perley et al., 2013
	Ks	20.38 ± 0.50	25.60 ± 11.79	Subaru/MOIRCS	Aoki et al., 2009
	3.6 μm	20.89 ± 0.07	16.00 ± 1.00	Spizer/IRAC1	L. K. Hunt et al., 2014
	4.5 μm	21.12 ± 0.08	13.00 ± 1.00	Spitzer/IRAC2	L. K. Hunt et al., 2014
	100 μm		1200.00 ± 600.00	Herschel/PACS	L. K. Hunt et al., 2014
	160 μm		3900.00 ± 1600.00	Herschel/PACS	L. K. Hunt et al., 2014
	250 μm		< 16800.00	Herschel/SPIRE	L. K. Hunt et al., 2014
	350 μm		< 19800.00	Herschel/SPIRE	L. K. Hunt et al., 2014
	500 μm		< 23400.00	Herschel/SPIRE	L. K. Hunt et al., 2014
	5.23 GHz		< 16.10	VLA	D. A. Perley et R. A. Perley, 2013
090926B	U	23.61 ± 0.13	1.30 ± 0.16	NTT/EFOSC	Krühler et al., 2011
	g'	23.23 ± 0.07	1.85 ± 0.12	GROND	Krühler et al., 2011
	r'	22.91 ± 0.06	2.49 ± 0.14	GROND	Krühler et al., 2011
	i'	22.88 ± 0.12	2.55 ± 0.28	GROND	Krühler et al., 2011

Host	Band	Magnitude	Flux (μJy)	Instrument	Reference
	z'	22.41 ± 0.10	3.94 ± 0.36	GROND	Krühler et al., 2011
	J	21.86 ± 0.13	6.52 ± 0.78	NTT/SOFI	Krühler et al., 2011
	H	21.89 ± 0.30	6.37 ± 1.76	NTT/SOFI	Krühler et al., 2011
	K	21.43 ± 0.19	9.70 ± 1.70	NTT/SOFI	Krühler et al., 2011
	3.6 μm	21.42 ± 0.02	9.85 ± 0.18	Spitzer/IRAC1	D. A. Perley et al., 2016b
100621A	*uvw2*	22.07 ± 0.04	5.42 ± 0.20	SWIFT/UVOT	Krühler et al., 2011
	uvm2	21.99 ± 0.06	5.82 ± 0.32	SWIFT/UVOT	Krühler et al., 2011
	uvw1	22.03 ± 0.07	5.62 ± 0.36	SWIFT/UVOT	Krühler et al., 2011
	u	21.82 ± 0.06	6.80 ± 0.38	SWIFT/UVOT	Krühler et al., 2011
	U	21.82 ± 0.10	6.79 ± 0.62	NTT/EFOSC	Krühler et al., 2011
	g'	21.76 ± 0.06	7.20 ± 0.40	GROND	Krühler et al., 2011
	r'	21.41 ± 0.06	9.89 ± 0.55	GROND	Krühler et al., 2011
	i'	21.10 ± 0.06	13.17 ± 0.73	GROND	Krühler et al., 2011
	z'	21.42 ± 0.06	9.79 ± 0.54	GROND	Krühler et al., 2011
	Y	21.07 ± 0.06	13.55 ± 0.75	VLT/HAWK-I	Krühler et al., 2011
	J	21.41 ± 0.06	9.92 ± 0.55	VLT/HAWK-I	Krühler et al., 2011
	F160W	21.32 ± 0.01	10.81 ± 0.06	HST/WFC3	Blanchard et al., 2016
	K	21.22 ± 0.11	11.80 ± 1.20	VLT/HAWK-I	Krühler et al., 2011
	3.6 μm	21.32 ± 0.08	10.77 ± 0.79	Spitzer/IRAC1	Vergani et al., 2015
	4.5 μm	21.36 ± 0.06	10.38 ± 0.57	Spitzer/IRAC2	Vergani et al., 2015
120119A	B	25.00 ± 0.13	0.36 ± 0.04	Keck-I/LRIS	Morgan et al., 2014
	g'	24.93 ± 0.05	0.39 ± 0.02	Keck-I/LRIS	Morgan et al., 2014
	R	24.64 ± 0.11	0.51 ± 0.05	Keck-I/LRIS	Morgan et al., 2014
	I	23.92 ± 0.13	0.98 ± 0.12	Keck-I/LRIS	Morgan et al., 2014
	z'	23.87 ± 0.15	1.03 ± 0.14	Keck-I/LRIS	Morgan et al., 2014
	F125W	23.06 ± 0.04	2.17 ± 0.08	HST/WFC3IR	Morgan et al., 2014
	F160W	23.48 ± 0.02	1.47 ± 0.03	HST/WFC3	Blanchard et al., 2016
	K	22.76 ± 0.13	2.85 ± 0.34	Gemini-N/NIRI	Morgan et al., 2014
	3.6 μm	22.87 ± 0.07	2.58 ± 0.17	Spitzer/IRAC1	D. A. Perley et al., 2016b

Table D.2– GRBH emission lines fluxes in 10^{-17} erg.cm^{-2}.s^{-1}

GRBH	H_α	H_β	Reference
050915A	–	1.80 ± 0.45	Krühler et al., 2015
051022A	110.00 ± 14.56	22.10 ± 2.14	Krühler et al., 2015
060306	8.90 ± 3.68	–	Krühler et al., 2015
060319	–	–	–
060814	28.00 ± 5.66	8.30 ± 3.35	Krühler et al., 2015
060912A	15.80 ± 4.12	5.90 ± 0.71	Krühler et al., 2015
061121	40.00 ± 2.19	7.90 ± 1.65	Vergani et al., 2017
070306	53.50 ± 3.96	11.60 ± 1.39	Krühler et al., 2015
070521	10.00 ± 5.83	–	Krühler et al., 2015
070802	5.10 ± 1.30	1.40 ± 0.36	Krühler et al., 2015
071021	8.90 ± 2.54	2.80 ± 0.58	Krühler et al., 2015
080207	10.90 ± 2.91	1.30 ± 0.58	Krühler et al., 2015
080325	–	–	–
080605	29.10 ± 4.52	7.70 ± 1.53	Krühler et al., 2015
080607	–	–	–
080805	11.00 ± 3.14	1.70 ± 0.78	Krühler et al., 2015
081109	20.90 ± 2.85	5.50 ± 0.94	Krühler et al., 2015
081221	9.50 ± 5.63	2.40 ± 2.14	Krühler et al., 2015
090407	4.40 ± 0.72	0.70 ± 0.22	Krühler et al., 2015
090417B	–	–	–
090926B	14.20 ± 3.46	2.70 ± 1.03	Krühler et al., 2015
100621A	128.00 ± 8.60	43.80 ± 2.60	Krühler et al., 2015
120119A	19.20 ± 3.86	4.90 ± 1.49	Krühler et al., 2015

D.2. Best-fitted SED for the GRBHs

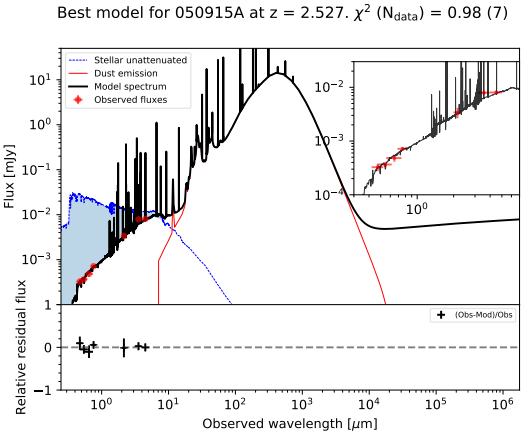

Figure D.1– Best-fitted SED for GRBH 050915A. Red points are the observed fluxes with their uncertainties. The black line represents the best fitted spectrum composed of attenuated stellar emission, dust emission, non-thermal radio emission and nebular lines. The dashed blue line represents the unattenuated stellar emission and the blue shaded area indicates the amount dust attenuation. The lower panel shows the relative residual.

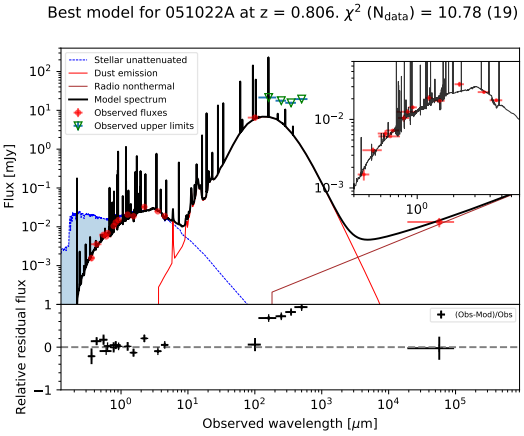

Figure D.2– Best-fitted SED for GRBH 051022. Colour and symbols convention as in Figure D.1.

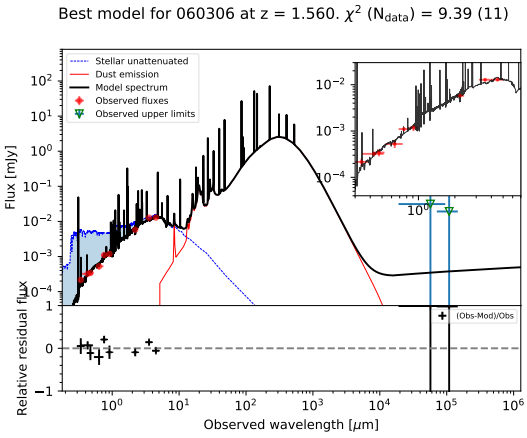

Figure D.3– Best-fitted SED for GRBH 060306. Colour and symbols convention as in Figure D.1.

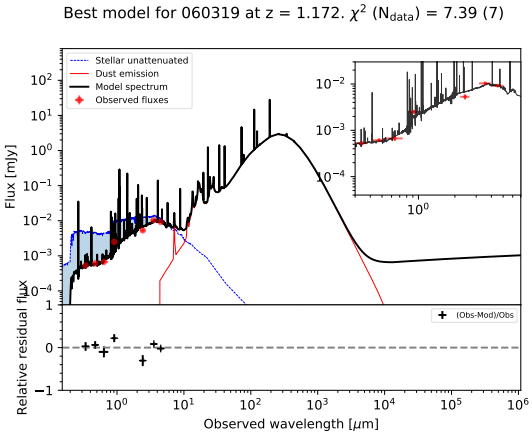

Figure D.4– Best-fitted SED for GRBH 060319. Colour and symbols convention as in Figure D.1.

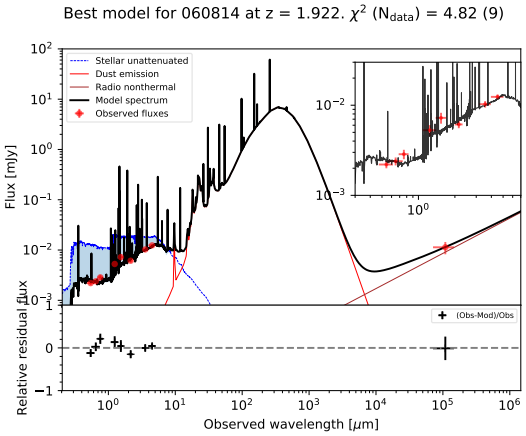

Figure D.5– Best-fitted SED for GRBH 060814. Colour and symbols convention as in Figure D.1.

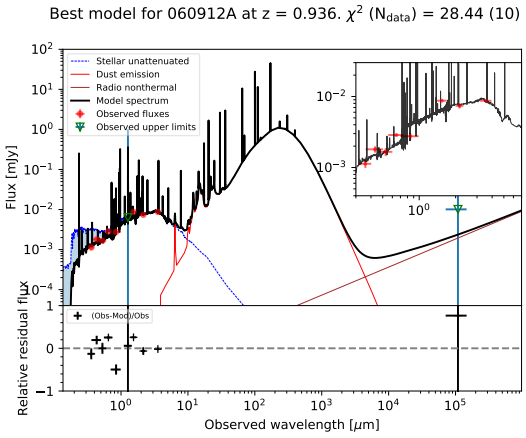

Figure D.6– Best-fitted SED for GRBH 060912A. Colour and symbols convention as in Figure D.1.

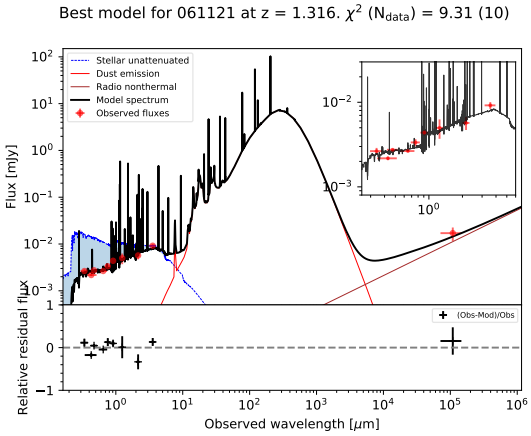

Figure D.7– Best-fitted SED for GRBH 061121. Colour and symbols convention as in Figure D.1.

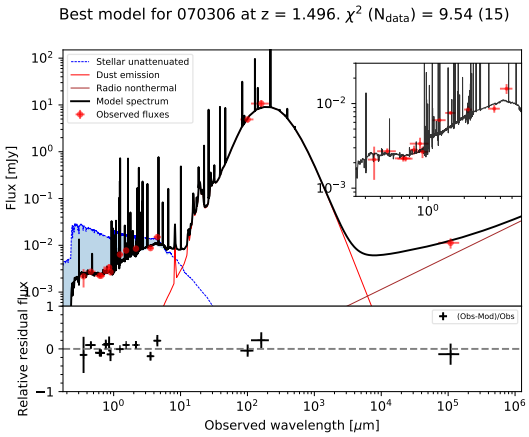

Figure D.8– Best-fitted SED for GRBH 070306. Colour and symbols convention as in Figure D.1.

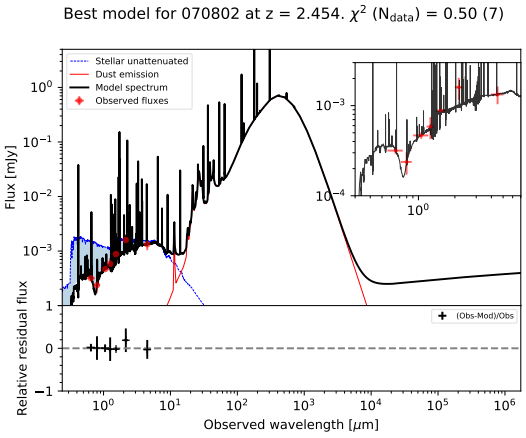

Figure D.9– Best-fitted SED for GRBH 070802. Colour and symbols convention as in Figure D.1.

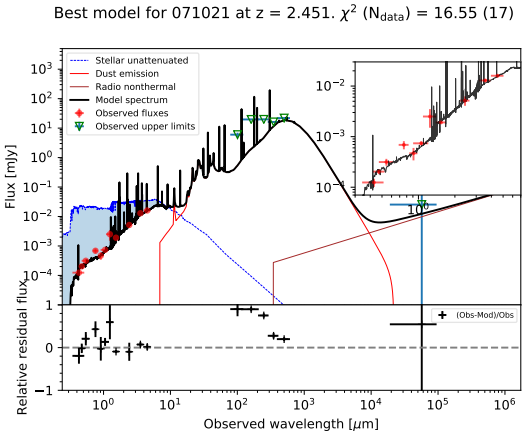

Figure D.10– Best-fitted SED for GRBH 071021. Colour and symbols convention as in Figure D.1.

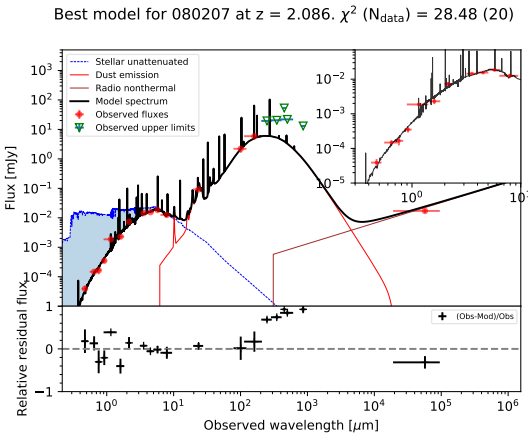

Figure D.11– Best-fitted SED for GRBH 080207. Colour and symbols convention as in Figure D.1.

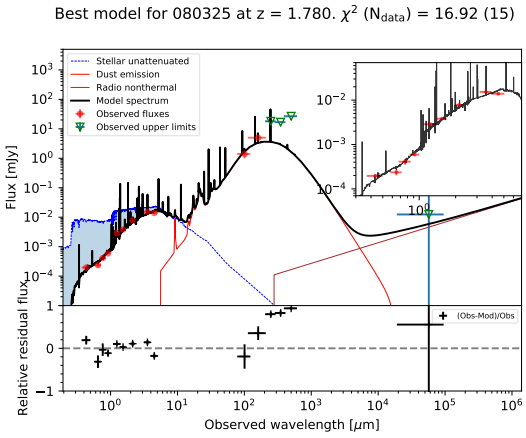

Figure D.12– Best-fitted SED for GRBH 080325. Colour and symbols convention as in Figure D.1.

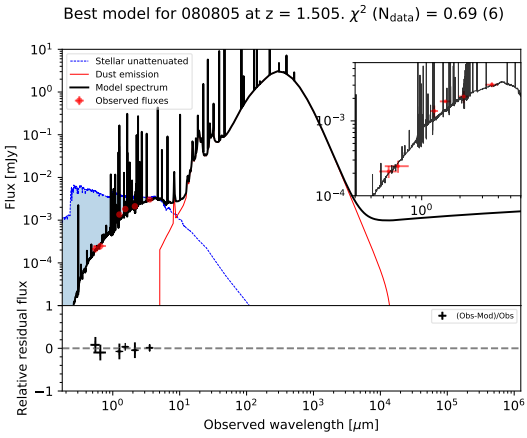

Figure D.15– Best-fitted SED for GRBH 080805. Colour and symbols convention as in Figure D.1.

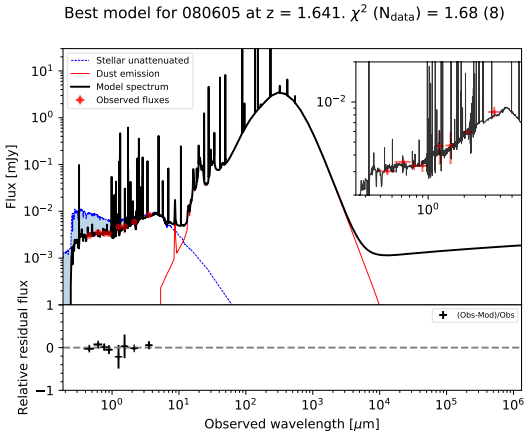

Figure D.13– Best-fitted SED for GRBH 080605. Colour and symbols convention as in Figure D.1.

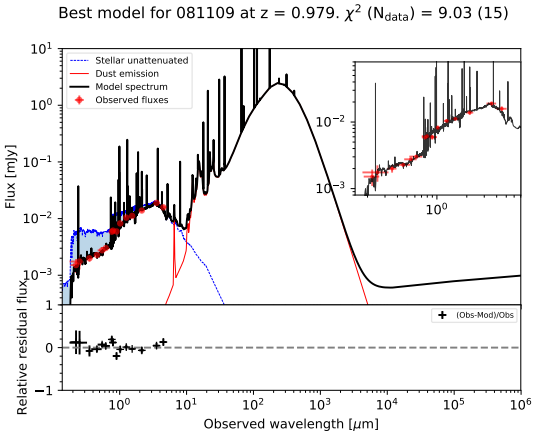

Figure D.16– Best-fitted SED for GRBH 081109. Colour and symbols convention as in Figure D.1.

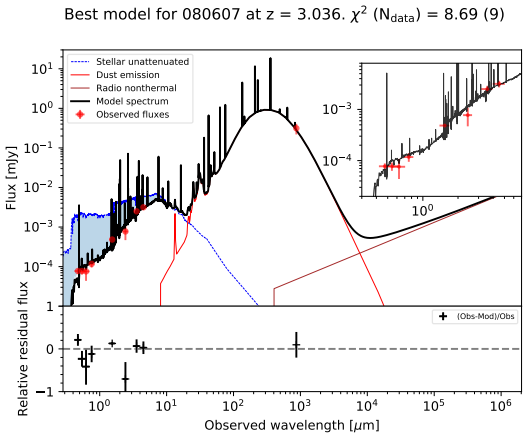

Figure D.14– Best-fitted SED for GRBH 080607. Colour and symbols convention as in Figure D.1.

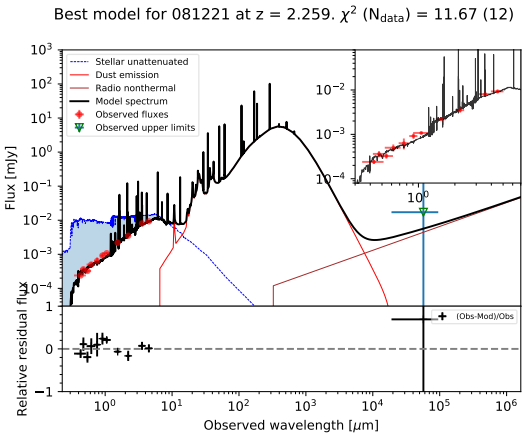

Figure D.17– Best-fitted SED for GRBH 081221. Colour and symbols convention as in Figure D.1.

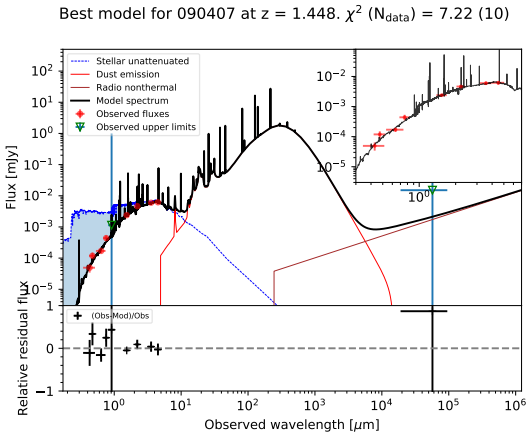

Figure D.18– Best-fitted SED for GRBH 090407. Colour and symbols convention as in Figure D.1.

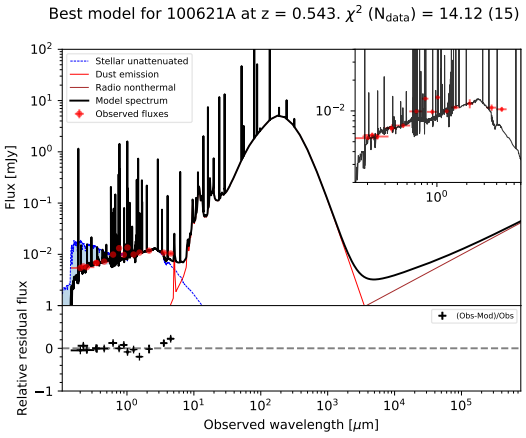

Figure D.21– Best-fitted SED for GRBH 100621A. Colour and symbols convention as in Figure D.1.

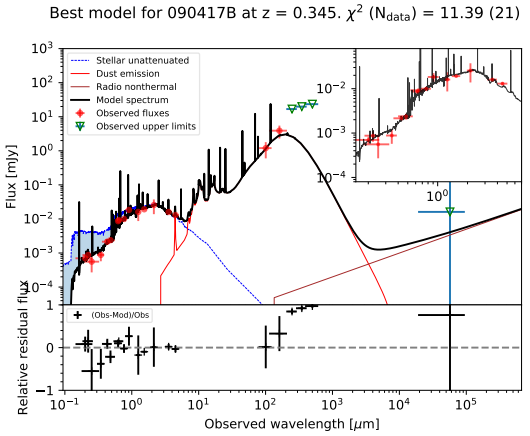

Figure D.19– Best-fitted SED for GRBH 090417B. Colour and symbols convention as in Figure D.1.

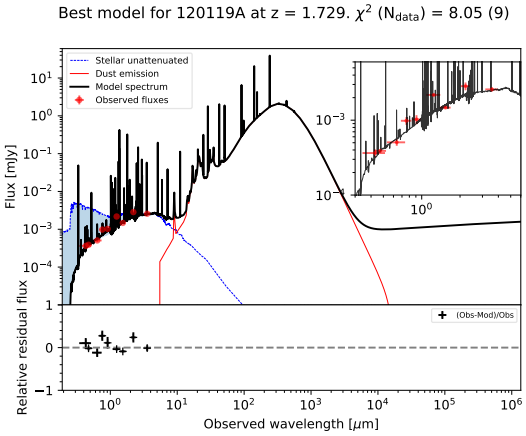

Figure D.22– Best-fitted SED for GRBH 120119A. Colour and symbols convention as in Figure D.1.

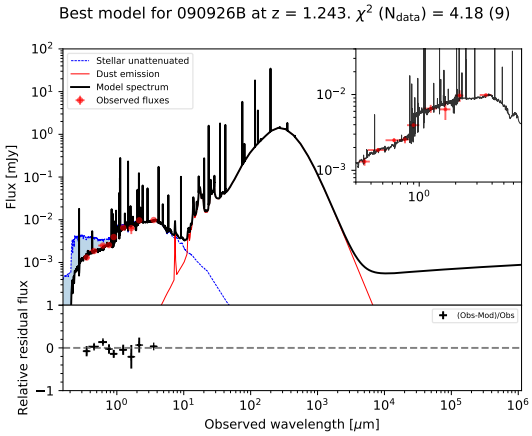

Figure D.20– Best-fitted SED for GRBH 090926B. Colour and symbols convention as in Figure D.1.

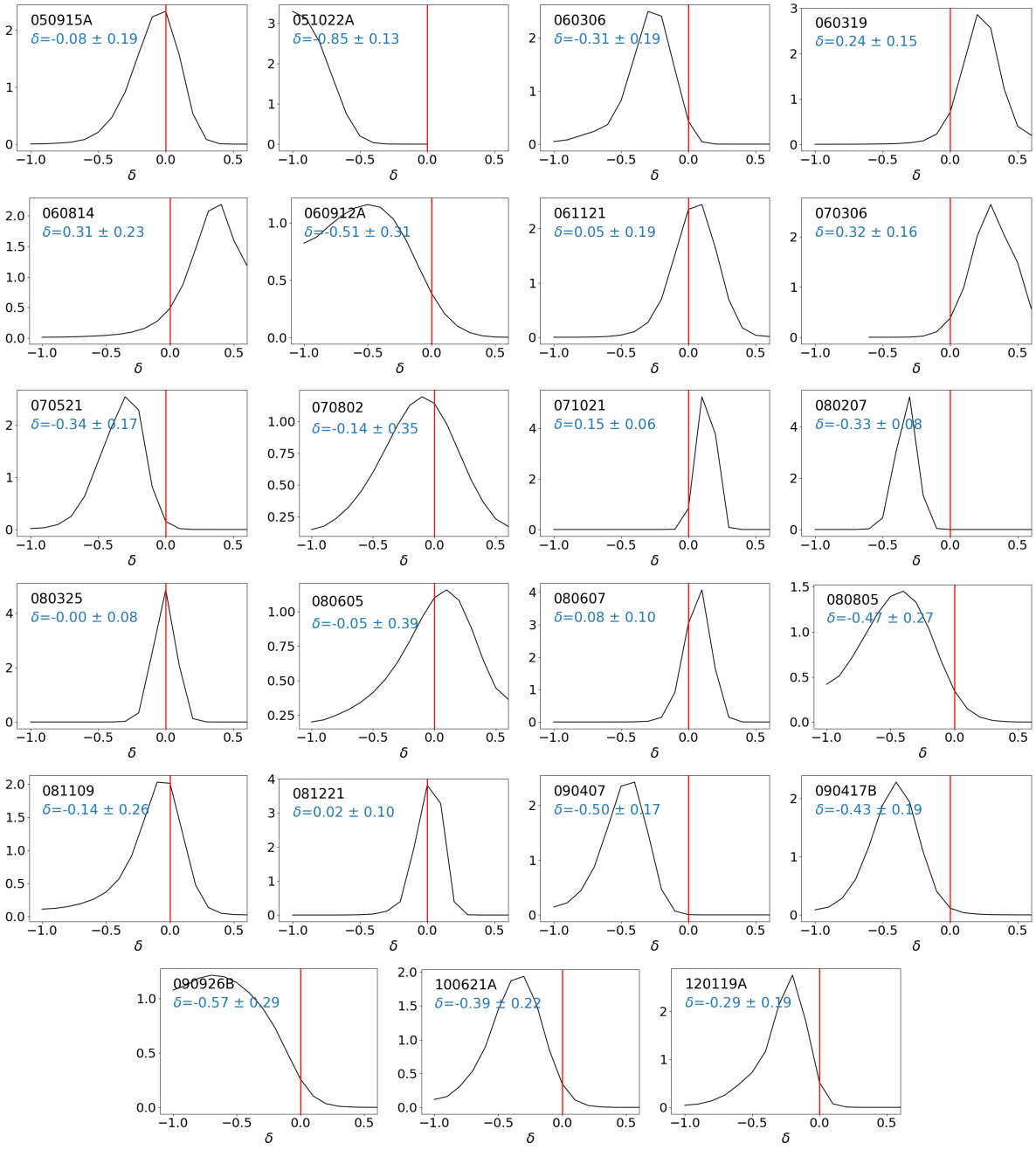

Figure D.23– Probability distribution function of the powerlaw slope for all GRBHs. The vertical red line corresponds to the slope of the original Calzetti law. The median value and standard deviation for each GRBH are reported.